

# UC San Diego

## UC San Diego Electronic Theses and Dissertations

### Title

Using Buckling-Restrained Braces on Long-Span Bridges Near Seismic Faults /

### Permalink

<https://escholarship.org/uc/item/9d77k2sc>

### Author

Lanning, Joel Thomas

### Publication Date

2014

Peer reviewed|Thesis/dissertation

UNIVERSITY OF CALIFORNIA, SAN DIEGO

Using Buckling-Restrained Braces on Long-Span Bridges Near Seismic Faults

A Dissertation submitted in partial satisfaction of the requirements for the degree

Doctor of Philosophy

in

Structural Engineering

by

Joel Thomas Lanning

Committee in charge:

Professor Chia-Ming Uang, Chair  
Professor Raymond de Callafon  
Professor Francesco Lanza Di Scalea  
Professor José Restrepo  
Professor Pui-Shum Shing

2014

Copyright

Joel Thomas Lanning, 2014

All rights reserved.

The Dissertation of Joel Thomas Lanning is approved, and it is acceptable in quality and form for publication on microfilm and electronically:

---

---

---

---

---

Chair

University of California, San Diego

2014

## DEDICATION

*To my loving and supportive parents, Thomas and Mary Lanning.*

*To Lauren for her love and selfless support, always, and during this writing.*

*To my all my great friends for helping me maintain perspective.*

*I owe you all a great deal of time and attention which I intend to give you.*

## EPIGRAPH

Luck affects everything. Let your hook always be cast; in the stream where you least expect it there will be a fish.

*Ovid*

## TABLE OF CONTENTS

SIGNATURE PAGE .....	iii
DEDICATION .....	iv
EPIGRAPH.....	v
TABLE OF CONTENTS .....	vi
LIST OF FIGURES .....	x
LIST OF TABLES .....	xix
LIST OF TABLES .....	xix
ACKNOWLEDGEMENTS .....	xxi
VITA.....	xxii
ABSTRACT OF THE DISSERTATION.....	xxiv
1 INTRODUCTION.....	1
1.1 Seismic Capacity Design Philosophy.....	1
1.2 Long-Span Bridge Seismic Retrofits.....	2
1.3 Buckling-Restrained Braces .....	3
1.3.1 Buildings .....	3
1.3.2 Bridges .....	5
1.4 Current Testing Practice .....	6
1.4.1 AISC Loading Protocol.....	6
1.4.2 Other Testing .....	7
1.4.3 Strength Adjustment Factors.....	8
1.5 Dissertation Outline and Chapter Summary.....	9
1.5.1 Chapter 1 .....	10
1.5.2 Chapter 2.....	10
1.5.3 Chapter 3.....	10
1.5.4 Chapter 4.....	11
1.5.5 Chapter 5.....	11
1.5.6 Chapter 6.....	12
1.5.7 Chapter 7.....	12

2	CASE STUDY OF VTB AND LOADING PROTOCOL DEVELOPMENT.....	17
2.1	Seismic Response Evaluation of BRB-Retrofit of VTB: A Parametric Case Study .....	17
2.1.1	Finite Element Modeling of the Vincent Thomas Bridge.....	18
2.1.2	Input Earthquake Ground Motion.....	19
2.1.3	Finite Element Modeling of the BRBs.....	20
2.1.4	Parameterization of BRB Characteristics .....	21
2.1.5	Monitored Response Quantities .....	23
2.1.6	Global Parametric Variation .....	24
2.1.7	Local Parametric Variation .....	25
2.1.8	Results and Summary of Parametric Study .....	27
2.2	Loading Protocol Development.....	28
2.2.1	Introduction.....	28
2.2.2	VTB Proof Protocol .....	29
2.2.3	Near Fault Protocol .....	30
2.2.4	Dynamic Loading Protocols .....	32
2.2.5	Development of Dynamic Near Fault Protocols.....	34
3	NEAR FAULT PROTOCOL TESTING OF FULL-SCALE BRBs.....	60
3.1	Specimens.....	60
3.2	Test Setup.....	60
3.3	Loading.....	61
3.4	Data Reduction .....	63
3.5	Basic Test Results.....	65
3.5.1	Specimen 1 .....	66
3.5.2	Strengthened Brackets .....	67
3.5.3	Specimen 2.....	67
3.5.4	Specimen 3.....	69
3.5.5	Specimen 4.....	70
3.5.6	Specimen 5.....	71
3.5.7	Specimen 6.....	71
3.6	Overall Performance.....	72
4	DESIGN AND TESTING IMPLICATIONS OF TEST RESULTS.....	154
4.1	Effect of Large Nonsymmetrical Cycles .....	154
4.2	A Consistent Measure of BRB Unbalanced Forces .....	156
4.3	Effect of Yielding Core Steel Type .....	159
4.4	Effect of Strain Rate .....	161



5	MENEGOTTO-PINTO MODEL FOR BUCKLING-RESTRAINED BRACES	173
5.1	Introduction .....	173
5.2	Literature Review .....	173
5.3	Correlation of Bilinear Truss Element .....	175
5.3.1	A36 BRB Subjected to the AISC Protocol .....	176
5.3.2	A36 and SS BRB Subjected to the Near Fault Protocol .....	176
5.4	Menegotto-Pinto Material Model .....	177
5.4.1	Background .....	177
5.4.2	Representation of BRBs .....	181
5.5	Modifications for Modeling BRBs .....	182
5.5.1	Bauschinger Region Parameters .....	182
5.5.2	Tension and Compression Post-Yield Stiffnesses .....	184
5.5.3	Isotropic Hardening Parameters .....	185
5.6	BRBMP Correlation with Pseudo-Static Test Results .....	187
5.7	Incorporation of Strain Rate .....	188
5.8	BRBMP Correlation with Dynamic Test Results .....	191
5.9	Conclusions and Future Improvements .....	192
6	BRB GUSSET PLATE OUT-OF-PLANE STABILITY .....	217
6.1	Introduction .....	217
6.2	Current Design Practice .....	217
6.3	BRBF System-Level Stability .....	219
6.4	Simplified System Stability .....	221
6.5	Gusset and Brace Finite Element Models .....	224
6.6	Gusset Elastic Rotational Stiffness .....	225
6.6.1	GRS Calculation .....	225
6.6.2	Comparisons to Finite Element Model Results .....	228
6.7	Gusset Plastic Moment Capacity .....	229
6.7.1	Yield Line Analysis .....	230
6.7.2	Calculation and Verification of Gusset Plate Plastic Moment Capacity .....	231
6.7.3	Gusset Plate Moment Capacity under Brace Axial Load .....	233
6.8	Framework Simplified Stability Model .....	235
7	SUMMARY AND CONCLUSIONS .....	261
7.1	Summary .....	261
7.2	Conclusions .....	263
7.3	Future Work .....	266

APPENDIX A. PARAMETRIC STUDY PLOTS .....	267
APPENDIX B. PROTOCOL DEVELOPMENT GROUND MOTIONS.....	285
APPENDIX C. BRB GUSSET PLATE DIMENSIONS .....	292
REFERENCES .....	297

## LIST OF FIGURES

Figure 1.1 BRB Makeup and Hysteretic Features.....	14
Figure 1.2 AISC Standard Loading Protocol for Buckling-Restrained Braces.....	14
Figure 1.3 Typical BRB Hysteretic Performance (Newell et al. 2006).....	15
Figure 1.4 Strength Adjustment Factor Definitions for the <i>i</i> -th Cycle.....	15
Figure 1.5 Example of Unbalanced BRB Force Resultant in Chevron Frame.....	16
Figure 2.1 Vincent Thomas Bridge .....	43
Figure 2.2 Vincent Thomas Bridge schematic and finite element model .....	43
Figure 2.3 Photos of VTB Damper Disassembly and Internal Damage.....	44
Figure 2.4 Damaged Viscous Damper Hysteretic Behavior .....	45
Figure 2.5 Bent 10 Longitudinal Ground Motion (Moffatt and Nichol 1996).....	46
Figure 2.6 Design-Level Earthquake Pseudo-Acceleration Response Spectra ( $\zeta=5\%$ ).....	47
Figure 2.7 Bilinear Truss Element for BRB.....	48
Figure 2.8 BRB Lengths Considered in Parametric Variation .....	48
Figure 2.9 Example of Global Variation of BRB Yield Force and Length.....	49
Figure 2.10 Example Parametric Study Response .....	50
Figure 2.11 Force-Phase Relationship of BRBs and Dampers.....	51
Figure 2.12 Tower Seismic Force Demand Envelopes: Design-Level Earthquake .....	52
Figure 2.13 SC BRB Hysteretic Resopnse, Design-Level Earthquake .....	53
Figure 2.14 Example of Protocol Parameters (Proof Protocol).....	53
Figure 2.15 VTB Proof Protocol .....	54
Figure 2.16 Protocol Development Process .....	55
Figure 2.17 BRB Demand Quantities and those of the Near Fault Protocol.....	56
Figure 2.18 Near Fault Protocol .....	57
Figure 2.19 Relative Cumulative Effects of Near Fault and AISC Protocols .....	57
Figure 2.20 Dynamic Proof Protocol.....	58
Figure 2.21 Dynamic Near Fault Protocol .....	59
Figure 3.1 Overall Specimen Geometry and Basic Instrumentation.....	81
Figure 3.2 ASTM A240, Type 304/304L Stainless Steel Tensile Coupon Tests at Pseudo-Static and Dynamic Rates.....	82

Figure 3.3 Specimen Installed in the SRMD Shake Table .....	82
Figure 3.4 Energy Based Ductility Calculation.....	83
Figure 3.5 Specimen 1 End Conditions .....	84
Figure 3.6 Specimen 2 and 5 End Conditions (Specimen 5 shown) .....	85
Figure 3.7 Specimen 1 Test Setup.....	86
Figure 3.8 Specimen 1 End Condition .....	86
Figure 3.9 Specimen 1 after Tension Direction Proof Protocol .....	87
Figure 3.10 Original Bracket after Specimen1 Compression Direction Proof Protocol .....	88
Figure 3.11: Specimen 1 and Gusset Plate after Compression Proof Protocol .....	89
Figure 3.12 Specimen 1: Brace Deformation Time Histories (Tension Proof Protocol) .....	90
Figure 3.13 Specimen 1: Brace Force vs. Axial Deformation (Tension Proof Protocol) .....	90
Figure 3.14 Specimen 1: Hysteretic Energy and Estimated Cumulative Ductility Time History (Tension Proof Protocol).....	91
Figure 3.15 Specimen 1: Brace Deformation Time Histories (Compression Proof Protocol) .....	91
Figure 3.16 Specimen 1: Brace Force vs. Axial Deformation (Compression Proof Protocol) .....	92
Figure 3.17 Specimen 1: Hysteretic Energy Time History (Compression Proof Protocol) .....	92
Figure 3.18 Specimen 1: Brace Deformation Time Histories (All Tests).....	93
Figure 3.19 Specimen 1: Brace Force vs. Axial Deformation (All Tests) .....	93
Figure 3.20 Specimen 1: Hysteretic Energy Time History (All Tests) .....	94
Figure 3.21: Specimen 1 Core Plate after All Tests .....	95
Figure 3.22 Original and New, Strengthened, Brackets on the Platen Reaction Block	96
Figure 3.23 Specimen 2: Test Setup.....	96
Figure 3.24 Specimen 2: End Condition (Specimen 5 shown) .....	97
Figure 3.25 Effectiveness of New Strengthened Brackets .....	97

Figure 3.26 Specimen 2: Brace Deformation Time Histories (Compression Proof Protocol) .....	98
Figure 3.27 Specimen 2: Brace Force vs. Axial Deformation (Compression Proof Protocol) .....	98
Figure 3.28 Specimen 2: Hysteretic Energy Time History (Compression Proof Protocol) .....	99
Figure 3.29 Specimen 2: Brace Deformation Time Histories (Near-Fault Protocol).	100
Figure 3.30 Specimen 2: Brace Force vs. Axial Deformation (Near-Fault Protocol)	100
Figure 3.31 Specimen 2: Hysteretic Energy Time History (Near-Fault Protocol).....	101
Figure 3.32 Specimen 2: Brace Deformation Time Histories (AISC Standard Protocol) .....	102
Figure 3.33 Specimen 2: Brace Force vs. Axial Deformation (AISC Standard Protocol) .....	102
Figure 3.34 Specimen 2: Hysteretic Energy Time History (AISC Standard Protocol) .....	103
Figure 3.35 Specimen 2: Brace Deformation Time Histories (All Tests) .....	104
Figure 3.36 Specimen 2: Brace Force vs. Axial Deformation (All Tests) .....	104
Figure 3.37 Specimen 2: Hysteretic Energy Time History (All Tests) .....	105
Figure 3.38: Specimen 2 Core Plate after All Tests .....	106
Figure 3.39 Specimen 3: Test Setup .....	107
Figure 3.40 Specimen 3: End Condition .....	107
Figure 3.41 Specimen 3: Brace Deformation Time Histories (Dyn. Proof Protocol)	108
Figure 3.42 Specimen 3: Brace Force vs. Axial Deformation (Dyn. Proof Protocol)	109
Figure 3.43 Specimen 3: Inertial Force vs. Axial Deformation (Dyn. Proof Protocol) .....	109
Figure 3.44 Specimen 3: Hysteretic Energy Time History (Dyn. Proof Protocol) ....	110
Figure 3.45 Specimen 3: Brace Deformation Time Histories (Dyn. Near Fault Protocol) .....	111
Figure 3.46 Specimen 3: Brace Force vs. Axial Deformation (Dyn. Near-Fault Protocol) .....	112

Figure 3.47 Specimen 3: Brace Force vs. Axial Deformation (Dyn. Near-Fault Protocol) .....	112
Figure 3.48 Specimen 3: Hysteretic Energy Time History (Dyn. Near-Fault Protocol) .....	113
Figure 3.49 Specimen 3: Brace Deformation Time Histories (Dyn. AISC Protocol)	114
Figure 3.50 Specimen 3: Brace Force vs. Axial Deformation (Dyn. AISC Protocol)	115
Figure 3.51 Specimen 3: Inertial Force vs. Axial Deformation (Dyn. AISC Protocol) .....	115
Figure 3.52 Specimen 3: Hysteretic Energy Time History (Dyn. AISC Protocol) ....	116
Figure 3.53 Specimen 3: Brace Deformation Time Histories (Dyn. Fracture Protocol) .....	117
Figure 3.54 Specimen 3: Brace Force vs. Axial Deformation (Dyn. Fracture Protocol) .....	118
Figure 3.55 Specimen 3: Brace Force vs. Axial Deformation (Dyn. Fracture Protocol) .....	118
Figure 3.56 Specimen 3: Hysteretic Energy Time History (Dyn. Fracture Protocol)	119
Figure 3.57 Specimen 3: Brace Deformation Time Histories (All Tests) .....	120
Figure 3.58 Specimen 3: Brace Force vs. Axial Deformation (All Tests) .....	121
Figure 3.59 Specimen 3: Brace Force vs. Axial Deformation (All Tests) .....	121
Figure 3.60 Specimen 3: Hysteretic Energy Time History (All Tests) .....	122
Figure 3.61 Specimen 4: Test Setup .....	123
Figure 3.62 Specimen 4: End Condition .....	123
Figure 3.63 Specimen 4 Incipient Connection Instability After All Tests .....	124
Figure 3.64 Specimen 4: Brace Deformation Time Histories (Proof Protocol) .....	125
Figure 3.65 Specimen 4: Brace Force vs. Axial Deformation (Proof Protocol) .....	125
Figure 3.66 Specimen 4: Hysteretic Energy Time History (Proof Protocol) .....	126
Figure 3.67 Specimen 4: Brace Deformation Time Histories (Near Fault Protocol) .	127
Figure 3.68 Specimen 4: Brace Force vs. Axial Deformation (Near-Fault Protocol)	127
Figure 3.69 Specimen 4: Hysteretic Energy Time History (Near-Fault Protocol) .....	128

Figure 3.70 Specimen 4: Brace Deformation Time Histories (AISC Standard Protocol)	129
Figure 3.71 Specimen 4: Brace Force vs. Axial Deformation (AISC Standard Protocol)	129
Figure 3.72 Specimen 4: Hysteretic Energy Time History (AISC Protocol)	130
Figure 3.73 Specimen 4: Brace Deformation Time Histories (All Tests)	131
Figure 3.74 Specimen 4: Brace Force vs. Axial Deformation (All Tests)	131
Figure 3.75 Specimen 4: Hysteretic Energy Time History (All Tests)	132
Figure 3.76 Specimen 5: Test Setup	133
Figure 3.77 Specimen 5: End Condition	133
Figure 3.78 Specimen 5: Brace Deformation Time Histories (Near Fault Protocol)	134
Figure 3.79 Specimen 5: Brace Force vs. Axial Deformation (Near Fault Protocol)	134
Figure 3.80 Specimen 5: Hysteretic Energy Time History (Near-Fault Protocol)	135
Figure 3.81 Specimen 5: Brace Deformation Time Histories (Compr. Near-Fault Protocol)	136
Figure 3.82 Specimen 5: Brace Force vs. Axial Deformation (Compr. Near-Fault Protocol)	136
Figure 3.83 Specimen 5: Hysteretic Energy Time History (Compr. Near-Fault Protocol)	137
Figure 3.84 Specimen 5: Brace Deformation Time Histories (All Tests)	138
Figure 3.85 Specimen 5: Brace Force vs. Axial Deformation (All Tests)	138
Figure 3.86 Specimen 5: Hysteretic Energy Time History (All Tests)	139
Figure 3.87: Specimen 5 Core Plate after All Tests	140
Figure 3.88 Specimen 6: Test Setup	141
Figure 3.89 Specimen 6: End Condition	141
Figure 3.90 Specimen 6: Brace Deformation Time Histories (Dyn. Proof Protocol)	142
Figure 3.91 Specimen 6: Brace Force vs. Axial Deformation (Dyn. Proof Protocol)	143
Figure 3.92 Specimen 6: Inertial Force vs. Axial Deformation (Dyn. Proof Protocol)	143

Figure 3.93 Specimen 6 Hysteretic Energy Time History (Dyn. Proof Fault Protocol)	144
Figure 3.94 Specimen 6 Brace Deformation Time Histories (Dyn. Near Fault Protocol)	145
Figure 3.95 Specimen 6 Brace Force vs. Axial Deformation (Dyn. Near-Fault Protocol)	146
Figure 3.96 Specimen 6 Inertial Force vs. Axial Deformation (Dyn. Near-Fault Protocol)	146
Figure 3.97 Specimen 6 Hysteretic Energy Time History (Dyn. Near-Fault Protocol)	147
Figure 3.98 Specimen 6: Brace Deformation Time Histories (Dyn. AISC Protocol)	148
Figure 3.99 Specimen 6: Brace Force vs. Axial Deformation (Dyn. AISC Standard Protocol)	149
Figure 3.100 Specimen 6: Inertial Force vs. Axial Deformation (Dyn. AISC Standard Protocol)	149
Figure 3.101 Specimen 6: Hysteretic Energy Time History (Dyn. AISC Standard Protocol)	150
Figure 3.102 Specimen 6: Brace Deformation Time Histories (All Tests)	151
Figure 3.103 Specimen 6: Brace Force vs. Axial Deformation (All Tests)	152
Figure 3.104 Specimen 6: Inertial Force vs. Axial Deformation (All Tests)	152
Figure 3.105 Specimen 6: Hysteretic Energy Time History (All Tests)	153
Figure 4.1 Unbalanced Forces from Conventional $\beta$ -Method	165
Figure 4.2 Unbalanced Forces from Proposed $\gamma$ -Method	165
Figure 4.3 Effect of Large Unsymmetrical Cycles on BRBs	166
Figure 4.4 Subsequent Large Excursions on Specimen 2	167
Figure 4.5 Examples of Potential BRB Bridge Configurations Affected by Unbalanced Forces	168
Figure 4.6 Significant Cycle Peaks of the Near-Fault Protocols	169
Figure 4.7 Effect of Yielding Core Material: Specimens 3 and 6	170
Figure 4.8 Effect of Yielding Core Material: Specimens 2 and 5, 2nd Test	170



Figure 4.9 Effect of Strain Rate: Specimens 3 and 6 .....	171
Figure 4.10 Effect of Strain Rate: Specimens 5 and 6, 2nd Test.....	171
Figure 4.11 Relative Normalized Peak Force Values as a Ratio.....	172
Figure 5.1 Correlation of Bilinear Element Prediction and Typical BRB Test.....	196
Figure 5.2 Bilinear BRB Element Simulation of Near Fault Test Results (Chapter 3) .....	197
Figure 5.3 Menegotto-Pinto Material Model.....	198
Figure 5.4 Basic Menegotto-Pinto (MP) Model versus Pseudo-Static A36 Specimen 5 .....	199
Figure 5.5 Basic MP Model versus Pseudo-Static SS Specimen 4 .....	200
Figure 5.6 Example Significant Cycles for MP Parameter Measurement (Specimen 4) .....	201
Figure 5.7 Variation of $R$ for SS BRB.....	201
Figure 5.8 Variation of Tension Post-Yield Stiffness, $b_T$ , (All Specimens).....	202
Figure 5.9 Variation of Compression Post-Yield Stiffness, $b_C$ , (All Specimens) .....	202
Figure 5.10 Isotropic Hardening, $P_{sh}$ , Surfaces .....	203
Figure 5.11 BRBMP Model versus Pseudo-Static Tested A36 Specimen 2P.....	204
Figure 5.12 BRBMP Model versus Pseudo-Statically Tested SS Specimen 4 .....	205
Figure 5.13 BRBMP Model versus Dynamically Tested SS Specimen 3.....	206
Figure 5.14 Concept for Proposed Instantaneous Strain Rate Response.....	207
Figure 5.15 Pseudo-Static and High Strain Rate Tensile Test .....	208
Figure 5.16 Dynamic Overstrength from SS Tensile Tests.....	208
Figure 5.17 Dynamic Overstrength Surface for SS.....	209
Figure 5.18 Dynamic Overstrength from Tensile Tests for A36 Steel.....	210
Figure 5.19 Dynamic Overstrength Cumulative Ductility Dependency .....	211
Figure 5.20 Dynamic BRBMP versus Dynamically Tested SS Specimen 3 .....	212
Figure 5.21 Dynamic BRBMP versus Dynamically Tested A36 Specimen 6 .....	213
Figure 5.22 BRBMP versus Pseudo-Statically Tested A36 Specimen 5 .....	214
Figure 5.23 Dynamic BRBMP versus Pseudo-Statically Tested A36 Specimen 5....	215
Figure 5.24 Dodd-Restrepo Model Backbone Curve Tangent for Stainless Steel .....	216

Figure 6.1 Aspects of Current BRB Gusset Plate Design Procedures .....	241
Figure 6.2 Observed BRB Gusset Failures in BRBF Testing .....	242
Figure 6.3 BRBF System Stability Model.....	242
Figure 6.4 BRB Connections.....	243
Figure 6.5 Simplified BRB-Gusset System Stability Model.....	244
Figure 6.6 Buckling Load of 2-Spring System with Initial Imperfection .....	245
Figure 6.7 Abaqus Finite Element Model of Gusset and Brace Connection.....	246
Figure 6.8 Specimen 1 Gusset Plate Instability and Bend Line Simulation.....	247
Figure 6.9 Dimensions for Calculating Gusset Plate Rotational Stiffness (GRS) .....	248
Figure 6.10 Gusset Plate Dimensions for GRS Calculation, Specimen 4 .....	248
Figure 6.11 Definitions of GRS Zone 1 .....	249
Figure 6.12 Definition of GRS Zone 2.....	249
Figure 6.13 Idealization of Plate for GRS Zone 1 and 2 .....	250
Figure 6.14 Strip Beam End Rotations.....	251
Figure 6.15 Internal Forces from Strip Beam Due to Brace Unit Rotation.....	251
Figure 6.16 Internal Moments from Strip Beam Due to Brace Unit Rotation .....	252
Figure 6.17 Geometry for YLA of Uninterrupted Bend Line Gusset .....	253
Figure 6.18 Geometry of YLA for Interrupted Bend Line Gusset .....	254
Figure 6.19 External Work by Transverse Force on Gusset .....	255
Figure 6.20 External Work by Axial Force on Gusset with Initial Imperfection.....	255
Figure 6.21 Abaqus Verification of Yield Line Analysis.....	256
Figure 6.22 Measured Initial Imperfection.....	259
Figure 6.23 Preliminary BRB Gusset Plate Stability Prediction .....	260
Figure A.1 Effect of BRB Post-Yield Stiffness, $\alpha$ , on VTB Response: Main/Tower	269
Figure A.2 Effect of BRB Yield Strength, $\gamma$ , on VTB Response: Side/Cable Bent...	270
Figure A.3 Effect of BRB Yield Strength, $\gamma$ , on VTB Response: Side/Tower .....	271
Figure A.4 Effect of BRB Yield Strength, $\gamma$ , on VTB Response: Main/Tower .....	272
Figure A.5 Comparison of Perform-3D and ADINA Responses: Side/Cable Bent...	273
Figure A.6 Comparison of Perform-3D and ADINA Responses: Side/Tower .....	274
Figure A.7 Comparison of Perform-3D and ADINA Responses: Main/Tower .....	275

Figure A.8 Effect of Local BRB Yield Strength, $\gamma$ , on VTB Response: Side/CableBent .....	276
Figure A.9 Effect of Local BRB Yield Strength, $\gamma$ , on VTB Response: Side/Tower	277
Figure A.10 Effect of Local BRB Yield Strength, $\gamma$ , on VTB Response: Main/Tower .....	278
Figure A.11 Local Parameter Refinement: Side/Cable Bent.....	279
Figure A.12 Localized Parameter Refinement: Side/Tower .....	280
Figure A.13 Localized Parameter Refinement: Main/Tower .....	281
Figure A.14 Local Parameter Refinement: Adjacent Location Insensitivities .....	282
Figure A.15 Final Feasible BRB Solutions .....	283
Figure A.16 Final Feasible BRB Solutions .....	284
Figure B.1 Ground Motions for Near-Fault Protocol Development .....	286
Figure C.1 Specimen 1 .....	292
Figure C.2 Specimen 4 .....	292
Figure C.3 3P.....	293
Figure C.4 3P.....	293
Figure C.5 Tsai 1 .....	293
Figure C.6 Specimen 5 .....	294
Figure C.7 Tsai 3-1.....	295
Figure C.8 Tsai 3-3.....	295
Figure C.9 Takeuchi .....	296

## LIST OF TABLES

Table 1.1 Examples Typical BRB Properties and Performance.....	13
Table 2.1 Existing Viscous Damper Properties.....	37
Table 2.2 Design Earthquake Seismic response of VTB with viscous dampers.....	37
Table 2.3 Basic mode shapes of the VTB with dampers and with BRBs .....	38
Table 2.4 Final Feasible BRB Parameters for VTB retrofit.....	39
Table 2.5 Proof Protocol Peak Core Strains and Rates .....	39
Table 2.6 Summary of Simulated and Near Fault Protocol Cyclic Demand Parameters .....	40
Table 2.7 Near Fault Protocol Peak Core Strains and Rates .....	41
Table 2.8 BRB Testing Strain Rates.....	42
Table 3.1 Specimen Dimensions .....	75
Table 3.2 Mechanical Properties of Core Plates .....	75
Table 3.3 BRB Yield Strength and Deformation .....	76
Table 3.4 Specimen Loading Information.....	76
Table 3.5 Sample Pseudo-Static Target BRB Deformation and SRMD Table Input ..	77
Table 3.6 Sample Dynamic Target BRB Deformations and Rates .....	78
Table 3.7 Sample AISC Standard Protocol Targets .....	79
Table 3.8 Maximum Response Values.....	80
Table 4.1 Measured Unbalanced Forces, $\gamma$ , from Equal and Opposite Tests: Specimens 1 and 2 .....	164
Table 5.1 Identified Menegotto-Pinto Parameters.....	195
Table 6.1 GRS Gusset Plate Dimensions .....	237
Table 6.2 Accuracy of GRS Calculation .....	238
Table 6.3 Gusset Plate Dimensions for YLA .....	239
Table 6.4 Accuracy of Gusset YLA .....	240
Table A.1 Parametric Matrices for Global Adjustment of BRB Mechanical Properties .....	267
Table A.2 Parametric Matrices for Local Adjustment of BRB Mechanical Properties .....	268

Table B.1 Near-Fault Pulse-Type Ground Motions Used for Near Fault Protocol Development.....	285
---	-----

## ACKNOWLEDGEMENTS

Many thanks are due to my advisor and committee chair, Professor Chia-Ming Uang, for his support during my time at UCSD. I owe him a great debt of gratitude for the many opportunities I have been afforded as a direct result of his faith and trust in me. My future is certainly better on his account, and this work would not be possible without his guidance.

Funding for this research was provided by California Department of Transportation under the management of Dr. C. Sikorsky. I would also like to thank CoreBrace, LLC for generously donating test specimens for this research. Thank you to the staff of the SRMD Facility at UCSD, my friends Danny Innamorato and Edward Stovin, for technical assistance and hard work during testing. I am also very grateful to Dr. Christopher Latham and the rest of the Charles Lee Powell Structures Laboratory staff for their camaraderie while sharing with me their knowledge on conducting large scale structural testing. I would also like to thank the Structural Engineering Department for supporting me with a fellowship during my last academic year.

Chapters 2, 3, and 4 in partial, are reprints of the material as it has been submitted for publication. The dissertation author was the first author of these papers.

## VITA

- 2006 B.S. Civil Engineering, The Ohio State University
- 2006-2007 Structural Designer, River Consulting, Columbus, Ohio.
- 2007-2008 M.S. Structural Engineering, University of California, San Diego
- 2009 Structural Designer, Barber & Hoffman Inc., Cleveland, Ohio.
- 2010-2014 Graduate Student Researcher, University of California, San Diego
- 2014 Ph.D. Structural Engineering, University of California, San Diego

## PUBLICATIONS

### Referred Technical Journal

Lanning, J., Uang, C.M. "Using buckling-restrained braces on long-span bridges: Full-scale testing and design implications" (*Submitted: J. of Bridge Eng.*)

Lanning, J., Uang, C.M., "Using buckling-restrained braces on long-span bridges: Case study and near-fault loading protocol development" (*Submitted: J. of Bridge Eng.*)

## Technical Reports

- Lanning, J., Uang, C.M., Benzoni, G., (2013) "The feasibility of using buckling-restrained braces on long-span bridges: Near-fault loading protocols and full-scale testing" *Report No. SSRP-13/17*, Dept. of Structural Engineering, Univ. of California, San Diego, La Jolla, Calif.
- Lanning, J., Uang, C.M., (2013) "Pilot testing of web-restraining braces (WRBs)" *Report No. TR-13/02*. Dept. of Structural Engineering, Univ. of California, San Diego, La Jolla, Calif.
- Lanning, J., Uang, C.M., Benzoni, G., (2012) "Subassemblage testing of CoreBrace buckling-restrained braces (P Series)" *Report Nos. TR-12/03, TR-12/04, and TR-12/06*. Dept. of Structural Engineering, Univ. of California, San Diego, La Jolla, Calif.
- Lanning, J., Benzoni, G., Uang, C.M., (2011) "The feasibility of using buckling-restrained braces for long-span bridges: A case study" *Report No. SSRP-11/09*. Dept. of Structural Engineering, Univ. of California, San Diego, La Jolla, Calif.



## ABSTRACT OF THE DISSERTATION

Using Buckling-Restrained Braces on Long-Span Bridges Near Seismic Faults

by

Joel Thomas Lanning

Doctor of Philosophy in Structural Engineering

University of California, San Diego, 2014

Professor Chia-Ming Uang, Chair

In the past decade highly ductile buckling-restrained braces (BRBs) have become popular in building seismic design. Design provisions and testing protocols considering far-field earthquakes have been developed by AISC. To extend the application to bridges, especially long-span bridges located near major seismic faults, research is lacking to support the development of bridge design provisions.

Viscous dampers used to retrofit the Vincent Thomas Bridge (VTB) in Long Beach, California have been leaking due to traffic and ambient vibrations. With the potential of using BRBs to replace the dampers in a case study, VTB finite element simulations lead to the development of Near Fault loading protocols for prequalification test of BRBs.

A testing program with six full-scale specimens is carried out to verify the ability of currently available BRBs to sustain a deformation demand about twice that commonly tested for building applications. This research identifies inconsistencies in current BRB testing and design conventions, so a rational methodology is proposed for both far- and near-fault ground motions.

In addition to the commonly used mild steel BRBs, four stainless steel (SS) BRBs are also tested in this research; the latter reveals significant cyclic strain hardening. Going beyond the current practice of testing BRBs pseudo-statically, dynamic testing was also conducted. A 20% increase in force response due to the high strain rate effect should not be ignored for near-fault applications. Design and testing recommendations for bridge applications are proposed.

For numerical simulation of BRB response, the commonly used bilinear model is shown to be insufficient. A modified Menegotto-Pinto (MP) material model, intended for OpenSees, that incorporates the following features is shown to provide excellent correlation to test results: (1) a larger strain hardening in compression than in tension, (2) appropriate isotropic hardening relation for SS BRB that includes the effect of cumulative ductility, (3) the instantaneous strain rate effect.

Buckling in the gusset connection of one BRB specimen, and the incipient buckling of another, observed in this research confirms the potential shortcoming of current practice in designing gusset connections when stiffeners are not used. An alternate model that considers the rotational restraint of the gusset and initial out-of-straightness is proposed.

# 1 INTRODUCTION

## 1.1 Seismic Capacity Design Philosophy

Seismic building and bridge codes follow a concept of the damage-tolerant structure. Portions of the structure are designed and detailed specifically to yield under large earthquake ground motions thereby serving as a structural fuse to limit the forces imparted to critical gravity load bearing components. The success of this concept is dependent upon accurate knowledge of the maximum resisting force achievable by the fuse such that the rest of the structure can be designed to remain elastic. Additionally, the fuse must be capable of sustaining relatively large inelastic deformations, providing ample ductility for the seismic force resisting system.

For buildings various types of steel frames have been developed utilizing different mechanisms of steel yielding such as the formation of plastic hinges in moment frame beams, shear yielding of short beam links between braces, and the yielding of diagonal braces. These frames are typically designed through a force-based methodology that distributes the inertial forces due to the ground acceleration based on an assumed vibrational mode shape. More critical buildings, such as hospitals, are increasingly being designed with a performance-based, or displacement-based, approach.

In the U.S. AASHTO *Guide Specifications for LRFD Seismic Bridge Design* (AASHTO 2011) permits the use of three global seismic strategies for bridge at risk of severe seismic, all of which involve the capacity-based philosophy. These include similar systems and force distribution methods as those used in buildings, the

use of ductile elements within the bridge piers, and the use of a fusing mechanism between elastic super- and substructures. Regardless of the system used, all designs must conform to the no-collapse performance criterion under the safety-level evaluation (or design-level) event. The third system is most applicable to the research presented in this dissertation.

## **1.2 Long-Span Bridge Seismic Retrofits**

A number of long-span bridges are parts of major transportation arteries in California. Many near seismic faults and were built before the above modern seismic design strategies were in place. As summarized by Seible (2000), retrofitting efforts have been undertaken to bring them into conformity to the no-collapse performance goal under a safety-evaluation, or design-level earthquake demand. More common events represent functional-evaluation earthquake demands and are required to be sustained with prescribed levels of service. Seismic isolation solutions have been applied to several of these major bridges, along with ductile framing, and the addition of viscous fluid dampers to mitigate. Seismic isolation has received much attention for bridges, as AASHTO has published the *Guide Specifications for Seismic Isolation Design* which also contains limited testing recommendations for types of energy dissipation devices (Zhang 2000).

One of these bridges, the Vincent Thomas Bridge (VTB), was retrofitted with viscous dampers in the mid-1990s. This, and other California bridges, also cross potentially active faults or are near-fault lines, requiring the attention of a Fault-Rupture design level or the near-fault condition. As discussed later in Chapter 2,

recent Caltrans maintenance inspections have revealed that the devices incur damage, characterized by loss of the viscous fluid, due to ambient bridge motion as evidenced by internal wearing. Without a portion of the viscous fluid, the hysteretic response exhibits a gap (Benzoni et al., 2008). Maintenance issues such as these are not desirable for structural seismic mitigation systems due to the spontaneity of earthquake.

### **1.3 Buckling-Restrained Braces**

#### **1.3.1 Buildings**

Buildings and bridges commonly utilize steel diagonal bracing to provide lateral strength and stiffness. In seismic design of buildings some braces are intended to yield in tension and designed and detailed to inelastically buckle out of plane in compression, serving as a structural fuse protecting vital elements and dissipating energy through material damage. In building frames these are called special concentrically braced frames (AISC 2010). But these braces are vulnerable to low-cycle fatigue failure due to highly concentrated deformation in the plastic hinge formed at mid-length during inelastic buckling (Bruneau et al. 2011).

Therefore, using braces capable of yielding in compression without buckling, or buckling-restrained braces (BRBs), has recently become popular in buildings as buckling-restrained braced frames (BRBFs). BRBs are relatively simple in fabrication and require essentially no maintenance. Primarily they consist of a yielding steel core surrounded by, and de-coupled from, concrete mortar within a hollow structural section, as shown in Figure 1.1 along with a schematic representation of the typical

stable hysteretic response. Since compressive loads induce buckling behavior, the core is supported against lateral deformation by the mortar and restraining tube, thereby allowing it to undergo yielding in both tension and compression. This produces excellent energy dissipation with stable and fairly symmetrical hysteretic behavior..

As the yielding core of a BRB experiences multiple inelastic excursions the material undergoes strain hardening, causing brace forces well beyond the initial yield force. Furthermore, during compression excursions Poisson expansion and restrained inelastic high-mode buckling of the yielding core result in contact friction between the core and the restraining assembly. Consequently, compression forces are somewhat larger than tension forces at equal and opposite deformations. Therefore, testing requirements have been set by AISC (see Section 1.4.1) to regulate the unbalanced brace forces, making BRBs more amenable to capacity based design of the adjoining structural members (Section 1.4.3)

Although pioneered in the 1970s in Japan, BRBs received little attention until after the 1994 Northridge and 1995 Kobe earthquakes. Afterwards, the excellent energy dissipation capabilities of BRBs were widely used in Japan. Once codified in AISC 341-05 for building applications (AISC 2005), BRBF also quickly became popular in the U.S. as a ductile seismic force resisting system (Uang et al. 2004). Three companies serve the U.S. market, and many building projects have been completed over that past 15 years or so.

### 1.3.2 Bridges

BRBs have almost exclusively been used for building applications but have been considered in a few bridge-related research projects and seismic retrofits. Usami et al. (2005) and Kanaji et al. (2005) summarized retrofits of the Owatari and Minato Bridges, respectively, in Japan. Both replaced conventional steel truss members with BRBs to provide ductile truss elements. In the U.S., Carden et al. (2004) performed tests using short BRBs in ductile end cross frames for steel plate girders. Pollino and Bruneau (2007) investigated rocking bridge piers with BRB as passive energy dissipation devices. One known U.S. bridge retrofitted using BRBs is the Auburn-Forest Hill Bridge in Auburn, CA, which was recently completed and is documented by Reno and Pohll (2010). The BRBs were used to limit the forces imparted to the superstructure, while providing longitudinal stability of the bridge, after yielding of a linkage plate during a large event.

There are currently no established bridge-specific BRB design guidelines or testing requirements. Just as in the early stages of building BRB applications (Uang et al. 2004), thus far only project-specific requirements and testing programs have been conducted to demonstrate satisfactory performance of proposed BRB for bridges. This research extends beyond this practice by utilizing a statistically developed loading protocol for long-span near-fault bridge application of BRB (discussed in Chapter 2).

BRBs are demanding more attention from the bridge design community, however, and long-span bridges like the Vincent Thomas Bridge, can benefit from these highly ductile braces, as demonstrated in this research.

## 1.4 Current Testing Practice

### 1.4.1 AISC Loading Protocol

The performance of proprietary BRBs is fairly uniform as observed in a number of test reports (e.g. Merritt et al. 2003, Black et al. 2004, Newell et al. 2006, Lanning et al. 2012). Almost exclusively, the braces are tested for implementation in buildings and, therefore, have a different performance expectation as compared to bridges due in part to the force based design approach used in building design.

Since BRBs are currently almost exclusively used in building structures, qualification tests are usually conducted in accordance with Appendix T of the AISC Seismic Provisions 2010 which requires the following loading sequence (shown in Figure 1.2) to be applied to the test specimen:

- (1) 2 cycles of loading at the deformation corresponding to  $\Delta_b = 1.0 \Delta_{by}$
- (2) 2 cycles of loading at the deformation corresponding to  $\Delta_b = 0.5 \Delta_{bm}$
- (3) 2 cycles of loading at the deformation corresponding to  $\Delta_b = 1.0 \Delta_{bm}$
- (4) 2 cycles of loading at the deformation corresponding to  $\Delta_b = 1.5 \Delta_{bm}$
- (5) 2 cycles of loading at the deformation corresponding to  $\Delta_b = 2.0 \Delta_{bm}$
- (6) Additional complete cycles of loading at the deformation corresponding to

$\Delta_b = 1.5 \Delta_{bm}$  as required for the brace test specimen to achieve a cumulative inelastic axial deformation of at least 200 times the yield deformation. where the deformation  $\Delta_b$  is the steel core axial deformation of the test specimen. Note that  $\Delta_{by}$  corresponds to the axial deformation at first significant yield, and  $\Delta_{bm}$  is the axial



deformation which corresponds to the design story drift of the building structure. This is not directly applicable to long-span bridges near-faults, as discussed in Chapter 2.

After steps (1) through (5), the cumulative ductility of 200 is required in step (6). This provides a reference of the resilient nature of BRBs. As will be later referenced, this bodes well for the idea that BRB members are capable of much more taxing demand time histories similar to those found in the current research.

A few examples of some basic BRB performance results are displayed in Table 1.1, and show that the AISC Standard Loading Protocol is by far the lower bound of acceptable BRB performance. Especially noticeable is the maximum cumulative ductility achieved compared to that obtained from the standard protocol. Furthermore, a representative example of BRB performance beyond the standard loading protocol is provided in Figure 2.4 of the case study report (Lanning et al. 2011).

#### **1.4.2 Other Testing**

Maximum strains achieved in the specimens shown in Table 1.1 are observed to be in the range of approximately 2 to 4%. The loading protocol is, as previously mentioned, generally dependent on the design story drift which directly influences the tested axial strain. More recent research has shown all-steel BRB is capable of satisfactory low-cycle fatigue cumulative ductility at constant strain amplitudes of 4.5%. Other researchers have reported constant strain amplitude testing of BRB in the range of  $\pm 2.4\%$ , or peak amplitude of 4.5%, achieving cumulative ductility factors much higher than that required by AISC Seismic Provisions (Nakamura et al. 2000). Additionally, larger strains have been imposed through increasing strain amplitude

tests which reached upwards of  $\pm 5.2\%$  (Takeuchi et al. 2005). Moreover, tests from shake table earthquake simulations exhibited a half-cycle pulse of 7% maximum strain amplitude, while still achieving very large cumulative ductility measures (Yamaguchi et al. 2004). The aforementioned testing, however, has been conducted in Japan and is reported only in Japanese references but are summarized by Takeuchi et al. 2008. Some of these results are shown in Table 1.1, along with the cumulative ductility factors reportedly obtained from increasing strain amplitude testing which more closely resembles the AISC Standard Loading Protocol. This is provided as a check to the very large cumulative ductility values. Additionally, the tests conducted through shake table excitation, which exhibited some pulse-like strain demands, are shown in Figure 4.26 of the report on the VTB case study (Lanning et al. 2011)..

### 1.4.3 Strength Adjustment Factors

The overstrength of BRBs is typically closely monitored in prequalification testing due to the importance in design of having good knowledge of the structural fuse maximum expected force for capacity design of the surrounding members and connections.

The tension strength adjustment factor provides a measure of the maximum tension force in each cycle compared to the nominal yield force, and is defined as:

$$\omega = \frac{T_{\max}}{P_{yn}} = \frac{T_{\max}}{F_{yn} A_{sc}} \quad (1.1)$$

where  $F_{yn}$  = nominal yield strength, and  $A_{sc}$  = area of the yielding core. The compression strength adjustment factor,  $\beta$ , is defined as:

$$\beta = \frac{P_{max}}{T_{max}} \quad (1.2)$$

where  $P_{max}$  is the maximum compressive force, and  $T_{max}$  is the maximum tension force corresponding to equal but opposite brace deformations,  $\Delta^+$  and  $\Delta^-$  in Figure 1.4, from the  $i$ -th cycle of the AISC Protocol. Note that  $\beta$  is measured from subsequent tension and compression excursions from a single tested brace specimen.

Since BRB very often used in the chevron configuration in U.S. buildings, the value of  $\beta$  is limited to 1.3 in AISC 341 (AISC 2010), as measured within the AISC protocol (Figure 1.2), to limit the resultant force imparted to the horizontal frame beam, as shown in Figure 1.5.

## 1.5 Dissertation Outline and Chapter Summary

This dissertation begins with a brief introduction to current seismic design philosophies for building and bridge structures, along with a discussion on the role that buckling-restrained braces (BRBs) play within these methodologies. Chapters 2 through 4 provide new information regarding the use of BRBs on long-span bridges. This includes analysis that applies BRBs to a bridge in a case study, the development of a new testing loading protocol, a novel physical testing program carried out on full-scale BRBs, a new consistent testing methodology, and observations on the effect of both high strain rate and the use of stainless steel (SS) for the BRB yielding core. Chapter 5 then modifies an popular hysteretic model, and measures parameters for its characterization of BRBs including the effects of SS and high strain rates. Chapter 6

offers new design-oriented tools for the analysis of the BRB gusset plate system stability.

### **1.5.1 Chapter 1**

A brief introduction is provided to current practices in seismic design of building and bridge structures. A particular building seismic force resisting element called buckling-restrained braces (BRBs) are then summarized, along with a background on their use in the U.S. and Japan bridge seismic design. The motivation is explained behind the studying the use of BRBs on long-span bridges, which was carried out through a case study of the Vincent Thomas Bridge (VTB). The overall research objectives are then summarized, and a brief description of each chapter in the dissertation is then provided in Sections 1.5.1 through 1.5.7.

### **1.5.2 Chapter 2**

Chapter 2 presents a case study carried out on the VTB to identify feasible BRBs that also provide acceptable or improved seismic response mitigation. A Near Fault Protocol is then developed which is intended for use as a prequalifying testing protocol for BRB implementation on long-span bridges near seismic faults. Included was a fully dynamic version to investigate the strain rate effect on BRB, to reflect the high strain rate imparted to the braces due to the near-fault pulse-type motions required by the seismic risk of this structure.

### **1.5.3 Chapter 3**

Chapter 3 presents an abridged summary of a full-scale testing program of six BRBs, carried out using the new near-fault protocols. Several specimens comprised

Type 304 stainless steel (SS) yielding cores, which had not been tested before. All braces performed very well, and the use of existing BRB technology was deemed to be feasible as a maintenance-free seismic response mitigation systems on long-span bridges near seismic faults.

#### **1.5.4 Chapter 4**

Inconsistencies in current BRB design and testing conventions were highlighted by the large nonsymmetrical cycles of the Near Fault Protocol testing results of Chapter 3. In response, a new consistent testing methodology is proposed which more accurately represents the actual BRB loading conditions in a frame. Implications of the very different inelastic response of SS, versus A36 steel, BRBs are discussed along with those of high strain rate in near-fault structures with BRBs.

#### **1.5.5 Chapter 5**

Several aspects of the BRB properties and loading conditions investigated in this research draw attention to the circumstances leading to poor representation of the experimental results by a bilinear truss element, commonly used by design and researchers to model BRB hysteretic behavior. In this chapter modifications are made to the well established Menegotto-Pinto hysteretic model to better reflect BRB behavior. The model is also updated to represent the instantaneous strain rate through an amplification function dependent on the instantaneous strain rate, ductility, and cumulative ductility. Parameters for this modified model are identified for both SS and A36 steels, and excellent BRB representation is demonstrated.

### **1.5.6 Chapter 6**

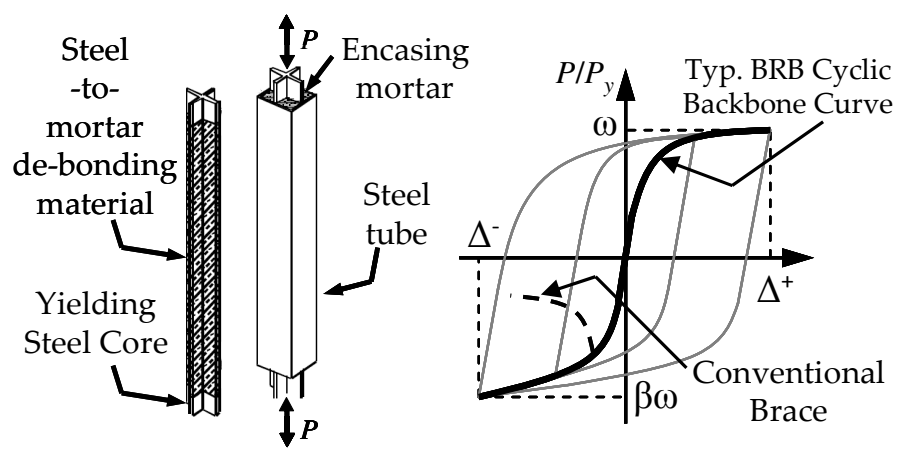
Chapter 6 investigates the BRB gusset plate instability observed from testing in Chapter 3, and in other testing found in the literature. Then design-oriented methods are proposed for obtaining the gusset rotational stiffness (GRS) and the gusset plastic moment (GPM), two critical values needed to assess the BRB gusset system stability. Finally, a preliminary framework for identifying an ultimate load for a given BRB gusset plate system is presented.

### **1.5.7 Chapter 7**

This chapter provides a summary of the work presented in this dissertation, and highlights areas of original contribution to the field of seismic design of structures. Recommendations for future work are offered.

Table 1.1 Examples Typical BRB Properties and Performance

Source / Specimen	Length (ft)	$P_y$ (kips)	$\beta\omega$	Max. Axial Strain (%)	Cumulative Ductility	
					Standard Protocol	Max. Achieved
(Merritt et al. 2003)						
1D, 2D	18	388	1.67	2.3	460	1100
3D, 4D	18	712	1.70	2.4	375	700
5D, 6D	19	897	1.63	2.3	345	1400
(Black et al. 2004)						
99-2	12	364	N/R	2.00	243.5	637
00-11	12	454	1.49		243.5	700
(Newell et al. 2005)						
1F	19	1013	1.56	3.92	161	759
2F	19	1013	1.51	3.67	149	632
(Newell et al. 2006)						
1G, 2G	22	450	1.59	3.51	246	1143
3G, 4G	21	1013	1.51	3.68	247	758



(a) BRB Anatomy

(b) Hysteretic Behavior

Figure 1.1 BRB Makeup and Hysteretic Features

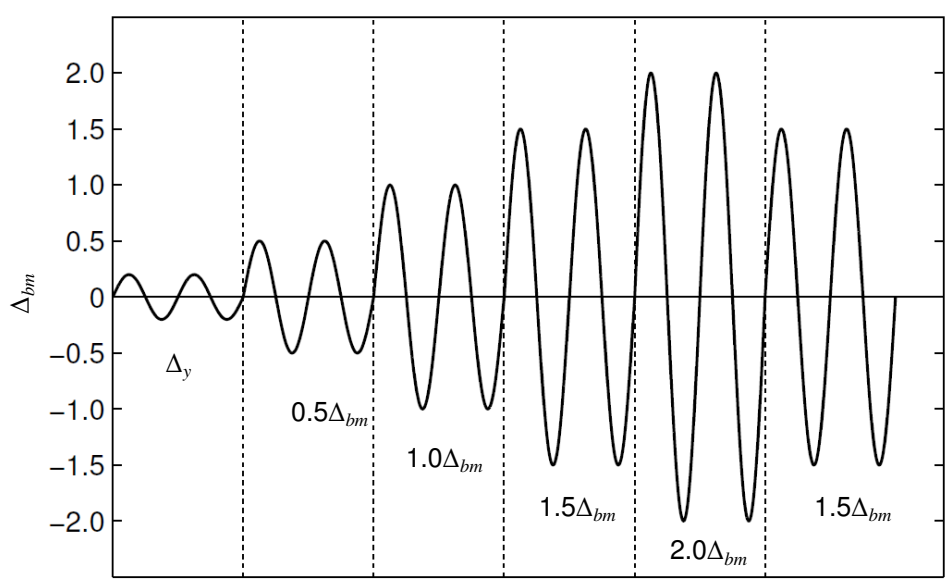


Figure 1.2 AISC Standard Loading Protocol for Buckling-Restrained Braces



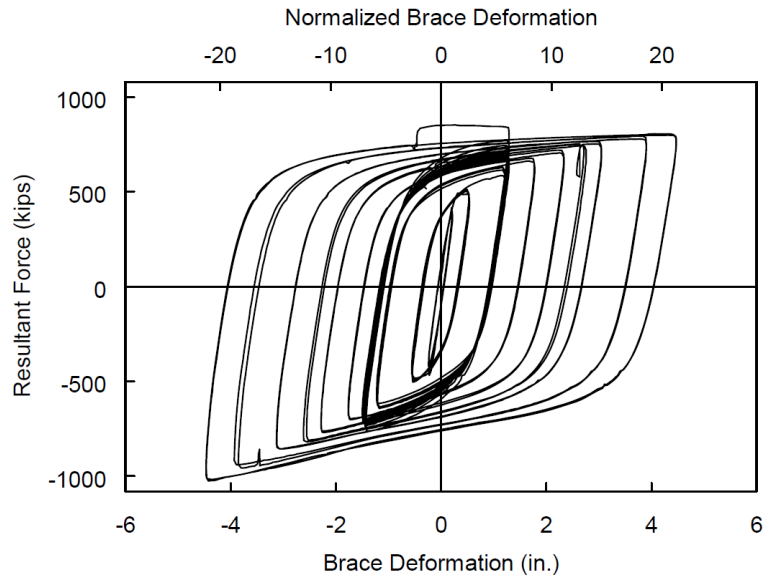


Figure 1.3 Typical BRB Hysteretic Performance (Newell et al. 2006)

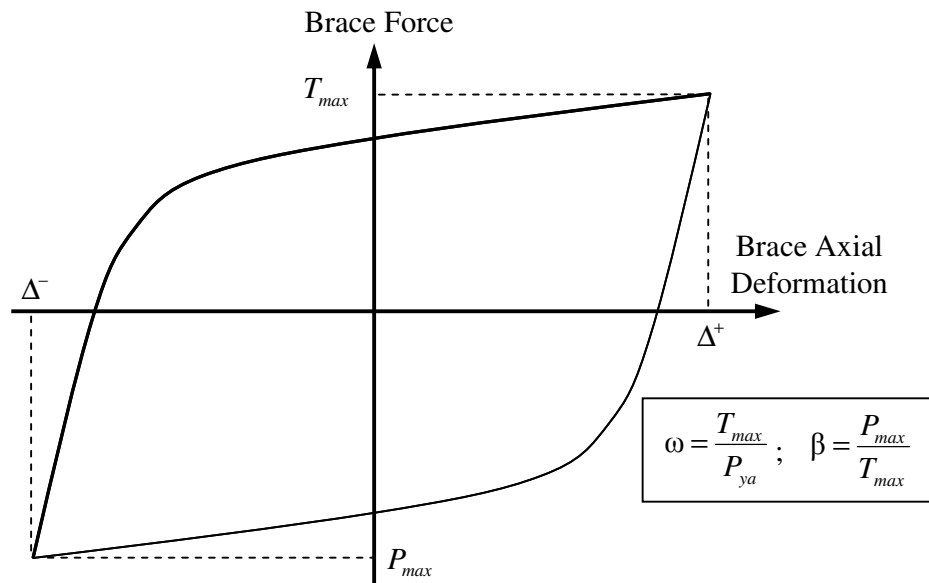


Figure 1.4 Strength Adjustment Factor Definitions for the  $i$ -th Cycle

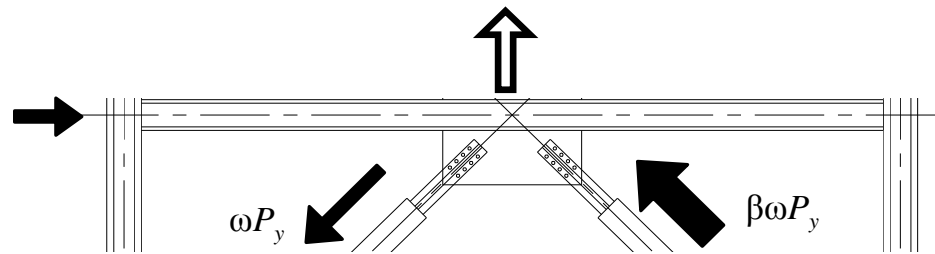


Figure 1.5 Example of Unbalanced BRB Force Resultant in Chevron Frame

## **2 CASE STUDY OF VTB AND LOADING PROTOCOL DEVELOPMENT**

### **2.1 Seismic Response Evaluation of BRB-Retrofit of VTB: A Parametric Case Study**

The feasibility of using buckling-restrained braces (BRBs) on long-span bridges is investigated in response to an effort to identify options for a maintenance-free seismic response mitigation system for the Vincent Thomas Bridge (VTB), in Figure 2.1, which the California Department of Transportation (Caltrans) originally designed and currently manages. Connecting San Pedro to Terminal Island and spanning the Palos Verdes Fault near Long Beach, California, the bridge is equipped with viscous-fluid dampers as part of a seismic retrofit completed in 1998. Figure 2.2 provides an overall schematic layout of the bridge along with a detailed view of the structure including the location of the dampers, and proposed BRBs, between the side spans and cable bents (SC), the side span and towers (ST), and the main span and towers (MT). The dampers are intended to mitigate impact between the suspended structure and the adjacent towers and cable bents by damping the relative motion between them during significant seismic events (Moffat & Nichol Engineers, 1996).

Recent Caltrans maintenance inspections have revealed that the devices incur damage, characterized by loss of the viscous fluid, due to ambient bridge motion as evidenced by internal wearing, shown in Figure 2.3. Without a portion of the viscous fluid, the hysteretic response exhibits a gap (Benzoni et al., 2008), displayed in Figure 2.4. Table 2.2 summarizes the simulated peak relative displacement responses obtained from a finite element model of the bridge subjected to its design earthquake

ground motion from a finite element model of the bridge subjected to its design earthquake ground motion (both are described later). Impact is predicted to occur with damaged viscous dampers, as indicated by the displacement ratios greater than 1.0, which could jeopardize the global structural integrity of the bridge.

An abridged version of the discussion provided by Lanning et al. (2011) is provided here. A full set of plots from the parametric study are provided in Appendix A for reference.

### **2.1.1 Finite Element Modeling of the Vincent Thomas Bridge**

A seismic retrofit study performed in the mid-1990s is summarized in the *Caltrans Strategy Report for the Toll Road Seismic Retrofit Project for the Vincent Thomas Bridge* (Moffatt and Nichol Engineers, 1996), and by Ingham et al. (1997). A major topic of these studies was the construction a sophisticated finite element model of the VTB (Figure 2.2) which was used to justify the installation of the existing viscous dampers. Built in the nonlinear finite element package ADINA (ADINA 2003), the same model was used for this research. It is a well established representation of the bridge, having been used in a number of different studies (e.g., Benzoni et al. 2008, He et al. 2008, Graziotti 2010). Throughout the model development, and the studies mentioned, simulated modal properties and seismic responses have been reported to show good correlation to those extracted from actual ambient and earthquake induced motions obtained from a system of accelerometers installed on the bridge in the 1980s.

The suspension system is modeled using tension-only 3D linear elastic truss elements, which are pre-strained during an initial gravity application analysis step resulting in an as-constructed bridge geometry. The suspended spans, consisting of a concrete slab on a system of stringers and stiffening-trusses, are represented using 3D linear elastic membrane and beam elements, respectively. Material nonlinearities are included in the tower structures, while various contact conditions are modeled with nonlinear elastic 1D springs. The viscous dampers are characterized by use of spring and dashpot elements which provide the hysteretic response appropriate for linear viscous dampers with element forces characterized by:

$$P_D = Cv^1 \quad (2.1)$$

where  $C$  = damping constant; and  $v$  = relative velocity of the element ends. The dampers are oriented parallel to the bridge length corresponding with the first mode (Table 2.3) and the design motion fault-normal component. Similar configurations were used for the BRBs. In total, over 20,000 degrees of freedom constitute the nonlinear finite element model of the VTB (Moffat and Nichol Engineers, 1996, Ingrahm et al., 1998).

### 2.1.2 Input Earthquake Ground Motion

As part of the retrofit study, a site-specific seismic hazard and geotechnical parameter analysis led to the development of a set of design ground motions tailored to the VTB allowing for non-synchronous multi-support shaking for seismic retrofit analyses. These ground motions represent an earthquake with approximately 2.3% probability of exceedance in 75 years. The seismic hazard of the design level spectrum

in the *AASHTO Guide Specifications for LRFD Seismic Bridge Design* (AASHTO 2011) is 7% in 75 years. The exposure, however, is based on an expected service life of a typical bridge, while that of the VTB was reported as 125 years in the *Caltrans Strategy Report*. Therefore, in terms of service life the VTB design ground motion represents a 3.8% exceedance which is considerably more severe than the AASHTO design spectrum. Since this design-level ground motion has been specifically developed for the VTB site and represents significantly greater hazard than given by AASHTO, it is considered to be the controlling motion for seismic demands on the structure.

The fully non-synchronous set of ground motions was used for the retrofit summarized in the *Caltrans Strategy Report*, with each of the six modeled supports subjected to a three dimensional (fault-normal, fault-parallel, and vertical) ground excitation. A simplified approach was used in this study with each side of the main span subjected to a set of three dimensional excitations for a total of six excitations. A detailed discussion of the simplifications made is presented in Lanning et. al (2011). The east side, Bent 10, component of ground acceleration corresponding to the bridge longitudinal direction is shown in Figure 2.5. The response spectra for each side and each direction of shaking are shown in Figure 2.6.

### **2.1.3 Finite Element Modeling of the BRBs**

A fairly common technique in the simulation of BRBs is the use of bilinear truss elements with kinematic hardening. The attributes of this element are displayed in Figure 2.7(a) and consist of an elastic stiffness ( $K_1$ ), yield force ( $P_y$ ), post-yield

stiffness ( $K_2$ ), and kinematic cyclic hardening rule governing the translation of the yield surface. A direct comparison is provided in Figure 2.7(b) which shows recent BRB testing data, collected by the authors, compared to the simulated response. Most notably, this nonlinear truss element does not capture the Bauschinger effect, thereby underestimating the hysteretic energy, but overall it sufficiently predicts the peak forces within the typical BRB testing range. BRBs in building frames were represented in this manner, with acceptable levels of error, by Black et al. (2004), Kim et al. (2004), and Ravi et al. (2007). Usami et al. (2005) also utilized this model while studying the replacement of regular bracing of a steel arch bridge with energy dissipating BRBs. This modeling technique is discussed further in Chapter 5, and the effectiveness is questioned. However, as is shown later, for A36 steel BRB the error for nonlinear-time history analysis is likely acceptable. And, for this case study the results are considered of an acceptable accuracy.

#### 2.1.4 Parameterization of BRB Characteristics

Viscous damper elements at all six locations within the VTB model (see Figure 2.2) were replaced by BRB elements. The primary characteristics of yield strength, post-yield stiffness, and lengths were parameterized as described below and shown in Figure 2.7(a) and (c).

In order to determine the sensitivity of the bridge response to the post-yield stiffness, the parameter was defined as:

$$\alpha = \frac{K_2}{K_1} \quad (2.2)$$

where the elastic axial stiffness ( $= EA/L$ ) is representative of the steel yielding core. The aforementioned studies exhibit  $\alpha$  values ranging from 1.5% to 3.5%. Therefore,  $\alpha$  was explored between 1% to 5%.

Buildings with BRB frames typically rely upon the equivalent lateral force procedure (ASCE 2010) to obtain initial brace yield forces. This method is not typically used in bridge designs, and the highly nonlinear suspension structure of the VTB is not well suited for this simplified method. Therefore, the brace yield force was investigated through the variation of:

$$\gamma = \frac{P_y}{P_{u,D}} \quad (2.3)$$

where  $P_{u,D}$  = viscous dampers design axial capacity. For this study BRB yielding cores were assumed to be of conventional A36 steel with an expected yield stress,  $F_{ye}$ , of 39.5 ksi ( $= 1.1 \times 36$  MPa) actual  $F_{ye}/F_{yn}$  ( $= R_y$ ) values from coupon tests conducted for prequalifying tests of BRBs, which are often less than  $R_y = 1.3$  specified by AISC 2010. Normalizing the BRB yield force in this way facilitates a reference between the existing bridge construction and the proposed braces. The investigated range for BRB yield force was 0 to 200% of the damper ultimate capacity (0% indicating no BRB present).

Three brace configurations defined as lengths 1 through 3 (L1, L2, L3) are shown in Figure 2.8(c). L1 represents a direct one-to-one BRB replacement of the dampers by using the existing damper connection locations. L2 and L3 take advantage of the stiffening truss geometry by assuming connections at the panel points. L3, also, somewhat corresponds to an upper bound to the feasible value, with an average core



length of about 40 ft among the three locations. Note that the BRB truss element represents only the yielding core length. The exposed ends of the core, which are relatively very short, and the brace connections are designed to remain elastic, and exhibit much larger cross-sectional areas making the stiffness much larger than the yielding core. Very often the yielding core is approximately 85% of the full brace stiffness. In this study, the length of the yielding core is assumed to be the same as the BRB length for simplicity.

### 2.1.5 Monitored Response Quantities

Four peak response quantities were examined in the evaluation of each parameter combination. The peak impact-direction displacement of the spans toward the supports, was normalized by the impact displacement (listed in Table 2.2) and compared to that of the fully functioning damper response; a lower value means greater mitigation.

Three BRB demands were evaluated as the peak core strain, peak brace force, and cumulative inelastic ductility (CID). Peak core strains of 4.3, 4.7, 3.6, and 4.6% have been successfully imposed on BRB specimens by Hasegawa et al., (1999), Carden et al., (2004), Yamaguchi et al., (2004), and Trembly et al., (2006), respectively. Hence, this range was considered as feasible, although uncommon as most testing is conducted with the AISC Protocol which typically requires peak core strain of about 2%. Peak BRB force, normalized by  $P_{u,D}$ , was monitored as an indication of the peak forces imparted to the VTB structure. The AISC Protocol requires a minimum achieved CID value of 200 times the yield deformation (i.e., the

sum of the sustained inelastic strain, normalized by the yield deformation, must be at least 200). CID from each BRB parameter combination was considered, but is not presented here for brevity as the demands were always well within measured CID capacities reported in many BRB testing studies (e.g. Merritt et al, 2003, Newell et al., 2006, and Lanning et al., 2012).

### 2.1.6 Global Parametric Variation

The dynamic behavior of the bridge was modified by replacing the dampers, with theoretically no elastic stiffness, with the relatively stiff BRB elements. In order to gain a general sense of the altered bridge behavior and the sensitivity to each parameter, the BRB properties were first applied and varied uniformly over the SC, ST, and MT locations.

The post-yield stiffness,  $\alpha$ , from 1 to 5% was explored for each of the three brace lengths, in Figure 2.8, while  $\gamma$  was held constant at 0.70. The small nearly linear trends suggested the use of mean  $\alpha$  value of 3%. However, the bilinear truss element with  $\alpha = 3.25\%$  provides a good prediction of peak forces and conservative levels of energy dissipation observed in many BRB experiments. The hysteretic response of the model is compared to one such BRB in Figure 2.7(b). Therefore,  $\alpha = 3.25\%$  was selected to remain constant for all BRBs for the remainder of the study.

The SC BRB results are presented in Figure 2.9 as an example of the responses due to global variation of both  $\gamma$  and length (L1, L2, L3). As might be expected the impact-direction displacement and peak core strain decreased with increasing  $\gamma$  and length, with the MT BRB being the most sensitive location. However, core strain

values in many cases with L1 fell far outside the feasible range, some reaching beyond 10%. Peak axial forces increase with  $\gamma$ , but the SC BRB with L1 was the most extreme reaching three times  $P_{u,D}$ .

The observations from global parameter variation are below:

- (1) The full yield force range should be explored in a local parameter study, except  $\gamma = 1.4$  as the forces imparted to the structure increase rapidly with  $\gamma$ . Instead the range was reduced to  $\gamma = 1.25$  so as not to excessively limit the parameter space.
- (2) L1 was eliminated due to unreasonably large core strains for many cases.
- (3) L3 provided lower strains, yet these lengths approach unrealistic BRB core lengths and were thereby eliminated.
- (4) Instead of continuing with only one length, two additional lengths were defined as those one- and two-thirds between L2 and L3. Therefore, L2, L2.1, and L2.2 were used in local parameter studies.

### 2.1.7 Local Parametric Variation

Next, local parameter variation provided an understanding of the interaction between BRBs. First, each location considered  $\gamma$  from 0 to 1.25 (1.05 for ST) with the others held constant at 1.05. Promising cases were then studied further through the local variation of BRB length. Similarly, lengths were varied from L2 to L2.2 with the others held constant at L2.

Figure 2.10(b) shows each span-to-support location exhibited impact with  $\gamma = 0$  (i.e., no BRB present). Relationships between each brace were observed as both impact-direction displacement and core strain increased at each location with

increasing  $\gamma$  at the adjacent BRBs. The cases of  $\gamma = 0.7, 1.05$  and  $1.25$  for the SC BRB appeared promising due to the relatively low impact displacements, core strains within the acceptable range ( $\approx 4\text{-}5\%$ ), and reduced peak axial forces. These three  $\gamma$  were, therefore, retained for length variation. The  $\gamma$  for ST BRB had a notable effect on the MT core strain, which was considered in the final parameter refinement. Only  $\gamma = 1.05$  was retained for length variation, however, due to the large impact-direction displacement or core strains with other yield forces. As in the global variation, the MT BRB was very sensitive to local change in  $\gamma$ . Interestingly,  $\gamma$  at this location had an evident effect on the impact displacement response of both side span BRBs. The  $\gamma = 1.05$  and  $1.25$  cases were the most feasible, despite the increase at the ST location for  $\gamma = 1.25$ .

The cases selected above were then investigated considering different BRB lengths in Figure 2.10(b). All response quantities stabilized to acceptable values for the SC BRB with  $\gamma = 1.25$  and L2.1, hence this combination was selected as the suggested retrofit parameter for this location. The ST BRB clearly exhibited the best core strain with  $\gamma = 1.05$  and L2.2; all other responses were satisfactory. Additionally, adjacent BRB demands were found to be insensitive to local refinement of SC and ST BRB lengths. The MT BRB presented two viable options,  $\gamma = 1.05$  with L2.1 and  $\gamma = 1.25$  with L2.2. Both provided acceptable levels of axial core strain, and so their influence on the adjacent BRB demands were examined. In this case, insensitivity was not observed and both impact displacement and core strain values were minimized at each location with MT  $\gamma = 1.05$  and L2.1. Therefore this was selected as the final

parameter combination suggested for retrofitting. Table 2.4(a) lists the final BRB parameters.

### **2.1.8 Results and Summary of Parametric Study**

BRB axial forces were moderately larger than those of the dampers. However, the net forces imparted to the towers were not severe due to the in-phase reactions of opposing ST and MT BRBs, as shown in Figure 2.11. Conversely, damper forces were out-of-phase, thereby causing the net BRB increase over damper reaction forces to be only 33%, as calculated in Table 2.4(b). This effect caused the global tower longitudinal moment and shear to increase only modestly despite the larger individual axial forces of the BRBs, shown in Figure 2.12.

The peak brace core strains were on average 4.4%, at maximum 4.9%, and occur during one large deformation pulse which corresponds to the ground motion pulse. Additionally, this deformations occurred over a very short time causing the strain rate to be  $16\% \text{ sec}^{-1}$  (or 0.16 in/in/sec) which is approximately 100 times faster than typical pseudo-static BRB testing rates (e.g. Merritt et al, 2003, Newell et al., 2006, and Lanning et al., 2012). These maximum demands were observed in the SC BRB; the simulated hysteretic response is shown in Figure 2.13.

The properties of the BRBs identified in the parametric study were within the range of those currently available commercially, and were shown to provide significant seismic mitigation. Table 2.4 shows a summary of the final BRB parameter values, their physical meanings, and the improved simulated bridge response due to the VTB design ground motion. All of these factors demonstrate BRBs to be a feasible

seismic mitigation solution for long-span bridges near seismic faults. However, since the peak strain, strain rate, and unsymmetrical pulse excursions differ so much from the requirements of the AISC provisions, a new prequalifying loading protocol and testing program was required to confirm the ability of BRBs to sustain such deformations.

## **2.2 Loading Protocol Development**

### **2.2.1 Introduction**

Cyclic loading protocols for testing the seismic performance of structural components should assess the capability of surviving statistically derived earthquake demands expected for a specific structure type and component configuration (Krawinkler et al., 1983). Generally this is achieved by subjecting a number of representative structural models to a set of ground motions which constitute a certain level of seismic risk. The simulated component responses are collected, analyzed, and then used to formulate a simplified, representative, and statistically significant demand time history. The resulting protocol should replicate a reasonably conservative cumulative damage that is expected for the specific structural component (Krawinkler et al., 1992).

The AISC Protocol was developed in a similar manner, using BRB deformations obtained from non-linear time history analysis of several building frames equipped with BRBs (also modeled with bilinear truss elements) subjected to a suite of far-field ground motions (Sabelli et al., 2003). The AISC Protocol, in Figure 2.19(a),

consists of symmetrical, gradually increasing amplitude cycles typically reaching a maximum core strain of approximately 2%.

Currently there is no bridge-specific standardized BRB testing protocol or design procedure and the effects of near-fault ground motion, including high strain rate, have been explicitly neglected in the AISC Seismic Provisions. Therefore, the following sections describe the development of two protocols which are intended to provide reasonably conservative near-fault seismic demands for BRB testing, with the second being applicable for prequalification of BRB for use on long-span bridges near seismic faults.

Note that an abridged version of the discussion in Lanning et al. (2013) is provided here.

### **2.2.2 VTB Proof Protocol**

Given the disparity between the deformation demands of the AISC Protocol and the severe BRB demands from the simulated VTB design ground motion response, it was pertinent to develop a so-called proof protocol, to serve as a key milestone to demonstrate that BRBs could sustain the 5% core strain pulse before more rigorous testing was conducted.

The SC BRBs, which exhibited the peak demands as described above, were selected as the prototypical responses for the proof loading cycles. Inelastic cycles were placed in the order in which they occurred and assembled with increasing amplitudes leading up to the large pulse (2 large excursions which cause the peak core strain). Amplitudes then decreased after the pulse and resulted in a residual

deformation. The VTB Proof Protocol is shown in Figure 2.15, and summarized in Table 2.5.

### 2.2.3 Near Fault Protocol

Since the VTB Proof Protocol considers only one ground motion, it is not appropriate for use as a prequalification test. Using the Pacific Earthquake Engineering Research Center (PEER) Strong Motion Database, 17 near-fault pulse-type ground motions were scaled to the VTB design response spectrum (Figure 2.6) up to a period of 6.5 sec., covering the first-mode period (= 6.3 sec.) of the bridge in the longitudinal direction as shown in Table 2.3. A summary of these motions and their respective scale factors is provided in Appendix B, Table B.1. The scaled and original ground motions and their response spectra are also provided in the figures of Appendix B.

These 17 ground motions and the VTB design earthquake were applied to the bridge finite element model with the suggested BRBs, resulting in a total of 54 brace deformation time histories (= 18 records  $\times$  3 locations), like those shown in Figure 2.16(a). The following loading characteristics were extracted for protocol development: (1) first through fourth largest magnitude core strains,  $\varepsilon_{max}$ ,  $\varepsilon_{2,max}$ ,  $\varepsilon_{3,max}$ , and  $\varepsilon_{4,max}$ , (2) maximum inelastic strain excursion,  $\delta\varepsilon_{max}$ , (3) order of inelastic excursions,  $\delta\varepsilon_i$ , (4) residual strain,  $\varepsilon_R$ , and (5) number of inelastic excursions, N. The rain-flow cycle counting algorithm (ASTM E 1049) similar to that used by Krawinkler et al., (1983) and Richards et al., (2006), was utilized to filter out elastic events, identify  $\delta\varepsilon_{max}$ , count N, and to obtain the order in which each event occurred ( $\delta\varepsilon_i$ ).



Each series of inelastic excursions was organized by aligning  $\delta\varepsilon_{max}$ , assumed to signify the pulse, thereby allowing the identification of the pre- and post-pulse excursions. An example of an aligned set of 18 inelastic excursions is shown in Figure 2.16(b). At each step the mean plus one standard deviation of the magnitudes was calculated based on the full number of records. Taking the statistical value in this way reduced the influence of excursions occurring away from the pulse, where every set may not have contained an inelastic event.

Cycles were formed as a sequence of core strains by summing the inelastic strain excursions by:

$$\varepsilon(i) = \sum_0^i (-1)^i \delta\varepsilon_i \quad (2.4)$$

where  $\varepsilon(i)$  is the  $i$ -th peak strain and  $\delta\varepsilon_i$  is the  $i$ -th excursion from each series. This produced cycles forming a raw protocol, shown in Figure 2.16(c), meaning that the core strain maxima and the residual strain are not necessarily represented. To incorporate these, only minor adjustments were required as follows. First, the pulse cycles were defined as those which most nearly caused the four peak strain maxima due to the alternating excursions in Eq. 2.4. Cycles within the pulse were amplified so as to attain the core strain maxima, however the maximum excursion,  $\delta\varepsilon_{max}$ , was generally not significantly affected. Second, pre-pulse excursions were sorted such that the magnitudes increase while post-pulse cycles were sorted in descending order. Lastly, a few post-pulse excursions were adjusted to result in the statistical residual strain,  $\varepsilon_R$ . All adjustments were minor and typically in the conservative direction, rounding up in strain or excursion magnitude. Figure 2.16(c) compares the raw

protocol to the final adjusted protocol, demonstrating the minor artificial adjustments made to the purely statistically obtained (raw) outcome.

This process was conducted for each BRB location, but the ST BRB resulted in the most severe loading sequence. A graphical summary of the demands obtained from each analysis at each BRB location is provided in Figure 2.17 along with the final protocol demands, while the statistical values are organized in Table 2.6. The absolute maximum strain was selected to be 5%, in keeping with the Proof Protocol, rather than the mean plus one standard deviation over all three BRB locations; however, the value is still conservative over all three locations. All other parameters deviate only slightly from the mean plus one standard deviation due to the minor adjustments described above.

The Near Fault Protocol is shown in Figure 2.18, while Table 2.7 summarizes the core strains at each step. Figure 2.19(a) and (b) together show the much smaller strains required by the AISC Protocol. Figure 2.19(c) demonstrates that the relative total cumulative inelastic ductility and the distribution of the ductility demand are much more severe. The Near Fault Protocol is proposed as a prequalifying test for BRBs intended for use on long-span bridges near seismic faults.

#### **2.2.4 Dynamic Loading Protocols**

Consideration of the strain rate effect on structural steel components is often constrained to the increase in the yield and ultimate stresses under monotonic loading, as summarized by Soroushian et al. (1987). Within the range of typical earthquake loading rates (around 1% to 10%  $\text{sec}^{-1}$ ) the increase is only about 7% (Di Sarno et al.,

2002), which is commonly considered to be negligible. Furthermore, cyclic testing of structural components is commonly performed at a pseudo-static rate, on the order of  $0.1\% \text{ sec}^{-1}$ , due to the limitations of many testing facilities.

Earthquake-induced strain rate effects are, however, recognized as being of more importance for structural bracing undergoing inelastic buckling (Di Sarno et al., 2002). Fell et al. (2009) estimated earthquake loading rates for, and conducted testing of, steel special concentrically braced frames resulting in a maximum strain rate of  $5\% \text{ sec}^{-1}$ , or 360 times faster than pseudo-static rates. Few studies are available in the literature that incorporate deliberate dynamic versus pseudo-static testing of BRBs. Cardin et al. (2004) performed dynamic tests on short BRB, within ductile end frames of bridge spans, under a constant frequency of 2 Hz, resulting in a maximum core strain rate of about  $14\% \text{ sec}^{-1}$ . Tremblay et al. (2006) subjected BRB to dynamic loading with a maximum rate of about  $25\% \text{ sec}^{-1}$ . These cases were reported to have increased BRB hysteretic forces by 15% and 5%, respectively, as compared to similar pseudo-statically loaded braces.

Chang et al. (2013) performed low-cycle fatigue testing on high strength carbon steel at rates of 0.1 and  $100\% \text{ sec}^{-1}$  in which the stress amplitude was increased by approximately 5%. A previous study by Chang et al. (1987) displayed A36 steel to be strain rate dependent but strain rate history independent; when loading rate changed during cycling the response changed to match that of the stabilized hysteresis at the corresponding rate. Therefore, the rate effect on inelastic cycling is perhaps significant for seismic response since the effect is present throughout the inelastic response, as opposed to only considering the effect on the initial yield and ultimate stresses. This

behavior could have significant influence on the complex constrained inelastic buckling condition of BRB yielding cores.

Table 2.8 also displays the rates from several standard BRB prequalification testing programs, those from available testing which were conducted at higher rates, and those of the simulated VTB BRB responses. Additionally, Dehghani et al., (2012) recently developed standard dynamic loading protocols for BRBFs considering Canadian seismic hazards which contain a maximum of approximately  $3\% \text{ sec}^{-1}$ , however no physical testing was reported.

In each of these cases either peak core strains, strain rates, or both are much lower than those of the simulated VTB BRB responses. Therefore, dynamic versions of the VTB Protocols were developed to investigate the strain rate effect on BRB performance.

### **2.2.5 Development of Dynamic Near Fault Protocols**

Pseudo-static protocols consist primarily of peak deformations organized in a particular order, or step, as indicated on the horizontal axis of Figure 2.19(a). The pseudo-static VTB Protocols were converted to dynamic, obviously, requires the incorporation of time rather than only loading step. For a pseudo-static rate of  $0.2\% \text{ sec}^{-1}$  the time step can be nearly uniform, but for the dynamic protocols a series of compatible sine waves were used with an adjusted time step to reflect the appropriate wave periods resulting in the target strain rate. Smooth velocity and acceleration time histories were also ensured to accommodate the operation of testing equipment.

The simulated VTB BRB strain rate histories followed similar trends as the core strains and excursion magnitudes; generally the rate increased leading up to the pulse excursions and decreased thereafter, with the peak rate usually corresponding with the peak strain (i.e., the excursions forming the peak strain contained the peak rate). In forming the Dynamic VTB Proof and Near Fault Protocols only the mean plus one standard deviation peak strain rate values of 16% and 30%  $\text{sec}^{-1}$  were explicitly included, respectively. This corresponded to a time step scaling within the pulse excursions by approximately 150 ( $= 30/0.2$ ), and 80 ( $=16/0.2$ ) times faster than pseudo-static time step. The pre- and post-pulse cycles were adjusted to result in increasing strain rates leading to the pulse and decreasing rates afterwards. The Dynamic Proof Protocol Figure 2.20, and is summarized in Table 2.5 . The Dynamic Near Fault Protocol is shown in Figure 2.21, while the strain rates are provided in Table 8, with those of the Proof Protocol in Table 2.7.

A dynamic AISC Protocol was also developed. Note the much smaller symmetric cycles of the prequalifying testing protocol given by AISC 341, in Figure 1.2 were established in consideration of the statistical demands of far-field ground motion on BRBFs (Sabelli et al. 2003). But the current provisions of AISC 341 ignore the strain rate effect by not requiring BRBs to be loaded dynamically. Here, by assuming the elastic period ( $\approx 0.6$  sec) for a 6-story BRBF, as calculated in ASCE/SEI 7-10 (ASCE 2010), used by Sabelli et al. (2003) the strain rate was estimated to be 11%  $\text{sec}^{-1}$  and was applied at the maximum amplitude cycles. The time scale for the remaining sets of cycles were scaled in proportion with their relative deformation to provide smooth velocity and acceleration time histories for machine operation. These

deformations were converted to yielding core strains, resulting in the Dynamic AISC Protocol.

Chapter 2 in partial, is a reprint of the material as it has been submitted for publication. The dissertation author was the first author of these papers.

Table 2.1 Existing Viscous Damper Properties

Location	Mid-Stroke Length	Design Axial Capacity (kips)	Total No. Units	$n$ (Eq. 2.1)
Cable Bent to Side (SC)	14'-2"	265	16	1.0
Tower to Side (ST)	12'-10"	75	16	1.0
Tower to Main (MT)	15'-1"	200	8	1.0

Table 2.2 Design Earthquake Seismic response of VTB with viscous dampers

Model with:	Damper Location	Axial Force	Displacement
		Peak / Capacity	Peak / Capacity
Fully Effective Dampers	SC	0.84	0.62
	ST	0.87	0.83
	MT	0.91	0.56
Fully Ineffective Dampers	SC	-	0.75
	ST	-	1.47
	MT	-	1.09

Table 2.3 Basic mode shapes of the VTB with dampers and with BRBs




Mode	Period (sec)		Mode Shape (Description)
	Damper Model	Final BRB Model	
1	7.7	6.3	 (First longitudinal)
2	5.6	4.3	 (First transverse)
3	4.4	4.2	 (First vertical, symm.)



Table 2.4 Final Feasible BRB Parameters for VTB retrofit

## (a) Final Properties

BRB Loc.	Final BRB Properties							
	$\gamma$	Area (in <sup>2</sup> )	$P_y$ (kips)	L	$L_y$ (ft)	$\alpha$ (%)	$K_1^*$	$K_2$
							(kip/in)	
SC	1.25	16.7	663	2.1	34.1	3.25	1,183	38
ST	1.05	3.9	153	2.2	29.8		316	10
MT	1.05	10.6	420	2.2	30.8		831	27

\*Corresponds to BRB yielding core stiffness

## (b) Design Earthquake Response with BRBs

Reduced Displacement (%)	Maximum BRB Strain (%)	Peak Axial Force (kips)		% Increase BRB-to- Damper
		In-phase BRB	Out-of-Phase Damper	
25.4	4.9	818	362	126 %
12.7	4.2	270	-51	433 %
58.1	4.1	549	413	33 %

Table 2.5 Proof Protocol Peak Core Strains and Rates

Step No.	Core Strain		Step No.	Core Strain	
	(%)	Rate (% sec <sup>-1</sup> )		(%)	Rate (% sec <sup>-1</sup> )
1	-0.2	-0.2	6	1.0	3
2	0.2	1.6	7	0	-1.5
3	-1.0	-5	7 cycles	0.6% amplitude 0.6% residual 1.4% sec <sup>-1</sup>	
4	5.0	16.2			
5	-1.0	-7.2			

Table 2.6 Summary of Simulated and Near Fault Protocol Cyclic Demand Parameters

Response Parameter	Simulated Response				Near Fault Protocol	AISC Standard Protocol
	BRB	Mean	$\sigma$	Mean + $\sigma$		
$\varepsilon_{max}$ (%)	SC	4.0	1.9	5.8	5.00	2.00 (Max.)
	ST	3.9	1.3	5.2		
	MT	3.6	1.5	5.1		
$\varepsilon_{2,max}$ (%)	SC	2.7	1.7	4.4	3.50	1.50 (Max.)
	ST	2.9	1.6	4.0		
	MT	3.0	0.7	2.1		
$\varepsilon_{3,max}$ (%)	SC	2.4	0.8	3.7	3.25	1.00 (Max.)
	ST	2.7	0.8	3.		
	MT	3.0	0.8	3.5		
$\varepsilon_{4,max}$ (%)	SC	1.5	1.5	4.5	3.00	0.50 (Max.)
	ST	2.5	1.4	4.4		
	MT	2.3	1.2	3.5		
$\delta\varepsilon_{max}$ (%)	SC	6.1	3.1	9.1	8.50	4.00 (Max.)
	ST	5.3	1.2	6.4		
	MT	5.5	2.5	7.9		
$\varepsilon_R$ (%)	SC	0.4	0.3	0.7	0.70	0
	ST	0.4	0.3	0.6		
	MT	0.4	0.2	0.6		
$N$	SC	21.3	7.7	29.0	45	25 (typ.)
	ST	28.6	15.5	44.0		
	MT	28.3	12.0	40.3		
Dissipated Energy ( $10^3$ kip-in)	SC	59.1	37.1	96.2	116	8.4 (min.)
	ST	36.1	15.8	51.9	48	48 (min.)
	MT	39.8	24.7	64.5	88	116 (min.)
CID ( $\times\Delta_y$ )	SC	161	101	262	524	200 (min.)
	ST	347	185	532	545	
	MT	188	117	305	545	
Strain Rate ( $\% \text{ sec}^{-1}$ )	SC	18.9	11.2	30.0	30.0	0.1 to 0.2 (typ.)
	ST	19.5	8.4	27.9		
	MT	17.8	7.5	25.2		

Table 2.7 Near Fault Protocol Peak Core Strains and Rates

Step No.	Core Strain		Step No.	Core Strain	
	(%)	Rate (% sec <sup>-1</sup> )		(%)	Rate (% sec <sup>-1</sup> )
1	-0.2	-0.5	24	1.6	6.6
2	0.3	0.9	25	0.0	-6.6
3	-0.2	-2.5	26	1.4	7.2
4	0.3	2.4	27	0.1	-3.6
5	-0.6	-2.8	28	1.3	3.6
6	0.4	4.3	29	0.1	-3.6
7	-0.6	-9.4	30	1.2	4.4
8	0.9	9.5	31	0.2	-1.6
9	-1.0	-13.3	32	1.1	1.4
10	1.0	13.7	33	0.2	-1.4
11	-1.7	-18.4	34	1.1	1.4
12	5.0	30.1	35	0.3	-1.4
13	-3.5	-30.4	36	1.0	1.4
14	3.3	30.8	37	0.3	-1.4
15	-3.0	-20.5	38	1.0	1.4
16	2.4	17.1	39	0.4	-1.4
17	-0.5	-14.4	40	0.9	1.4
18	1.7	12.7	41	0.5	-1.4
19	-0.3	-11.3	42	0.9	1.4
20	1.7	11.3	43	0.5	-1.4
21	-0.3	-11.3	44	0.8	1.4
22	1.6	11.2	45	0.6	-1.4
23	-0.1	-6.6			

Table 2.8 BRB Testing Strain Rates

Source	Protocol	Maximum Strain	
		(%)	Rate (% sec <sup>-1</sup> )
(Romero, 2007)	AISC 2005	1.7	6×10 <sup>-3</sup>
(Merritt, 2003)	SEAOC/AISC 2001	1.7	0.1
(Newell, 2006)	AISC 2005	1.7	0.3
(Lanning, 2012)	AISC 2010	1.7	0.2
(Merritt, 2003)	Real-time, 1994 Northridge, Sylmar	3.1	9.0
(Carden, 2004)	Reverse, SEAOC-AISC 2001	1.9	23.9
	Real-time, 1995 Kobe	4.7	Not Reported
(Tremblay, 2006)	Dyn. BRBF Protocol (Tremblay, 2002)	1.3	11.6
Simulated VTB Demand	Design Level	4.9	16.2
	Suite of 18 Records	7.2	50.0
VTB Dynamic Proof Protocol		5.0	16.0
VTB Dynamic Near Fault Protocol		5.0	30.0



Figure 2.1 Vincent Thomas Bridge

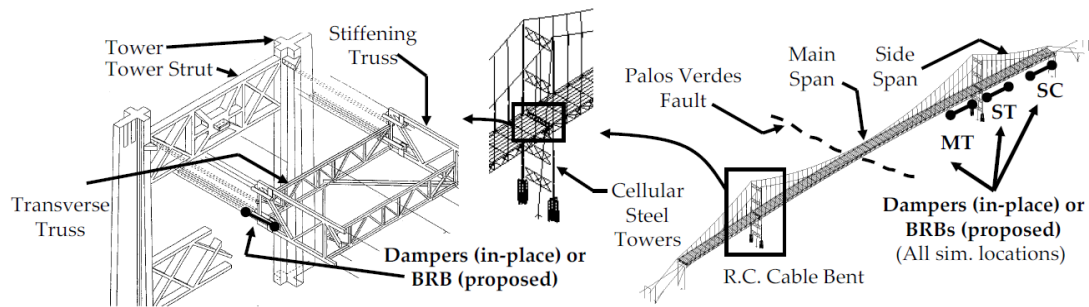


Figure 2.2 Vincent Thomas Bridge schematic and finite element model



Figure 2.3 Photos of VTB Damper Disassembly and Internal Damage  
(Graziotti 2010)

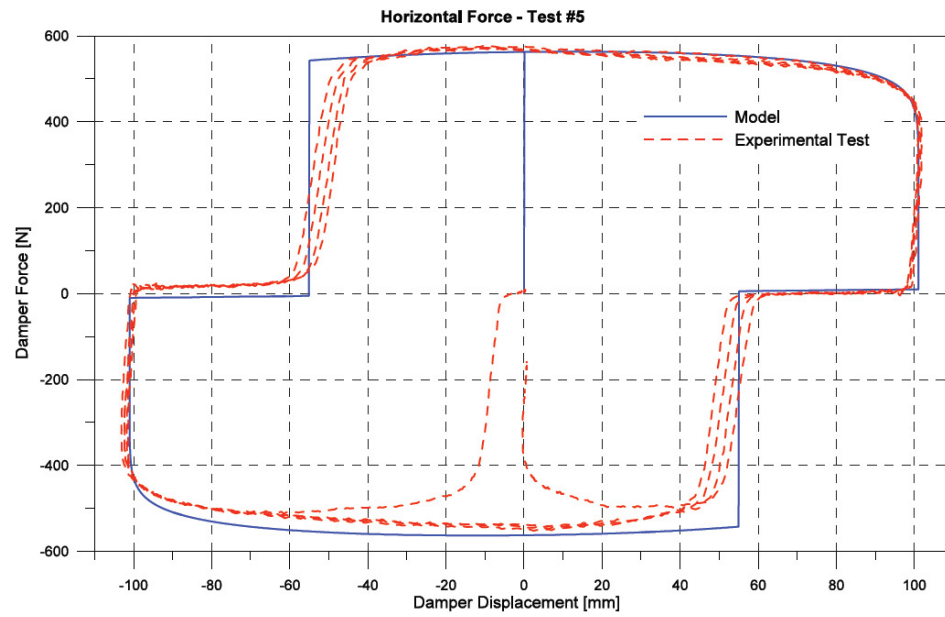


Figure 2.4 Damaged Viscous Damper Hysteretic Behavior (Benzoni et al. 2008)

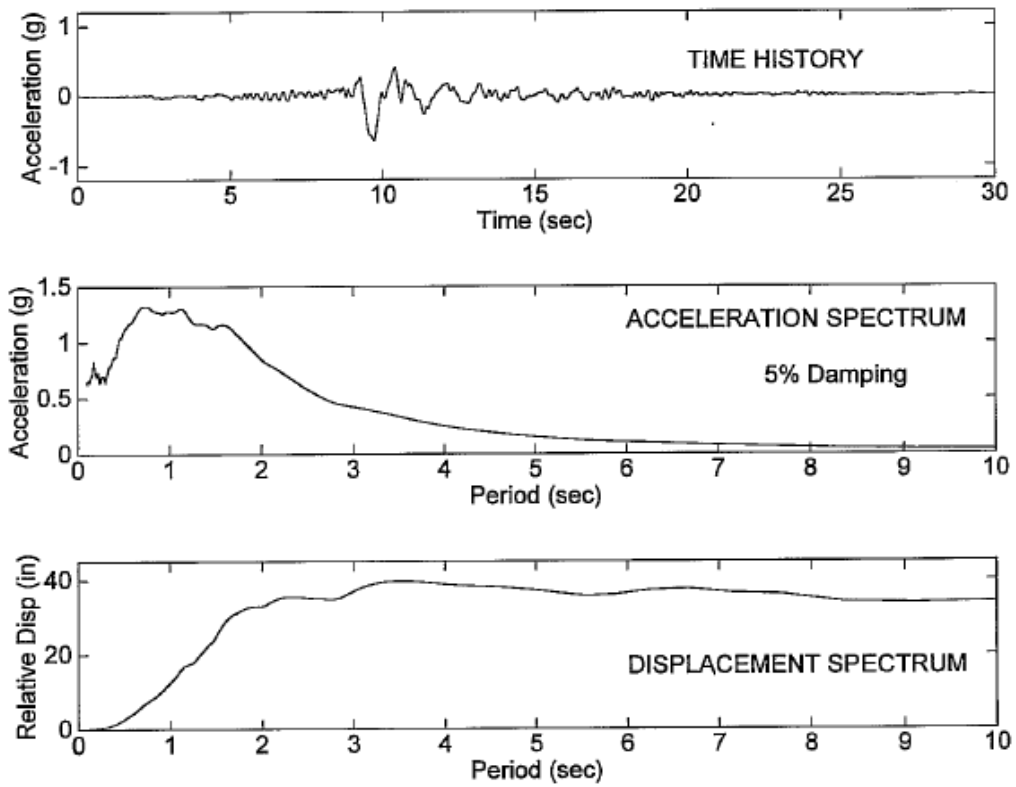
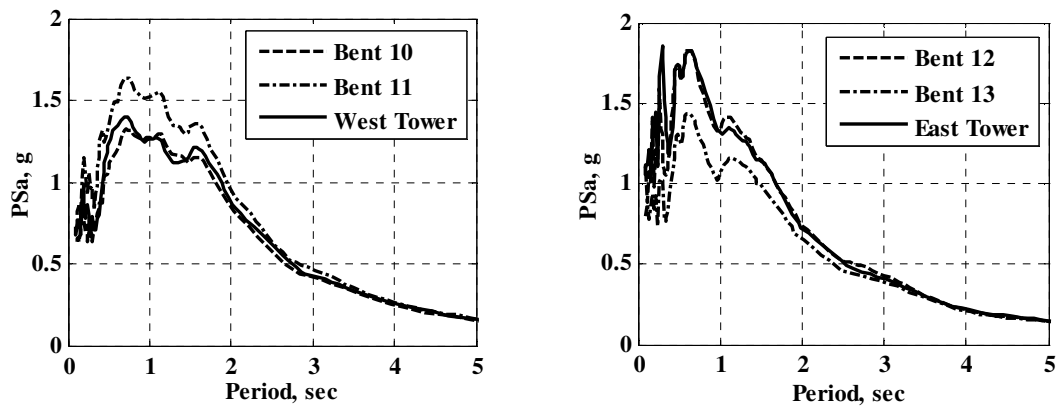
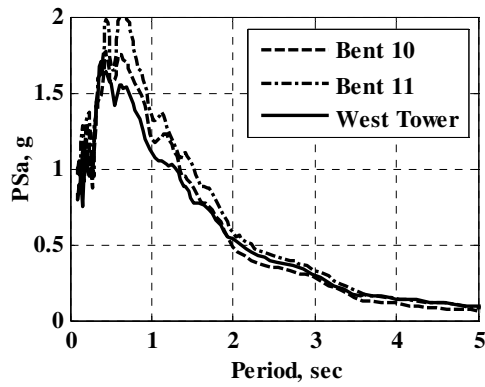


Figure 2.5 Bent 10 Longitudinal Ground Motion (Moffatt and Nichol 1996)

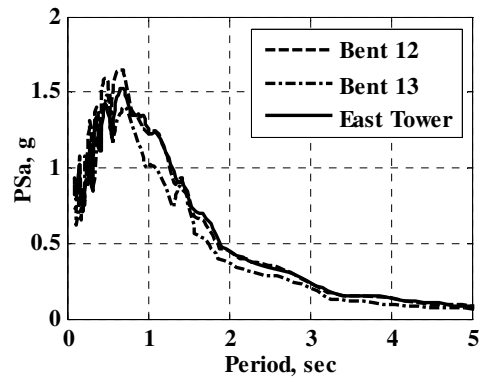


(a) West Supports, Longitudinal Direction (b) East Supports, Longitudinal Direction

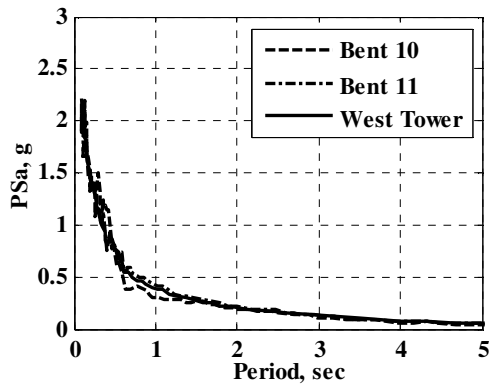




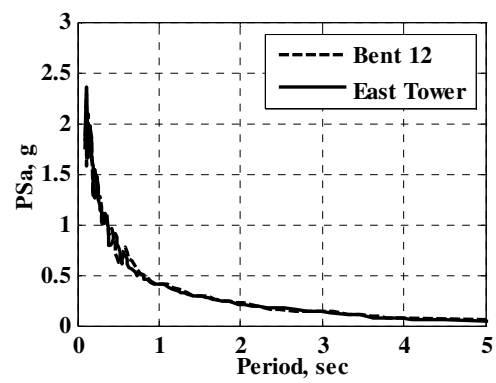
(c) West Supports, Transverse Direction



(d) East Supports, Transverse Direction

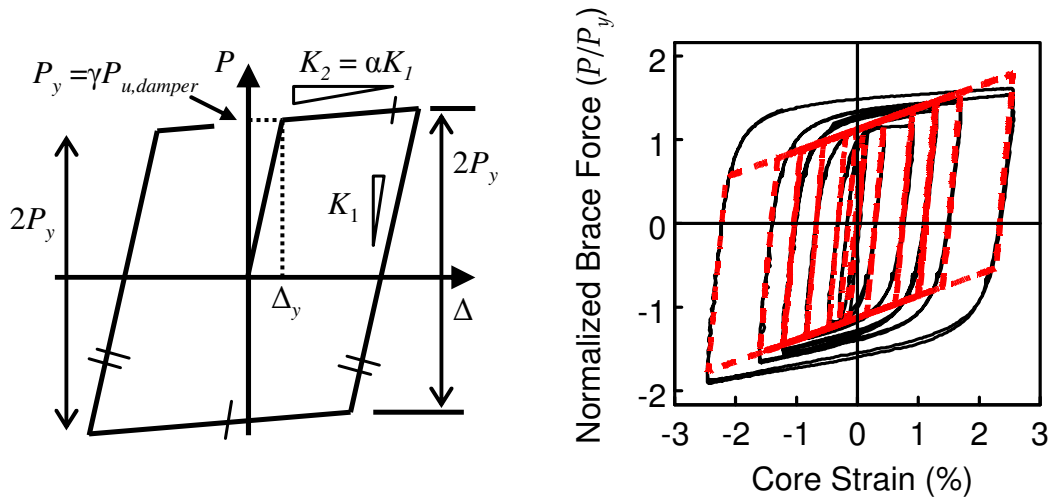


(e) West Supports, Vertical Direction



(f) East Supports, Vertical Direction

Figure 2.6 Design-Level Earthquake Pseudo-Acceleration Response Spectra ( $\zeta=5\%$ )



(a) Bilinear Truss Element Parameters (b) Good Agreement with Typical Testing

Figure 2.7 Bilinear Truss Element for BRB

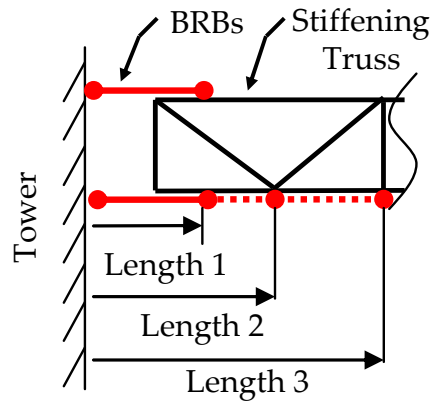


Figure 2.8 BRB Lengths Considered in Parametric Variation

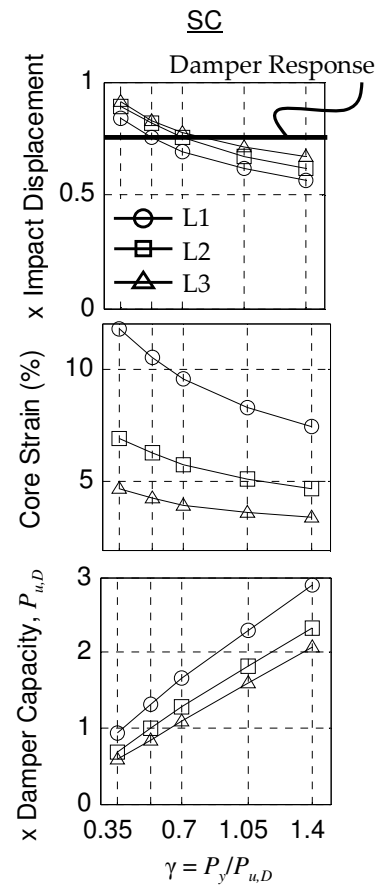
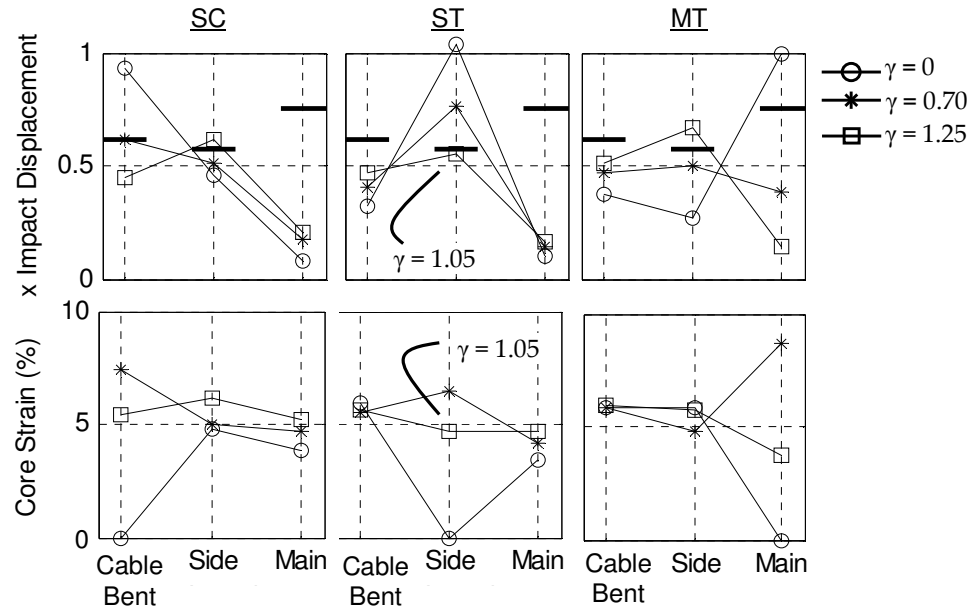
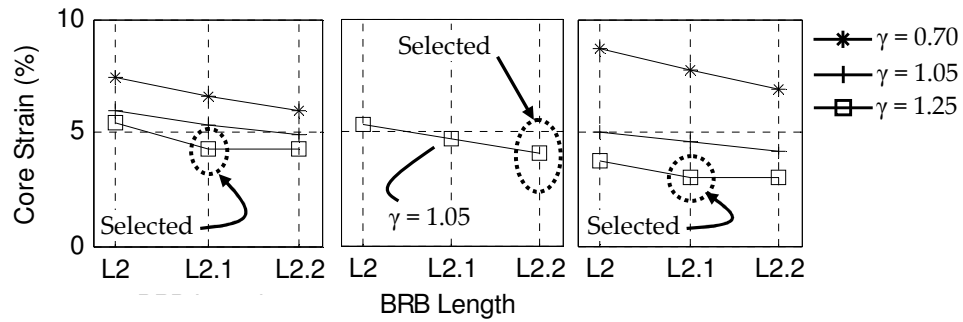


Figure 2.9 Example of Global Variation of BRB Yield Force and Length\*

\*(See Appendix ## for full presentation of parametric study plots)



(a) Local Variation of Yield Forces\*



(b) Refined Local Length Variation\*

Figure 2.10 Example Parametric Study Response

(\*See Appendix A for full set of parametric study plots)

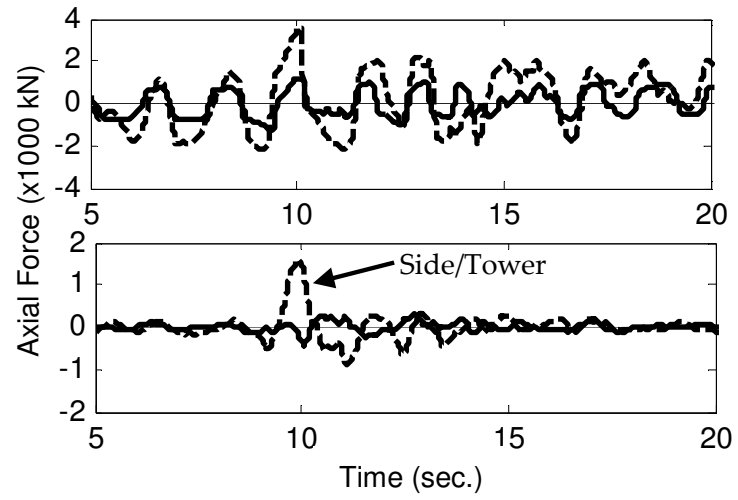
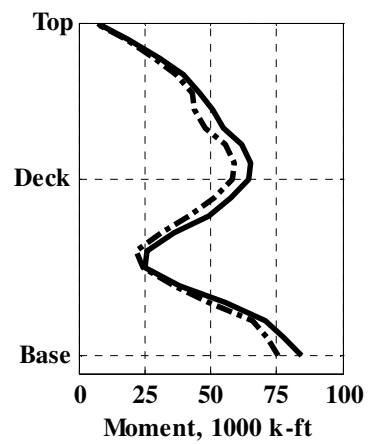
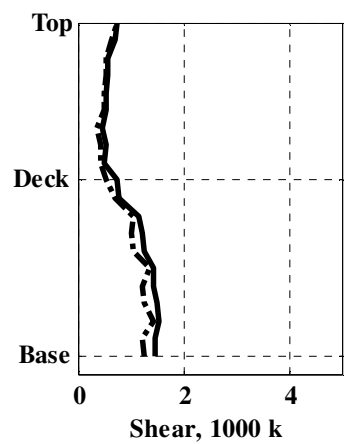


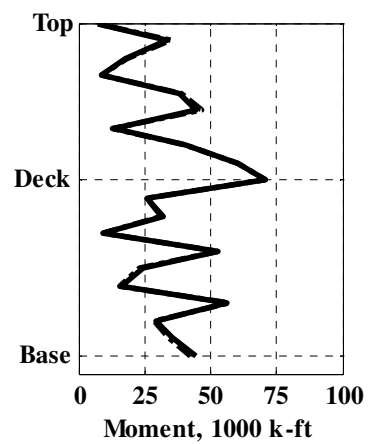
Figure 2.11 Force-Phase Relationship of BRBs and Dampers



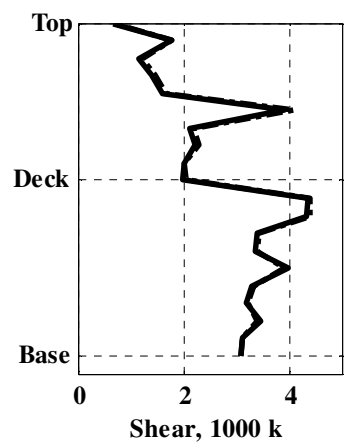
(a) Longitudinal Moment



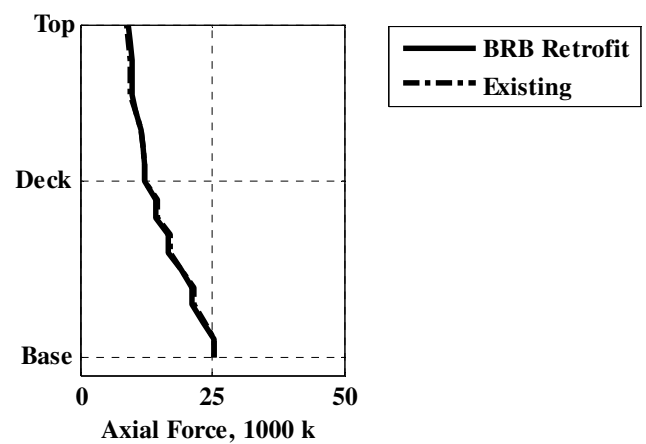
(b) Longitudinal Shear



(c) Transverse Moment



(d) Transverse Shear



(e) Axial Force

Figure 2.12 Tower Seismic Force Demand Envelopes: Design-Level Earthquake

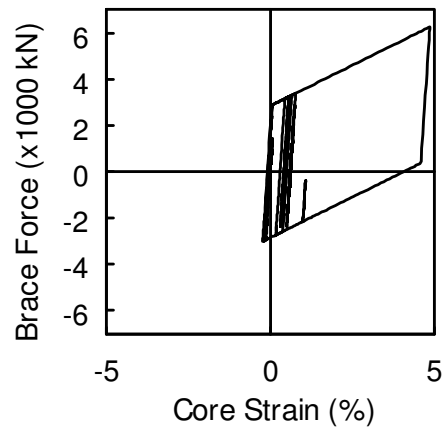


Figure 2.13 SC BRB Hysteretic Response, Design-Level Earthquake

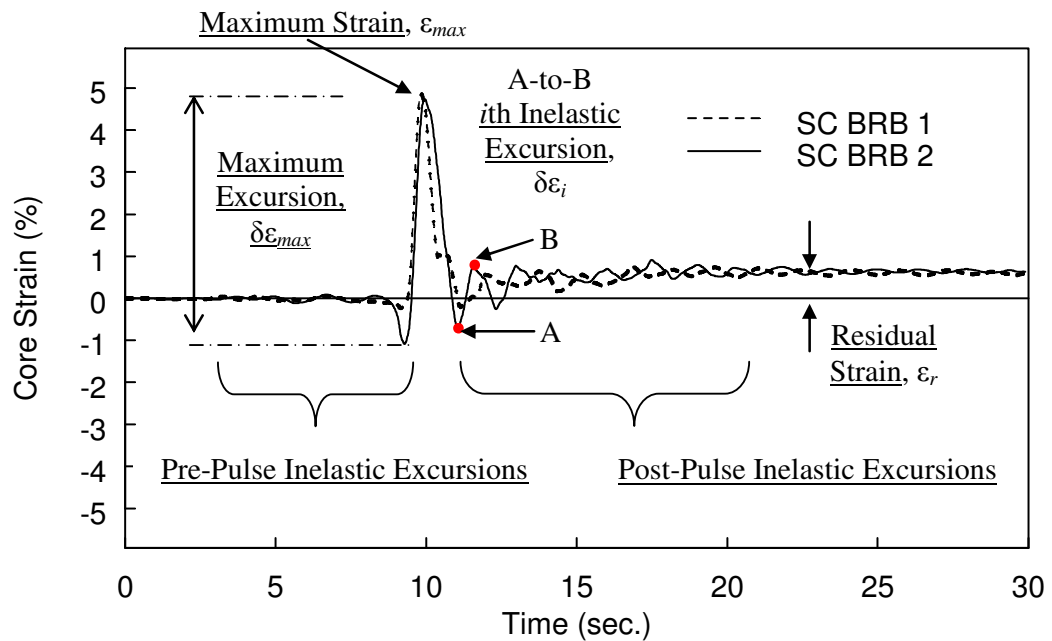


Figure 2.14 Example of Protocol Parameters (Proof Protocol)

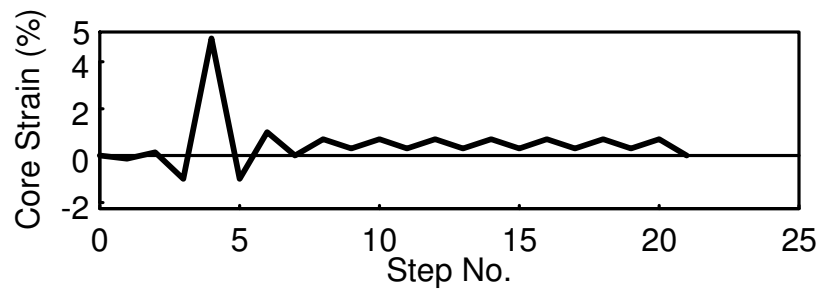
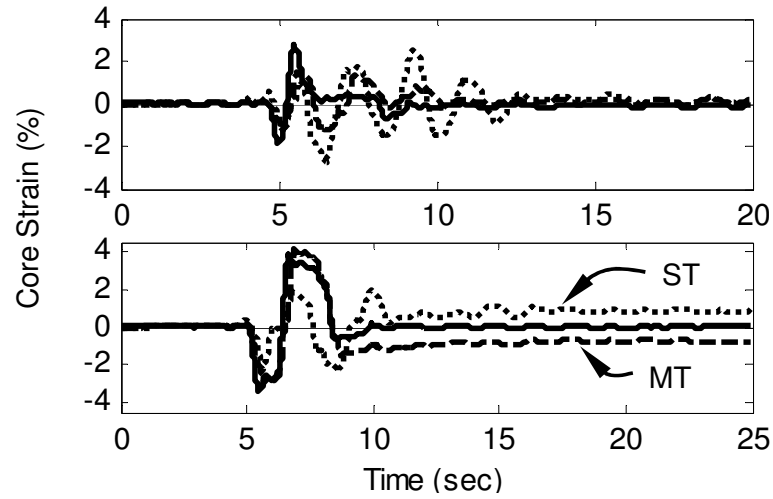
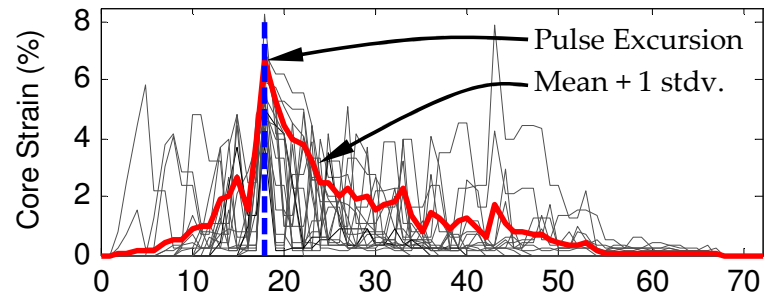


Figure 2.15 VTB Proof Protocol

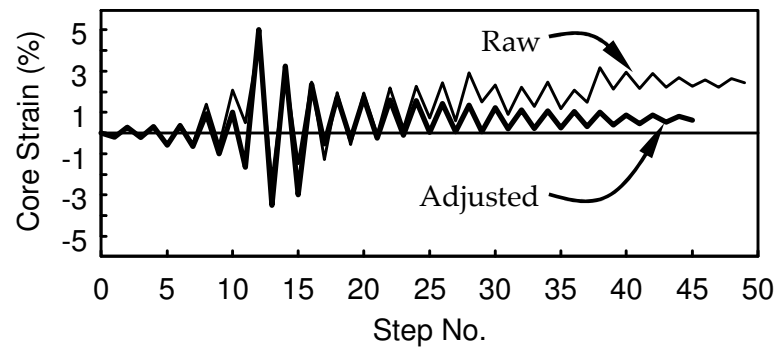




(a) Example of VTB BRB Core Strain Time Histories



(b) Example of Pulse-Aligned Inelastic Excursions



(c) Raw and Adjusted Near Fault Protocol

Figure 2.16 Protocol Development Process

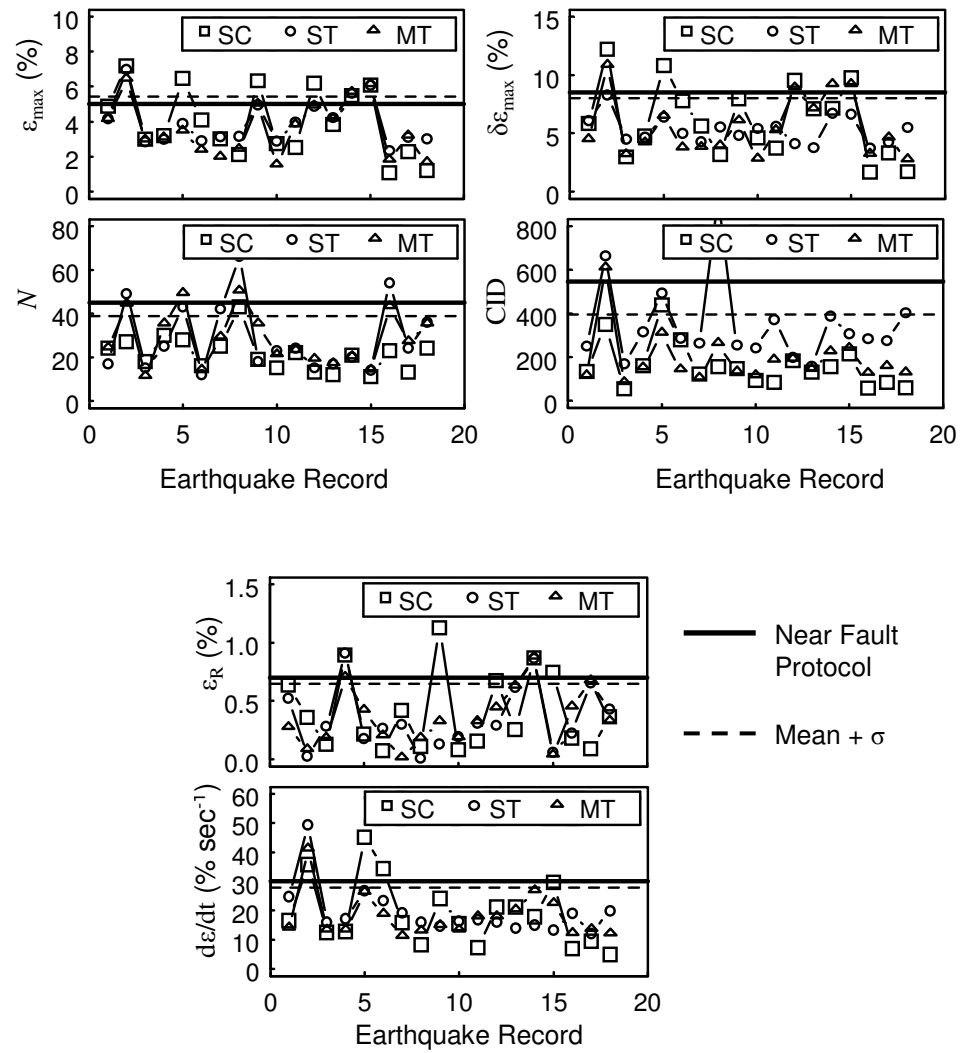


Figure 2.17 BRB Demand Quantities and those of the Near Fault Protocol

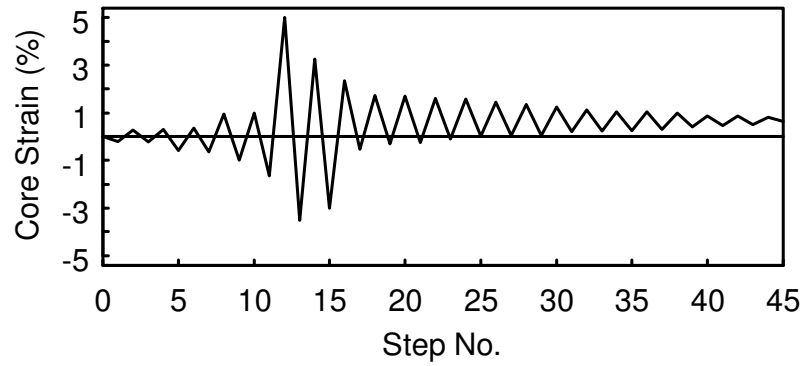
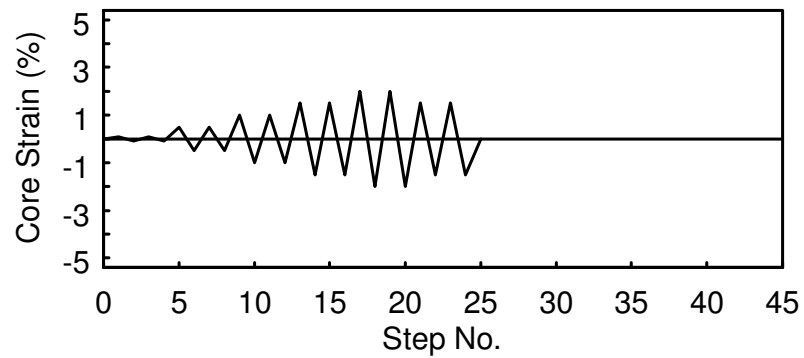
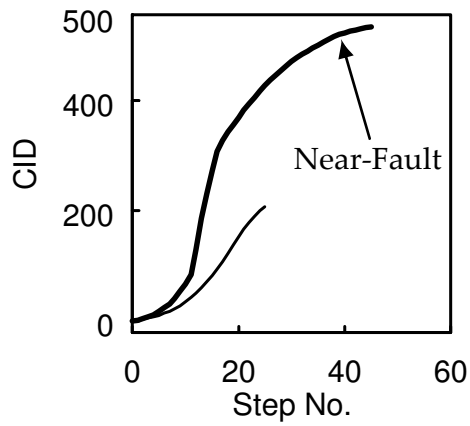


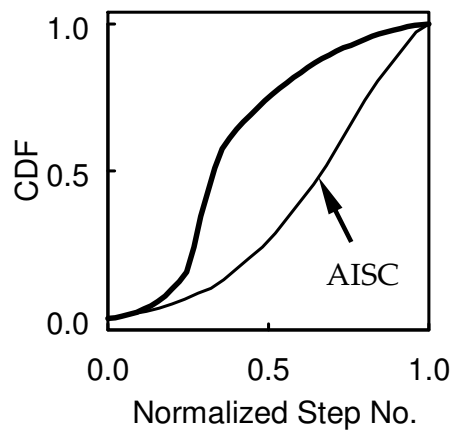
Figure 2.18 Near Fault Protocol



(a) AISC Protocol

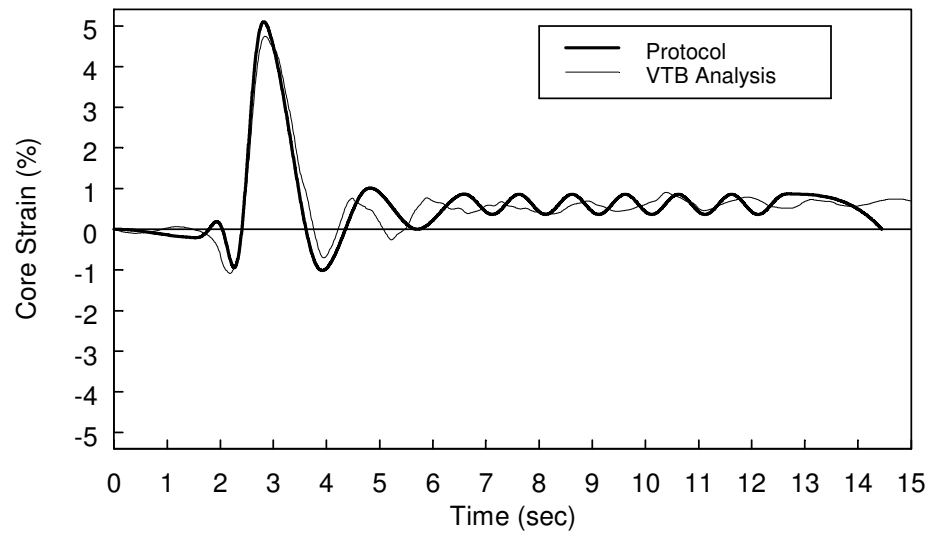


(b) Cumulative Inelastic Deformation

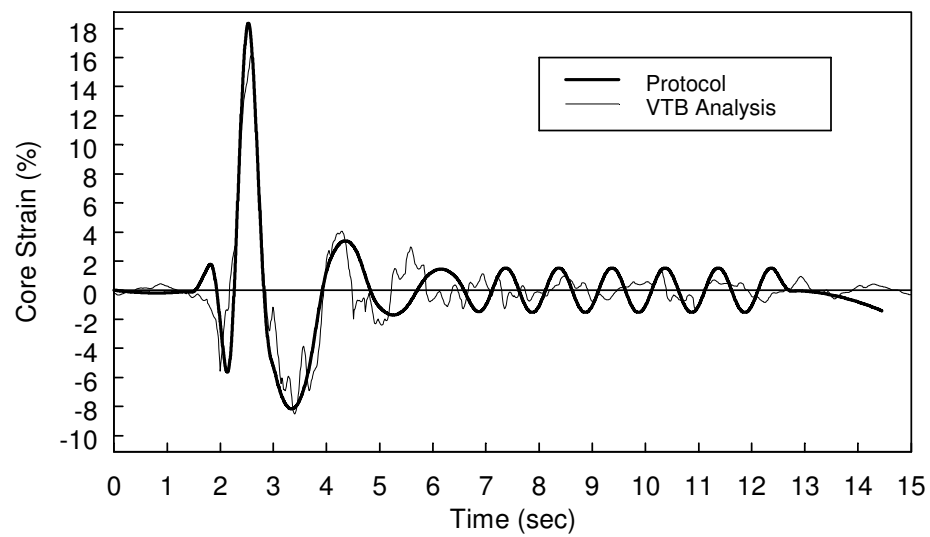


(c) Cumulative Distribution Function

Figure 2.19 Relative Cumulative Effects of Near Fault and AISC Protocols



(a) Strain Time History



(b) Strain Rate Time History

Figure 2.20 Dynamic Proof Protocol

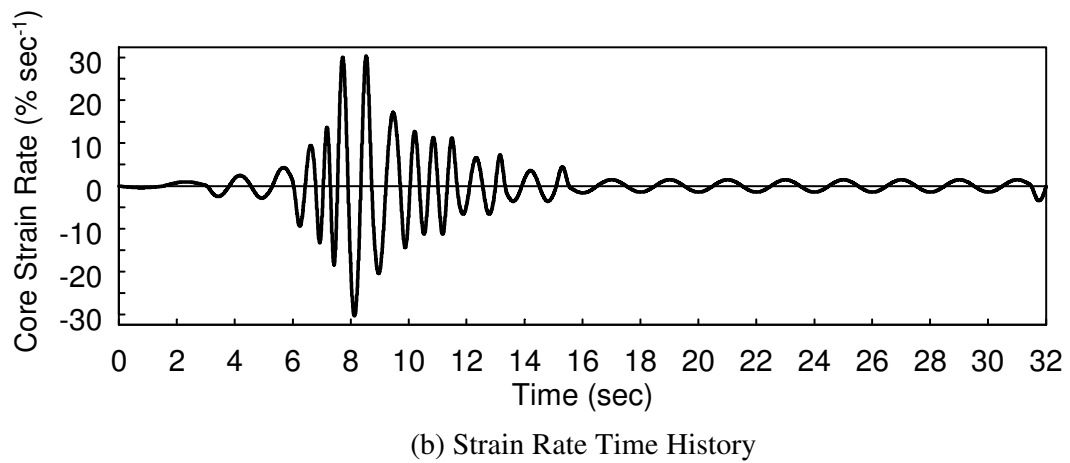
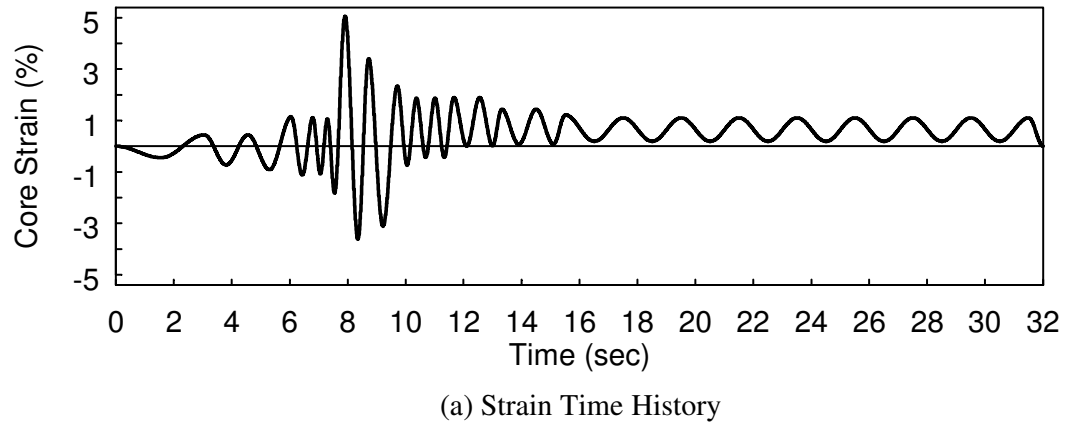


Figure 2.21 Dynamic Near Fault Protocol

### **3 NEAR FAULT PROTOCOL TESTING OF FULL-SCALE BRBs**

#### **3.1 Specimens**

A total of six full-scale BRBs comprised two sets of three geometrically identical braces. The six yielding cores were fabricated from four steel plates; cores of Specimens 1 through 4 were made from two ASTM A240 Type 304/304L stainless steel plates (SS), while those of Specimens 4 and 5 were from two different A36 steel plates. According to the available literature, BRBs with SS yielding core had never been studied before. Using SS for bridge BRB applications is a logical option and will inevitably be considered due to its superior corrosion resistance and ductility properties over conventional A36 steel.

Yielding core material and brace properties are provided in Table 3.1 and Table 3.2. Basic brace dimensions are provided in Figure 3.1. Along with material tensile tests provided by the BRB manufacture, the authors conducted independent tensile coupon tests of the SS plates at pseudo-static and high strain rates ( $= 0.25\text{in/in/sec}$  or  $25\% \text{ sec}^{-1}$ ). The resulting monotonic loading curves are shown in Figure 3.2; the results are discussed later.

#### **3.2 Test Setup**

The specimens were tested at the Seismic Response Modification Device (SRMD) facility at the University of California, San Diego. Figure 3.3 shows an installed specimen on the SRMD shake Table. One end of the brace was connected to a strong wall (left side in photo) and the other was connected to a reaction block on

the shake table. Each end of the extended core plate was connected to gusset plates with ASTM F2280 tension-controlled bolts, creating a slip-critical connection. This connection was designed to resist slip up to the brace initial yield force and, therefore, bolt slip was expected and experienced in all tests; however no effect on the hysteretic behavior was observed. The end conditions for Specimen 1 and the condition which is similar to that of all the other specimens are provided in Figure 3.5 and Figure 3.6, respectively.

Only uniaxial deformations were imposed in this study, unlike those in the AISC Protocol which incorporate transverse motions consistent with member end rotations in a frame. Although three specimens underwent the AISC Protocol, only Specimen 2 included these lateral deformations.

A redundant set of string potentiometers, labeled L1 through L6 in Figure 3.1, were used on each specimen to measure the core deformation. The brace forces were measured by the load cell in each of the four actuators which drive the SRMD Table. Video was recorded for each test specimen, several of which are provided on the internet (YouTube, Lanning et al. 2014).

### **3.3 Loading**

The Proof and Near Fault Protocols (developed in the previous Chapter 2) and the AISC Protocol were applied as laid out in Table 3.4. Proof and Near Fault Protocol tests were conducted with the peak strain pulse in both tension and compression directions, referred to as Proof-T, Proof-C, Near Fault-T, and Near Fault-C. Various combinations and sequences of these protocols were applied to the specimens to

investigate the inelastic capacities of the braces and to explore any resulting sequence effects. Dynamic versions of the near-field protocols (also from Chapter 2) were also used to study the effect of large strain rates from near-fault ground motion.

The input motions to the SRMD shake table were adjusted, from the target deformations, to account for the following:

- (1) Elastic deformation due to flexibility of the end supports and reaction wall at the SRMD facility based on a known total system stiffness, and
- (2) Anticipated bolt slippage within the oversized holes in the gusset and standard holes in the lug plates (see Section 3.2).

Examples of the resulting SRMD platen input motion is shown for the pseudo-static tests in Table 3.5, while Table 3.6 displays an example of target deformations and deformation rates for the dynamic tests. The VTB Near-Fault Protocol was slightly modified for ease of input signal implementation. Only a few small amplitude cycles were added at the beginning and end of the protocol, and some small variations between adjacent amplitudes were made more uniform. Nonetheless, all changes were made to provide a more conservative demand and are of minimal impact to the results [compare to Table 2.7 to Table 3.5(b)].

The specimen test order, loading protocols used, sequence in which they were applied, and the type of loading rate for each specimen is provided in Table 3.4. Specimens 1, 2, and 5 were tested with increasingly demanding protocols in order to obtain confidence in the ability of BRBs to withstand the aggressive deformation demands. After three successfully tested braces, Specimens 3, 4, and 6 were then subjected to the exact same deformations to facilitate comparisons. Specimens 3 and 6



were loaded dynamically with the same strain rates in order to readily compare the rate effects of yielding core steel type. Specimen 4 was tested pseudo-statically to provide a one-to-one comparison with Specimen 3 with loading rate as the only variable.

### 3.4 Data Reduction

#### Brace Axial Deformation, $\Delta$

In the next chapter, the brace axial deformation,  $\Delta$ , corresponding to the average of those measured by displacement transducers, L1 and L2, is reported. The brace axial strain, or core strain, was calculated as:

$$\varepsilon = \frac{\Delta}{L_y} \quad (3.1)$$

where  $L_y$  equals the length of the steel core plate yielding zone (see Figure 3.1 and Table 3.1). The brace axial deformation is also normalized by the yield deformation, which is computed based on the measured yield stress, non-uniform cross-section of the core plate, and the stiffened regions of the brace. Note that  $\Delta$  includes some minor elastic deformation of the core plate outside of the yielding length,  $L_y$ .

#### Hysteretic Energy, $E_h$

The area enclosed by the brace force,  $P$ , versus  $\Delta$  hysteresis loops represents the hysteretic energy dissipated by the brace:

$$E_h = \int P \cdot d\Delta \quad (3.2)$$

For cross-specimen comparison the dissipated energy can be normalized as:

$$\Psi_h = \frac{E_h}{P_{ya} \Delta_{by}} \quad (3.3)$$

where  $P_{ya}$  is the actual brace yield force calculated from the measured yield stress of the core plate,  $F_{ya}$ .

#### Cumulative Inelastic Ductility, $\eta$

Consider the  $i$ -th cycle at a deformation level greater than the yield deformation. The normalized total inelastic axial deformation for that cycle is given by:

$$\mu_i = \frac{2|\Delta_i^+ + \Delta_i^-|}{\Delta_{by}} - 4 \quad (3.4)$$

where  $\Delta_i^+$  and  $\Delta_i^-$  are the values of the maximum and minimum deformations, respectively, for the  $i$ -th cycle, and  $\Delta_{by}$  is the brace yield deformation. The deformation-based cumulative inelastic axial deformation,  $\eta$ , is determined by the summation of the normalized inelastic axial deformation for each of the  $i$ -th cycles:

$$\eta = \sum \mu_i \quad (3.5)$$

For uniaxial testing of BRBs, the AISC *Seismic Provisions* requires that a value of  $\eta$  at least 200 be achieved for brace qualification. For comparison purposes, the  $\eta$  values will be presented in Table 3.8. Note that this requirement does not apply to this testing program.

Figure 3.4 provides a diagram describing the energy-based ductility measure. The calculation is approximate as it assumes an elastic-perfectly-plastic hysteretic response. The deformation-based approach (Equations 3.6 and 3.7) is also approximate, as it neglects the Bauschinger effect of the hysteretic response. The

energy-based approach may be more appropriate for tracking a damage index for predictive failure. The deformation-based approach is the typical measure utilized in the AISC 2010 prequalification of BRBs for use in BRBF buildings.

### 3.5 Basic Test Results

The VTB Proof, Near Fault, and AISC Standard Loading Protocols, developed in Section 2.2, were applied to the test specimens as described in the following sections. This section presents the basic overall performance of each specimen. Every specimen was subject to multiple protocols. In addition to showing results for each loading protocol, these results are also combined in another set of plots to demonstrate the relative cumulative effects. The following results are given in the full research and testing report (Lanning et al. 2013), of which items (3), (4), and (5) are provided in this Section:

- (1) A table summarizing the peak deformations and their corresponding forces. In general, the brace axial deformation refers to the average deformation measured by displacement transducers L1 and L2 shown in Figure 3.1. This table also reports the cumulative ductility achieved throughout the test.
- (2) A similar table reporting the strength adjustment factors, corresponding to the peak forces, with respect to an effective cyclic axial deformation amplitude,  $\Delta_{eff}$  (as described in Section 3.6 of the SSRP), along with the effective tensile and compressive excursions (as defined in Figure 3.13 of the SSRP).
- (3) Measured brace axial displacement time histories: These displacements represent the actual axial deformation experienced by the brace specimen.

- (4) Brace force ( $P$ ) versus brace axial deformation ( $\Delta$ ) plot.
- (5) Hysteretic energy ( $E_h$ ) time history and normalized energy ( $\psi_h$ ) time history: These were computed in accordance with Eq. 3.2 and 3.3, respectively.
- (6) Tension strength adjustment factor ( $\omega$ ) versus brace effective cyclic axial deformation amplitude ( $\Delta_{eff}$ ) plot: The calculation of  $\omega$  is based on Eq. 3.2.
- (7) Compression strength adjustment factor ( $\beta$ ) versus brace effective cyclic axial deformation amplitude ( $\Delta_{eff}$ ) plot: See Eq. 1.2 for the description of and discussion on the value  $\beta$ .

### 3.5.1 Specimen 1

Specimen 1 was tested on March 16, 2012. Figure 3.7 shows the specimen prior to testing, and Figure 3.8 displays the end condition. As it was the first specimen to be tested, the VTB Proof Protocol was applied, pseudo-statically, before attempting the more demanding VTB Near-Fault Protocol. It was decided that the large core strain pulse, within the Proof Protocol, would be applied in the tension direction as a first venture into testing BRBs at 5% core strain.

The specimen performed well during the tension direction Proof Protocol. Figure 3.9 shows the specimen after the test. Since the specimen showed no signs of strength degradation or damage, it was decided to repeat the Proof Protocol with the core strain amplitudes reversed in sign, resulting in a compressive core strain pulse.

During the compression direction Proof Protocol the gusset plate connection failed on the platen side of the brace, apparently due to inadequate out-of-plane rotational stiffness, which resulted in the permanent deformation of the connection

brackets shown in Figure 3.10. Figure 3.11(a) displays the deformed connection and gusset plate before the specimen was removed from the SRMD table. Figure 3.11(b) shows the specimen with deformed gusset plate after being removed from the test setup.

It should be noted that the Proof Protocol represents the deformation demand from a rare seismic event as described in Section 2.1 (approximately 2.3% probability of exceedance in 75 years, for the BRB installed on the VTB under the design earthquake) and repeating it with the same specimen does not represent a realistic situation for practical applications. After testing, the specimen was disassembled to inspect the yielding segment of the BRB core. Figure 3.21 shows two photos of the stainless steel core which shows no visible signs of damage or imminent rupture. New strengthened brackets were fabricated and used for all subsequent specimens (see Section 3.5.2).

### **3.5.2 Strengthened Brackets**

After the damage was incurred during the Specimen 1 test, further testing required the fabrication of new brackets to replace the old damaged brackets. Figure 3.22 shows the main features of the strengthened design which include a set of thicker (1-1/4 in. as compared to 3/4 in.) plates bolting plates, and vertical edge stiffeners on each side of the gusset.

### **3.5.3 Specimen 2**

Specimen 2 was tested on April 25 and 26, 2012. Figure 3.23 shows the specimen prior to testing, while Figure 3.24 displays the end condition. Due to the fact

that Specimens 1 and 2 were nominally identical (besides stainless steel core yield strength) and Specimen 1 had previously been shown to sustain the tension direction Proof Protocol, it was decided to begin testing of Specimen 2 with the VTB Proof Protocol with the pulse in the compression direction. The loading rate for this specimen was also pseudo-static.

The specimen performed well during the compression direction Proof Protocol test. The new connection detail was proven effective as shown in Figure 3.25. Since the specimen showed no signs of strength degradation or immanent failure, the testing was continued by subjecting Specimen 2 to the VTB Near-Fault Protocol. Because the proof pulse had been conducted in the compression direction, the 5% core strain value was applied in the tension direction, resulting in the strain time history shown in Figure 3.26.

Specimen 2 performed well during the tension direction Near-Fault Protocol test. Finally, as there were still no signs of strength loss, it was then decided to continue testing by applying the AISC Standard Loading Protocol. This additional test served to demonstrate the robust ductility capacity of the BRB as well as to obtain some measurements pertaining to the standard response values ( $\omega$  and  $\beta$ ) typically collected for BRB prequalification test. Additionally, this response was desired for comparison to the braces subjected to the Dynamic AISC Standard Protocol (Specimens 3, 4, and 6). The brace sustained this protocol as well, and afterwards the brace was removed from the SRMD platen for inspection of the steel core.

### 3.5.4 Specimen 3

Specimen 3 was tested on December 13, 2012. Figure 3.39 shows the specimen prior to testing. Figure 3.40 displays the end condition, which does not exhibit bolted side-stiffeners as on Specimen 2. As shown in Table 3.4, Specimen 3 was the fourth specimen to be tested in this program, and Specimens 2, 3, 4, and 6 were subjected to the same loading protocol sequence. This specimen exhibited a yielding core of A240 stainless steel and was tested dynamically to provide a comparison to those braces subjected to typical pseudo-static rates. SRMD platen input motions were slightly larger than those given by the protocol in an attempt to overcome the connection bolt slip through the oversized bolt holes. Therefore, the measured brace deformation and rate surpassed the targets (See Section 2.2 and 3.3). The maximum peak strain rate achieved was approximately 0.37 in/in/sec.

The brace performed well during the entire test, showing no sign of strength degradation or fracture of the core plate throughout both the Dynamic Proof, Near-Fault, and AISC Loading Protocols. The restraining portion of the brace did, however, shift drastically towards one end of the brace during each the major excursions throughout the two VTB protocols. This resulting unsymmetrical location of the HSS restraining did not seem to affect the response. This behavior was observed to occur much less in the pseudo-static specimens.

In order to determine the cumulative ductility capacity, in the presence of high loading rates, the brace was then subjected to a fracture protocol. The target cyclic amplitude was made constant at a deformation equal to 1.5 times the maximum experienced in the AISC protocol ( $= 15\Delta_y$ ), while the target peak strain rate was held

constant as the maximum within the Dynamic AISC protocol ( $= 0.10$  in/in/sec). The yielding core plate eventually fractured upon the fourth tension excursion, thereby completing 3 full cycles of the fracture protocol.

The specimen completed two protocols representing severe near-field earthquake demands, followed by the typical AISC protocol for building prequalification, and 3 additional cycles of relatively large core strain ( $= 3.67\%$ ). Furthermore, all protocols were performed dynamically with high strain rates.

### **3.5.5 Specimen 4**

Specimen 4 was tested on December 14, 2012. Figure 3.61 shows the specimen prior to testing, and Figure 3.62 displays the end condition. Specimen 4 was the fifth specimen to be tested in this program, and subjected to the same loading as Specimens 2 and 4. This brace exhibited a yielding core of A240 stainless steel and was tested pseudo-statically to provide a comparison to braces subjected to high strain rates.

The specimen performed well during all tests, showing no sign of strength degradation through the Proof, Near-Fault, and AISC Standard Loading Protocol. However, a connection instability very similar to that experienced during testing of Specimen 1 was imminent. This behavior was observed beginning with the second large 5% compression excursion during the Near-Fault test. The AISC protocol was considered sufficiently less demanding such that it was not expected to cause the connection instability to fully form. The extent of out-of-plane deformation of the connection is shown in Figure 3.63, and connection failure was expected with an increase in compressive force, therefore the test was terminated.



### **3.5.6 Specimen 5**

Specimen 5 was tested on April 27, 2012. Figure 3.76 shows the specimen prior to testing and Figure 3.77 shows the specimen end condition. After the first and second tests, Specimens 1 and 2 displayed the ability of BRB to sustain the tension and compression direction Proof Protocols, respectively, it was decided to begin Specimen 5 directly with the VTB Near-Fault Protocol at a pseudo-static loading rate. Despite the core plate being A36, unlike Specimens 1 and 2, it was deemed likely that the brace would be capable of sustaining at least one VTB Near-Fault Protocol, considering the success of the other braces.

The specimen performed well during the VTB Near-Fault Protocol test, which was oriented with the largest core strain (= 5%) in the tension direction. The brace exhibited no signs of strength loss or failure, so the protocol strain values were reversed in sign and the Near-Fault Protocol test was performed a second time, again loaded pseudo-statically. Specimen 5, again, performed well, showing no signs of immanent failure. The brace was not taken to failure in order to inspect the condition of the core. Upon inspection of the core (see Figure 3.87) there was very little sign of distress.

### **3.5.7 Specimen 6**

Specimen 6 was tested on December 18, 2012. Figure 3.88 shows the specimen prior to testing, and Figure 3.89 displays the end condition. Specimen 6 was the final specimen to be tested in this program. Again, Specimens 3, 4, and 6 were subjected to the same loading protocol sequence. This specimen exhibited a yielding core of A36

steel and was tested dynamically, just as was Specimen 3, to provide a comparison of A36 and A240 yielding cores subjected to high strain rates. The maximum strain rate was approximately 0.37 in/in/sec.

The brace performed well during the entire test, showing no sign of strength degradation until fracture of the core plate was experienced during the AISC Standard Loading Protocol, which was the third consecutive test.

The restraining portion of the brace did, however, shift drastically towards one end of the brace after each of the major excursions throughout the two VTB protocols. This resulting unsymmetrical location of the HSS restraining casing did not seem affect the response. This behavior was not observed to occur nearly as drastically in the pseudo-static specimens.

Prior to the third protocol, the brace sustained two consecutive loading protocols that each represented rare near-fault earthquakes with large inelastic core strain of 5% in the compression direction.

After testing, the specimen was disassembled to inspect the yielding segment of the BRB core. The flat plate core showed no signs of distress other than the location of the fracture.

### **3.6 Overall Performance**

Hysteretic performance of each specimen is displayed in Sections 3.5.1 through 3.5.7. As indicated in Table 3.4, only Specimens 3 and 6 were taken to fracture, while the other specimens were not to facilitate their removal from the testing equipment and for further examination of the steel core buckling shape. Each

specimen withstood at minimum one loading protocol test with a BRB core strain of 5% (bolt-slip occasionally lead to minor deviations from target core deformation), while most were subjected to two near-fault loading protocol tests and a subsequent AISC Protocol.

All braces performed very well, showing no signs of strength degradation before test termination or fracture. Each sustained large cumulative inelastic ductility,  $\eta$ , an indication of the accumulated sustained material damage and is commonly approximated in AISC prequalifying tests per Eqs. 3.4 and 3.5. AISC 341 requires  $\eta$  of at least 200 be achieved during the AISC Protocol for prequalification. Strictly speaking, this AISC requirement does not apply to this testing program because near-field loading protocols were used. But it is evident that all BRBs (except Specimen 1) far out perform this requirement.

Specimen 3 exhibited a slight casing bulge near one end of the restrained core. This type of deformation, which has been documented by others (e.g., Iwata 2004, Chou et al. 2010) for BRBs with flat plate cores, is indicative of restrained strong-axis buckling of the core within the restraining member. Note, though, no loss of brace resistance was experienced due to this internal buckling, even at the relatively large deformation levels of 5% compressive core strain.

Specimen 1, which was the first specimen tested, successfully completed the Proof-T test. In an attempt to apply a subsequent Proof-C test, however, the specimen experienced connection instability, as shown in Figure 3.11. This failure mode has been observed in several other BRB testing programs and is discussed further in Chapter 6.

Chapter 3 in partial, is a reprint of the material as it has been submitted for publication. The dissertation author was the first author of these papers.

Table 3.1 Specimen Dimensions

## (a) Core Plate and Casing Size

Specimen No.	W1 (in.)	W2 (in.)	W3 (in.)	W4 (in.)	$t_{cp}$ (in.)	Core Plate Shape	HSS Casing Size (in.)
1, 2, 5	12-1/2	16-7/8	7	2-7/8	1-1/4	Cruciform	14×14×3/8
3, 4, 6	8-7/8	8-9/16	6-3/8	-	1-1/4	Flat	14×14×5/16

## (b) Lengths

Specimen No.	$L$ (in.)	$L_b$ (in.)	$L_y$ (in.)	$c$ (in.)	$x$ (in.)	$L_T$ (in.)	$L_{sp}^*$ (in.)
1, 2, 5	251-3/16	197-5/16	126-13/16	26-15/16	8-3/16	27-1/16	14
3, 4, 6	260-11/16	219-1/8	150-3/16	20-13/16	7	27-7/16	N/A

\* Specimens 1 and 2 only

## (c) Bolting

Specimen No.	Lug PL Hole Diam. (in.)	Gusset PL Hole Diam. (in.)	Rows of Bolts	$s$ (in.)	$g_1$ (in.)	$g_2$ (in.)
1, 2, 5	1-3/16	1-7/16	9	2-1/2	2-5/16	4-5/8
3, 4, 6	1-3/16	1-7/16	5	3-1/4	2-13/16	-

Table 3.2 Mechanical Properties of Core Plates

Specimen No.	Steel Type	Strain Rate <sup>a</sup> (% sec <sup>-1</sup> )	$F_{ya}$ (ksi)	$R_y^c$	$F_{ua}$ (ksi)	$R_u$	2" Gage Length Elongation
1, 4	Stainless Type 304, Type 304/304L	PS	39.5 <sup>b</sup>	1.58	92.2	2.34	54
2, 3		PS	33.3 <sup>b</sup>	1.33	88.3	2.65	57
		25	39.2 <sup>b</sup>	1.58	88.3	2.26	69
5	A36	PS	41.4	1.15	65.3	1.58	40
6			41.0	1.14	71.1	1.73	33

<sup>a</sup> "PS" designates pseudo-static test provided by BRB manufacturer; rate assumed to be approximately 0.025 % sec<sup>-1</sup>.<sup>b</sup> Based on 2% strain offset

Table 3.3 BRB Yield Strength and Deformation

Specimen No.	$A_{sc}$ (in. <sup>2</sup> )	$F_{ya}$ (ksi)	$P_{yn}$ (kips)	$P_{ya}$ (kips)	$\Delta_{by}$ (in.)
1	16	39.5	480	631.2	0.23
2		33.3	480	532.8	0.20
3	8		240	266.6	0.22
4		39.5	240	315.6	0.26
5	16	41.4	576	662.4	0.23
6	8	41.0	288	328	0.26

Table 3.4 Specimen Loading Information

Specimen No.	Test Order	Core Plate		Loading Rate <sup>b</sup>	Tested Protocol Sequence			
		Steel Grade	Shape <sup>a</sup>		1st	2nd	3rd	4th
1	1	SS	+	PS	Proof-T	Proof-C <sup>c</sup>	n/a	n/a
2	2			PS	Proof-C	Near Fault-T	AISC	n/a
3	4		-	D	Proof-C	Near Fault-C	AISC	LCF <sup>d</sup>
4	5			PS	Proof-C	Near-Fault-C	AISC	n/a
5	3	A36	+	PS	Near Fault-T	Near Fault-C	n/a	n/a
6	6		-	D	Proof-C	Near Fault-C	AISC <sup>d</sup>	n/a

<sup>a</sup> (+) and (-) designate cruciform and flat plate cross-section, respectively

<sup>b</sup> "PS" and "D" designate pseudo-static and dynamic loading rates, respectively

<sup>c</sup> Specimen 1 experienced a connection instability

<sup>d</sup> Low-cycle fatigue protocol, fracture occurred

<sup>e</sup> Fracture occurred

Table 3.5 Sample Pseudo-Static Target BRB Deformation and SRMD Table Input

## (a) VTB Proof Protocol, Specimen 1

Step	Target Axial Deform. (in.)	Table Displ. (in.)	Step	Target Axial Deform. (in.)	Table Displ. (in.)	Step	Target Axial Deform. (in.)	Table Displ. (in.)
1	-0.25	-0.37	8	1.08	1.55	15	0.44	0.61
2	0.25	0.37	9	0.44	0.61	16	1.08	1.54
3	-1.27	-1.88	10	1.08	1.54	17	0.44	0.61
4	6.34	7.14	11	0.44	0.61	18	1.08	1.54
5	-1.27	-1.88	12	1.08	1.54	19	0.44	0.61
6	1.27	1.91	13	0.44	0.61	20	1.08	1.54
7	0	-0.50	14	1.08	1.54	21	0.44	0

## (b) VTB Near-Fault Loading Protocol, Specimen 5

Step	Target Axial Deform. (in.)	Table Displ. (in.)	Step	Target Axial Deform. (in.)	Table Displ. (in.)	Step	Target Axial Deform. (in.)	Table Displ. (in.)
1	-0.24	-0.98	17	-0.67	-1.40	33	0.29	-0.15
2	0.36	0.98	18	2.21	2.90	34	1.33	1.85
3	-0.28	-1.36	19	-0.38	-1.00	35	0.32	-0.15
4	0.38	0.98	20	2.16	2.90	36	1.32	1.85
5	-0.75	-1.60	21	-0.32	-1.00	37	0.38	-0.15
6	0.46	1.90	22	2.02	2.90	38	1.27	1.85
7	-0.81	-1.90	23	-0.14	-0.40	39	0.51	-0.15
8	1.18	1.90	24	2.00	2.90	40	1.10	1.85
9	-1.27	-1.90	25	0.04	-0.40	41	0.58	-0.15
10	1.27	1.90	26	1.83	2.30	42	1.10	1.85
11	-2.11	-2.90	27	0.06	-0.30	43	0.66	-0.15
12	6.35	7.10	28	1.70	2.30	44	1.04	1.85
13	-4.44	-5.20	29	0.06	-0.30	45	0.80	-0.15
14	4.12	4.90	30	1.57	2.00	46*	-	1.85
15	-3.80	-4.50	31	0.25	-0.15	47*	-	0.85
16	2.98	3.50	32	1.42	1.85	48*	-	-0.40

\*Additional small cycles added during testing

Table 3.6 Sample Dynamic Target BRB Deformations and Rates

## (a) VTB Proof Protocol

Step	Target Peak		Step	Target Peak		Step	Target Peak	
	Deform. (in)	Deform. Rate (in/sec)		Deform. (in)	Deform. Rate (in/sec)		Deform. (in)	Deform. Rate (in/sec)
1	-0.30	-0.3	8	1.27	2.1	15	0.53	-2.3
2	0.30	2.6	9	0.53	-2.2	16	1.28	2.3
3	-1.40	-8.3	10	1.28	2.3	17	0.53	-2.3
4	7.51	27.0	11	0.53	-2.3	18	1.28	2.3
5	-1.50	-12.0	12	1.28	2.3	19	0.53	-2.3
6	1.50	5.0	13	0.53	-2.3	20	1.28	2.3
7	0	-2.5	14	1.28	2.3	21	0.53	-2.3

\*Table input slightly larger for all reported values due to losses described in Section 3.3

## (b) VTB Near-Fault Protocol

Step	Target Peak		Step	Target Peak		Step	Target Peak	
	Deform. (in)	Deform. Rate (in/sec)		Deform. (in)	Deform. Rate (in/sec)		Deform. (in)	Deform. Rate (in/sec)
1	-0.67	-0.7	17	-1.10	-21.6	33	0.28	-2.2
2	0.66	1.4	18	2.81	19.1	34	1.66	2.2
3	-1.10	-3.7	19	-0.65	-16.9	35	0.28	-2.2
4	0.66	3.7	20	2.82	16.9	36	1.66	2.2
5	-1.37	-4.3	21	-0.65	-16.9	37	0.28	-2.2
6	1.72	6.5	22	2.85	16.8	38	1.66	2.2
7	-1.69	-14.2	23	0.01	-9.9	39	0.28	-2.2
8	1.67	14.2	24	2.85	9.9	40	1.66	2.2
9	-1.61	-19.9	25	0.01	-9.9	41	0.28	-2.2
10	1.59	20.5	26	2.17	10.8	42	1.66	2.2
11	-2.74	-27.6	27	0.12	-5.4	43	0.28	-2.12
12	7.51	45.2	28	2.17	5.4	44	1.65	2.2
13	-5.43	-45.6	29	0.12	-5.4	45	0.28	-2.2
14	5.12	45.6	30	1.83	6.7			
15	-4.67	-30.7	31	0.28	-2.4			
16	3.51	25.7	32	1.66	2.2			

\*Table input values larger for all reported values due to losses described in Section 3.3



Table 3.7 Sample AISC Standard Protocol Targets

## (a) Pseudo-Static, Specimen 2

Cycles	Target Axial Deformation (in)	Table Displacement*	
		Tension Direction (in)	Compression Direction (in)
2	0.20	0.97	0.60
2	0.63	1.39	0.92
2	1.25	1.90	1.44
2	1.9	2.40	1.96
2	2.5	2.89	2.46
2	1.9	2.40	1.96

\*Protocol slightly offset by prior testing

## (b) Dynamic, Specimen 3

Cycles	Target Peak	
	Deform. (in)	Deform. Rate (in/sec)
2	0.22	0.7
2	0.75	3.3
2	1.5	6.6
2	2.25	9.9
2	3.0	17.2
2	2.25	11.6

Table 3.8 Maximum Response Values

Spec.	Normalized Force ( $P_y/P_{ya}$ )		Core Strain (%)		Strain Rate (% sec <sup>-1</sup> )	$E_h$ (1,000 kip-in)	$\psi_h$	$\eta$
	Tension	Compression	Tension	Compression				
1	1.38	-1.87	4.72	-2.62	*	19.4	133	112
2	2.47	-2.67	4.57	-5.14	*	109.1	1,024	724
3	2.55	-3.01	3.68	-5.45	36.5	120.4	2,052	1,221
4	2.35	-2.76	3.75	-5.36	*	96.6	1,177	820
5	1.51	-1.69	5.02	-4.83	*	130.9	859	747
6	1.76	-2.01	3.71	-5.39	36.7	75.8	888	733

\* Pseudo-static test



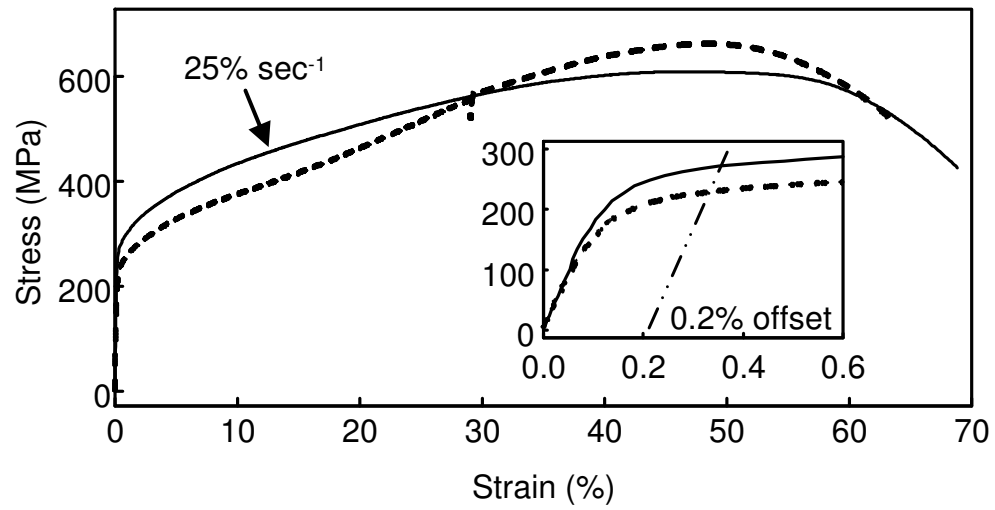


Figure 3.2 ASTM A240, Type 304/304L Stainless Steel Tensile Coupon Tests at Pseudo-Static and Dynamic Rates



Figure 3.3 Specimen Installed in the SRMD Shake Table

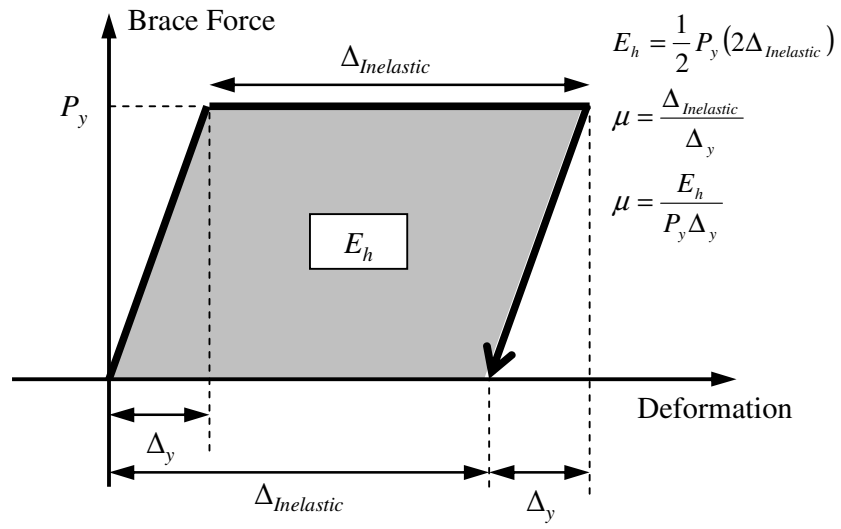


Figure 3.4 Energy Based Ductility Calculation



(a) Wall End Support (West End)



(b) Platen End Support (East End)

Figure 3.5 Specimen 1 End Conditions



(a) Wall End Support (West End)



(b) Platen End Support (East End)

Figure 3.6 Specimen 2 and 5 End Conditions (Specimen 5 shown)

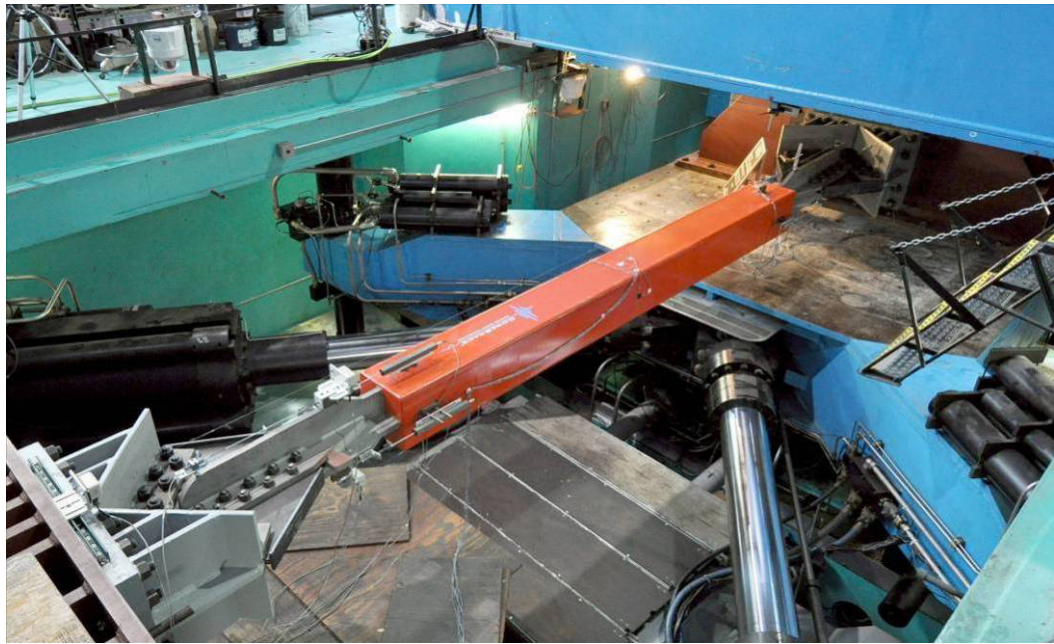


Figure 3.7 Specimen 1 Test Setup



Figure 3.8 Specimen 1 End Condition





(a) Overall



(b) Platen End Condition

Figure 3.9 Specimen 1 after Tension Direction Proof Protocol



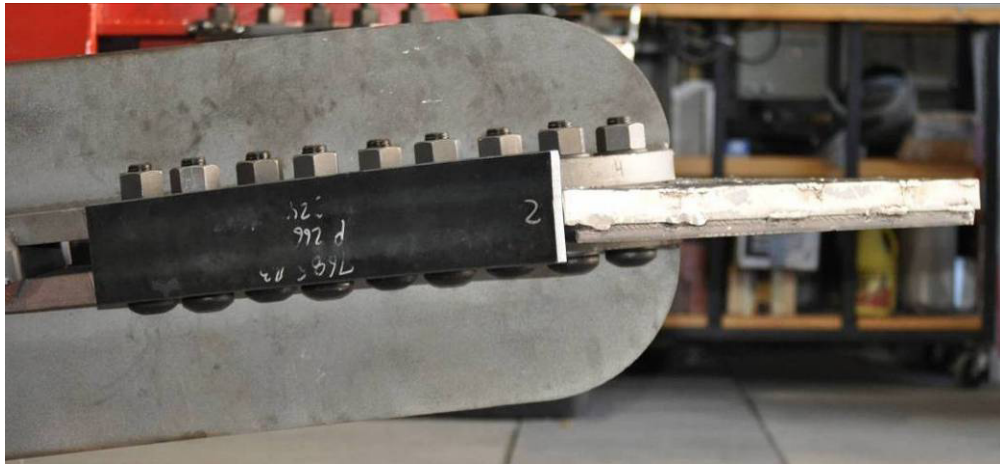
(a) Strong Wall Bracket

(b) Platen Reaction Block Bracket

Figure 3.10 Original Bracket after Specimen1 Compression Direction Proof Protocol



(a) Overall



(b) Gusset Plate

Figure 3.11: Specimen 1 and Gusset Plate after Compression Proof Protocol

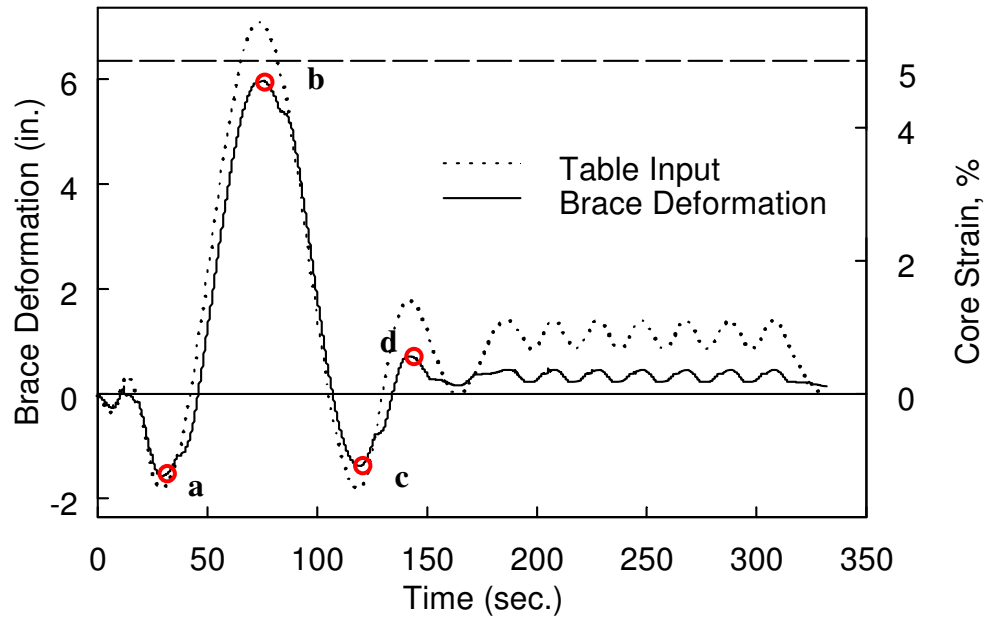


Figure 3.12 Specimen 1: Brace Deformation Time Histories (Tension Proof Protocol)

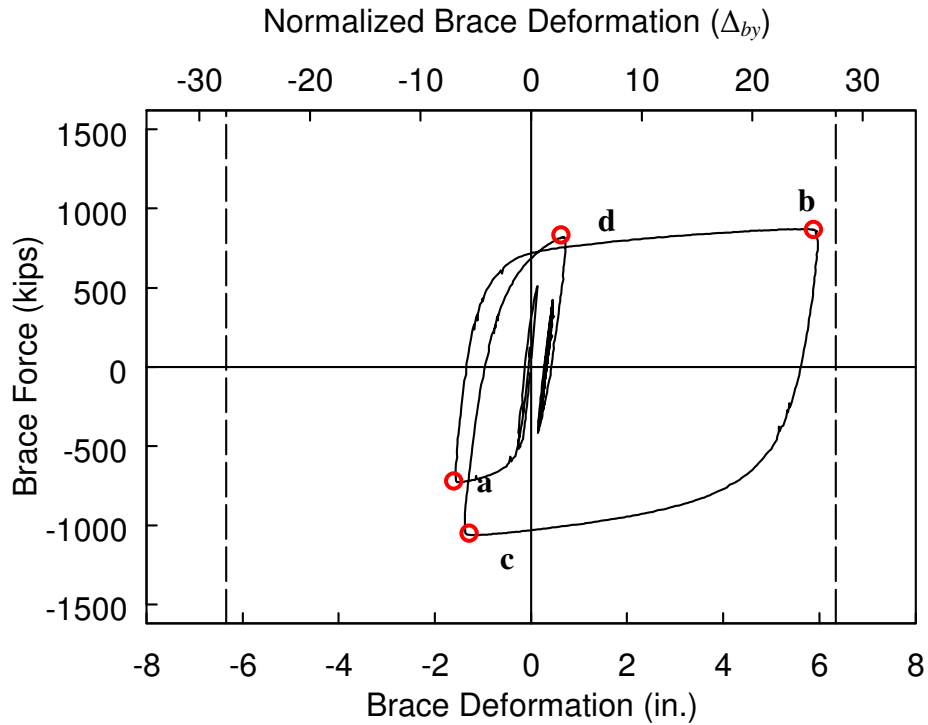


Figure 3.13 Specimen 1: Brace Force vs. Axial Deformation (Tension Proof Protocol)

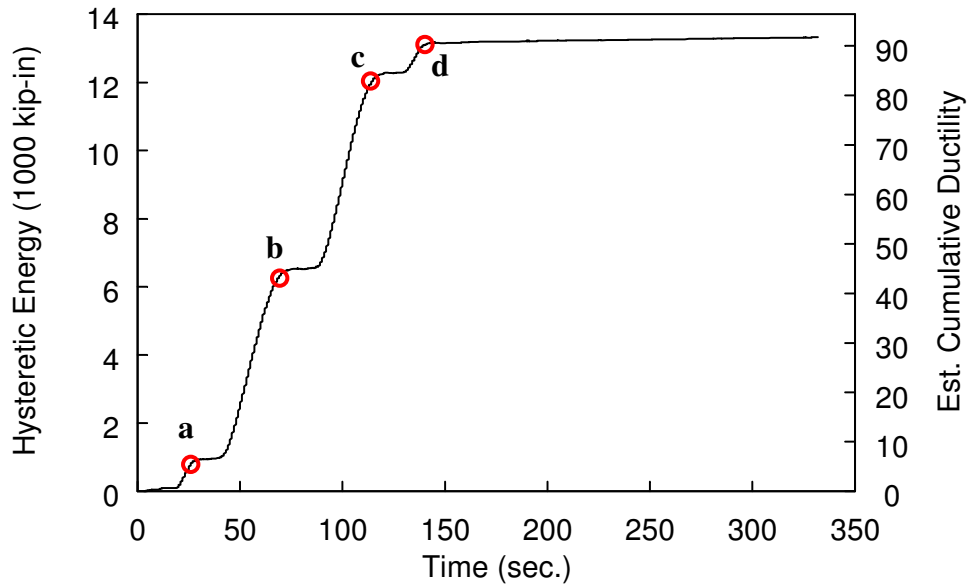


Figure 3.14 Specimen 1: Hysteretic Energy and Estimated Cumulative Ductility Time History (Tension Proof Protocol)

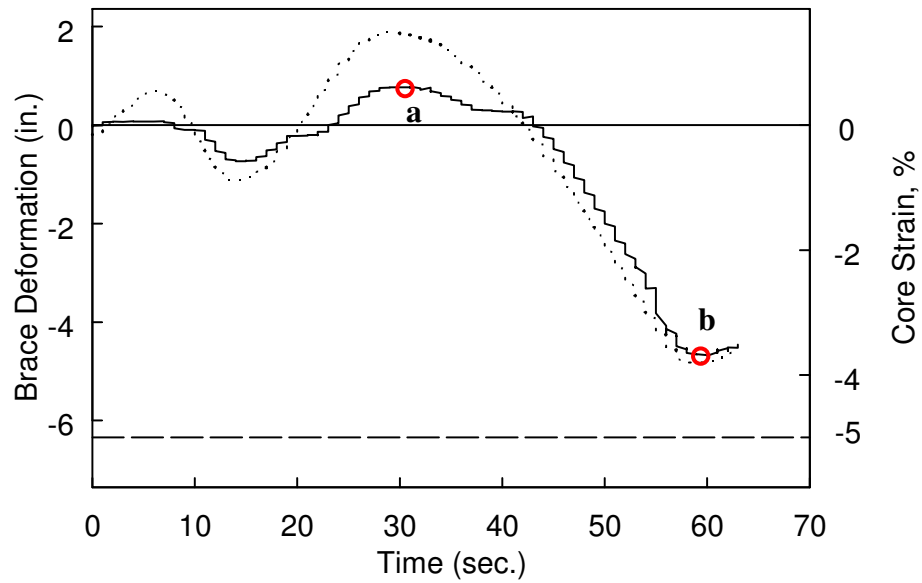


Figure 3.15 Specimen 1: Brace Deformation Time Histories (Compression Proof Protocol)

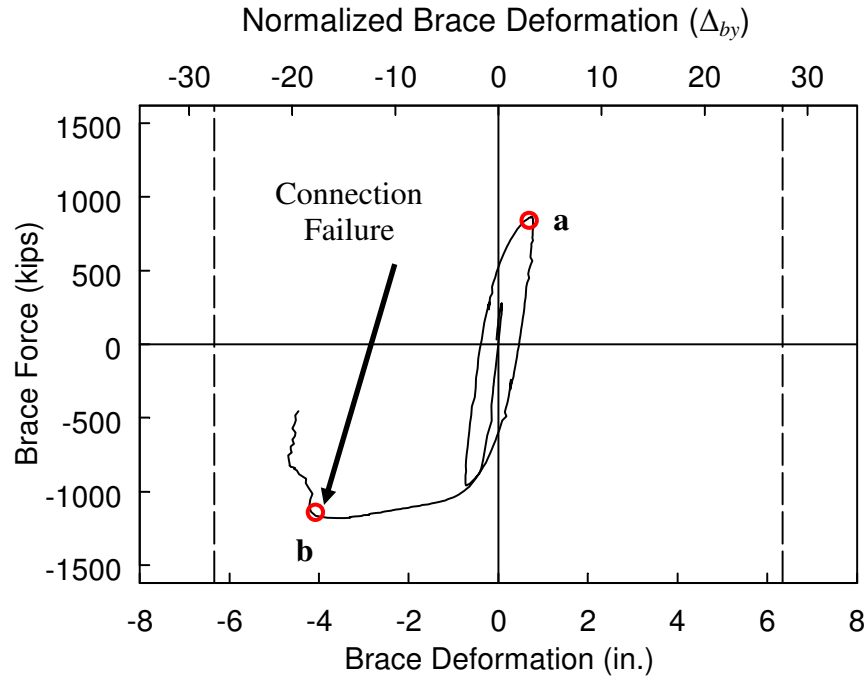


Figure 3.16 Specimen 1: Brace Force vs. Axial Deformation (Compression Proof Protocol)

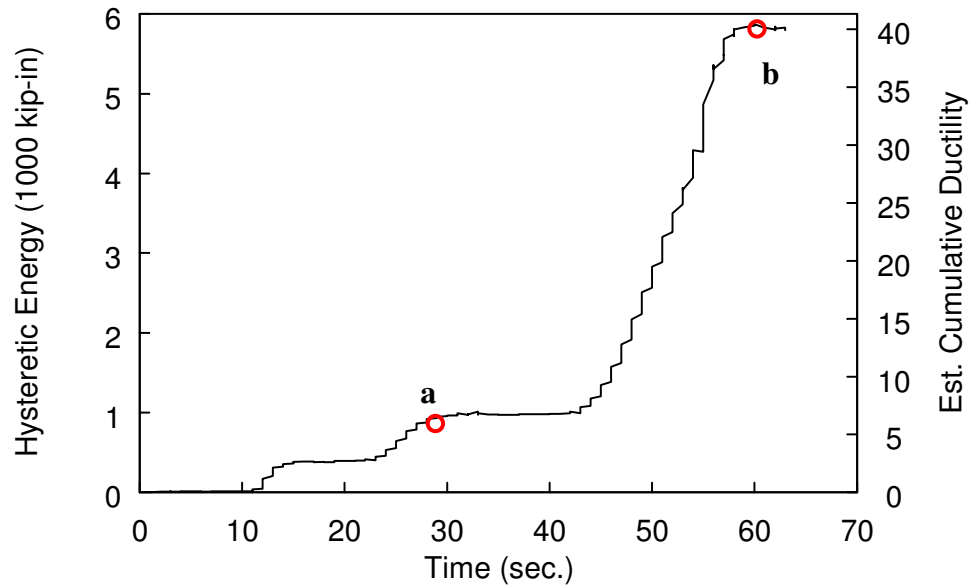


Figure 3.17 Specimen 1: Hysteretic Energy Time History (Compression Proof Protocol)

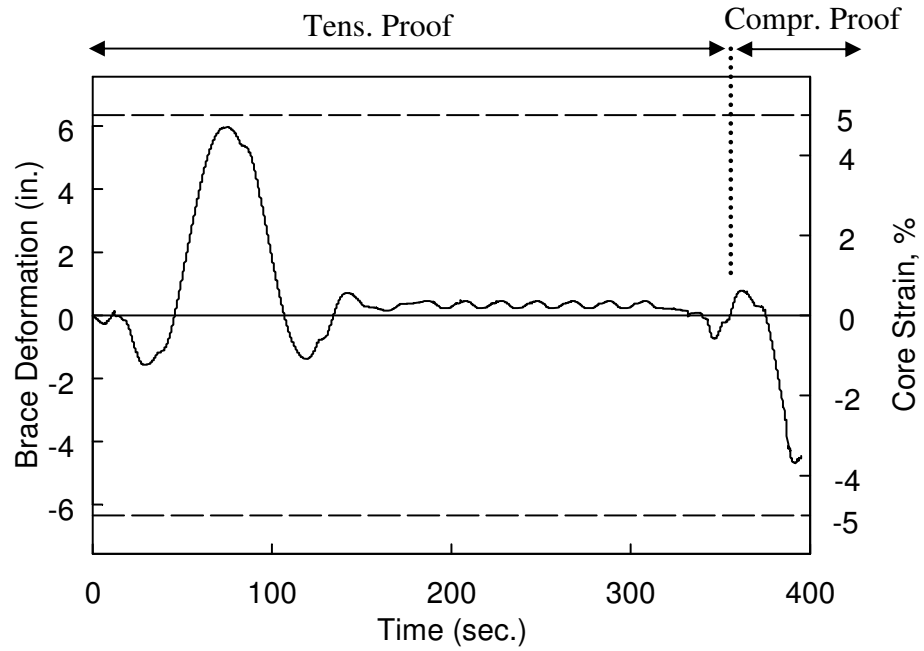


Figure 3.18 Specimen 1: Brace Deformation Time Histories (All Tests)

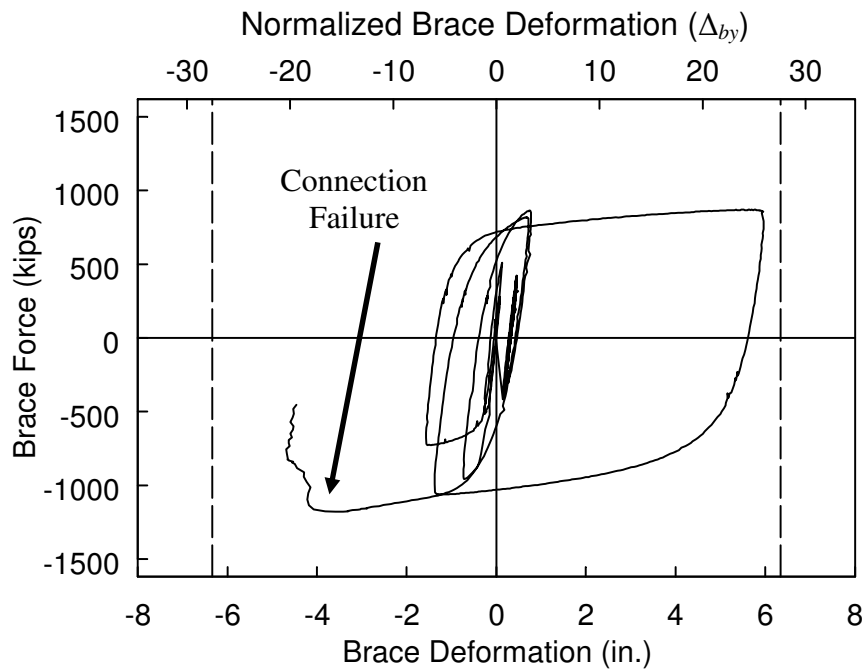


Figure 3.19 Specimen 1: Brace Force vs. Axial Deformation (All Tests)

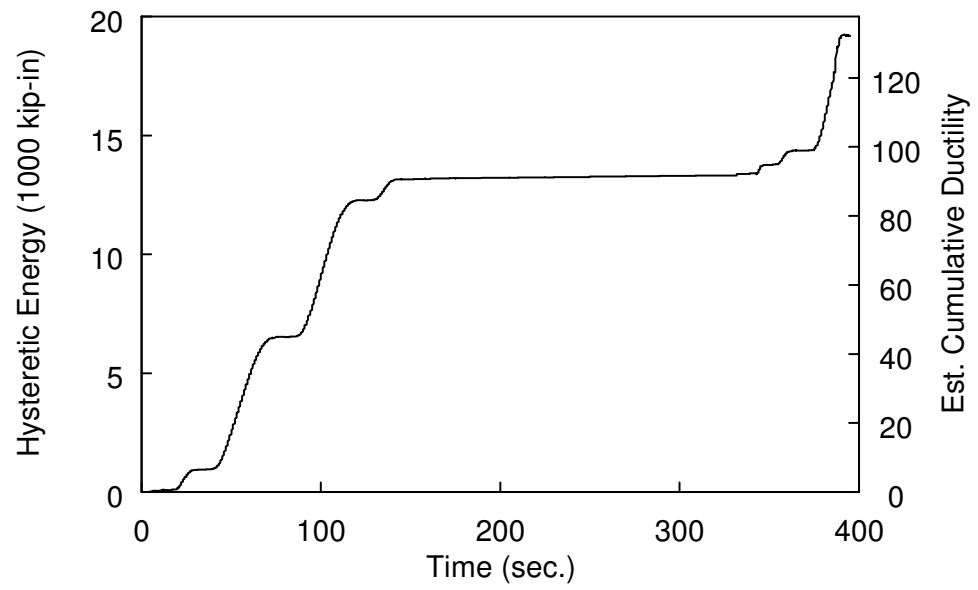


Figure 3.20 Specimen 1: Hysteretic Energy Time History (All Tests)



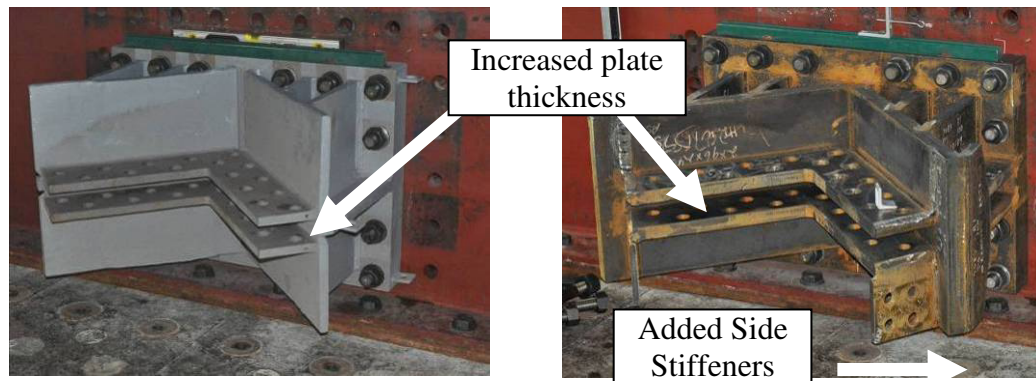


(a) Photo 1



(b) Photo 2

Figure 3.21: Specimen 1 Core Plate after All Tests



(a) Original Bracket

(b) New, Strengthened, Bracket

Figure 3.22 Original and New, Strengthened, Brackets on the Platen Reaction Block



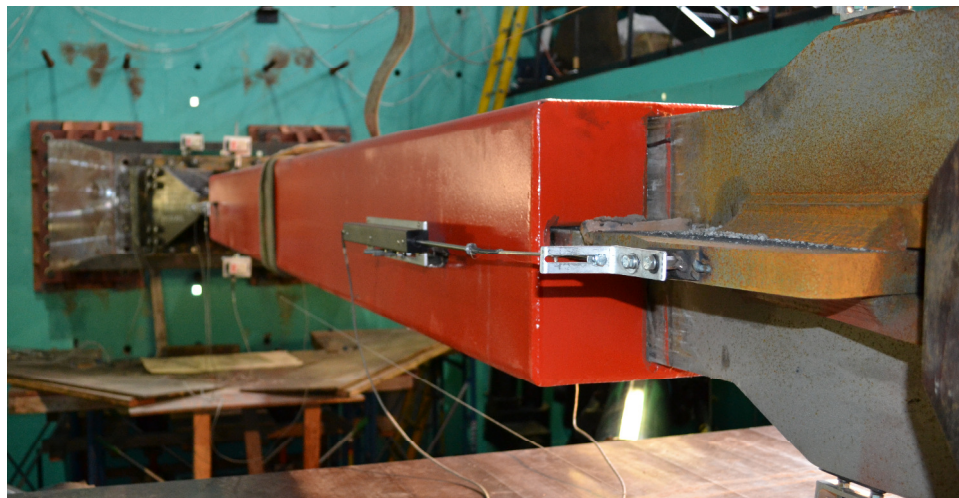
Figure 3.23 Specimen 2: Test Setup



Figure 3.24 Specimen 2: End Condition (Specimen 5 shown)



(a) Specimen 1 Overall, after Compression Proof Protocol



(b) Specimen 2 Overall, after Compression Proof Protocol

Figure 3.25 Effectiveness of New Strengthened Brackets

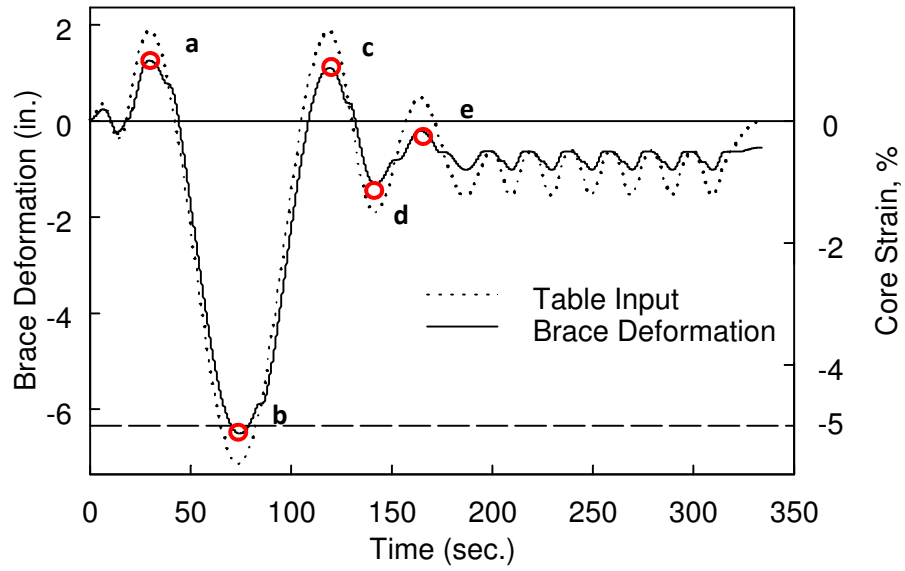


Figure 3.26 Specimen 2: Brace Deformation Time Histories (Compression Proof Protocol)

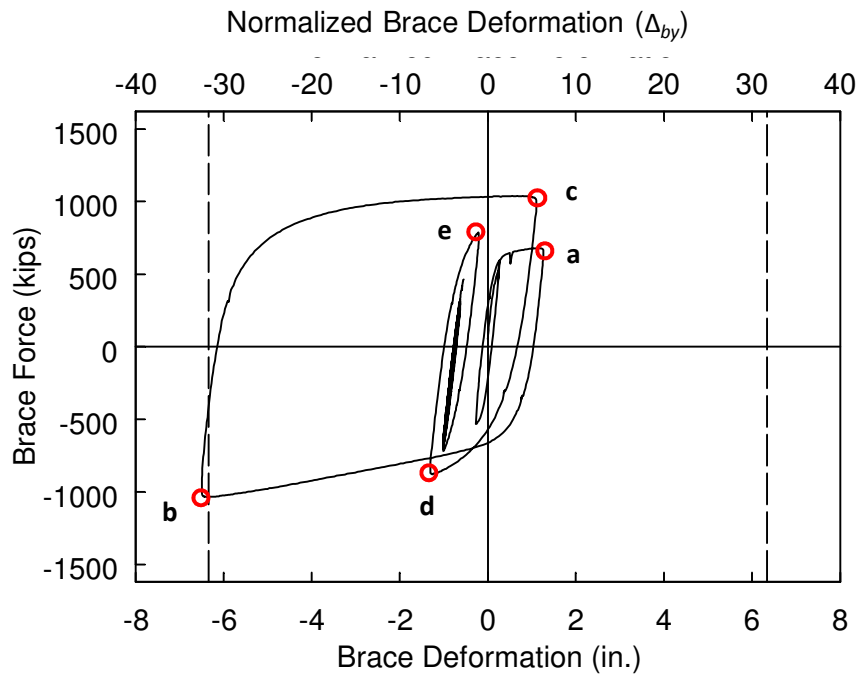


Figure 3.27 Specimen 2: Brace Force vs. Axial Deformation (Compression Proof Protocol)

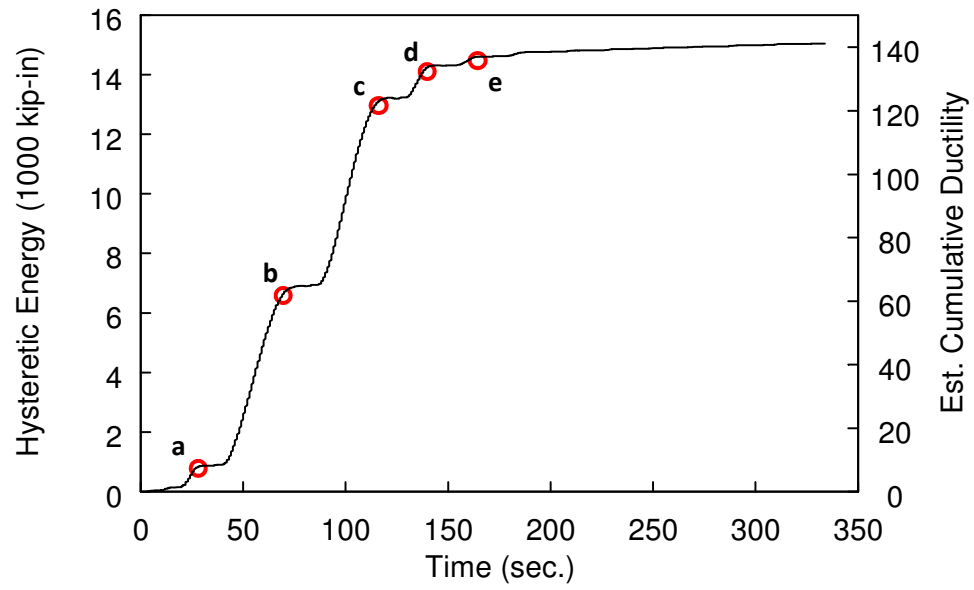


Figure 3.28 Specimen 2: Hysteretic Energy Time History (Compression Proof Protocol)

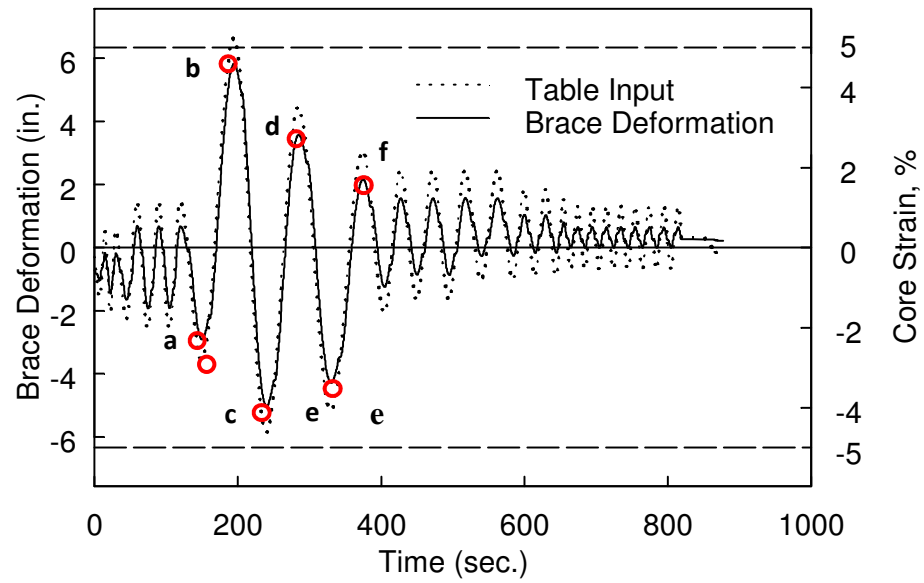


Figure 3.29 Specimen 2: Brace Deformation Time Histories (Near-Fault Protocol)

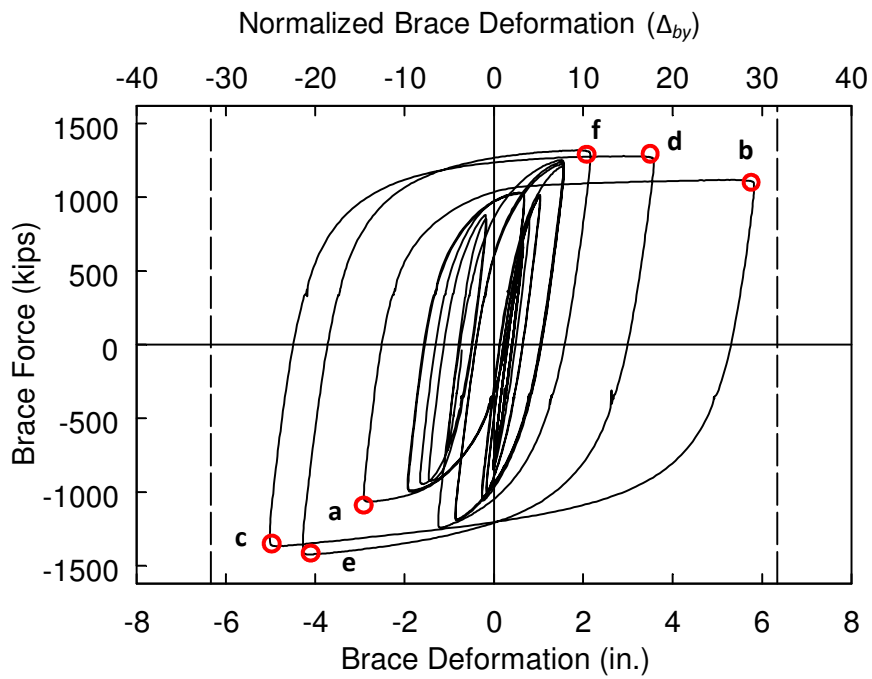


Figure 3.30 Specimen 2: Brace Force vs. Axial Deformation (Near-Fault Protocol)

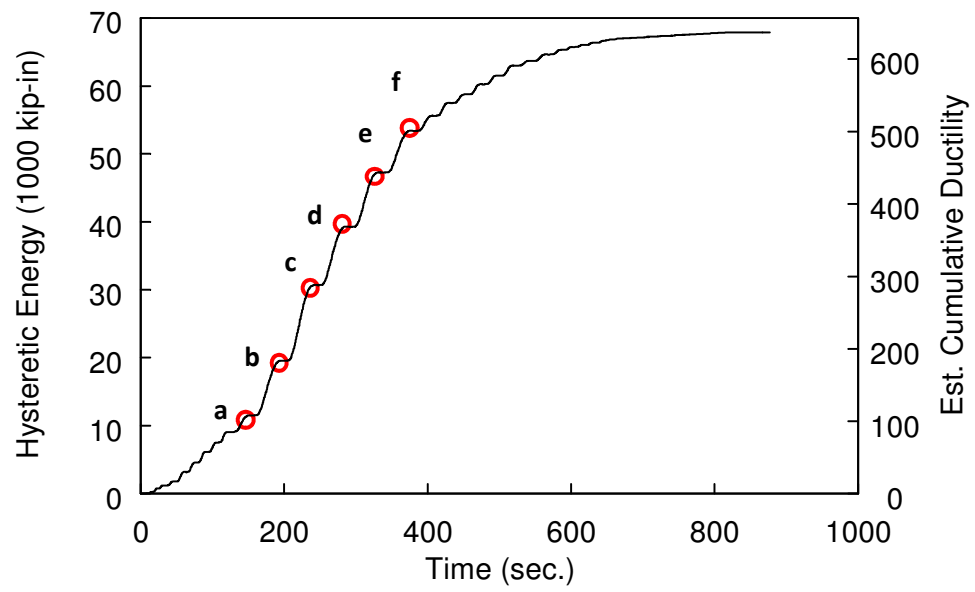


Figure 3.31 Specimen 2: Hysteretic Energy Time History (Near-Fault Protocol)

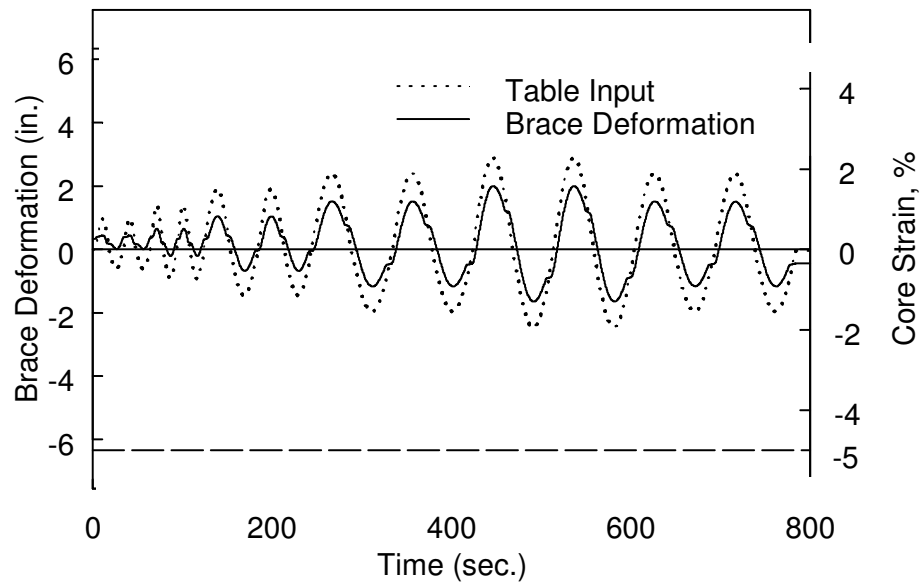


Figure 3.32 Specimen 2: Brace Deformation Time Histories (AISC Standard Protocol)

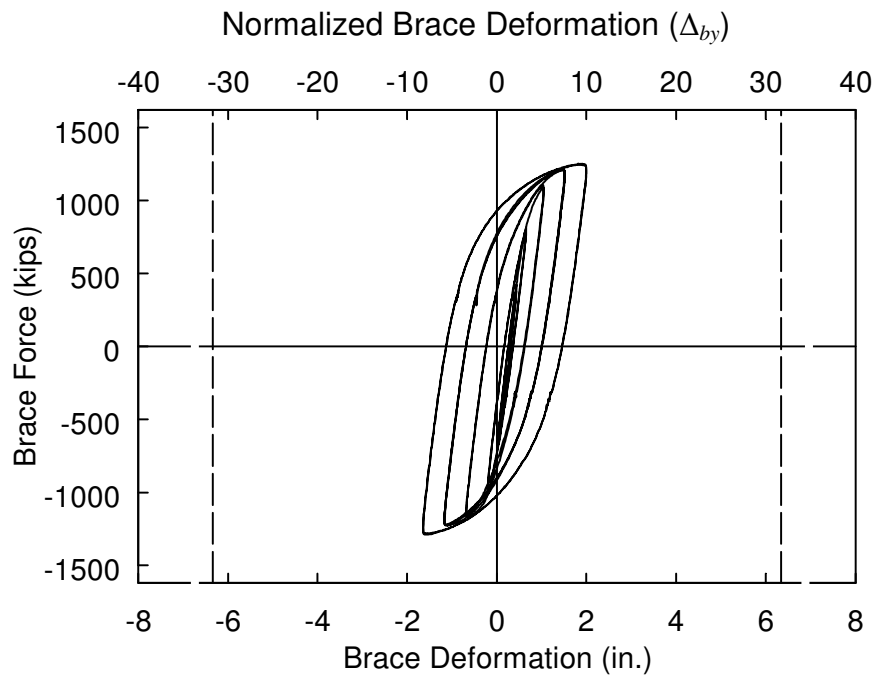


Figure 3.33 Specimen 2: Brace Force vs. Axial Deformation (AISC Standard Protocol)



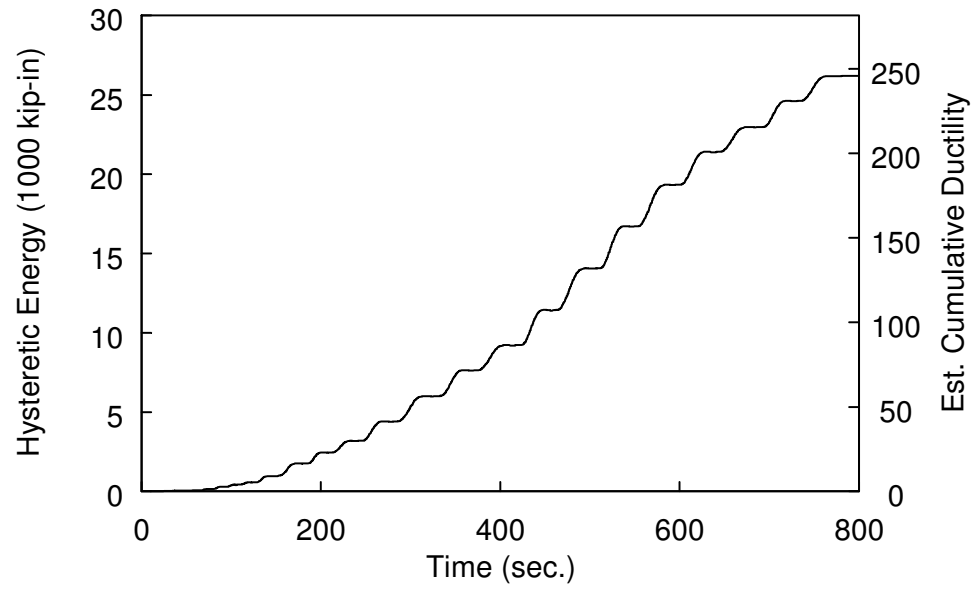


Figure 3.34 Specimen 2: Hysteretic Energy Time History (AISC Standard Protocol)

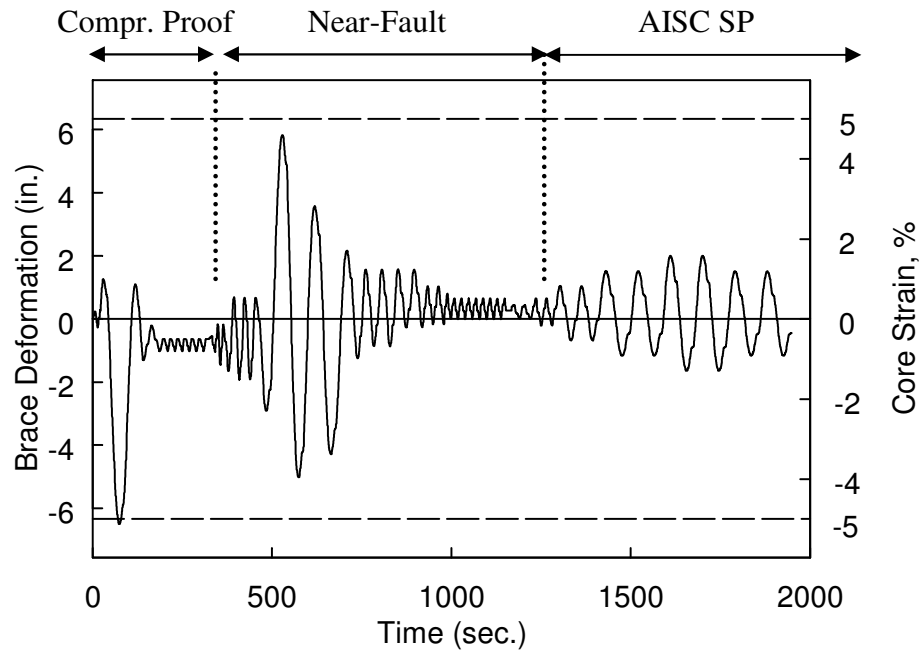


Figure 3.35 Specimen 2: Brace Deformation Time Histories (All Tests)

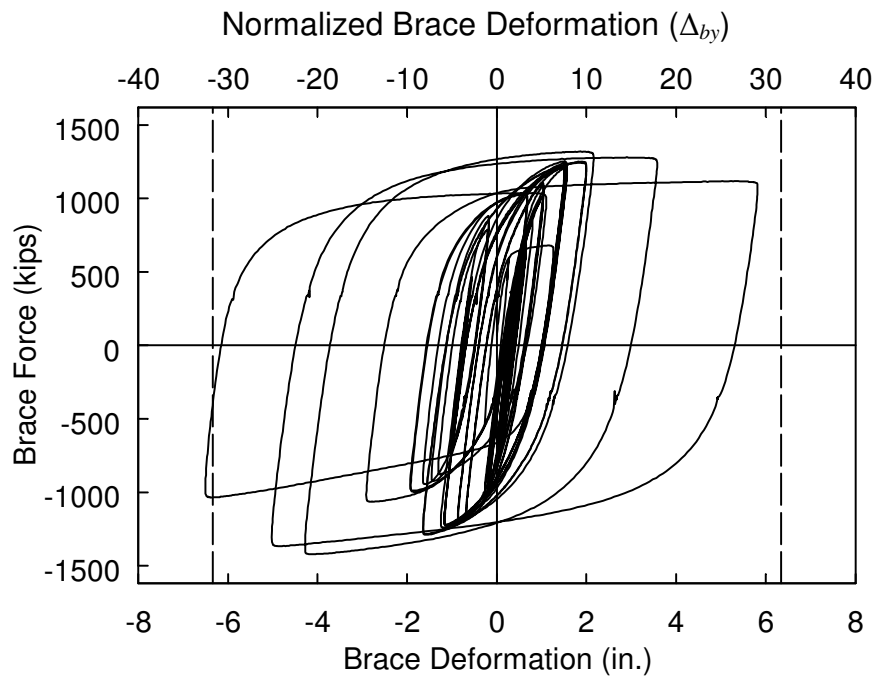


Figure 3.36 Specimen 2: Brace Force vs. Axial Deformation (All Tests)

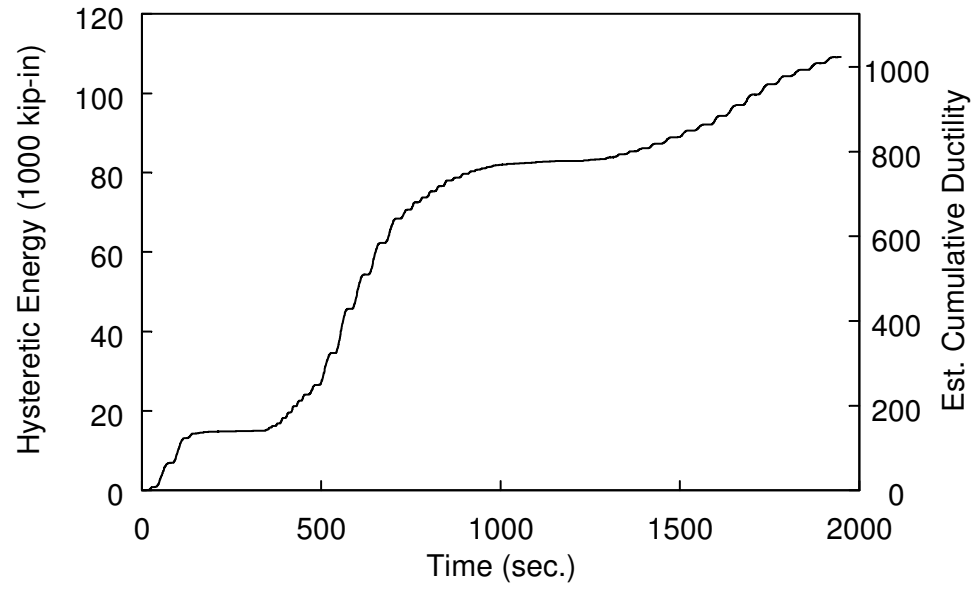


Figure 3.37 Specimen 2: Hysteretic Energy Time History (All Tests)



(a) Photo 1



(b) Photo 2

Figure 3.38: Specimen 2 Core Plate after All Tests

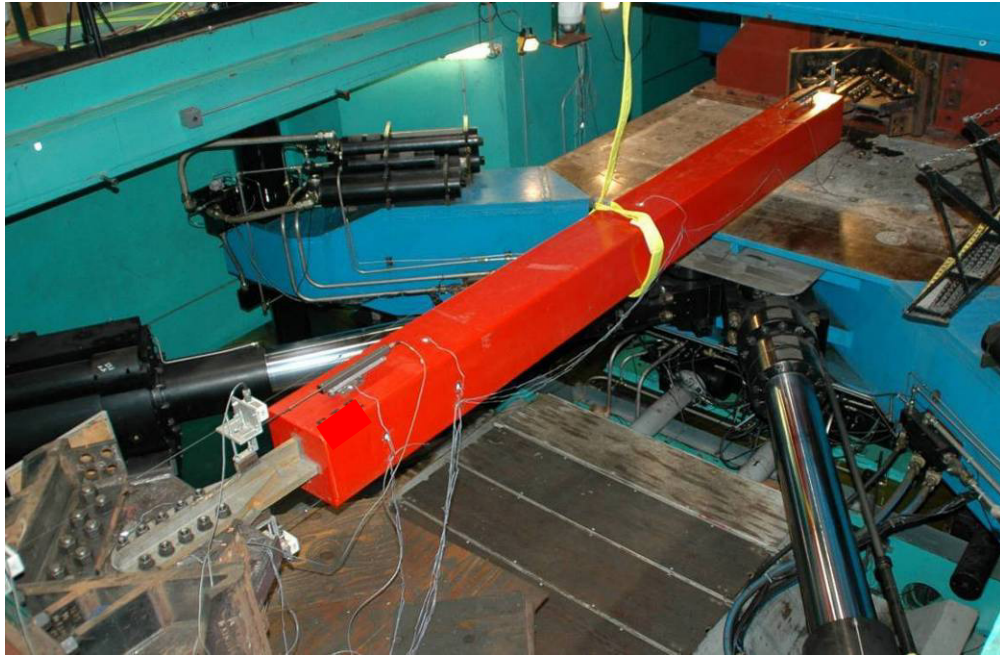
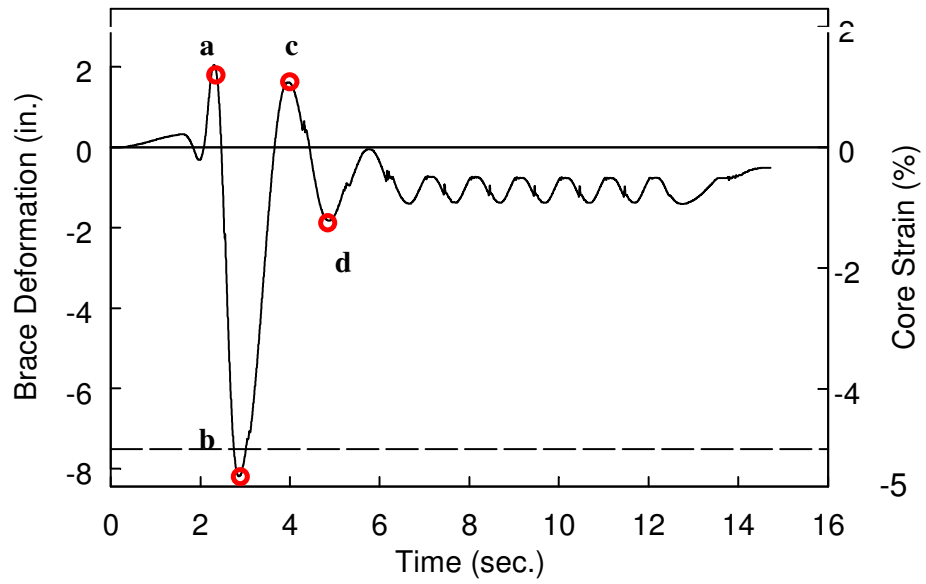


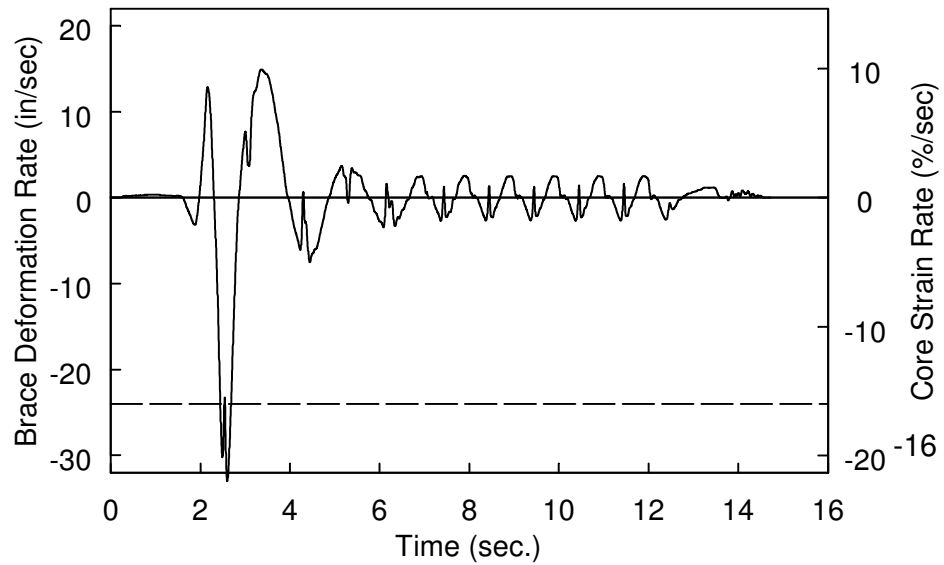
Figure 3.39 Specimen 3: Test Setup



Figure 3.40 Specimen 3: End Condition



(a) Measured Brace Deformation



(b) Core Deformation Rate

Figure 3.41 Specimen 3: Brace Deformation Time Histories (Dyn. Proof Protocol)

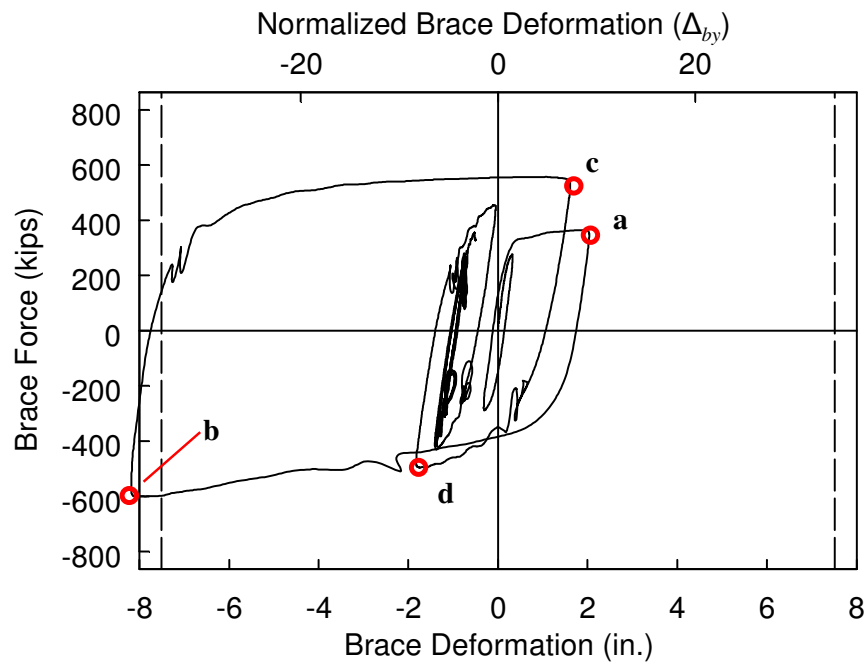


Figure 3.42 Specimen 3: Brace Force vs. Axial Deformation (Dyn. Proof Protocol)

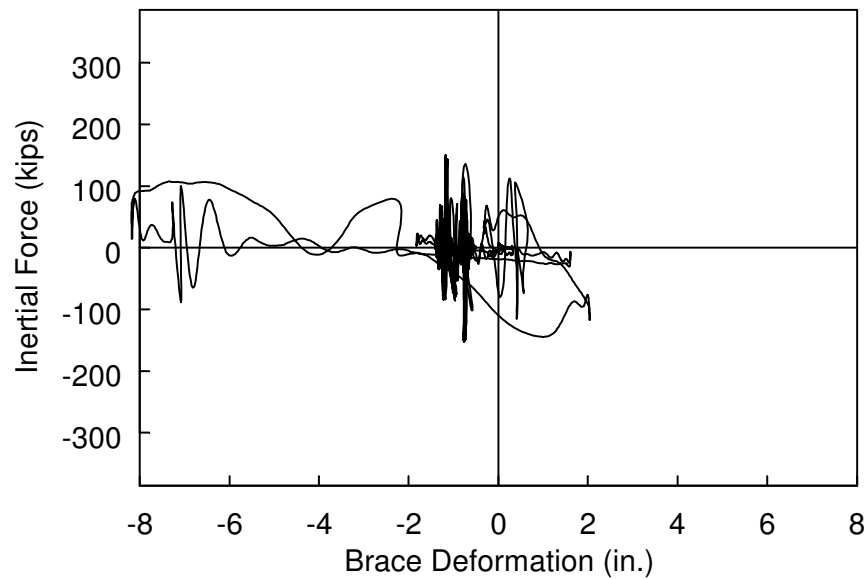


Figure 3.43 Specimen 3: Inertial Force vs. Axial Deformation (Dyn. Proof Protocol)

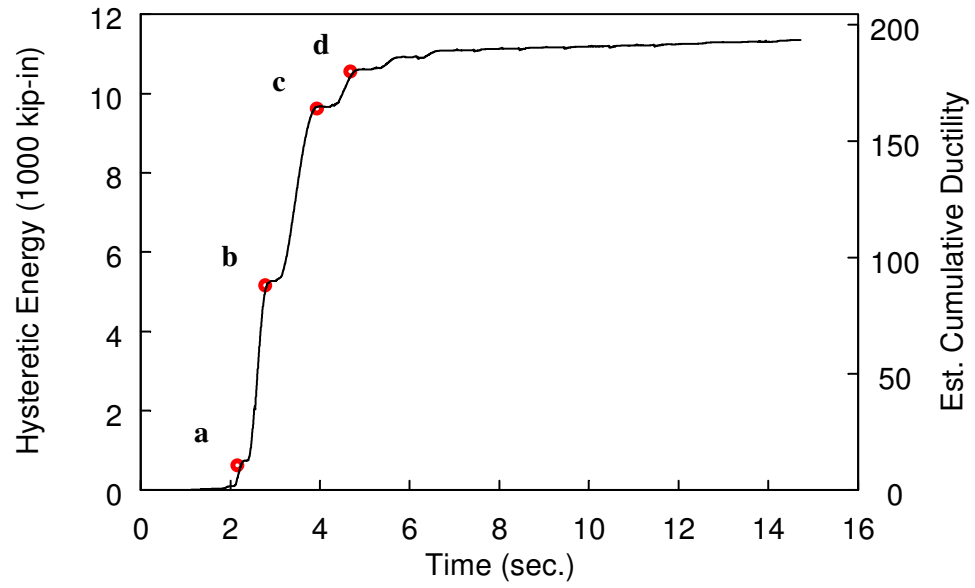
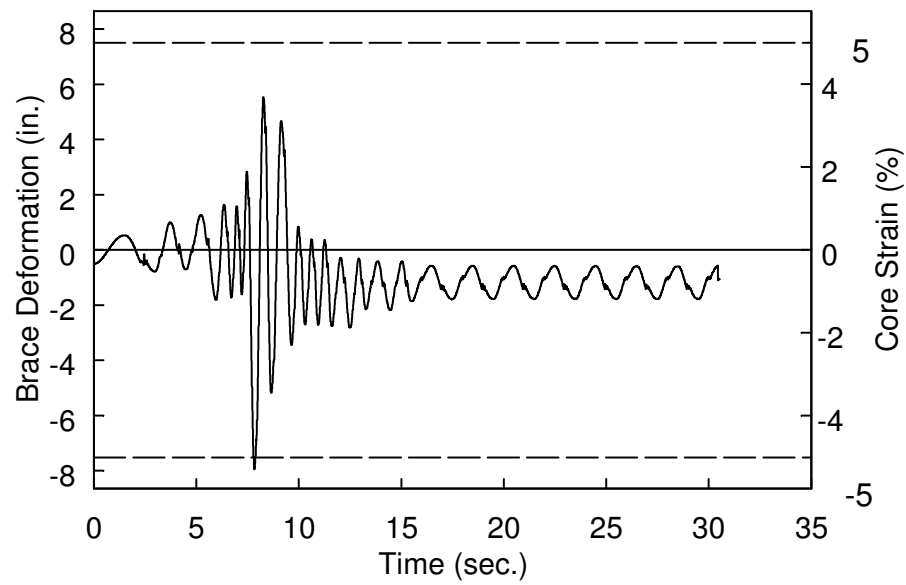
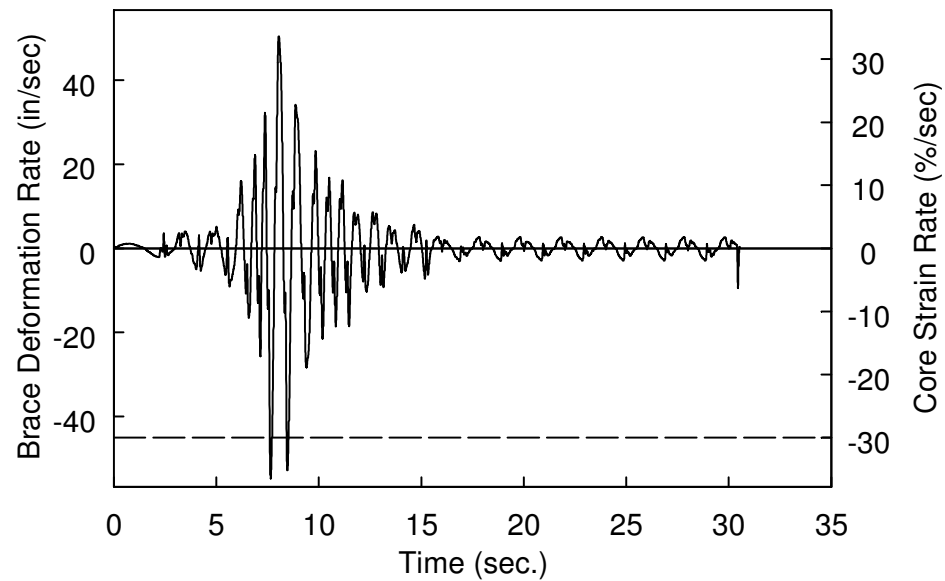


Figure 3.44 Specimen 3: Hysteretic Energy Time History (Dyn. Proof Protocol)





(a) Measured Brace Deformation



(b) Measured Core Deformation Rate

Figure 3.45 Specimen 3: Brace Deformation Time Histories (Dyn. Near Fault Protocol)

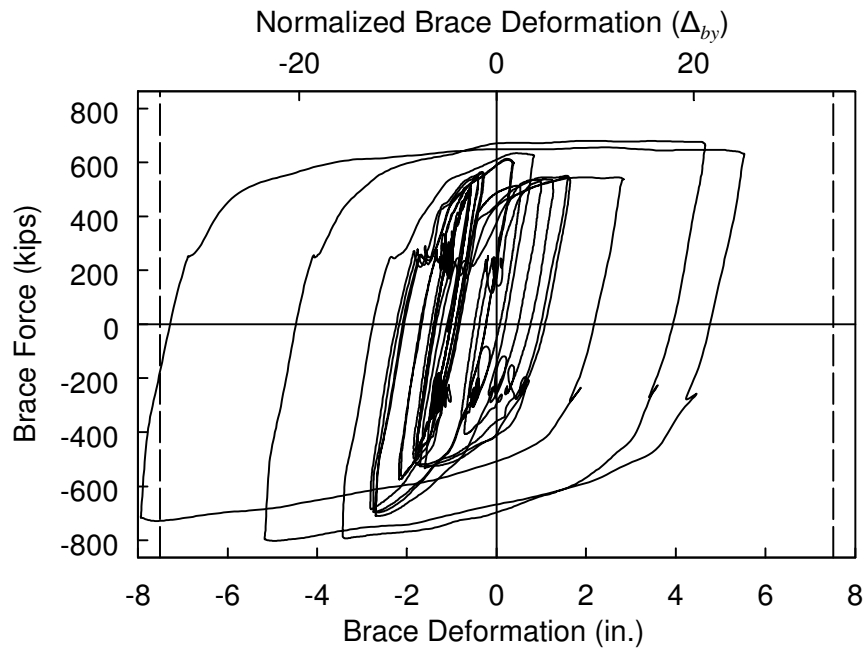


Figure 3.46 Specimen 3: Brace Force vs. Axial Deformation (Dyn. Near-Fault Protocol)

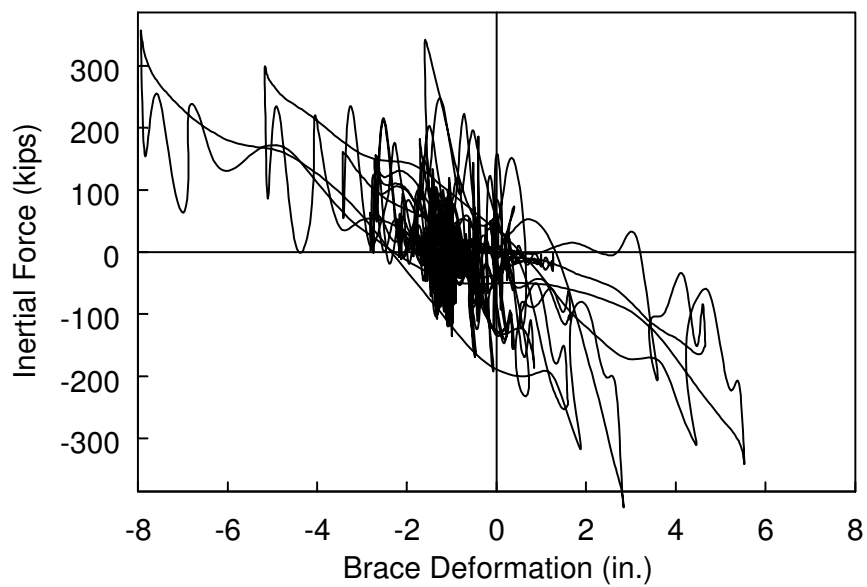


Figure 3.47 Specimen 3: Brace Force vs. Axial Deformation (Dyn. Near-Fault Protocol)

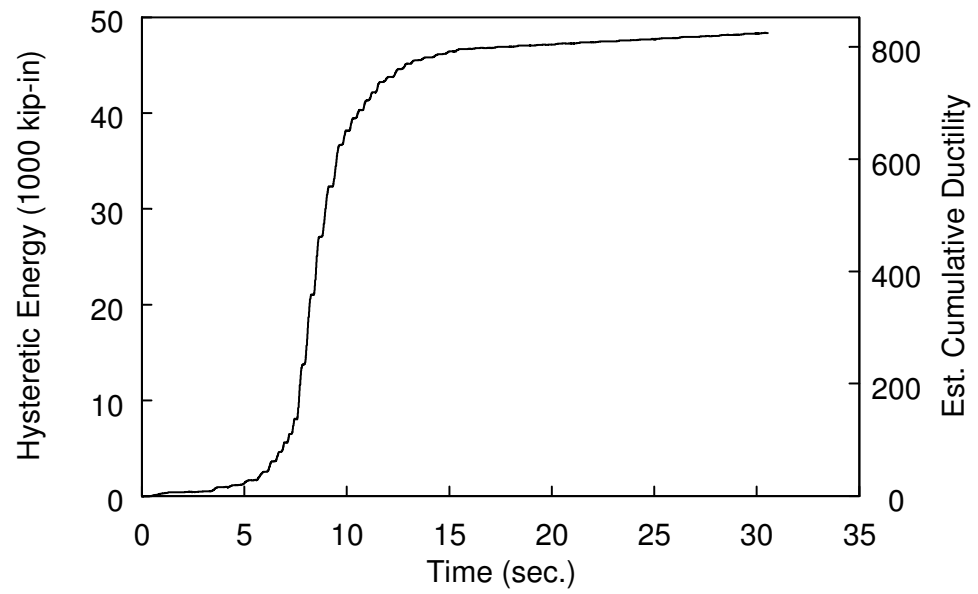
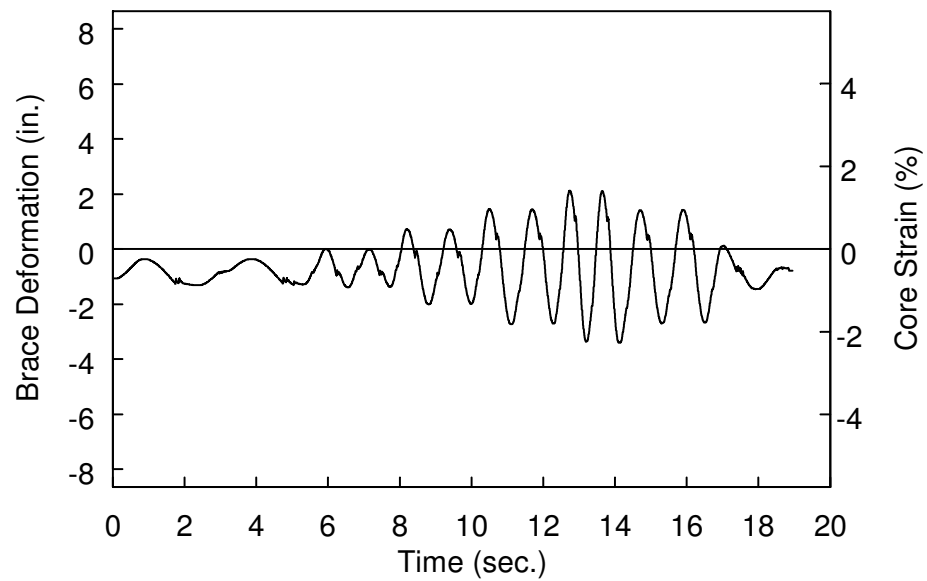
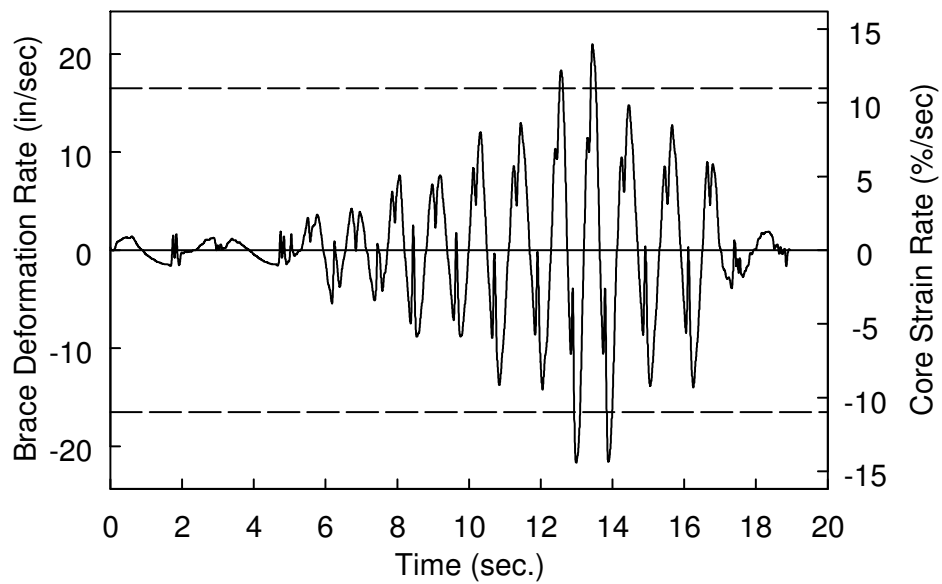


Figure 3.48 Specimen 3: Hysteretic Energy Time History (Dyn. Near-Fault Protocol)



(a) Measured Brace Deformation



(b) Brace Deformation Rate

Figure 3.49 Specimen 3: Brace Deformation Time Histories (Dyn. AISC Protocol)

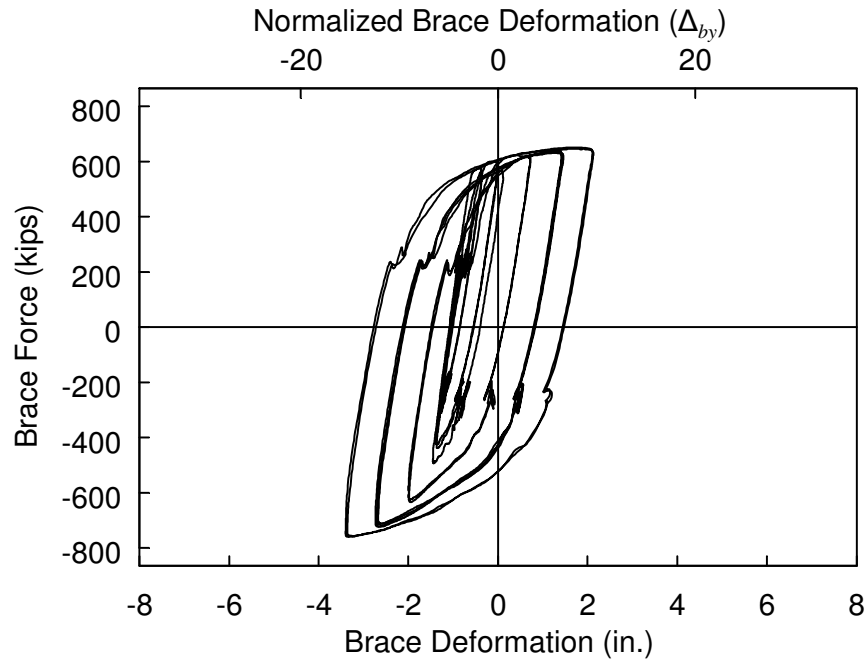


Figure 3.50 Specimen 3: Brace Force vs. Axial Deformation (Dyn. AISC Protocol)

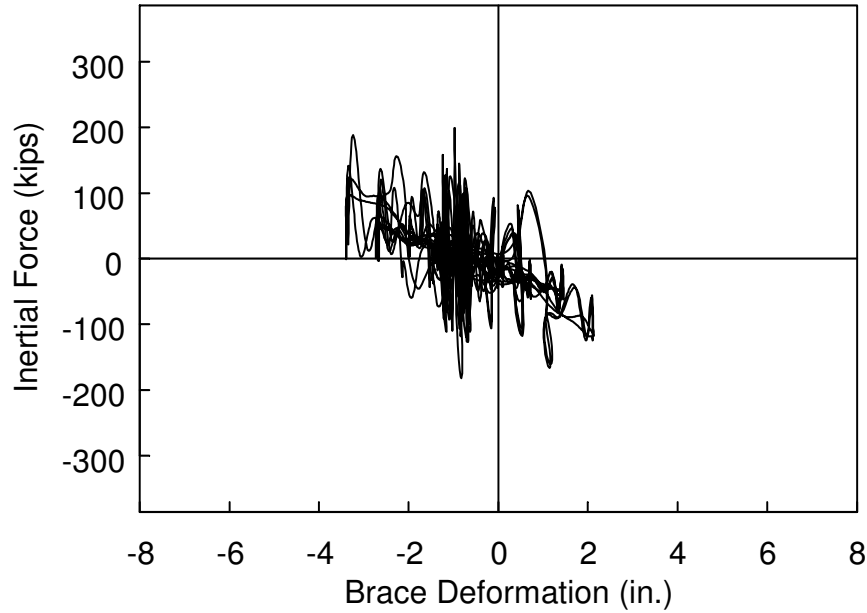


Figure 3.51 Specimen 3: Inertial Force vs. Axial Deformation (Dyn. AISC Protocol)

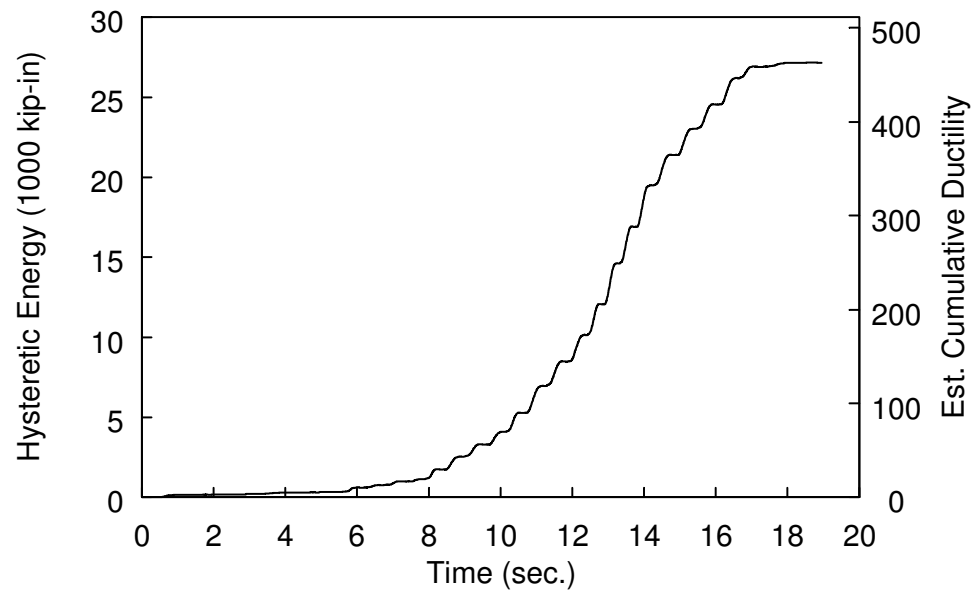
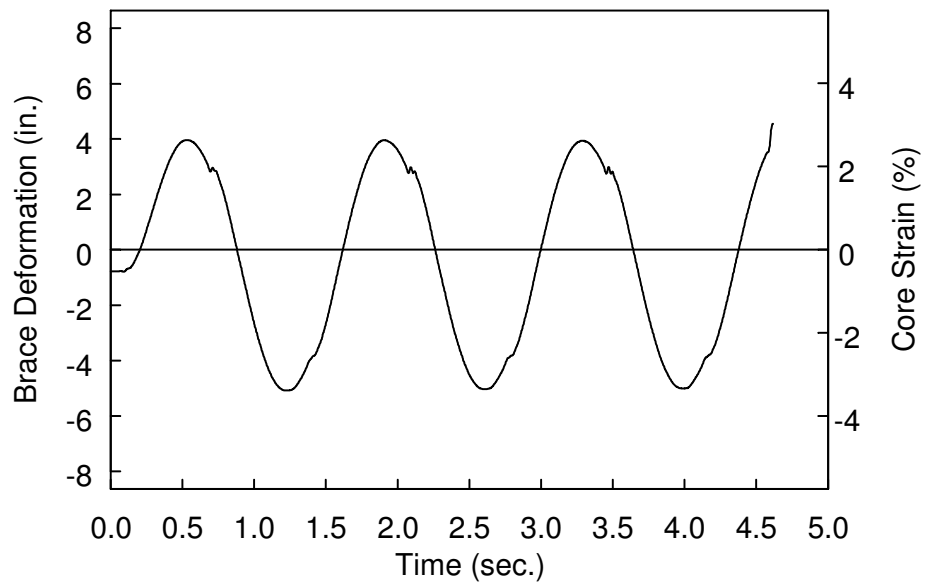
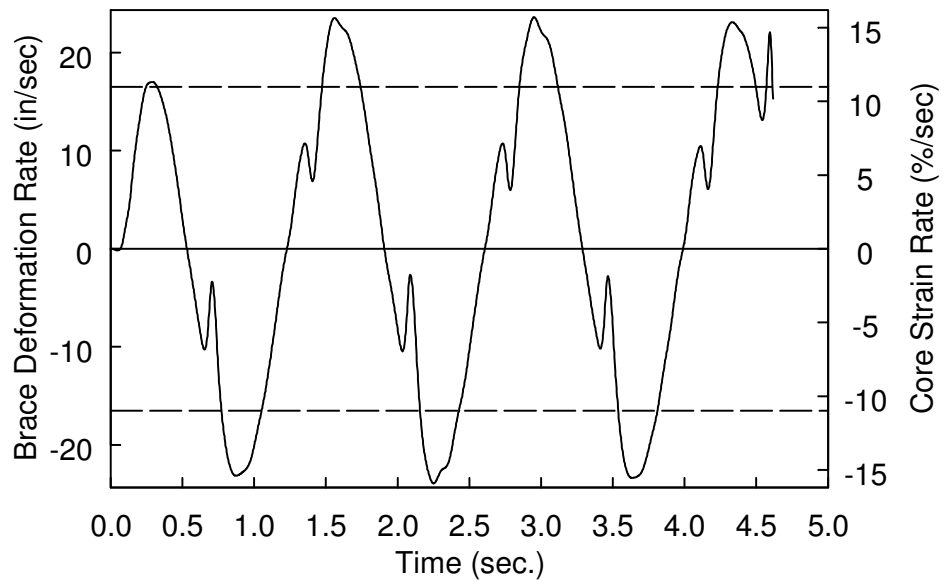


Figure 3.52 Specimen 3: Hysteretic Energy Time History (Dyn. AISC Protocol)



(a) Brace Deformation



(b) Brace Deformation Rate

Figure 3.53 Specimen 3: Brace Deformation Time Histories (Dyn. Fracture Protocol)

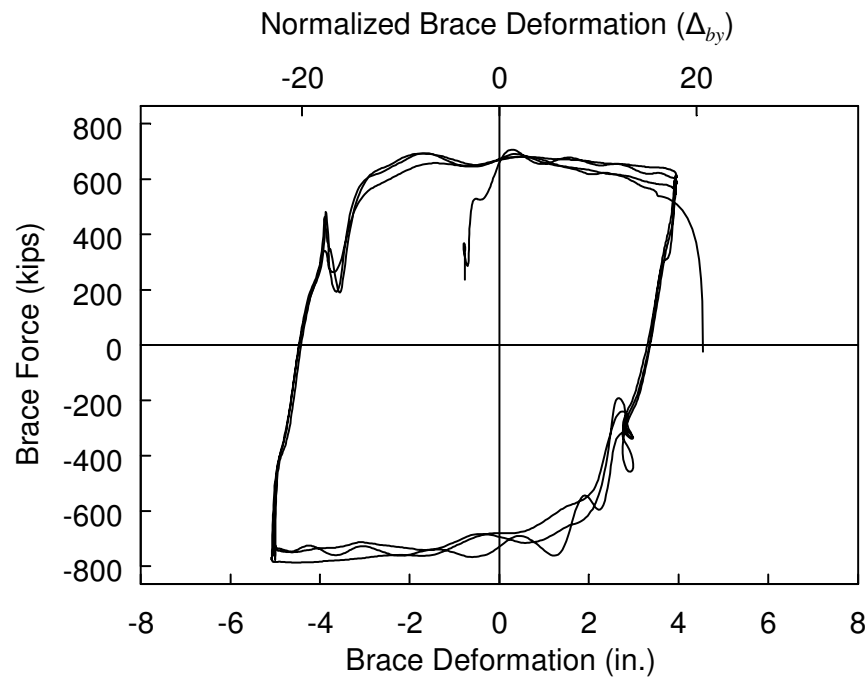


Figure 3.54 Specimen 3: Brace Force vs. Axial Deformation (Dyn. Fracture Protocol)

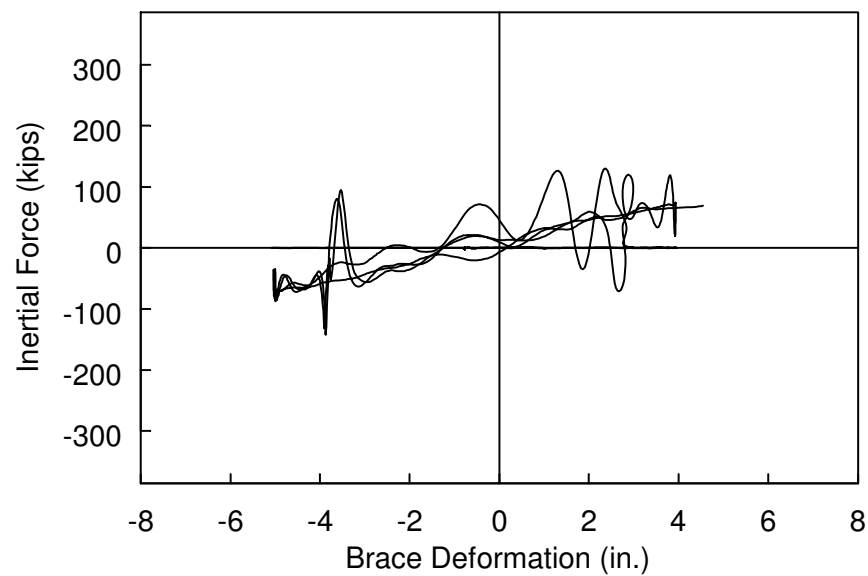


Figure 3.55 Specimen 3: Inertial Force vs. Axial Deformation (Dyn. Fracture Protocol)



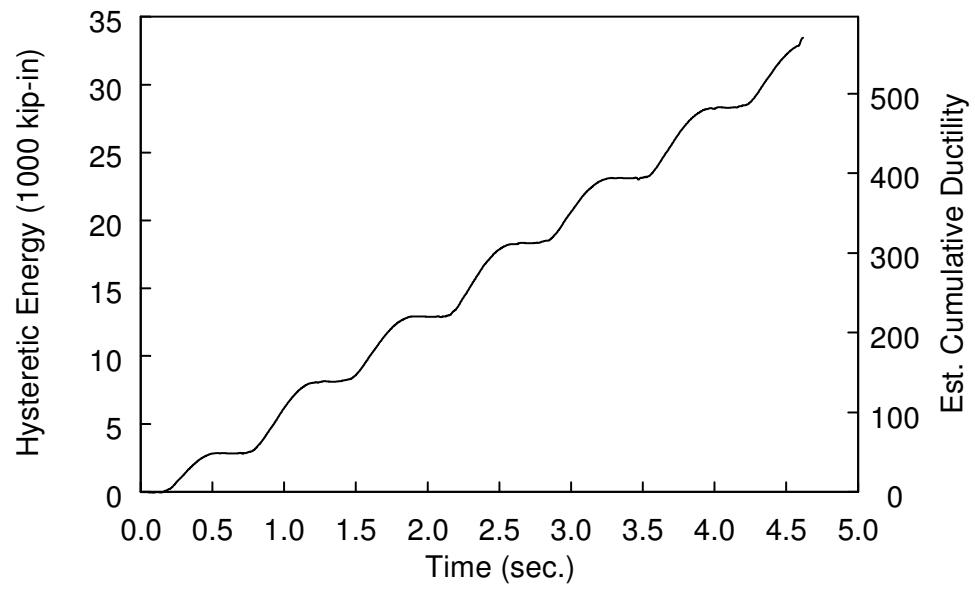
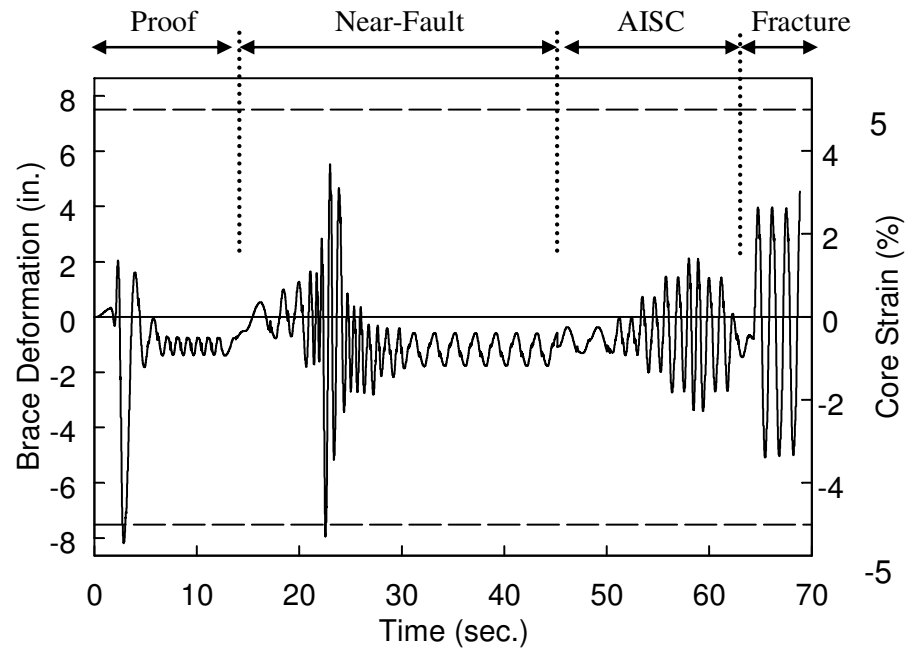
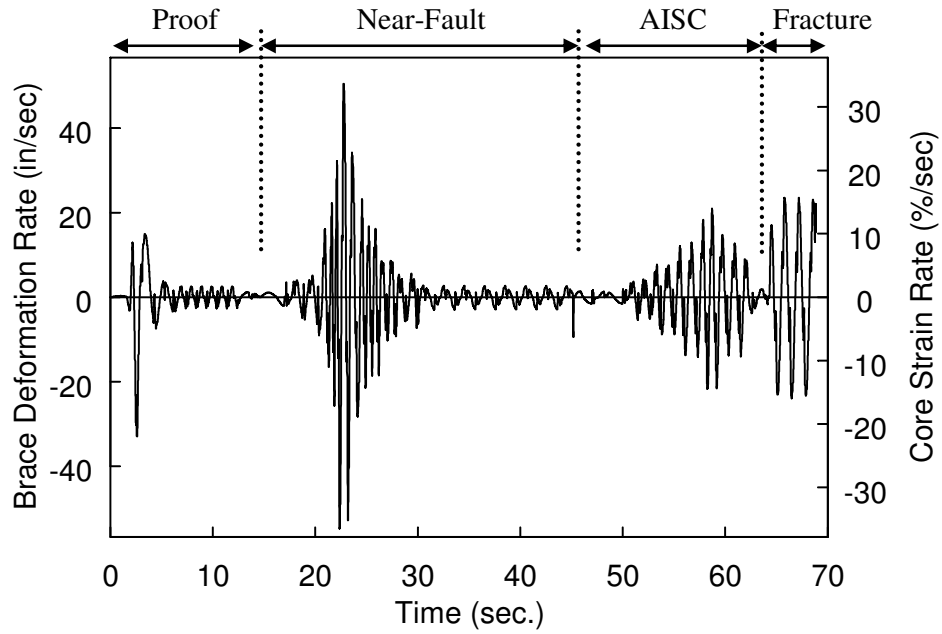


Figure 3.56 Specimen 3: Hysteretic Energy Time History (Dyn. Fracture Protocol)



(a) Brace Deformation



(b) Brace Deformation Rate

Figure 3.57 Specimen 3: Brace Deformation Time Histories (All Tests)

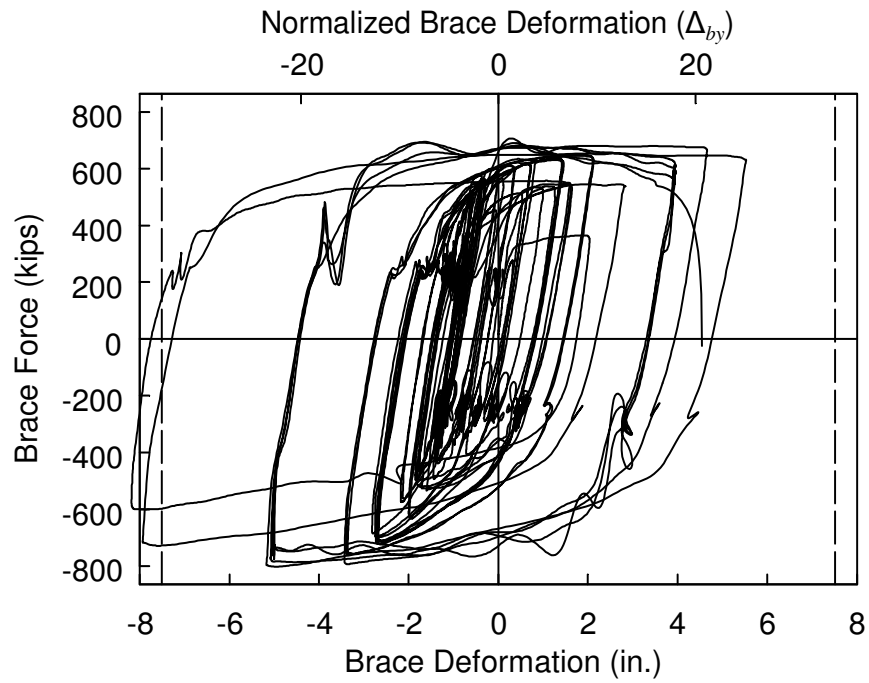


Figure 3.58 Specimen 3: Brace Force vs. Axial Deformation (All Tests)

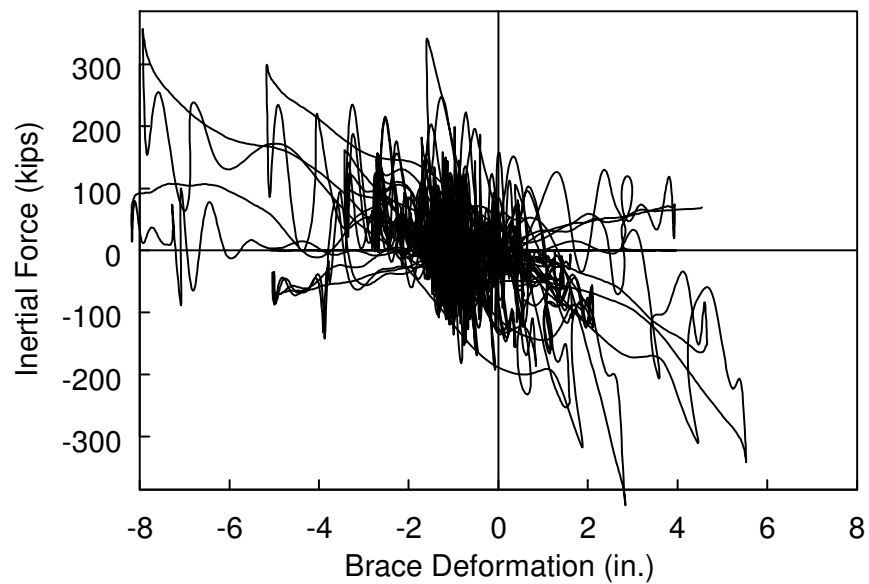


Figure 3.59 Specimen 3: Inertial Force vs. Axial Deformation (All Tests)

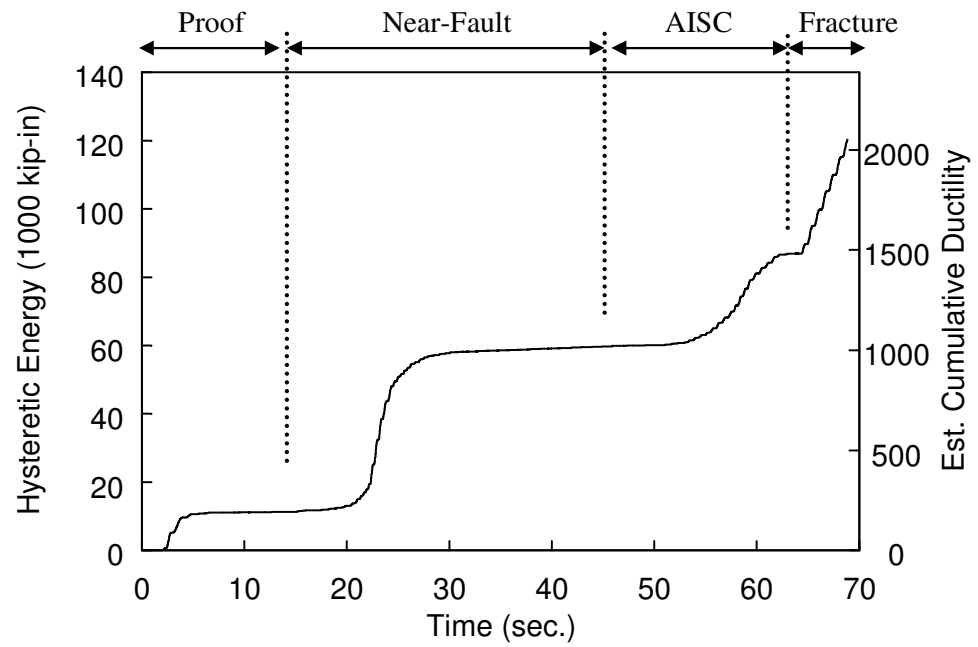


Figure 3.60 Specimen 3: Hysteretic Energy Time History (All Tests)



Figure 3.61 Specimen 4: Test Setup



Figure 3.62 Specimen 4: End Condition



(a) Level Gusset Plate



(b) Close Up, Brace Hinged within Core Plate

Figure 3.63 Specimen 4 Incipient Connection Instability After All Tests

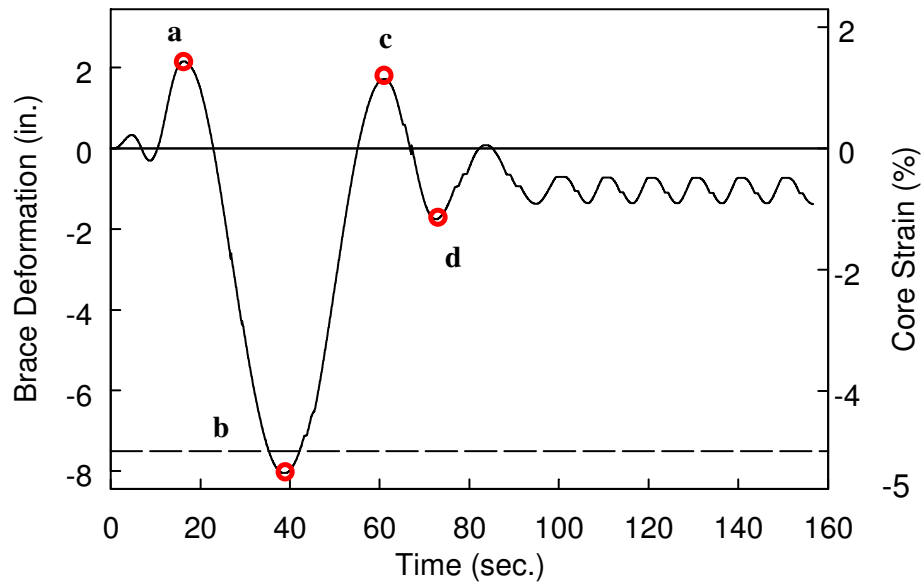


Figure 3.64 Specimen 4: Brace Deformation Time Histories (Proof Protocol)

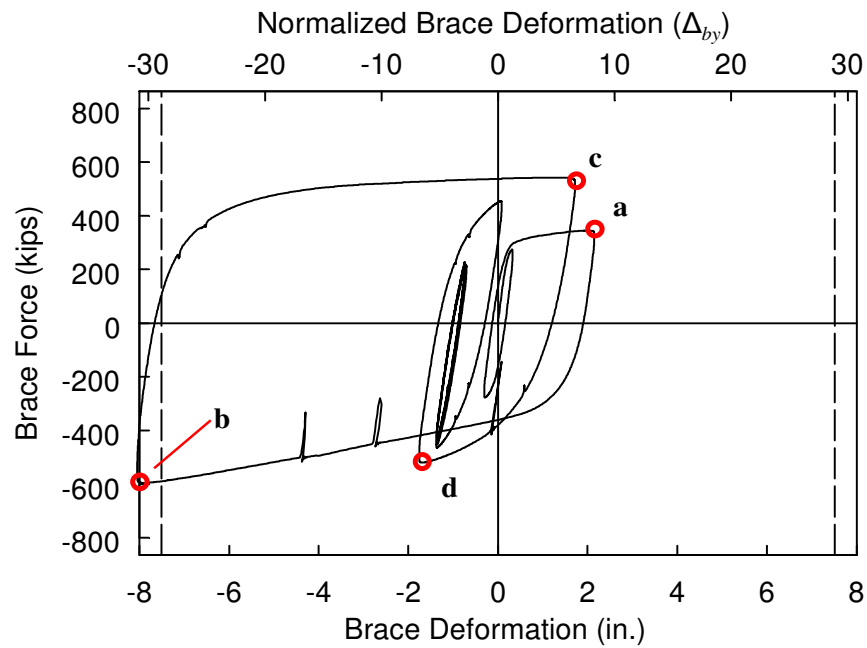


Figure 3.65 Specimen 4: Brace Force vs. Axial Deformation (Proof Protocol)

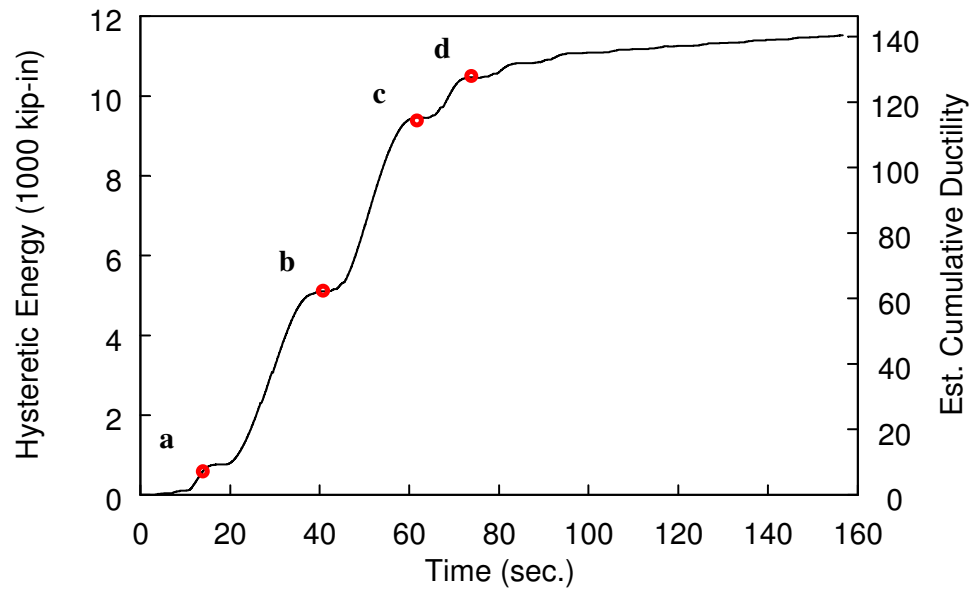


Figure 3.66 Specimen 4: Hysteretic Energy Time History (Proof Protocol)



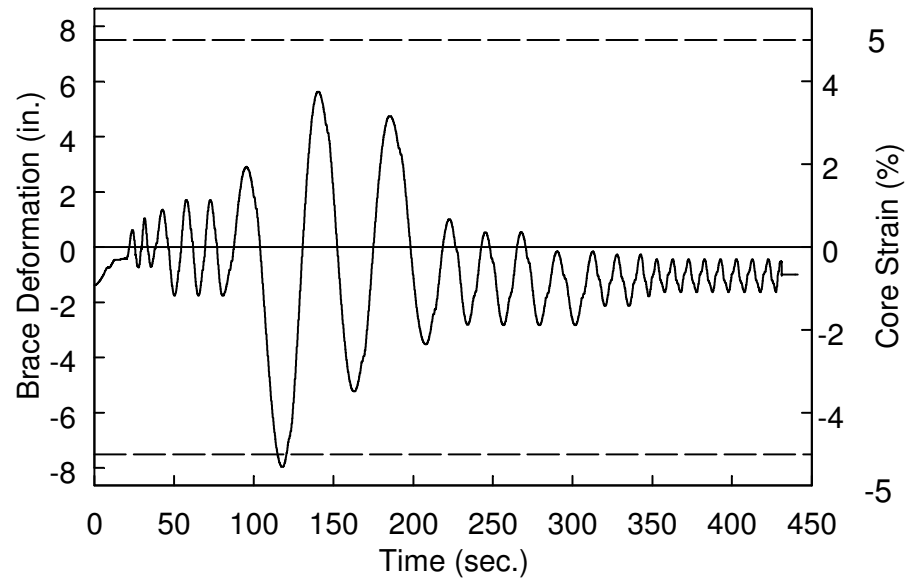


Figure 3.67 Specimen 4: Brace Deformation Time Histories (Near Fault Protocol)

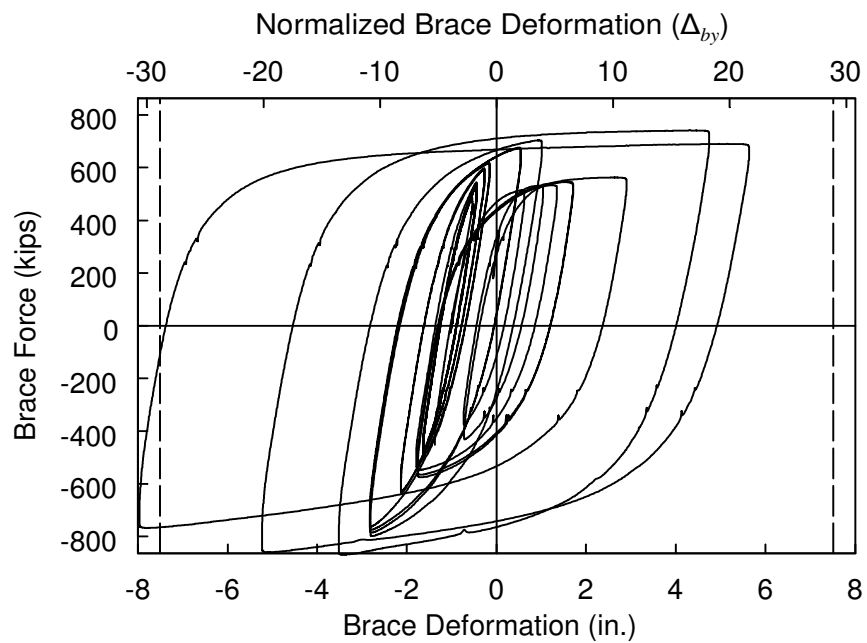


Figure 3.68 Specimen 4: Brace Force vs. Axial Deformation (Near-Fault Protocol)

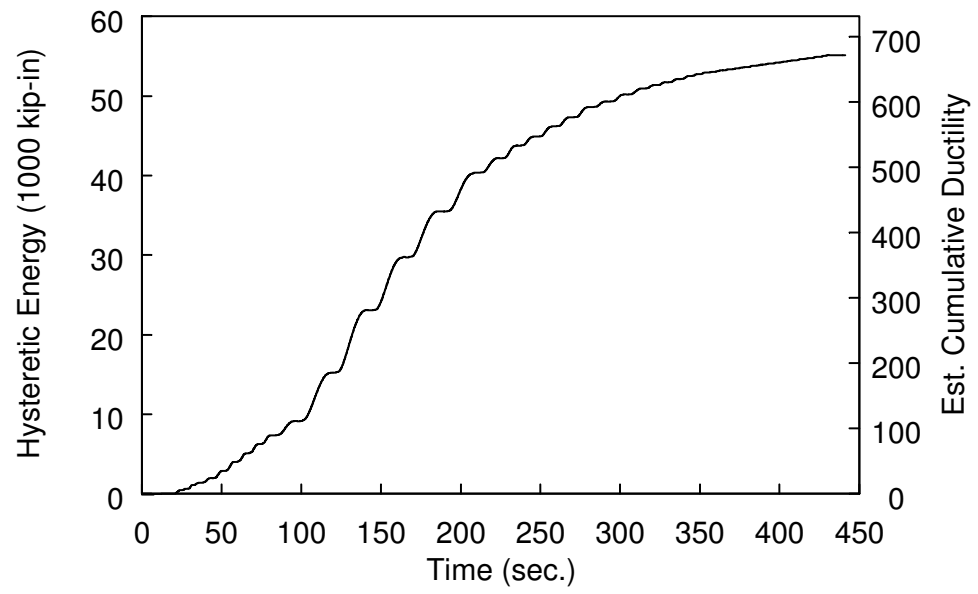


Figure 3.69 Specimen 4: Hysteretic Energy Time History (Near-Fault Protocol)

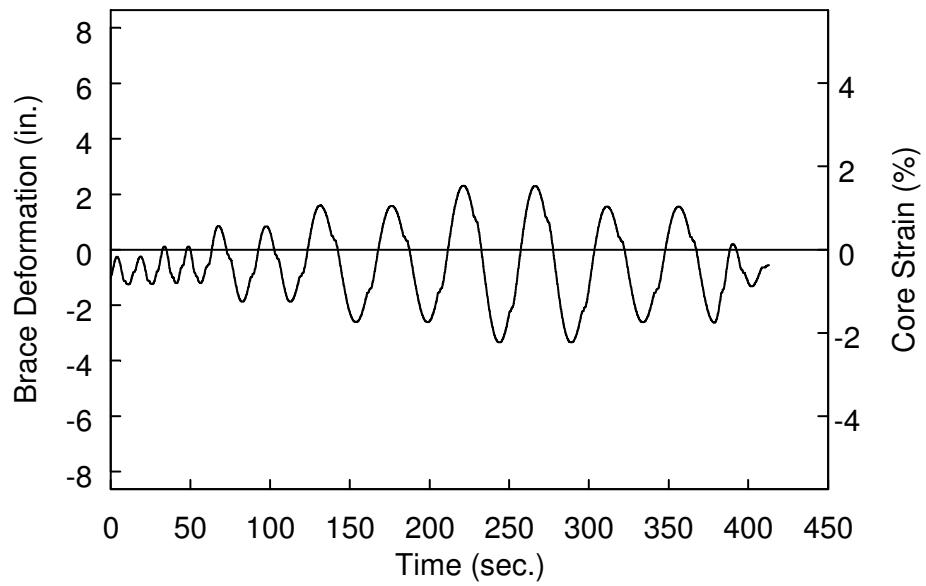


Figure 3.70 Specimen 4: Brace Deformation Time Histories (AISC Standard Protocol)

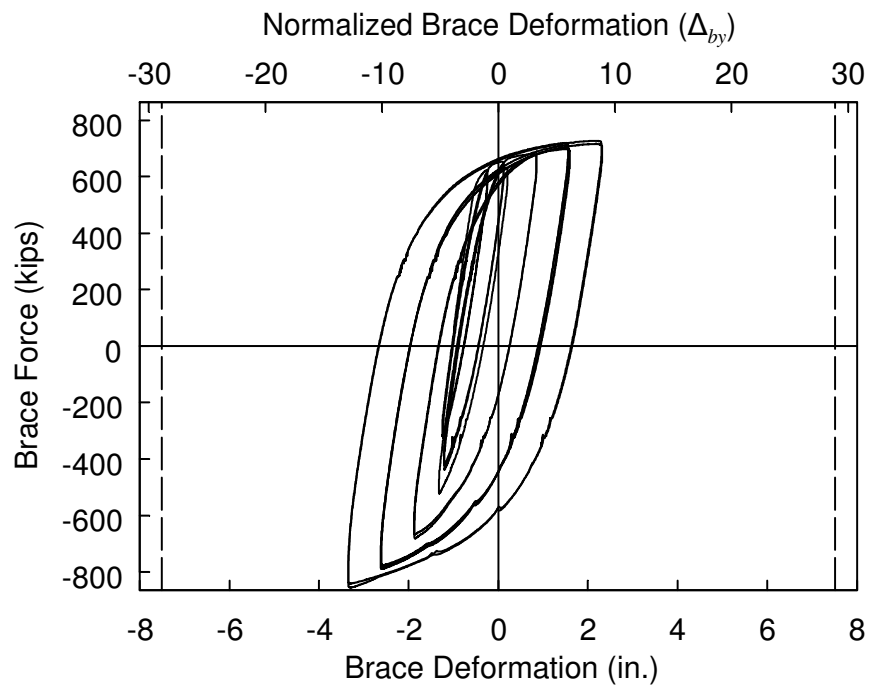


Figure 3.71 Specimen 4: Brace Force vs. Axial Deformation (AISC Standard Protocol)

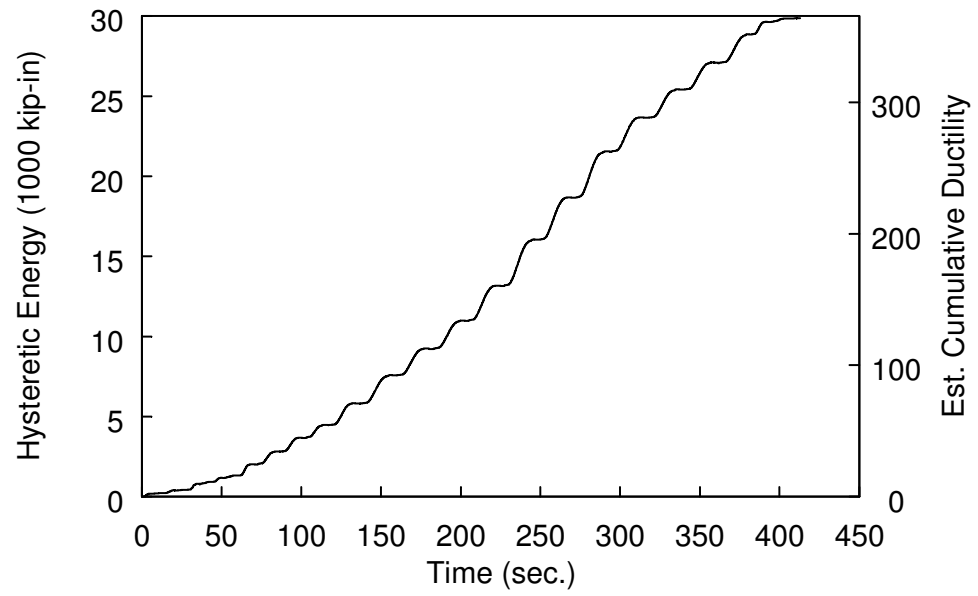


Figure 3.72 Specimen 4: Hysteretic Energy Time History (AISC Protocol)

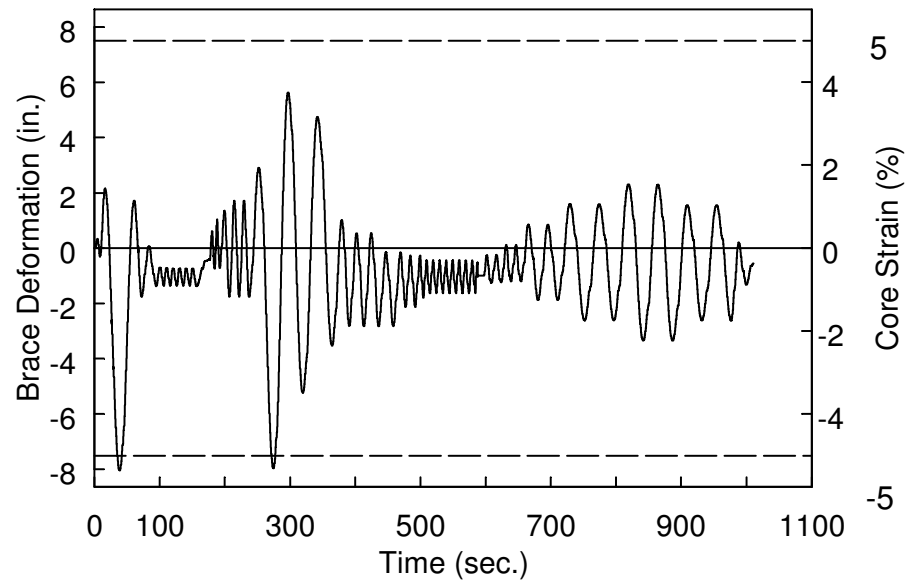


Figure 3.73 Specimen 4: Brace Deformation Time Histories (All Tests)

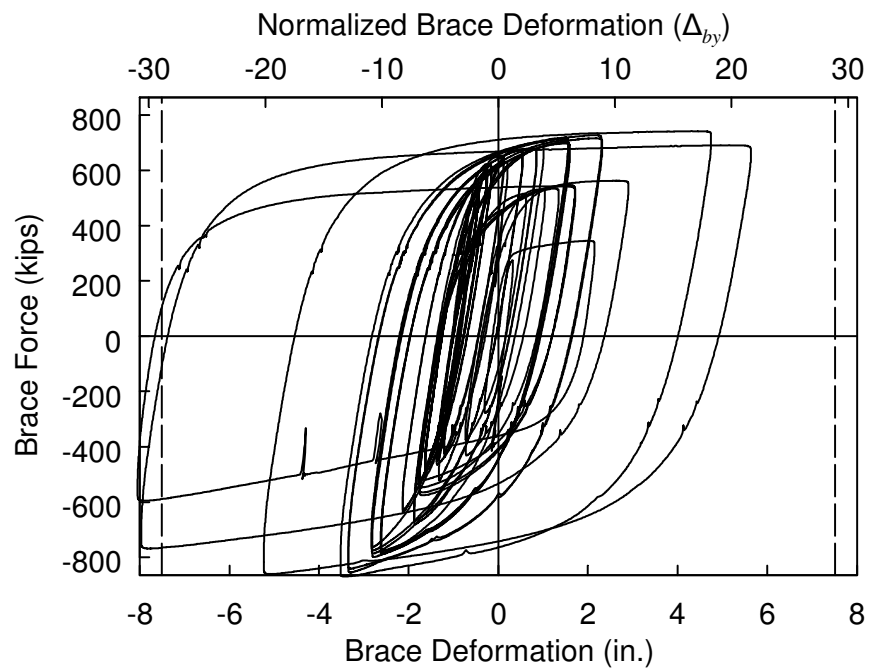


Figure 3.74 Specimen 4: Brace Force vs. Axial Deformation (All Tests)

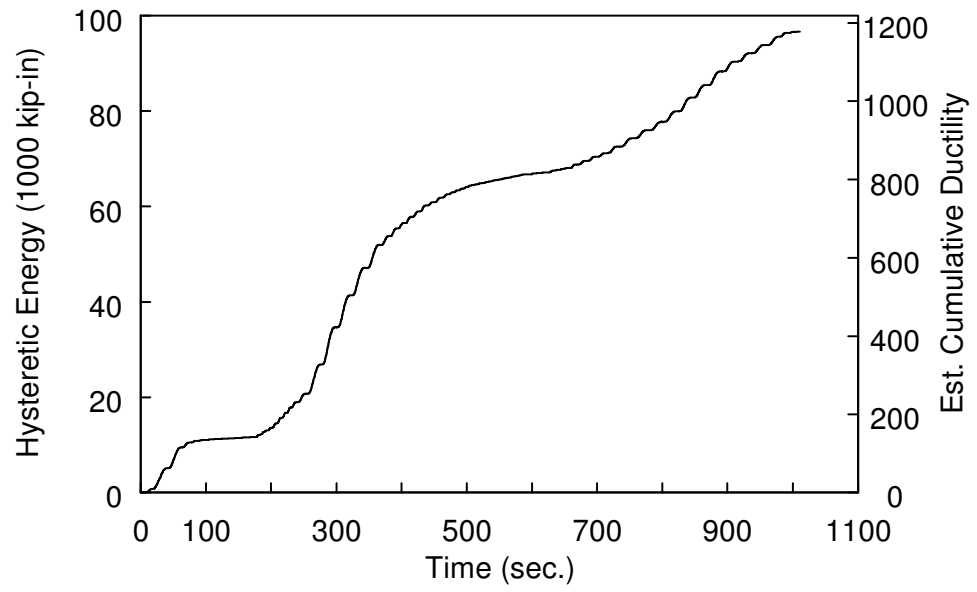


Figure 3.75 Specimen 4: Hysteretic Energy Time History (All Tests)



Figure 3.76 Specimen 5: Test Setup



Figure 3.77 Specimen 5: End Condition

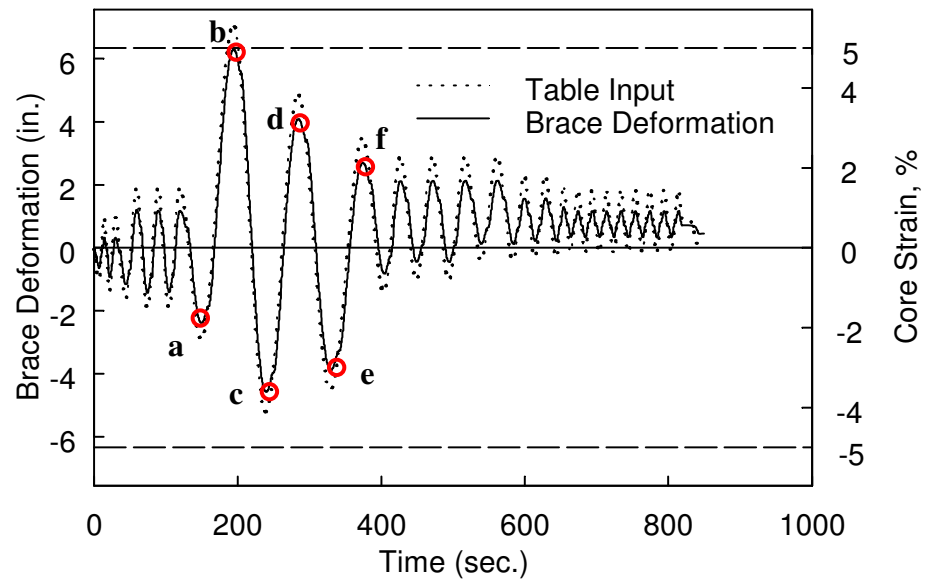


Figure 3.78 Specimen 5: Brace Deformation Time Histories (Near Fault Protocol)

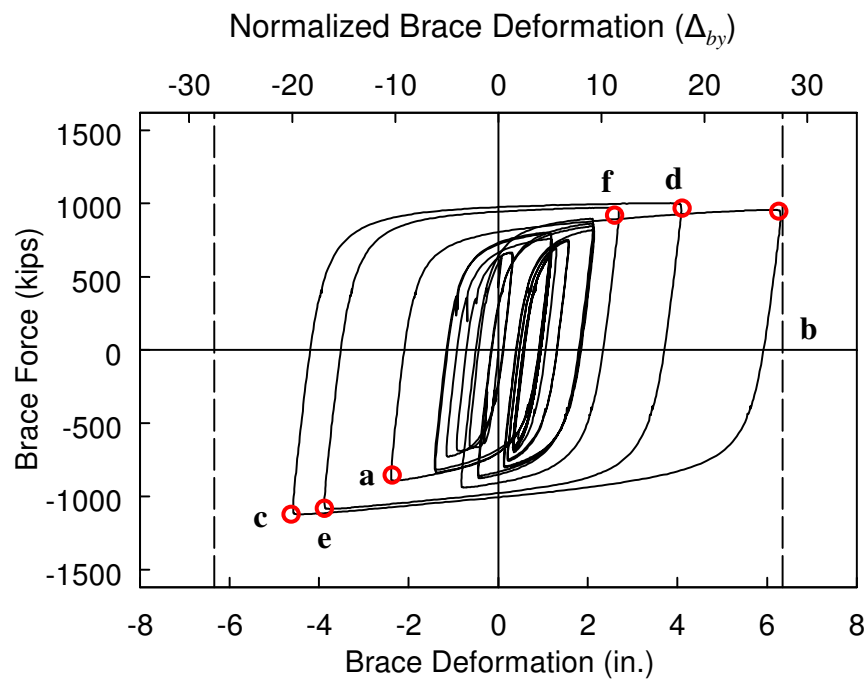


Figure 3.79 Specimen 5: Brace Force vs. Axial Deformation (Near Fault Protocol)



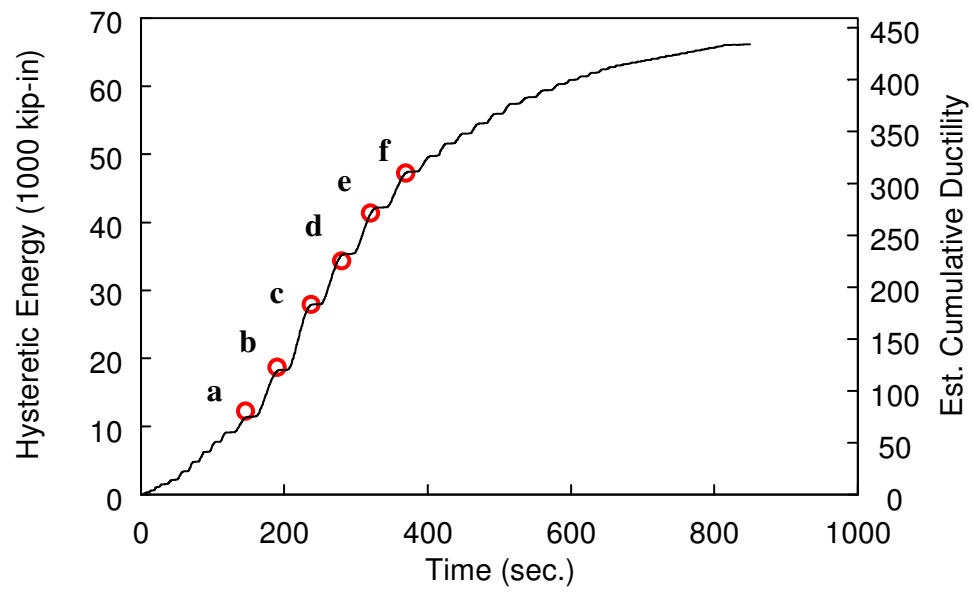


Figure 3.80 Specimen 5: Hysteretic Energy Time History (Near-Fault Protocol)

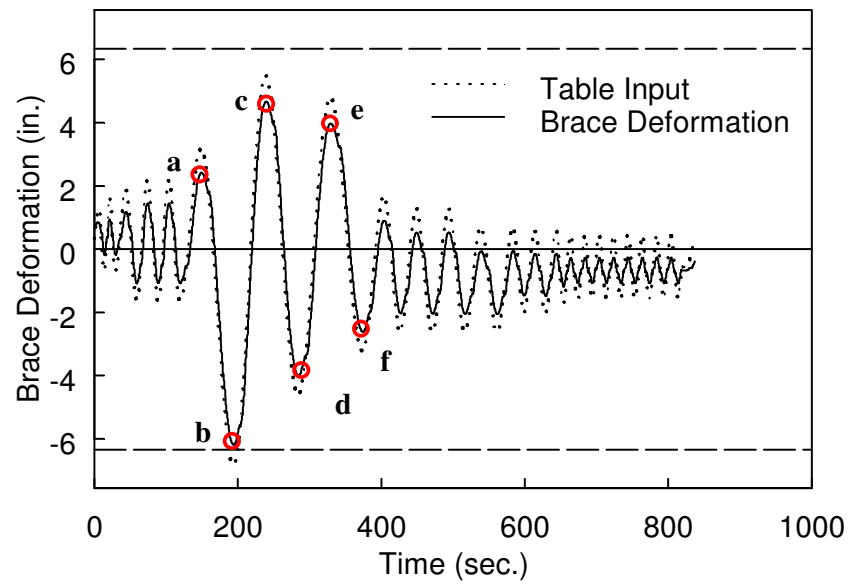


Figure 3.81 Specimen 5: Brace Deformation Time Histories  
(Compr. Near-Fault Protocol)

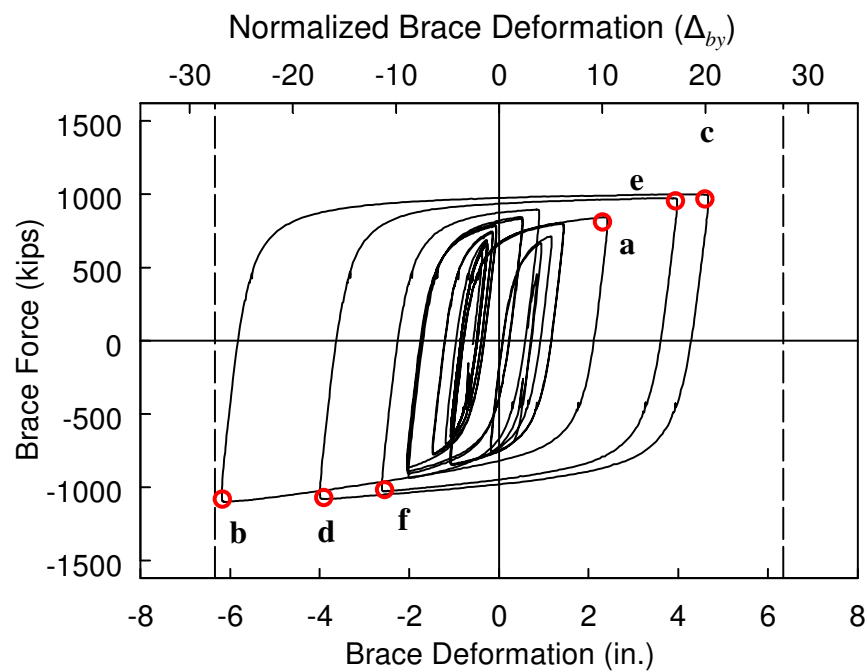


Figure 3.82 Specimen 5: Brace Force vs. Axial Deformation (Compr. Near-Fault Protocol)

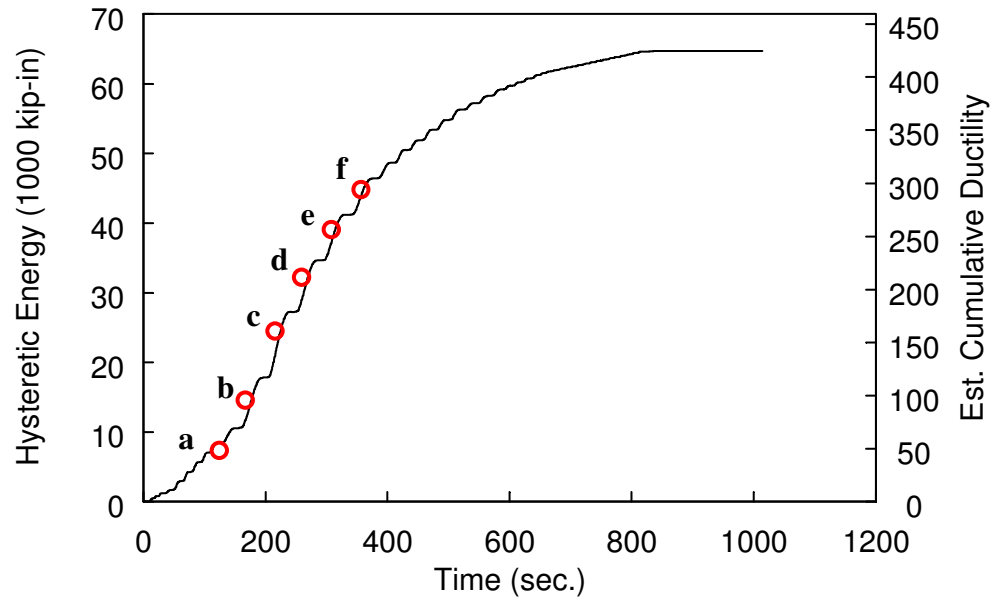


Figure 3.83 Specimen 5: Hysteretic Energy Time History (Compr. Near-Fault Protocol)

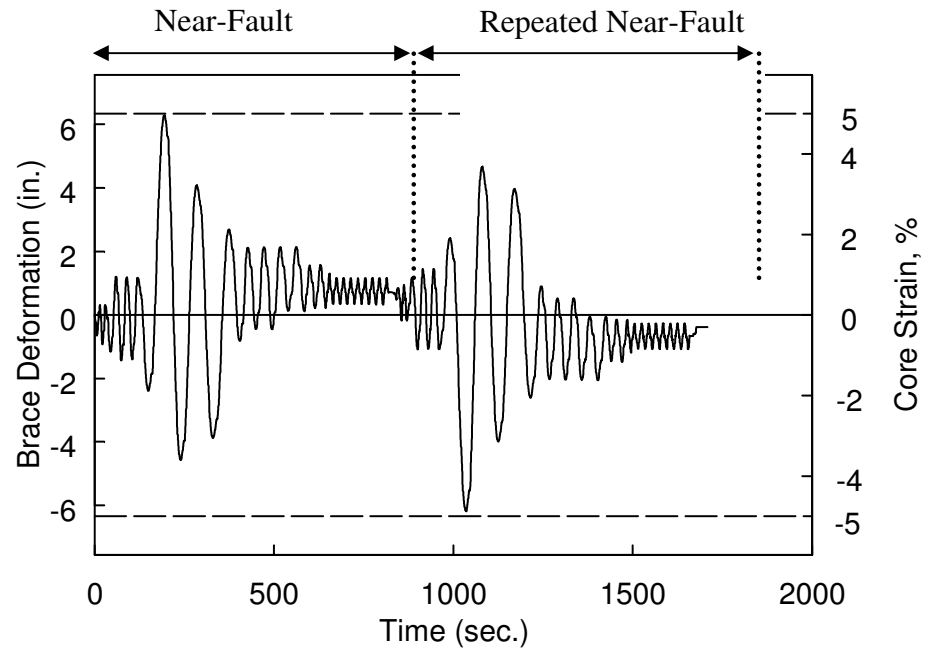


Figure 3.84 Specimen 5: Brace Deformation Time Histories (All Tests)

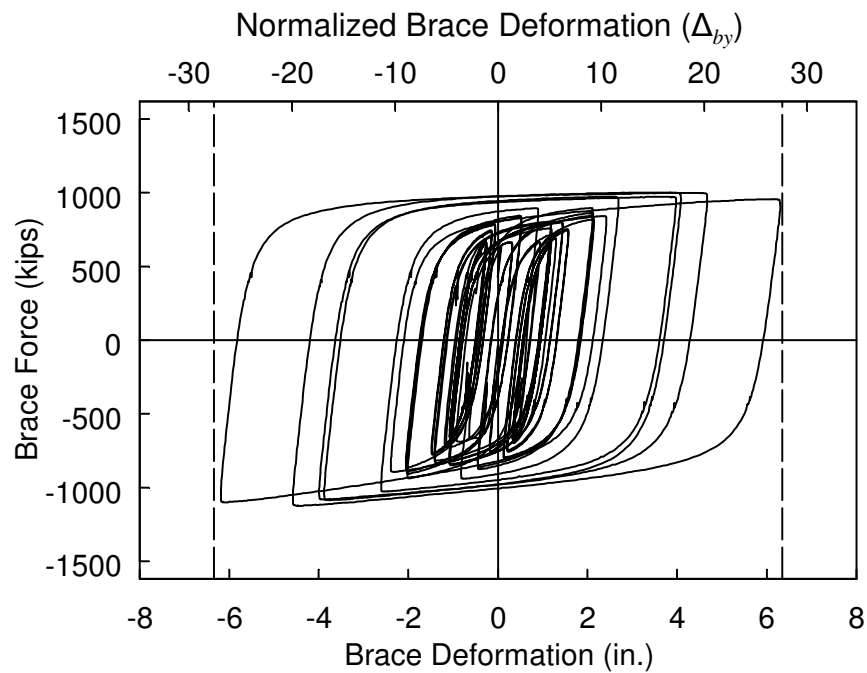


Figure 3.85 Specimen 5: Brace Force vs. Axial Deformation (All Tests)

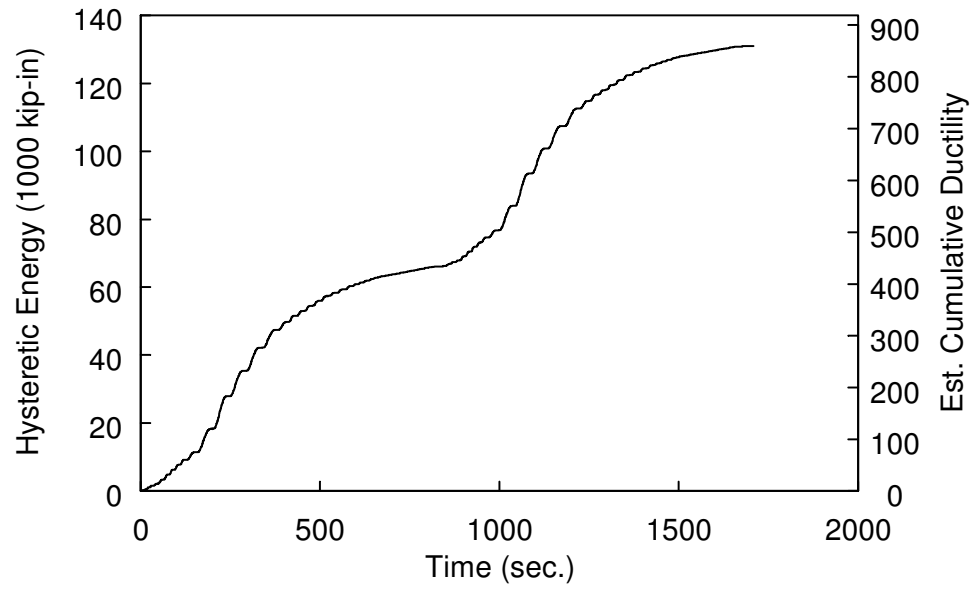


Figure 3.86 Specimen 5: Hysteretic Energy Time History (All Tests)



(a) Photo 1



(b) Photo 2

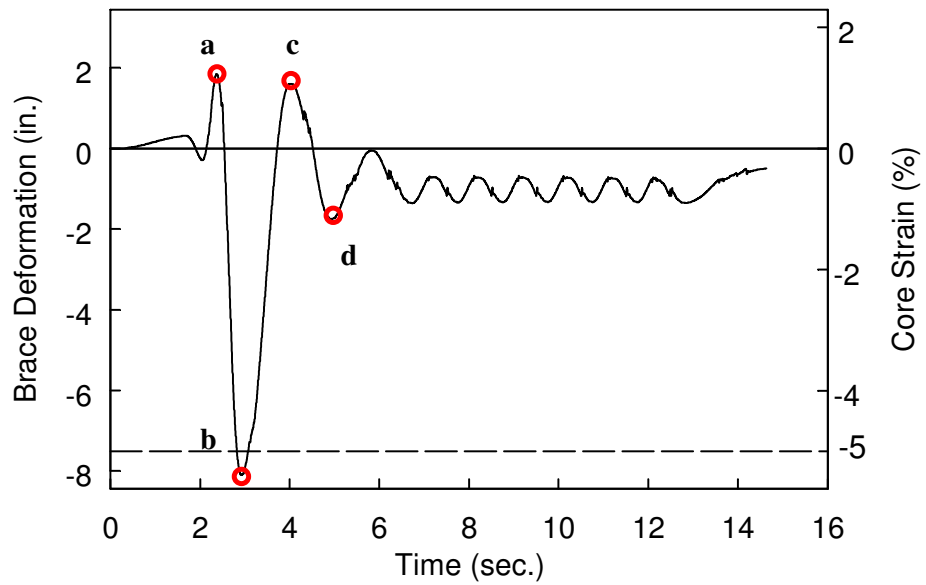
Figure 3.87: Specimen 5 Core Plate after All Tests



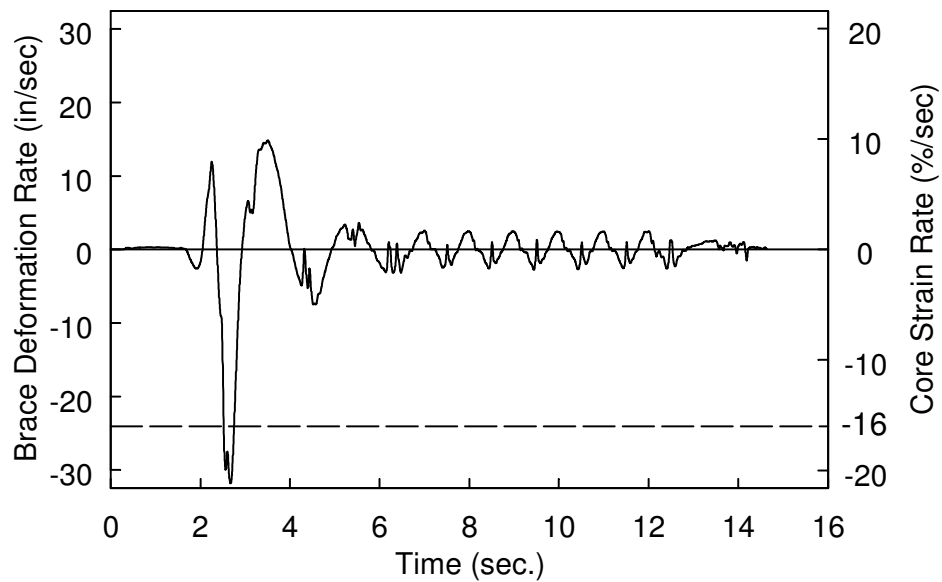
Figure 3.88 Specimen 6: Test Setup



Figure 3.89 Specimen 6: End Condition



(a) Measured Core Deformation



(b) Measured Core Deformation Rate

Figure 3.90 Specimen 6: Brace Deformation Time Histories (Dyn. Proof Protocol)



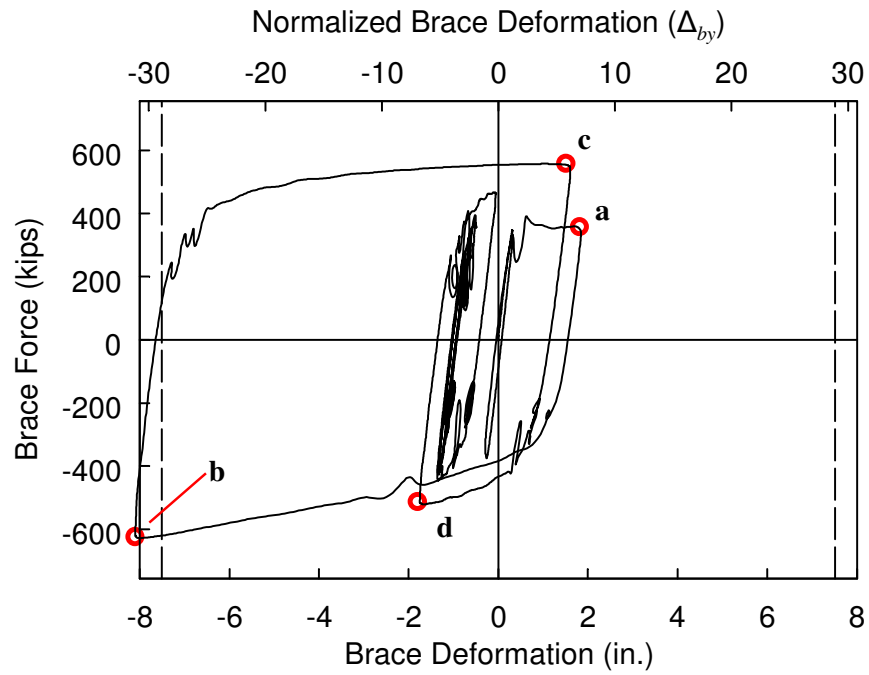


Figure 3.91 Specimen 6: Brace Force vs. Axial Deformation (Dyn. Proof Protocol)

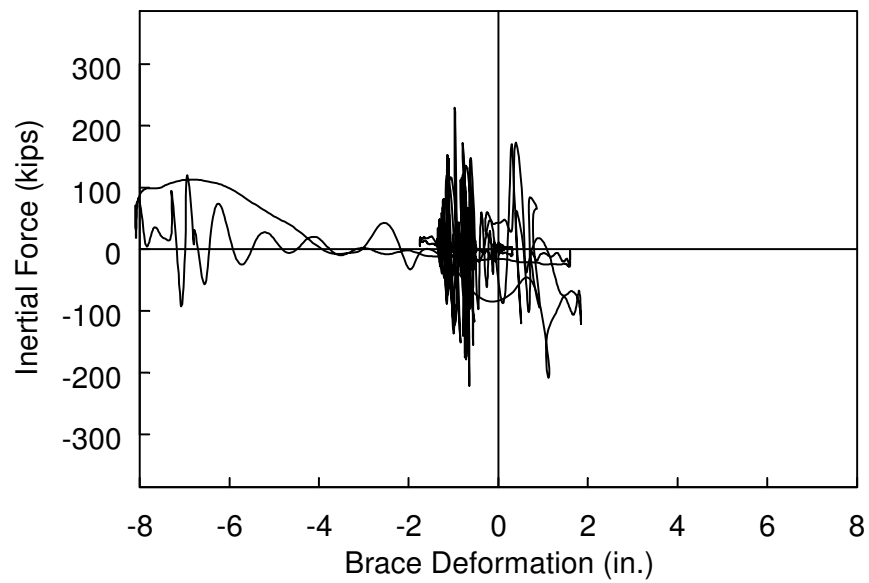


Figure 3.92 Specimen 6: Inertial Force vs. Axial Deformation (Dyn. Proof Protocol)

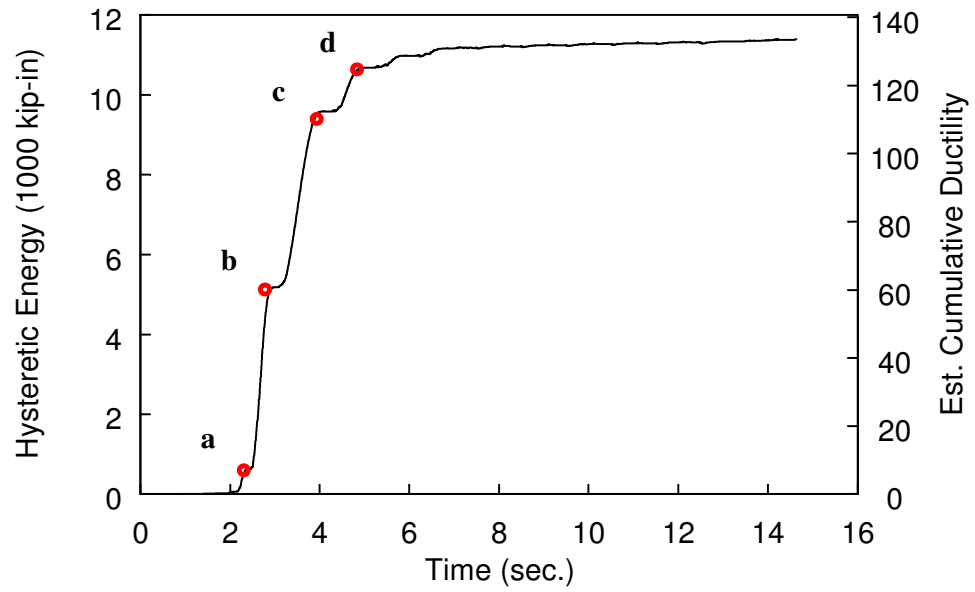
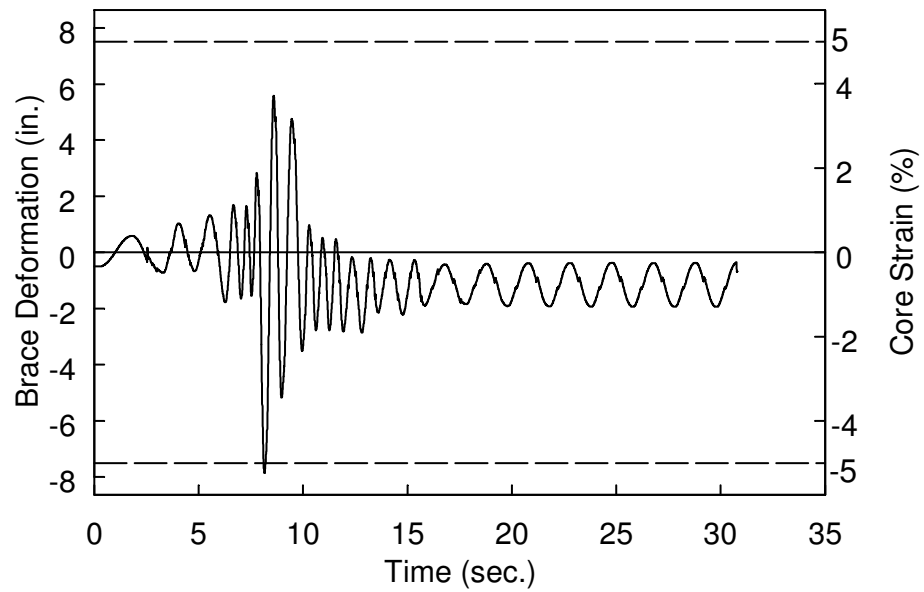
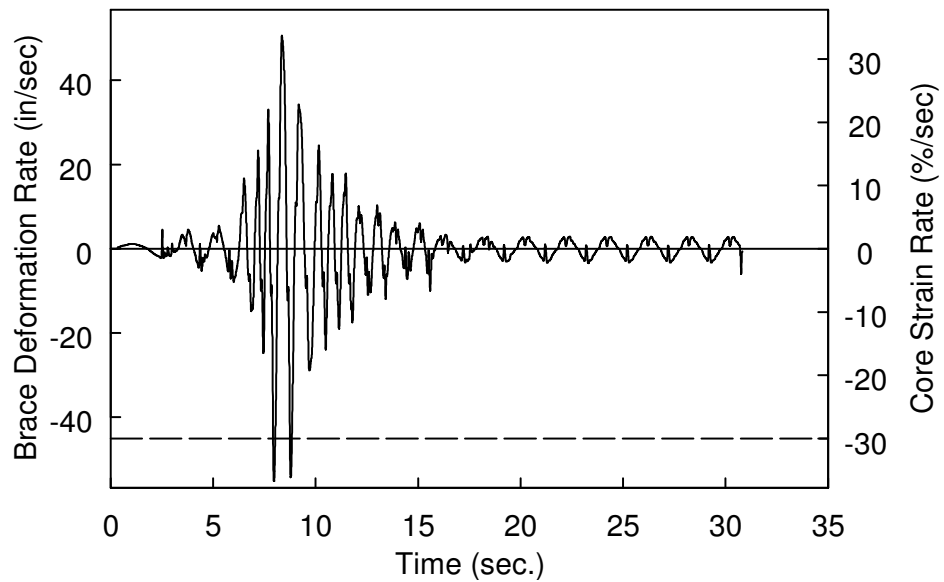


Figure 3.93 Specimen 6 Hysteretic Energy Time History (Dyn. Proof Fault Protocol)



(a) Measured Core Deformation



(b) Measured Core Deformation Rate

Figure 3.94 Specimen 6 Brace Deformation Time Histories (Dyn. Near Fault Protocol)

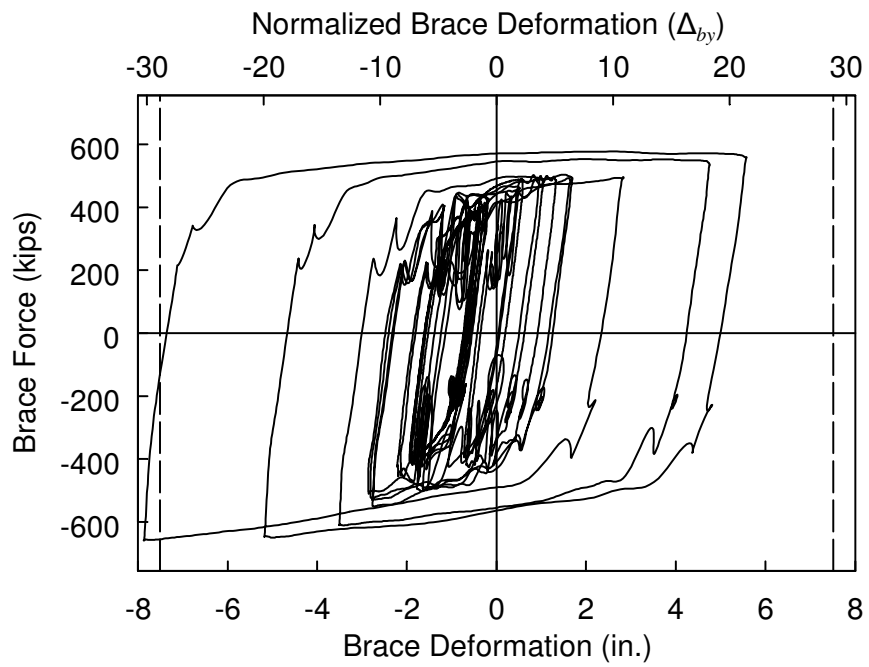


Figure 3.95 Specimen 6 Brace Force vs. Axial Deformation (Dyn. Near-Fault Protocol)

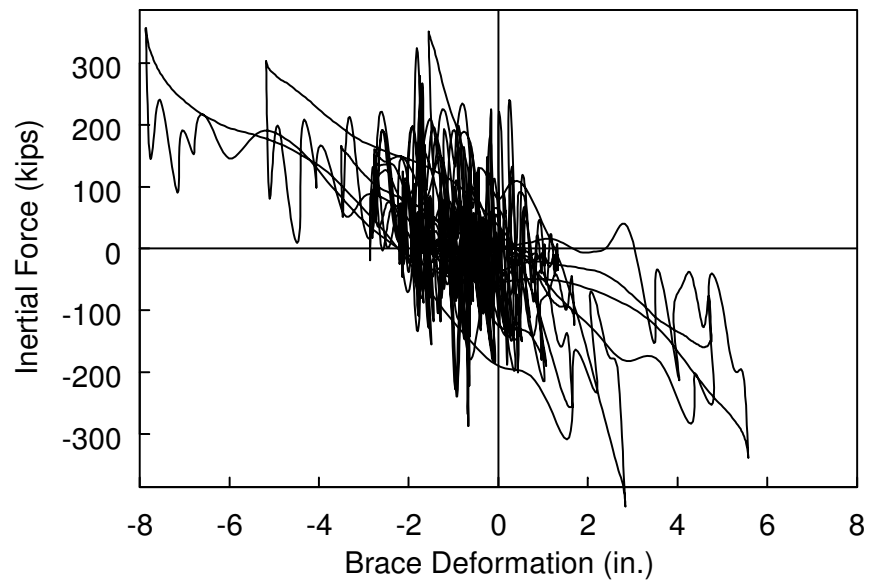


Figure 3.96 Specimen 6 Inertial Force vs. Axial Deformation (Dyn. Near-Fault Protocol)

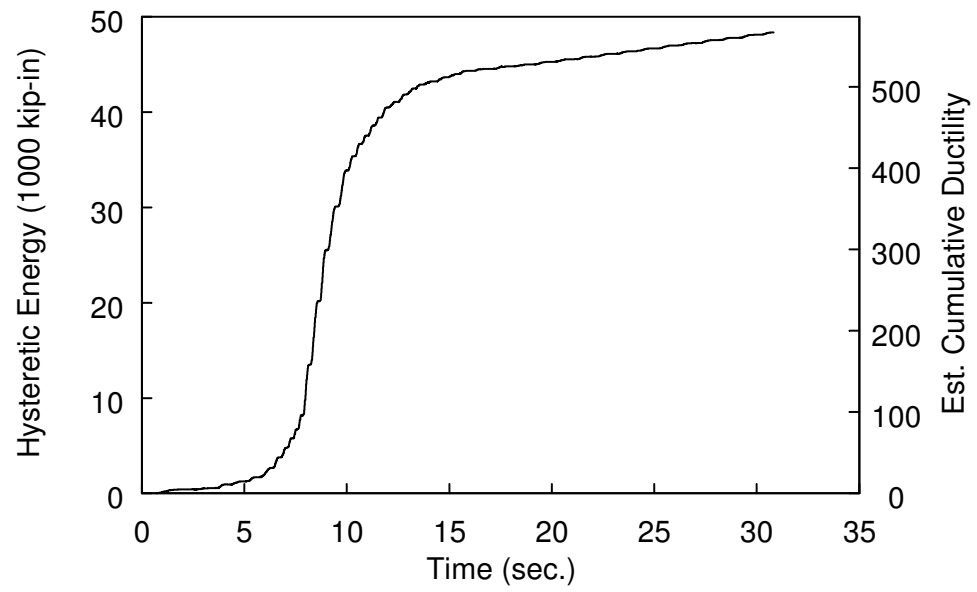
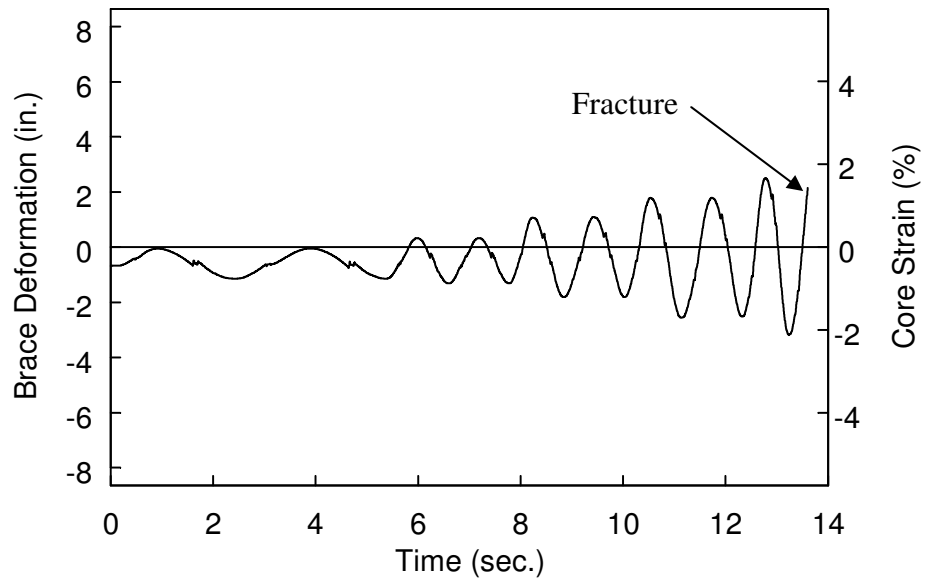
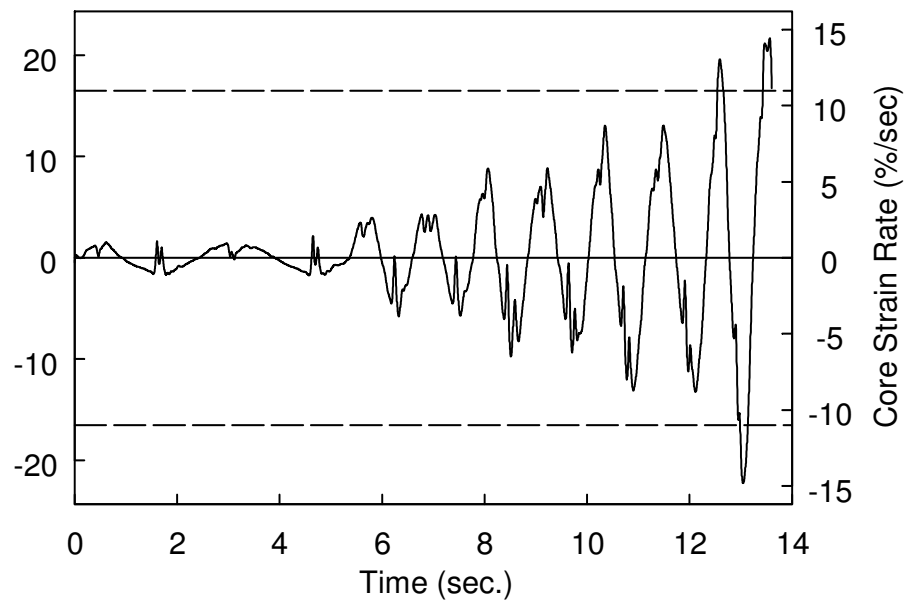


Figure 3.97 Specimen 6 Hysteretic Energy Time History (Dyn. Near-Fault Protocol)



(a) Measured Core Deformation



(b) Measured Core Deformation Rate

Figure 3.98 Specimen 6: Brace Deformation Time Histories (Dyn. AISC Protocol)

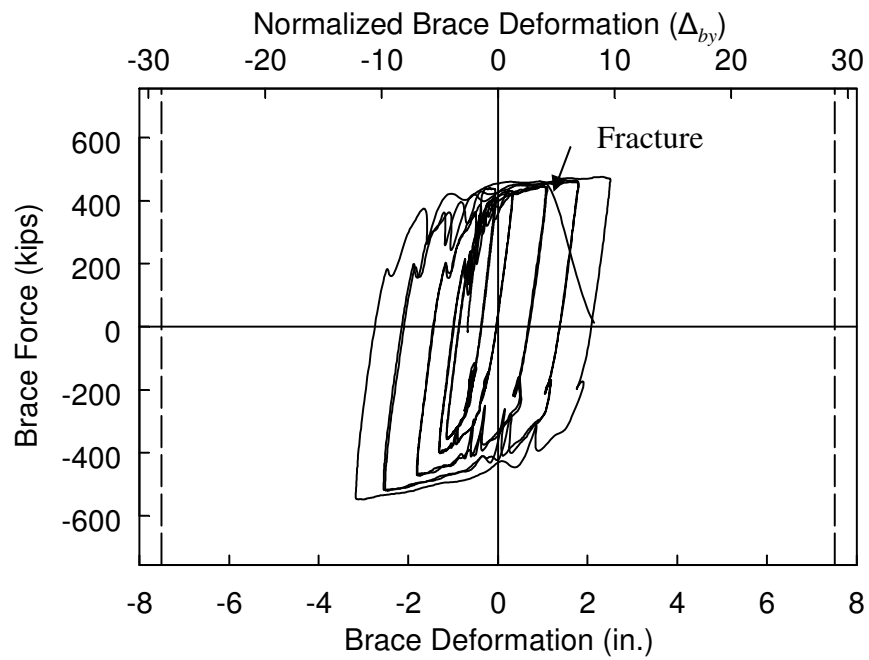


Figure 3.99 Specimen 6: Brace Force vs. Axial Deformation (Dyn. AISC Standard Protocol)

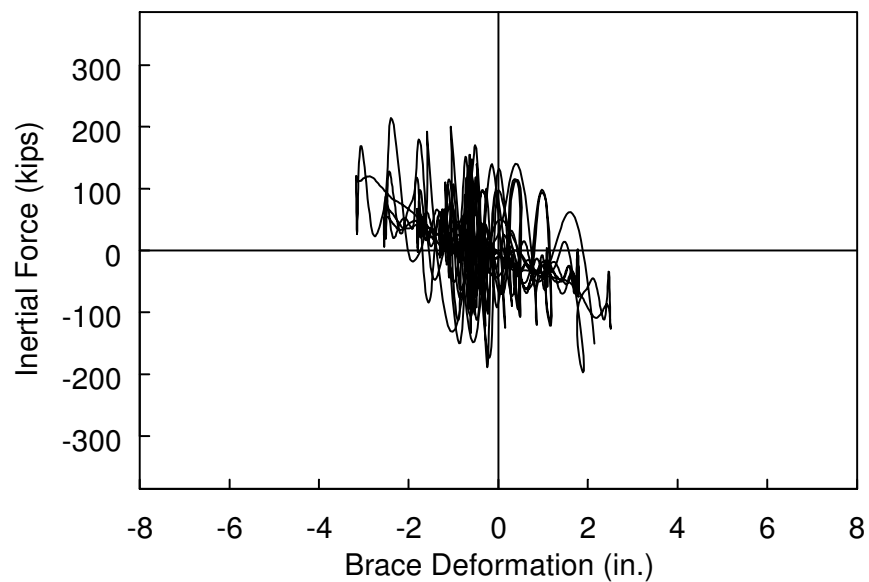


Figure 3.100 Specimen 6: Inertial Force vs. Axial Deformation (Dyn. AISC Standard Protocol)

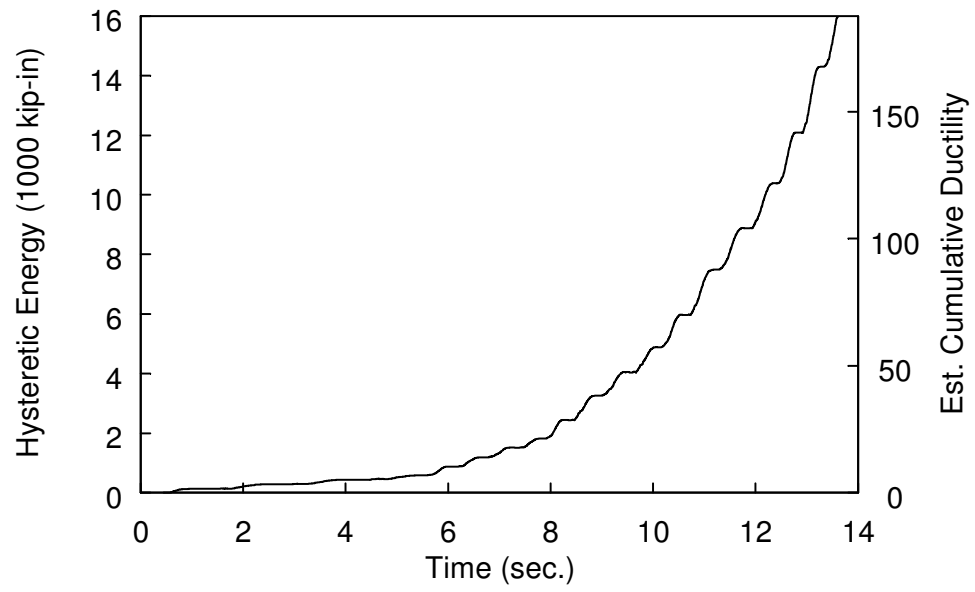
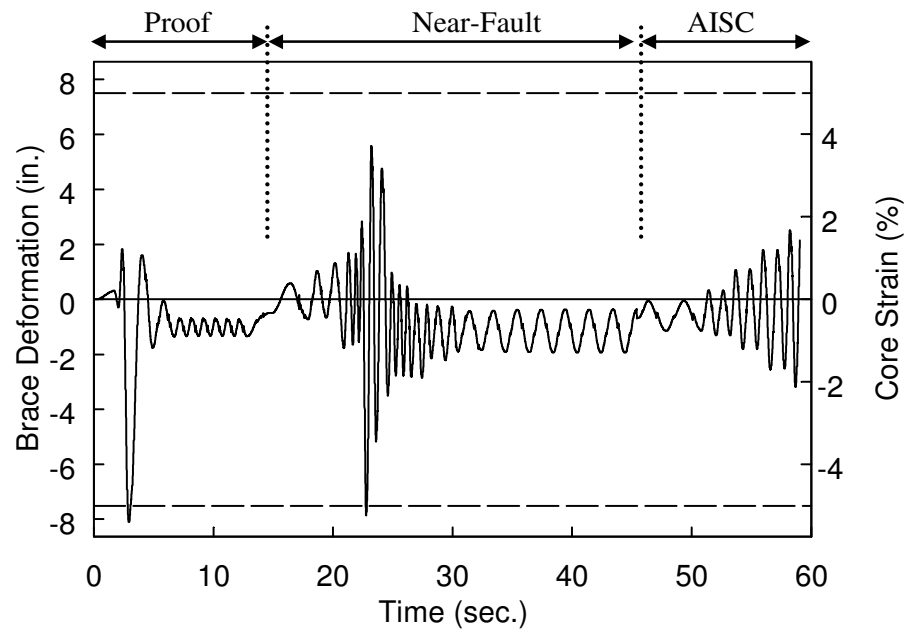
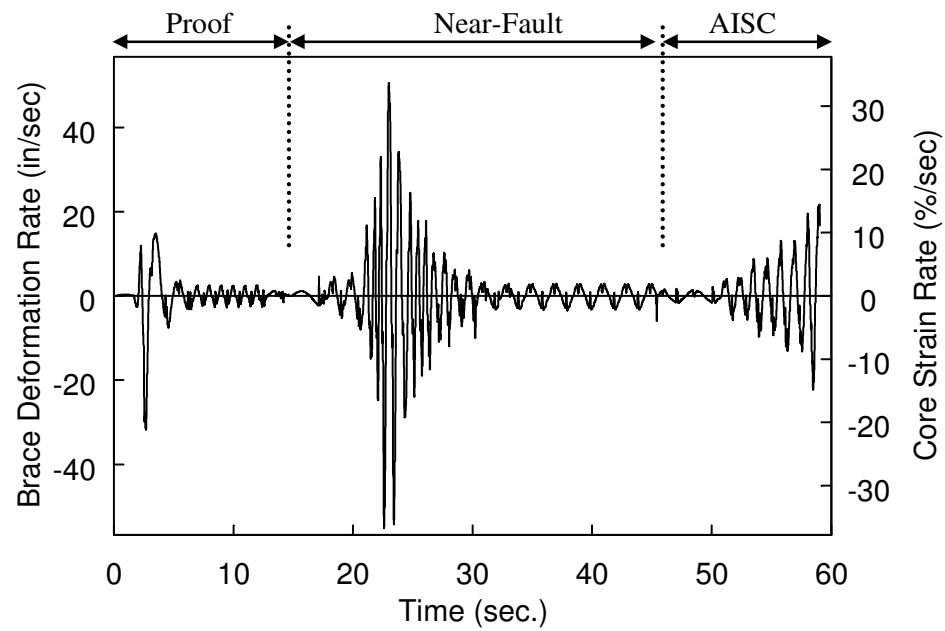


Figure 3.101 Specimen 6: Hysteretic Energy Time History (Dyn. AISC Standard Protocol)





(a) Measured Core Deformation



(b) Measured Core Deformation Rate

Figure 3.102 Specimen 6: Brace Deformation Time Histories (All Tests)

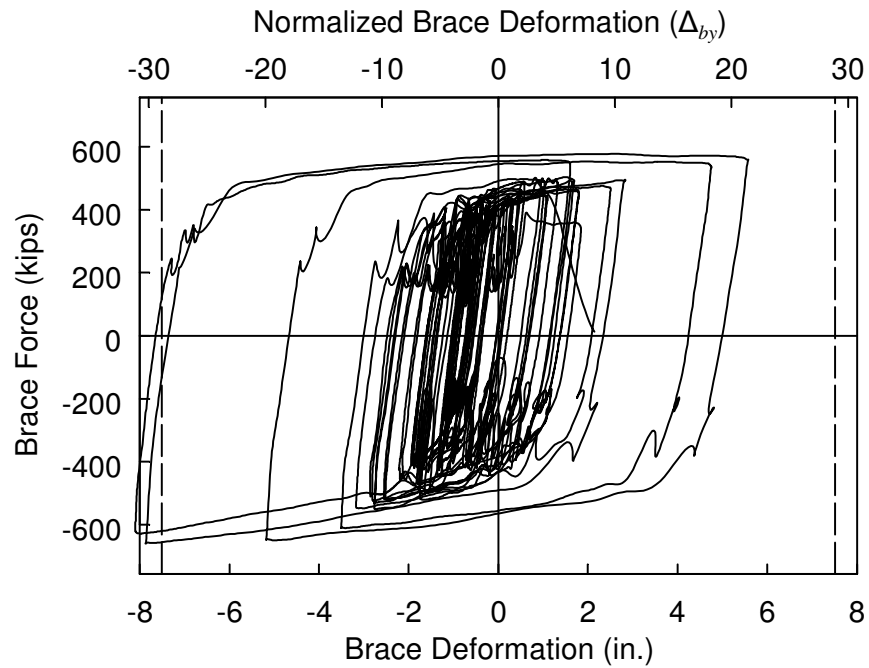


Figure 3.103 Specimen 6: Brace Force vs. Axial Deformation (All Tests)

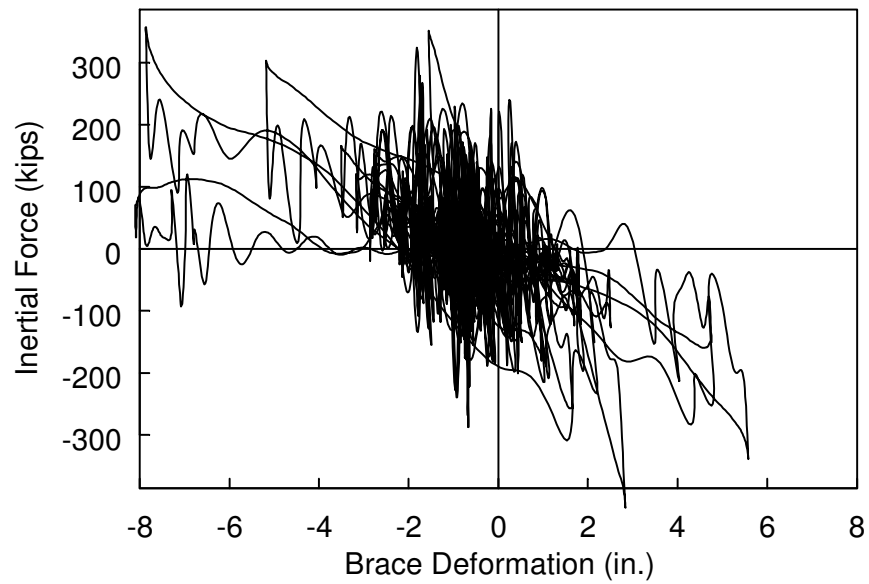


Figure 3.104 Specimen 6: Inertial Force vs. Axial Deformation (All Tests)

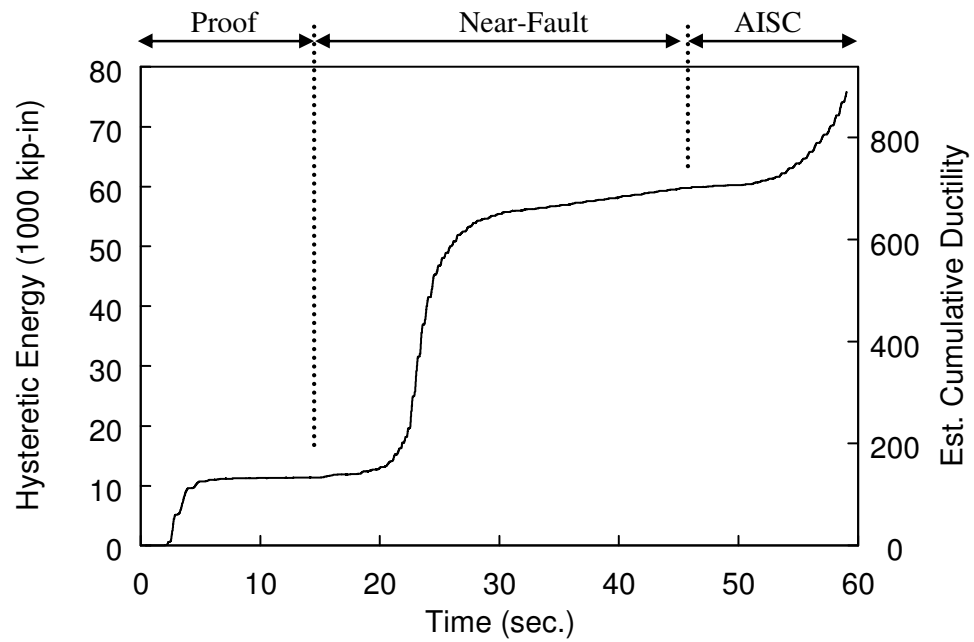


Figure 3.105 Specimen 6: Hysteretic Energy Time History (All Tests)

## 4 DESIGN AND TESTING IMPLICATIONS OF TEST RESULTS

### 4.1 Effect of Large Nonsymmetrical Cycles

The conventional measurement of the imbalance between compression and tension force responses of a BRB is the compression strength adjustment factor,  $\beta$ , described above. Figure 1.4 and Figure 4.1 display the way in which  $\beta$  is experimentally measured and how it is applied to a frame in design, where  $\beta > 1.0$  per AISC. The value is measured as the ratio of the subsequent peak compression to tension forces,  $P_{t_2}$  ( $= \beta\omega P_y$ ) and  $T_{t_1}$  ( $= \omega P_y$ ), during each of the symmetric cycles of the AISC Protocol applied to a single BRB. Then, for the capacity design of the horizontal member with two adjoining braces, in Figure 4.1(c), the resultant force between the two is proportional to  $\beta$ . Note, when following the current provisions, the resultant force is always applied upward as  $\beta$  is only taken as greater than 1.0 and the resultant is always found from the difference between  $\beta\omega P_y$  and  $\omega P_y$ , as indicated in Figure 4.1(c). This method, however, is not consistent with actual loading in the structure because it considers the loading sequence and brace response of a single brace, while there are two braces in the structure which are loaded in nominally equal but opposite sequence.

However, the deformation time history and hysteretic behavior of two such braces illustrated in Figure 4.2 would provide a consistent representation of the brace forces and the ensuing resultant force between the two. Brace 1 is loaded in tension while Brace 2 is simultaneously in compression at time  $t_1$ , and vice versa at time  $t_2$ .

Here the unbalanced force is found at each deformation peak for each brace, with maximum tension and compression forces taken from the appropriate BRB. In Figure 4.2(c), the unbalance at each time instance is shown as two scenarios. Scenario 2 illustrates the case where the resultant force is in the downward, not upward, direction which is a case the current methodology ignores.

However, to facilitate the economy of prequalification testing, currently only one BRB is required to be tested for the measurement of  $\beta$  per the provisions of AISC 341-10. Also, given the fairly symmetric and regular hysteretic behavior of many braces tested to the symmetrical cycles of the AISC Protocol (e.g. Merritt et al. 2003, Tremblay et al. 2006, among others) this inconsistent approach may still provide equal or even conservative estimates of the unbalanced forces, due to the relatively small deformations of many cycles and low amounts of strain hardening exhibited by typical A36 yielding core BRBs.

On the other hand, the meaning, validity, and measurement of  $\beta$  are unclear when amplitudes in a cycle are not symmetric. Refer to the deformation time histories and hysteretic responses for the first three Proof Protocol excursions of Specimens 1 and 2 shown in Figure 4.3(a) and (b). If  $\beta$  is conventionally evaluated for Specimen 1 the strength ratio  $P_3/T_2$ , a value of 1.22 will result. But a much larger value (= 1.52) will result for the nominally identical brace Specimen 2 if  $\beta$  is calculated as the force ratio  $P_2/T_1$ . Such inconsistency is due to the unequal magnitude deformations at which the forces are measured, which violates the implied definition of  $\beta$  in AISC 341. This conventional method for is not consistent with actual loading and is not well

suiting for non-symmetric loading, especially when cycles contain large strain amplitude. A better definition of the unbalanced force is desirable.

Consider, again, the chevron configuration shown in Figure 4.2, and assume the nominally identical Specimens 1 and 2 represent the two braces in the frame. As shown in Figure 4.3(b), asymmetric cycles from a near-field seismic event can result in more than one scenario of unbalanced forces, like the two in Figure 4.2(c), causing a resultant force in either direction perpendicular of the horizontal member. An upward resultant is experienced during loading of  $t_2$  because  $P_{t_2} > T_{t_2}$ , shown in Figure 4.3(b). Likewise during loading of  $t_3$ , the resultant is in the downward direction as  $T_{t_3} > P_{t_3}$ . Both scenarios must be addressed in designing the horizontal member.

#### 4.2 A Consistent Measure of BRB Unbalanced Forces

Due to these inadequacies of  $\beta$  as defined and utilized in AISC 341 for far-field ground motions, the unbalanced strength factor is proposed which can be measured during near-field BRB prequalifying tests as:

$$\gamma_i = \frac{|\omega_{C,i}|}{\omega_{T,i}} \quad (5)$$

where  $\omega_{C,i}$  and  $\omega_{T,i}$  are the compression and tension overstrength factors, respectively, for the  $i$ -th excursion measured from a pair of nominally identical braces subjected to equal and opposite loading protocols. The compression and tension factors are numerically equal to the peak force normalized by  $P_{yd}$ . Measuring the unbalance in this way is consistent with the interaction between adjacent, or opposing, braces of many possible BRB configurations. Multiple cases of unbalanced brace

forces can be identified, unlike in the current provisions, by recording a maximum and a minimum value of  $\gamma$ . Additionally, the maximum values of  $\omega_C$  and  $\omega_T$  in the two tests provides the maximum individual brace compressive and tensile forces, respectively, under two loading sequences as opposed to only one required by the current testing convention. The maximum  $\omega_C$  can be utilized within the modified Thornton method conventionally for the design of the brace gusset plates, while  $\omega_T$  can provide the maximum tension force in checking the Whitmore section of gusset plate for yielding and rupture.

The values of  $\omega_C$ ,  $\omega_T$ , and  $\gamma$  corresponding to the tests conducted on Specimens 1 and 2, shown in Figure 4.3, are provided in Table 4.1. At  $t_2$ , with nearly 5% core strain,  $\gamma$  is shown to be 1.39 indicating that the brace in compression exhibits a larger magnitude force than the brace in tension. Conversely, at  $t_1$  and  $t_3$  produce  $\gamma$  values less than 1.0, meaning tension forces are larger than compression forces. Since only one pair of specimens were tested to equal and opposite protocol, the full effects and range of acceptable  $\gamma$  values are yet unknown for other BRB designs. Limiting the unbalance in either case to 30% (i.e., limiting  $\beta$  to 1.3 in AISC 341) seems reasonable, however exception may be required for large core strains of the near-fault pulse excursions since the unbalance was found to be almost 1.40 at 5% core strain. Testing of more BRB designs will provide more information to set limits for  $\gamma$  in both tension and compression unbalance scenarios. However, before more test data is available, reasonable limits for  $\gamma$  are a minimum of 0.70 and a maximum of 1.40.

To provide meaningful strain hardening factors for near-field applications, it is suggested that a pair of nominally identical specimens, not one specimen, be tested. To further demonstrate the problem associated with the latter, consider the first and second tests applied to Specimen 2, shown in Figure 4.4. These contain subsequent 5% core strain excursions from which a  $\gamma$  value can be attempted. Figure 4.4(b) shows the two branches of the hysteretic curve for these excursions. Per Eq. 5, the value of  $\gamma$  is then found to be 0.91 ( $= |-1.92|/2.1$ ) for the subsequent, nearly, 5% core strains. Clearly the sequence of loading has a dramatic effect on  $\gamma$  and hence the considered unbalanced loading cases. Had the excursions occurred in the reverse order (tension before compression) the value of  $\gamma$  found would likely be very different. This and the reasons listed above suggest that proper BRB testing should include two nominally identical braces subjected to equal yet opposite loading protocols.

Measuring  $\omega_c$ ,  $\omega_t$ , and  $\gamma$  in the proposed manner permits the proper design of chevron-style frames, such as BRBFs in buildings and in the bridge applications studied by Usami et al. (2005) and Kanaji et al., (2005). Knowledge of the multiple possible cases of unbalanced BRB loading given by  $\gamma$ , and not by  $\beta$ , is particularly important in designing the reinforcing steel for reinforced concrete beams, slabs, or abutment structures for BRB bridge applications like those used in ductile end diaphragms investigated by Celik et al. (2009), shown in Figure 4.5(a). Other possible BRB arrangements, like those of viscous dampers on the Rion-Antirion Bridge (Infanti et al. 2004) similar to that shown in Figure 4.5(b), where unbalanced forces cause torsion on the bridge span. For common bracing systems in which BRBs do not



oppose each other, like in diagonal bracing configurations with parallel braces in each bay, testing as proposed provides the maximum overstrength achieved under two different loading sequences, unlike in the current AISC provisions, for use in capacity based design of the frame and connections.

### 4.3 Effect of Yielding Core Steel Type

The geometrically identical Specimens 3 (SS) and 6 (A36) were subjected to the same dynamic loading protocols with equal strain magnitudes, which were tested to fracture. The superior ductility capacity and energy dissipation capability of SS is displayed by Specimen 3, which sustained  $\eta$  of 1.67 and  $\psi_h$  of 2.31 times greater than Specimen 6, as summarized in Table 3.8. Extrapolating only from these two BRBs, Specimen 5 (A36) appears to have been very close to fracture, while Specimens 1, 2, and 4 (all SS) were likely capable of sustaining at minimum one additional protocol. Furthermore, tensile coupon tests of the two materials in this research (Table 3.2 and Figure 3.2) show on average the elongation at failure to be 1.56 ( $= 0.56/0.36$ ) times greater for the SS over A36.

Compared to that of A36 steel, the desirable corrosion resistance and ductility of SS, Type 304/304L among other grades, is accompanied by significantly different strain hardening behavior. An indicating factor of the hardening potential of a steel material is the  $R_u (= F_{ud}/F_{ya})$  value obtained from tensile coupon tests. The material test results in Table 1 show the average SS-to-A36  $R_u$  ratio to be 1.51 (assuming pseudo-static loading) indicating that SS has much more potential for strain hardening than A36. This is reflected by the very different cyclic strain hardening (CSH)

behavior of the two materials, which can be compared in terms of two common rules known as kinematic and isotropic hardening, or the translation and dilation of the material yield surface, respectively. Stainless steels are known to exhibit significant isotropic hardening, as shown by Paul et al. (2010), while cyclic tests on A36 steel coupons by Kaufmann et al. (2001) show its hardening to be mostly kinematic in nature. Also, Nip et al. (2010) performed extremely-low-cycle fatigue tests on carbon steel and SS coupons, which also clearly showed these CSH differences. The CSH behaviors are clearly displayed by the BRB tests performed in this research.

Significant cycles from the BRB tests are shown in Figure 4.7, for clarity, where the marked events correspond to those shown in Figure 4.6. As shown in Figure 4.11(a), the SS to A36 normalized peak force ratio averages 1.19 for events A through C, and continues to increase throughout the second test averaging 1.45 and reaching a maximum of 1.52. These hysteretic loops reveal the isotropic CSH behavior of SS and the kinematic hardening of A36 by inspecting points B, D, and F. At event D, the deformation is nearly equal to that of event B, yet the peak force for SS increases by 1.21 ( $= 2.73/2.25$ ), while that of the A36 brace increases by only 1.05 ( $= 2.01/1.91$ ) times greater than at event B. Further, the deformation level of event F is attained by each brace twice, occurring first along the curve leading to D. Comparing the normalized peak forces upon returning to deformation of F, the SS force increases by 1.18 ( $= 3.01/2.57$ ) while the A36 increases by only 1.05 ( $= 1.98/1.88$ ). This clearly demonstrates the significantly different isotropic CSH behavior of the two materials. Note that despite the considerable deformation and  $\eta$  differences at all three points, the A36 brace exhibits essentially the same normalized peak forces at both D and F ( $\approx$

2.0). An even more marked increase is displayed between Specimens 2 and 5, as shown in Figure 4.8. Specimen 2, SS, underwent much lower cumulative ductility in test 1 than did Specimen 5, and yet the isotropic hardening of SS is shown to cause a large overstrength compared to A36.

#### **4.4 Effect of Strain Rate**

Mild structural steels such as A36 are generally assumed as rate-independent because the yield stresses are typically only about 7% higher under seismic loading rates (Di Sarno et al. 2002). SS is recognized as more strain-rate-dependent, as summarized by Nordberg (2004) with flow stresses (stress required to continue deforming plastically) at both 0.2% and 2% strains approximately 1.28 times greater due to an increase in strain rate from 0.1% to 100%  $\text{sec}^{-1}$ . Despite the general dismissal of the strain rate effect for structural steels due to the relatively low strain rates expected in structures under earthquake loading on the order of 10 %  $\text{sec}^{-1}$  (Shing et al. 1988), several researchers have recognized that bracing members can experience high rates at sites of local inelastic behaviors, such as plastic hinges at mid-length in buckled braces, during large seismic loading. Cardin et al. (2004) performed dynamic tests on short BRB, within ductile end frames of bridge spans, under a constant frequency of 2 Hz, resulting in a maximum core strain rate of 13.8%  $\text{sec}^{-1}$ . Tremblay et al. (2006) subjected BRB to dynamic loading to a maximum rate of 25%  $\text{sec}^{-1}$ . These cases were reported to have increased BRB hysteretic responses by 15% and 5%, respectively, as compared to similar pseudo-statically loaded braces. During the protocol development by the authors (Lanning et al. 2014) simulated BRB yielding

core strain rates had a mean ( $= 18.9\% \text{ sec}^{-1}$ ) plus one standard deviation ( $= 11.2\% \text{ sec}^{-1}$ ) of  $30\% \text{ sec}^{-1}$ , with a maximum of  $50\% \text{ sec}^{-1}$ . The former is represented in the Dynamic Near Fault Protocol, shown in Figure 2.21.

The nominally identical SS Specimens 3 and 4 were subjected to the same protocols, but with dynamic and pseudo-static loading rates, respectively. Significant cycles are shown in Figure 4.9(a) and (b), with brace forces normalized by  $P_{ya}$  assuming the BRB manufacturer-provided coupon test results conducted at pseudo-static loading rate (Table 1). In Figure 4.11(a), events A through C of Specimens 3 and 4 show that initially on average the dynamic-to-static normalized peak force ratio averages 1.22. Throughout the second test, despite strain rates and  $\eta$  being much larger, the peak force ratio decreases to an average of 1.11 (events D through G). Over both tests dynamic-to-pseudo-static normalized forces were approximately 1.16 larger. This is consistent with the dynamic effect on BRB found by the researchers mentioned above. The excursions of the second test reflect the SS strain-rate behavior summarized by Di Sarno et al. (2002), as the larger strain excursions exhibit less rate effect. Also in agreement with those findings, is the reduction of  $R_u$  found in the dynamic coupon test presented in Table 3.2 and Figure 3.2. This indicates a decreased spread of plasticity along the coupon at higher rate, and therefore the increase in force due to high rate is expected to decrease or stabilize with increasing  $\eta$  under high strain-rate loading conditions.

Finally, similar ratios were found from the significant cycles of the second tests performed on Specimens 5 (pseudo-static) and 6 (dynamic) of A36 steel, shown in Figure 4.10(c). Similarly, the dynamic normalized forces averaged 17% greater than

those from the pseudo-static tests, shown in Figure 4.11(b). Despite their differing first test protocols, the primarily kinematic CSH of A36 permits the direct comparison of these two specimens (i.e., the material is essentially strain history independent).

Chapter 4 in partial, is a reprint of the material as it has been submitted for publication. The dissertation author was the first author of these papers.

Table 4.1 Measured Unbalanced Forces,  $\gamma$ , from Equal and Opposite Tests:  
Specimens 1 and 2

Excursion No.	Peak Core Strain			Normalized Peak Forces		$\gamma$	
	Time	Specimen	(%)	$\omega_T$	$\omega_C$		
1	$t_1$	1	-1.0		-1.15	0.90	
		2	1.0	1.28			
2	$t_2$	2	-4.7		-1.92	1.39	
		1	4.7	1.38			
3	$t_3$	1	-0.9		-1.68	0.86	
		2	0.9	1.95			
						$\gamma_{max}$	1.39
						$\gamma_{min}$	0.86

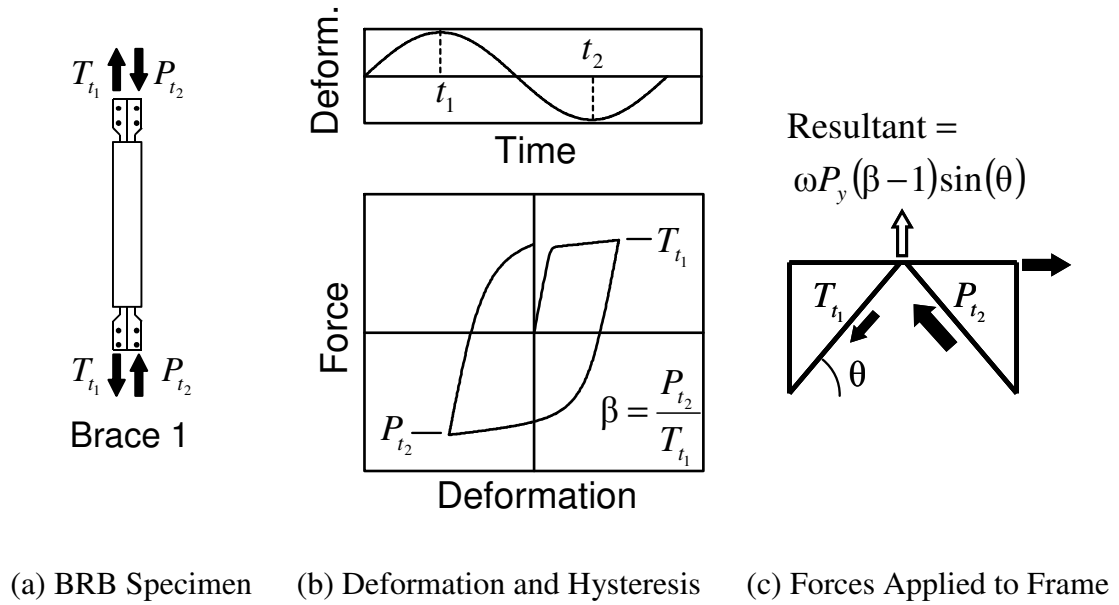


Figure 4.1 Unbalanced Forces from Conventional  $\beta$ -Method

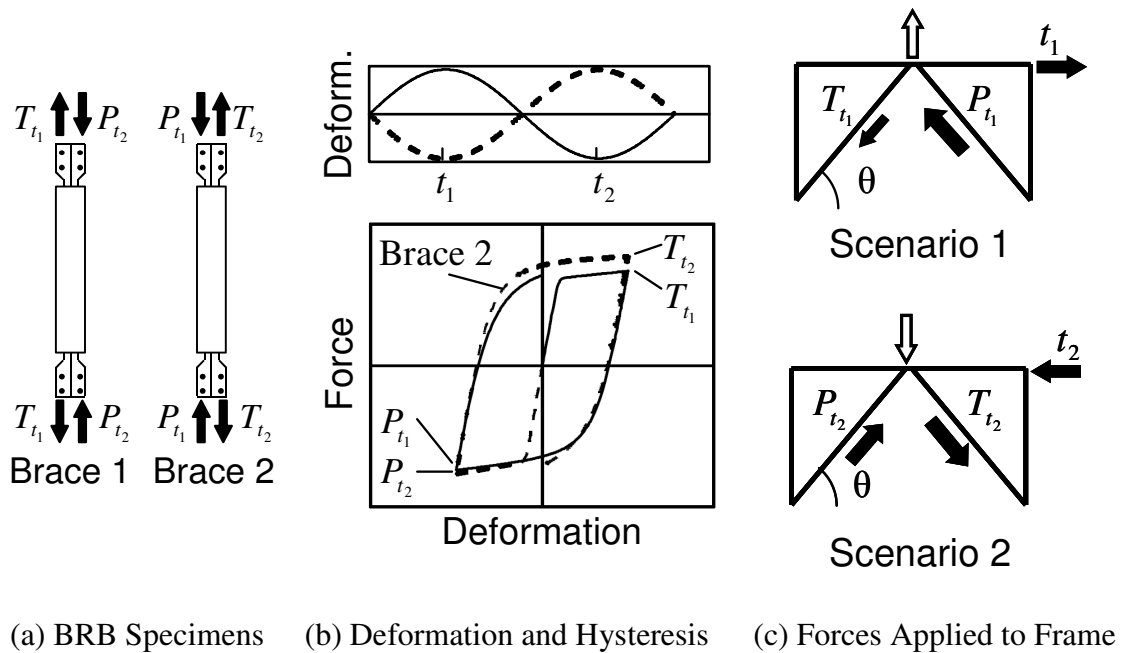
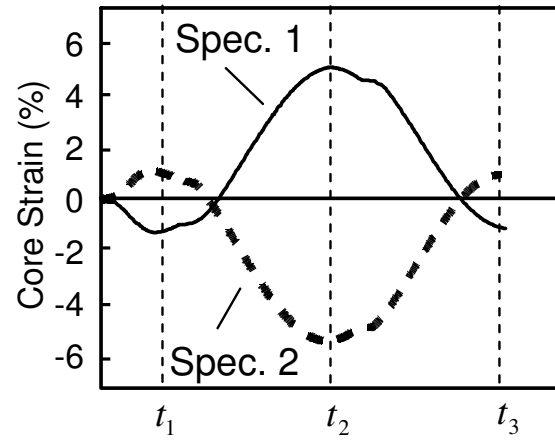
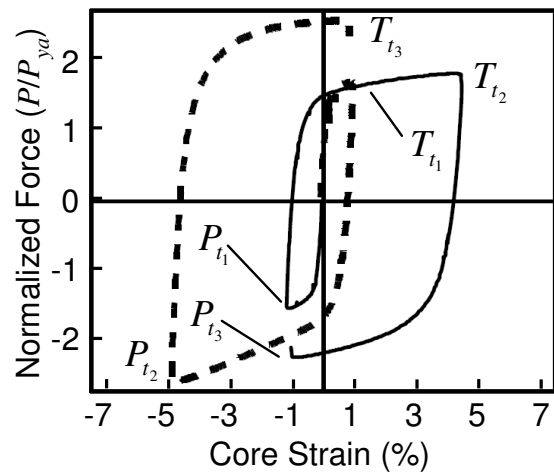


Figure 4.2 Unbalanced Forces from Proposed  $\gamma$ -Method



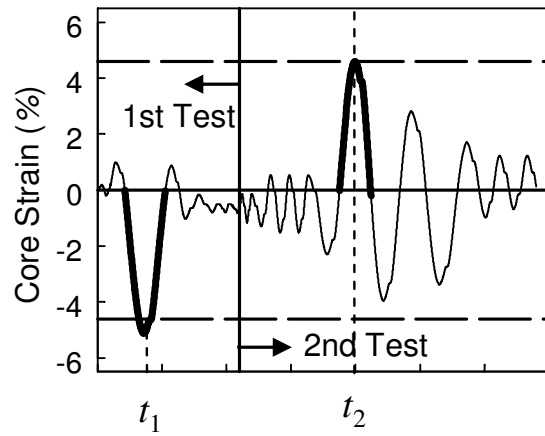
(a) Deformation Time History



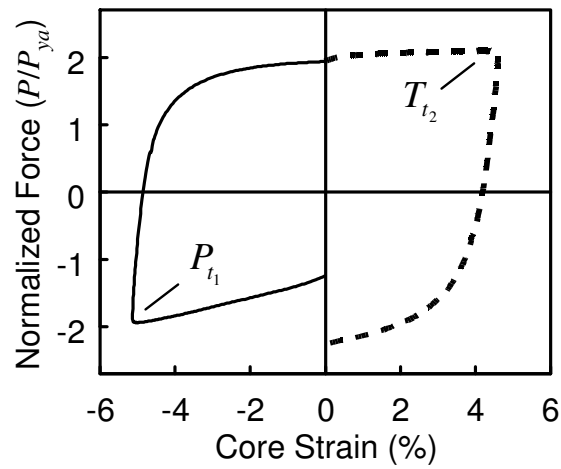
(b) Hysteretic Response

Figure 4.3 Effect of Large Unsymmetrical Cycles on BRBs



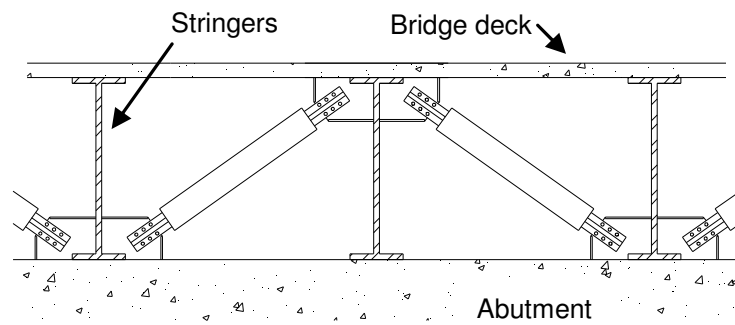


(a) Deformation Time History

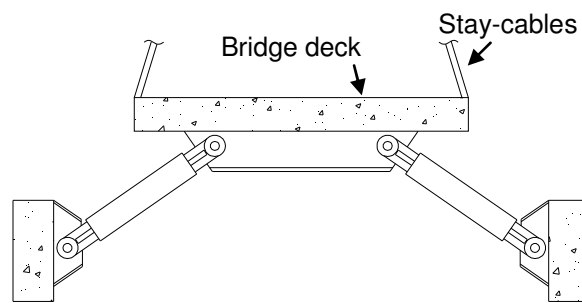


(b) Hysteretic Response

Figure 4.4 Subsequent Large Excursions on Specimen 2

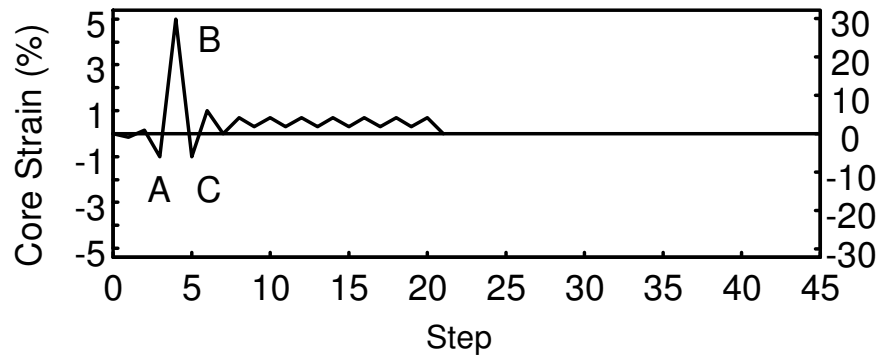


(a) BRBs in Ductile End Diaphragms

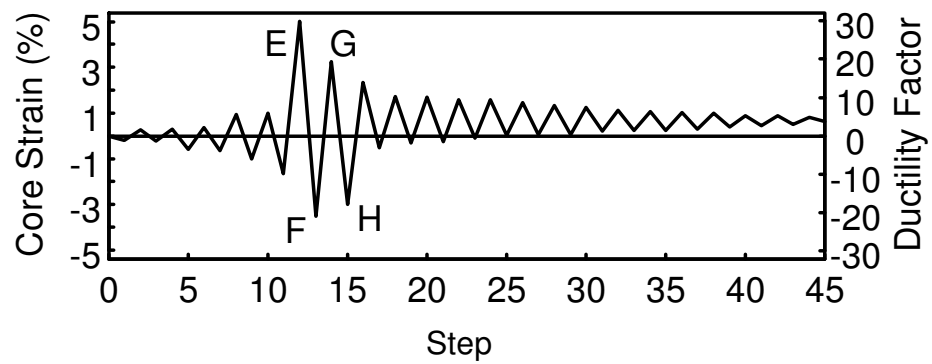


(b) BRBs in Configuration of Viscous Dampers on the Rion-Antirion Bridge

Figure 4.5 Examples of Potential BRB Bridge Configurations Affected by Unbalanced Forces

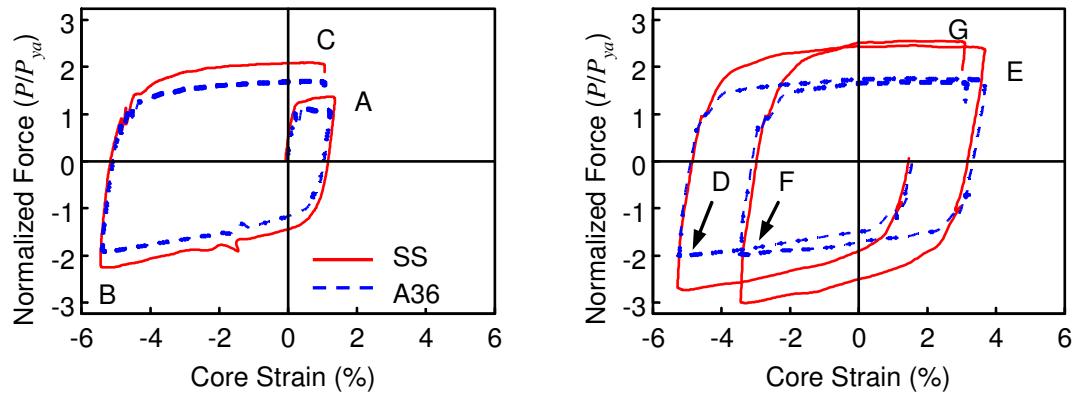


(a) Proof Protocol



(b) Near Fault Protocol

Figure 4.6 Significant Cycle Peaks of the Near-Fault Protocols



(a) 1st Test: Proof-C

(b) 2nd Test: Near Fault-C

Figure 4.7 Effect of Yielding Core Material: Specimens 3 and 6

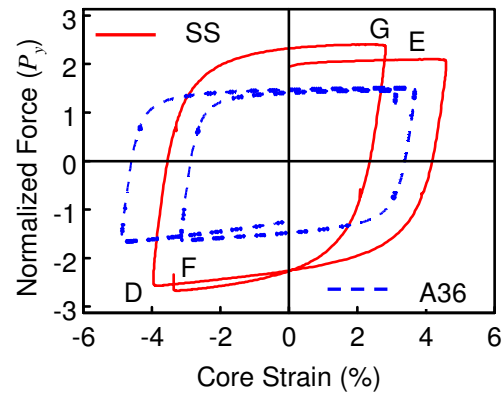


Figure 4.8 Effect of Yielding Core Material: Specimens 2 and 5, 2nd Test

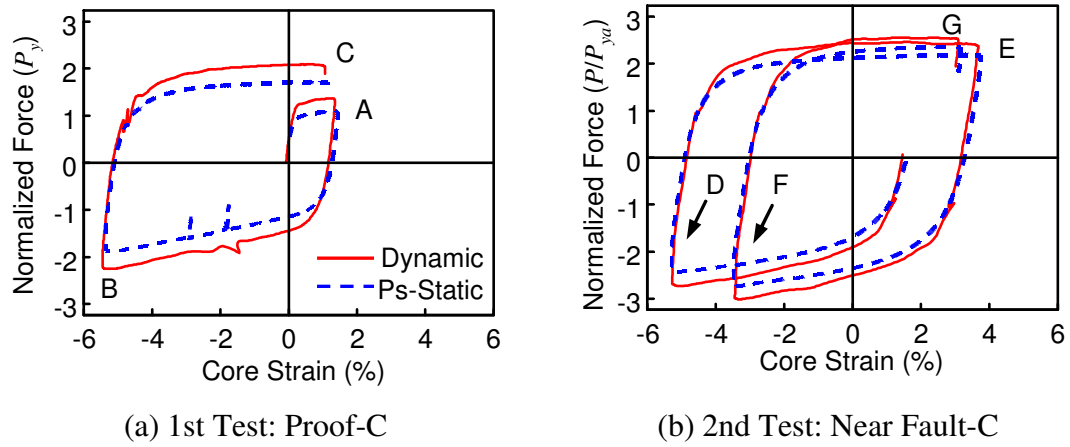


Figure 4.9 Effect of Strain Rate: Specimens 3 and 6

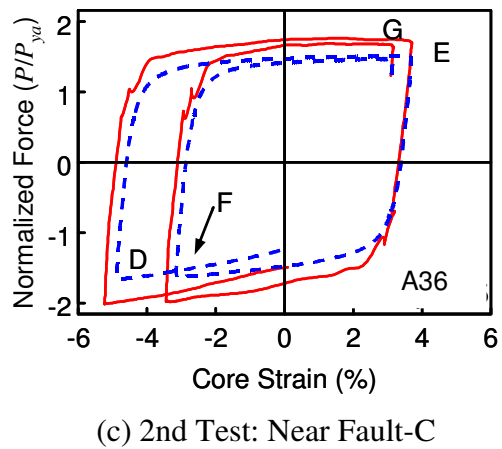
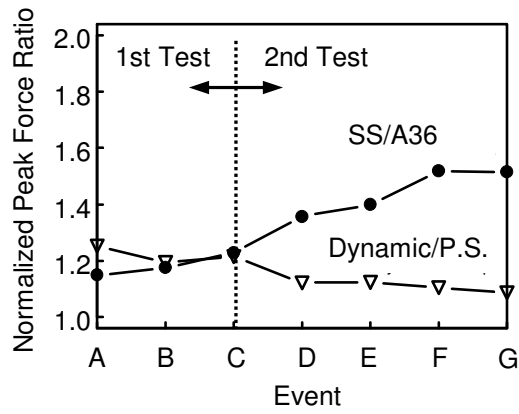
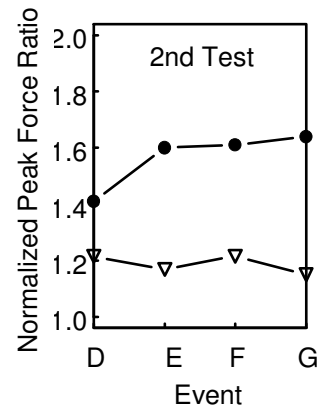


Figure 4.10 Effect of Strain Rate: Specimens 5 and 6, 2nd Test



(a) Specimens 3-to-6, and 3-to-4



(b) Specimens 2-to-5, and 5-to-6

Figure 4.11 Relative Normalized Peak Force Values as a Ratio

## 5 MENEGOTTO-PINTO MODEL FOR BUCKLING-RESTRAINED BRACES

### 5.1 Introduction

As discussed in Chapter 2, nonlinear time history analysis of structures subjected to earthquake loading utilizes the inelastic member properties to simulate incurred yielding, thereby providing energy dissipation. The nonlinear inelastic response is also needed to solve the equation of motion at each time step using the instantaneous tangent stiffness in iterations towards equilibrium of external forces and internal resistance. Therefore, an accurate representation of the cyclic inelastic force-deformation, or hysteretic, behavior is needed for those elements expected or intended to yield.

This chapter provides a brief background on the practice of representing the hysteretic behavior of BRBs. Shortcomings of a commonly used modeling technique are demonstrated for near-fault loading conditions as well as for stainless steel (SS) BRBs. Then the popular Menegotto-Pinto (MP) hysteretic model is summarized. Modifications and model parameters are proposed for its adaptation to BRB cyclic response simulation, including the use of SS and strain rate effects. Finally, using the proposed BRB Menegotto-Pinto model the brace tests in Chapter 3 are simulated and compared to the test results.

### 5.2 Literature Review

A number of techniques are found in the literature for characterizing BRB cyclic behavior. These range in complexity which scales along with the type of

analysis performed. For instance, Usami et al. (2009) and Chou and Chen (2010) directly modeled the yielding core, restrainer, and the contact between them in finite element (FE) modeling environments such as Abaqus (Abaqus 2011) to investigate the effect of local phenomena on the component-level behavior. This type of detailed model is not conducive to structural design-oriented system-level analysis. In this case, simpler phenomenological models that mimic those behaviors through inelastic finite element hysteretic rules is preferred.

Black et al. (2004) provided parameters for the smooth hysteretic Bouc-Wen model, governed by a differential equation controlling the Bauschinger effect between the linear elastic and post-yield stiffness regions. The representation was very good; however, the isotropic hardening action was not represented which is critical for SS BRB, as shown later in this Chapter. Others have used multi-linear truss elements like that implemented in the FE model package Perform-3D (CSI 2006). The effectiveness of bilinear and multi-linear hysteretic rules is acceptable, capturing the basic behavior of BRBs to varying degrees, however the tangent stiffness (i.e., the smoothness of the simulated response) is not representative of the nonlinear region of the Bauschinger effect (noted in Figure 5.1). Related to this deficiency, Moaveni et al. (2012) concluded that more accurate modal representation was obtained from structures with smooth hysteretic models over those with bilinear models in a system identification procedure aimed at characterizing nonlinear dynamic structural systems. Therefore, the use of smooth hysteretic models is preferred for nonlinear time history analysis. Some improvements can be made by tailoring the post-yield stiffness values, however there is tradeoff between peak force representation and energy dissipation. Tremblay



et al. (2004) utilized a modified Ramberg-Osgood formulation referred to as the Pyke Model, which was reportedly able to incorporate the isotropic and kinematic hardening effects. However, in the comparisons provided, the peak compression forces not appear to correlate well with the test results. Although, other characteristics were fairly well matched.

Recently an elastoplastic model has been developed by Zona and Dall'Asta (2012) which is governed by the behavior of a rheological model of a spring in series with a parallel spring and friction slider. This configuration provides excellent BRB representation through calibration of several parameters. Strain rate effects are not addressed, and the complexity of the model, albeit manageable, may be somewhat superfluous for use in system-level structural analysis. Therefore, a balanced approach between accurate representation of BRB hysteresis and simplicity is desirable.

### **5.3 Correlation of Bilinear Truss Element**

As discussed in Chapter 2 and above, a common modeling technique for representing the hysteretic behavior of BRBs in a FE model is the use of a bilinear truss element with the kinematic strain hardening rule (see Figure 2.7). Several researchers have utilized this element, such as Sabelli et al. (2003) in the study leading to the development of the current AISC Protocol. Kim et al. (2004), Ravi et al. (2007), and Usami et al. (2005) all used versions of this model in global structural response studies including bridge BRB application by Usami. The Bouc-Wen model discussed by Black et al. (2004) was also shown to produce nearly identical SDOF structure spectral response as that one with bilinear truss BRB produced almost identical

spectral response under the 1971 San Fernando ground motion. This modeling approach was used in the VTB case study of Chapter 2, and for the loading protocol development discussed in Chapter 3.

### **5.3.1 A36 BRB Subjected to the AISC Protocol**

Many BRB prequalifying test results are available in the literature and through brace manufacturers. In the cases mentioned above, utilization of the bilinear element is typically justified by comparing the element and recorded responses of these kinds of tests. Figure 5.1 shows such a comparison from recent testing at UCSD. Here, the post-yield stiffness ( $K_2$ ) is chosen as 3.25% of the elastic stiffness, just as in the VTB case study of Chapter 2. The bilinear element does provide a reasonable account of the experimental results, with approximately 10% overall error in the dissipated energy and most peak forces slightly overpredicted by the model as shown in parts (b) and (c) of the figure.

Actual BRB displacement response in structures subjected to ground shaking, real or simulated, will be not be symmetrical and uniformly increasing in magnitude like that of the AISC Protocol. The issue of loading sequence effects is ignored in this approach, and the study of only mild carbon steel (A36) neglects the possibilities of different strain hardening behaviors.

### **5.3.2 A36 and SS BRB Subjected to the Near Fault Protocol**

Test results from the Near Fault Protocol applied to Specimen 5, with A36 yielding core, and Specimen 4, with SS core, were simulated with the bilinear BRB model. The model utilized the same yield force as the corresponding brace, and the

post-yield stiffness was as discussed in the previous section. The full hysteretic response is shown in Figure 5.2, along with the normalized dissipated energies. Note that both test specimens exhibit dissipated energy distribution over normalized time history was nearly identical, and so only one experimental curve is shown in the figure for response comparison.

For the A36 brace, in part (a), it is evident the peak forces are not well reflected well at large deformation levels and, even though much of the area under the experimental force-deformation curve is not represented. Although the energy dissipation is only about 10% underpredicted [see Figure 5.2(c)], the correlation of the hysteretic response, in the Bauschinger effect region, is poor. A better model is obviously desirable.

Inspection of Figure 5.2(b) makes obvious the poor overall performance of the model for stainless steel BRB. As discussed in Chapter 4 the significant isotropic hardening of SS leads to severely underestimated peak forces by the simple bilinear truss element with kinematic hardening. The overall error in hysteretic energy is nearly 40%. Obviously a better model with proper account of SS hardening is also required for simulation of SS BRB.

## **5.4 Menegotto-Pinto Material Model**

### **5.4.1 Background**

The popularity of the smooth hysteretic model proposed by Menegotto and Pinto (1973) is due its simplicity and relatively high computational efficiency, while providing good representation of the hysteretic response of steel. An updated version

of this model is widely used within the OpenSees finite element system (OpenSees, McKenna et al. 2010) as the uniaxial material model *Steel02*.

The model was originally developed for characterizing reinforcing steel in concrete structures subjected to earthquake loading. Stress is found directly as a function of strain in the context of a normalized coordinate system which provides a smooth curve between two lines representing the loading and unloading slopes, Young's modulus  $E_o$ , and the post yield modulus,  $E_2$ . Therefore, the Bauschinger region can be well reflected by the model. The relation, as summarized by Filippou et al (1983) and depicted in Figure 5.3, is given by:

$$\sigma^* = b\varepsilon^* + \frac{(1-b)\varepsilon^*}{(1+\varepsilon^{*R})^{1/R}} \quad (5.1)$$

where

$$\varepsilon^* = \frac{\varepsilon - \varepsilon_r}{\varepsilon_o - \varepsilon_r} \quad (5.2)$$

and

$$\sigma^* = \frac{\sigma - \sigma_r}{\sigma_o - \sigma_r} \quad (5.3)$$

The coordinate  $(\varepsilon_o, \sigma_o)$ , in the original coordinate system, is the intersection point of aforementioned slopes which is updated within the algorithm at each strain reversal  $(\varepsilon_r, \sigma_r)$ . The parameter  $b$  is the ratio between the elastic modulus and post-yield modulus ( $= E_2/E_o$ ). The exponent,  $R$ , controls the curvature of the transition between  $E_o$  and  $E_2$ , for each excursion within the cyclic loading. It is updated throughout cycling by the empirical relation:

$$R_i = R_o - \frac{cR1 \xi_i}{cR2 + \xi_i} \quad (5.4)$$

where  $\xi_i$  is the previous excursion ductility measurement

$$\xi_i = \frac{\varepsilon_{p,min} - \varepsilon_{o,i}}{\varepsilon_y} \quad (5.5a)$$

for the  $i$ -th excursion if in the tension direction, and

$$\xi_i = \frac{\varepsilon_{p,max} - \varepsilon_{o,i}}{\varepsilon_y} \quad (5.5a)$$

for the  $i$ -th excursion if in the compression direction, where  $\varepsilon_{p,min}$  and  $\varepsilon_{p,max}$  are previously attained largest magnitude compressive and tensile strains, respectively, and  $\varepsilon_{o,i}$  is the strain coordinate of the updated intersection point between the initial and post yield slopes. In other words, for a reversal from compression to tension loading,  $\xi_i$  is found as the difference between the new,  $i$ -th, intersection strain coordinate,  $\varepsilon_{o,i}$ , and the maximum tensile strain experienced throughout the loading history up to the current reversal. The parameters  $cR1$  and  $cR2$  are found from curve fitting of test data, as will be discussed in the upcoming sections. Figure 5.3(a) shows the overall components of the model and how  $R$  changes with each reversal in cyclic loading. The normalized coordinate system with an example reversal and asymptote intercept points are marked as C and A, respectively.

In order to capture the isotropic hardening behavior, Filippou et al. (1983) implemented a shift in the  $\sigma_{sh}$  shown in Figure 5.3(a), which is calculated and applied to the new intercept point found at each instance of strain reversal. The shift is based on the absolute maximum inelastic strain before each reversal:

$$\sigma_{sh} = \sigma_y a_1 \left( \frac{\varepsilon_{max} - a_2}{\varepsilon_y} \right) \quad (5.6)$$

where  $a_1$  and  $a_2$  are found from testing. However, an updated formulation of this rule is used in the current OpenSees implementation of *Steel02*; the origin of the new form is not well documented. It is, instead, related to the difference between maximum tension and compression deformation, converted to a ductility, at each reversal as calculated by:

$$\sigma_{sh} = \sigma_y a_{1,3} \left( \frac{\varepsilon_{max} - \varepsilon_{min}}{2a_{2,4} \varepsilon_y} \right)^{0.8} \quad (5.7)$$

where  $a_1$  and  $a_2$  are applied in tension excursions;  $a_3$  and  $a_4$  are applied in compression excursions. Again, these parameters are to be found from test data. This newer relation was found somewhat more consistent with the shift stresses measured in this research, as shown in a following section, but an improved version is later provided.

There are some deficiencies in the current implementation as it is in OpenSees. As mentioned by Filippou et al. (1983), when small reversals occur within the Bauschinger effect region a new intercept point is found which causes the reloading path to deviate from the previous loading path. This is shown in Figure 5.3(b), with the dashed line representing the actual reloading path and the solid line showing the incorrect modeled path. Dodd and Restrepo (1995) also pointed out that proper hysteretic representation requires the identification of major, minor, and simple reversals. They defined a major reversal as one which takes place after the stress has changed least  $2F_y$  from the previous reversal point, which is similar to the suggestion made by Balan and Filippou (1998). In modifying the MP model to represent rebar

inelastic buckling, Fragiadakis et al. (2007) proposed a solution of forcing the reloading path to join tangentially to the previous path when the strain reversal occurs within a selected range of the previous major reversal.

Zona and Dall'Asta (2012) pointed out that the Menegotto-Pinto model does not have a distinction between elastic and plastic deformations for calculating an exact cumulative plastic deformation,  $\eta$ . Conventionally,  $\eta$  is calculated (as shown in Section 3.4) for current AISC prequalification testing. This can easily be, and is later, implemented in the MP, as described previously.

#### **5.4.2 Representation of BRBs**

Inspection of Figure 5.3(a) and the BRB behavior studied throughout this dissertation it is clear that the MP model is well suited for reflecting the basic parts of BRB behavior discussed above. However, blindly using the model parameters found by Filippou et al. (1983), as referenced in the OpenSees formulation of *Steel02*, is not suggested. Figure 5.4 shows the basic MP versus the experiment carried out on A36 Specimen 5 with post-yield ratio,  $b$ , set to 0.02. Similarly, Figure 5.5 displays the basic model against the measured response of SS BRB Specimen 4. Clearly the hysteresis is not well represented for either due in part to the fact that the compression and tension post-yield slopes are not equal. However, the peak forces are quite well matched for A36. The SS representation is very poor, mainly part to the significant isotropic hardening of SS. The dissipated energy is also low throughout for both, and therefore a better characterization is needed.

## 5.5 Modifications for Modeling BRBs

### 5.5.1 Bauschinger Region Parameters

Little documentation is available for determining the parameters in Eqs. 5.1 through 5.7. So here a strategy was devised based on the workings of the model and the method for finding the exponent,  $R$ , given by Bruneau et al. (2011). Note that the force-deformation coordinates were used instead of stress-strain; the MP formulation is independent of this change.

Significant excursions from each test specimen in Chapter 3, as well as from recent commercial BRB testing performed by the author at UCSD, were examined individually. Each measured excursion resembled that shown in Figure 5.3(a) between the reversal point C and point B, with point A as the intercept between the two characteristic slopes. The significant excursions used from Specimen 4 are shown in Figure 5.6 with post yield slope, beginning at the circle marker and ending at the peak deformation of each excursion, found as the least squares fit with coefficient of correlation,  $R^2$ , values of nearly 0.99. The elastic unloading portion of each excursion was verified to be very nearly identical to that of the brace initial stiffness.

After each excursion was identified, each intersection,  $(\Delta_o, P_o)$ , of the unloading and post-yield lines was found by equating the two in point-slope line form and solving the simultaneous equations. Each excursion was normalized by its respective intersection coordinates and then shifted to start at the origin, putting the deformation and force in terms of Eqs. 5.2 and 5.3. Then Eq. 5.1, expressed in the form of normalized force and deformation, simplifies greatly when  $\Delta^* = 1$ , then:



$$P^* = b\Delta^* + \frac{(1-b)\Delta^*}{(1+\Delta^{*R})^{1/R}} = b + \frac{(1-b)}{2^{1/R}}$$

or

$$P^* - b = \frac{(1-b)}{2^{1/R}} \quad (5.8)$$

where  $b$  for each excursion is the ratio of the post-yield stiffness  $K_2$  and the initial stiffness of the brace,  $K$ . The left-hand side can be found directly from the measured data, leading to the solution of the value  $R$ :

$$R = \frac{\ln 2}{\ln\left(\frac{1-b}{P^* - b}\right)} \quad (5.9)$$

Parameter  $R$  varies with the excursion ductility,  $\xi$ , of Eqs. 5.5a and 5.5b, which is labor intensive to manually calculate for a nonsymmetrical deformation history. An elastic-perfectly-plastic ( $b \approx 0$ ) hysteretic behavior was used within a surrogate MP model to generate the  $\xi$  time history, for each tested brace, from which the value for each utilized excursion was retained. This was deemed a reasonable assumption due to the fact that the true  $\xi$  differs only slightly from the estimated one, since the difference in deformation lies only along the elastic slope. The degradation of  $R$  is likely not affected by this small difference. Moreover, the results for the A36 BRB were very similar to those found by Filippou et al (1983) for steel reinforcing bars, which indicates that this assumption is indeed appropriate. The SS braces were found to have a smaller initial value,  $R_o$ , and gave way to a softer response. This was expected as SS does not exhibit a well defined yield plateau, leading to an overall softer transition from elastic unloading to post-yield stiffness throughout loading. The values for each

material are listed in Table 5.1(a), and the curve fit to the SS data is shown in Figure 5.7, which correlated fairly well with the data as  $R^2 = 0.93$ . The A36 curve was slightly better matched with  $R^2 = 0.95$ .

### 5.5.2 Tension and Compression Post-Yield Stiffnesses

One of the major aspects of BRB cyclic performance is the differing tension and compression post-yield stiffnesses. In order to better characterize this attribute, the MP model was expanded with the use of two separate post yield stiffness values,  $b_T$  and  $b_C$ , corresponding to the tension and compression post-yield slopes respectively (slope and stiffness are herein used interchangeably). Further, these separate two slope values are permitted to change throughout the cyclic loading, therefore abandoning the constant single slope parameter currently used in *Steel02*.

From the previous steps both tension and compression slopes were already collected. The trends for each were investigated in terms of several independent variables. However, the tension post-yield stiffness was found to relate most directly to  $\xi$  in the same fashion as  $R$ . This degradation of the post-yield tension slope with larger ductility is intuitive as the larger excursions tend towards perfectly plastic. The measured values are shown together with the fitted curve in Figure 5.8. The  $R^2$  for this fit was approximately 0.9, and was deemed sufficient as most of the behavior is governed by  $b_{T0} - b_{T1}$  ( $= 0.003$ ) being approximately the average at the larger measured  $\xi$  values. The equation is given by:

$$b_T(\xi) = b_{T0} - \frac{b_{T1}\xi}{b_{T2} + \xi} \quad (5.10)$$

For the compression post yield stiffness, again several independent variables were examined. No clear trend was observed, with all relationships resembling that shown in shown in Figure 5.9, with  $\xi$  as the independent variable. Despite the slight variation observed, good representation was obtained (as demonstrated below) by assuming:

$$b_{Co} = 0.02 \quad (5.11)$$

Many test results (e.g. Merritt et al. 2003, Newell et al. 2006) demonstrate similar behavior, albeit from the steadily increasing deformations of the AISC Protocol. Further investigation into this behavior could provide even better modeling using this technique. But for the current study, the results were sufficiently accurate for the first set of BRB modifications to the MP model.

### 5.5.3 Isotropic Hardening Parameters

The importance of the isotropic hardening characteristic of a BRB hysteretic model has been mentioned several times, and discussed throughout this dissertation. A method was used in this study to measure the isotropic strain hardening,  $\sigma_{sh}$  described by Eqs. 5.6 and 5.7, from the separated significant excursions. Note, again, that the force-deformation coordinates were used instead of stress-strain, and therefore  $P_{sh}$  is used herein; the MP formulation is independent of this change.

The definition of isotropic hardening is the dilation of the yielding surface of a material, thereby causing the effective yield force, after initial yielding to increase in magnitude. So  $P_{sh}$  was measured as:

$$P_{sh} = P_{max} + \Delta_y K_1 - (2P_y + \Delta_{max} K_2) \quad (5.12)$$

where  $P_{max}$  and  $\Delta_{max}$  are the peak brace force and deformation, respectively,  $K_2$  is the current tension or compression post-yield slope, and  $\Delta_y$  is the brace yield deformation. This represents the difference of the force-axis intercept given by the peak brace force and the post-yield slope line, and that of a purely bilinear kinematic hardening hysteretic model. Hence, this measurement is the isotropic shift, essentially, by definition.

Here, the current formulation in *Steel02* was enhanced to reflect the decrease in isotropic strain hardening with accumulated damage observed from testing data, and as summarized by Di Sarno et al. 2002, was indeed present in the measured values of  $P_{sh}$ . This change is important for BRBs in particular, due to their ability to accumulate high levels of cyclic ductility. Accurate reflection of the isotropic hardening behavior over a large ductility life is critical.

Figure 5.10 displays the proposed isotropic hardening surfaces for both A36 and SS BRBs, given by the equation:

$$P_{sh} = P_y \left[ a_1 \left( \frac{\mu_{max} - \mu_{min}}{2} \right)^{a_2} - a_3 \eta \right] \quad (5.13)$$

where  $\eta$  is the cumulative ductility, as calculated in Eq. 3.7 and 3.8, and  $\mu_{max}$  and  $\mu_{min}$  are the maximum tension and compression ductility levels obtained prior to a given deformation reversal (as in Eq. 5.7). This formulation was kept the same as is currently implemented in OpenSees *Steel02*, but with the unnecessary  $a_{2,4}$  removed, the added exponent, and the last term added. The values found for both A36 and SS are listed in Table 5.1. Note, that for the A36 BRB the exponent,  $a_2$ , is the same value of 0.8 as in *Steel02* of OpenSees, while SS required an exponent of almost 1.0.

In order to apply this new equation in the MP framework, the addition of  $\eta$  from Eq. 3.7 and Eq. 3.8 was required to be implemented into the algorithm. This has little effect on the computational efficiency of the model. However, it does permit this and possible future expansion of the model where this measure may be needed.

With these modifications made to the MP model to better correlate with BRBs, the model is herein referred to the BRBMP model.

## **5.6 BRBMP Correlation with Pseudo-Static Test Results**

Here BRBs loaded at pseudo-static rates, typical of physical testing, should be well represented by the BRBMP model. In Figure 5.11, the recent prequalification testing response from A36 BRB Specimen 2P (Lanning et al. 2012) is provided against that of the BRBMP model. The parameters used are those for A36 BRB in Table 5.1(a) and (b). It is evident that the Bauschinger effect, peak forces, and dissipated energy are all very well represented. This provides convincing evidence of the effectiveness of the BRBMP model for A36 steel BRB.

In Figure 5.12, the test result from Specimen 4 of Section 3.5.5 is shown together with the BRBMP model simulation using the SS parameters listed in Table 5.1(a) and (b). A similar level of accuracy is demonstrated for the first known SS BRBs to be tested and simulated. Note that many of the over predicted model forces are either due to small excursions or are present only in the third test, part (d) of the figure. This third test represents an unrealistic BRB loading scenario as Tests 1 and 2 represent subsequent rare near-fault demands. Therefore, the level of cumulative

ductility during Test 3 is well beyond what a BRB would be expected or designed to be subjected to within a structure.

Note that since the MP and BRBMP models do not currently have the ability to treat minor reversals correctly, any minor reversals were removed from the model input strain time history. In testing these were caused by the bolt slip during testing. Removing these minor unloadings does not affect the representation of the primary behavior of the braces or model.

### **5.7 Incorporation of Strain Rate**

The correlations presented so far demonstrate the effectiveness of the BRBMP model for both A36 and SS BRBs with no consideration given, yet, to the strain rate. Since high strain rates were observed to affect the BRB force response in Chapter 4, it was essential to address this aspect in the BRBMP model. Figure 5.13 demonstrates a few key misrepresentations that the model makes when comparing to a dynamically tested SS BRB. Note in Test 1, Figure 5.13(a), that the two of the three major excursions are underpredicted. These are events A through C of the test results discussed in Section 4.4 and shown in Figure 4.9. Note, that the model in Figure 5.13 overpredicts peak forces in the later cycles, parts (b) and (d) of the figure or events D through E from Figure 4.9. The diminishing of the strain rate effect with increased inelastic deformation of SS is noted by Di Sarno et al. (2002). Also the decreased ultimate stress of high strain rate SS coupon tests were observed in dynamic tensile tests in Section 3.1. Therefore, not only does the instantaneous strain rate amplify the brace force, early in the loading, but a decreasing influence is also observed with

accumulated inelasticity. Both should to be reflected by the incorporation of the strain rate effect in the BRBMP model.

Krempf et al. (1979) and Chang et al. (1989) demonstrated the strain rate history independence of both SS and A36 steel, respectively. Figure 5.14(a) displays a monotonic test on A36 steel with varied loading rate by Chang et al. (1989), and Figure 5.14(b) provides additional explanation the curves. It is clear that the response is dependent only on the instantaneous strain rate, as the curve returns to the corresponding constant-rate-dependent path (dashed lines). This strain rate property lends itself to convenient scaling of the pseudo-statically calculated brace force within the BRBMP model at any given step in the strain, based on the calculated instantaneous strain rate. All that is required is the input of the time step within the algorithm and an identified strain rate relation. In fact, *Steel02* in OpenSees already has a placeholder for strain rate, however no calculations currently utilize it.

Figure 5.14(b) shows, schematically, the proposed instantaneous strain rate behavior in the denoted curve. If the hypothetical strain rate, in the figure, were to be applied to a pseudo-static response, a scaling function could provide the proper response appropriate for the instant strain rate.

To implement this scaling, a relation is needed between the pseudo-static forces (or stresses) and those conducted at various strain rates. The dynamic coupon testing discussed in Chapter 0 was perfectly suited for this relation. In Figure 5.15 an example of the selection of dynamic and pseudo-static stresses at explicit strain increments is shown. These were then compared as a ratio of dynamic-to-pseudo-static overstrength at the three tested rates, shown in Figure 5.16(a), in terms of deformation

ductility ( $= \varepsilon/\varepsilon_y$ ). Clearly the ratio is not a solely a function of rate. The surface, with ductility and ductility-rate as independent variables, is provided in Figure 5.17. This surface is represented in the BRBMP model as:

$$\frac{\sigma_{dyn}}{\sigma_{p.s.}} = SR1 \dot{\mu} + SR2 \dot{\mu}^{SR3} + SR4 \mu \quad (5.14)$$

The number of variables used to fit this surface was incrementally varied within the model, and reduced to only four with very little improvement added by incorporating the nonlinear dependence evident in the ductility dependence seen in Figure 5.17(b).

Similar test data was taken from Chang et al. (1989), as displayed in Figure 5.18. As this test data did not extend to the high ductility of the SS coupon test, the long yield plateau region from this data was ignored since most of the BRB loading of interest is well beyond this deformation level, and the influence on the overall curve was not representative of the overall observed dynamic effect on the A36 BRB. The same parameters in Eq. 5.14 were found for A36 BRB.

This amplification function was applied to both SS and A36 versions of the BRBMP model, and the overpredicted forces were then used to find the strain rate effect dependence on cumulative ductility. Figure 5.19 shows the model-to-experimental overpredicted force ratios, and the adjustment for the accumulated damage dependence of the strain rate overstrength is given by:

$$R_{\eta} = \left( \eta^{SR5} - SR6 \cdot \eta \right) \quad (5.15)$$

Note minor excursions whose force comparisons were outside of the mean correlation were ignored, and are indicated by "x" markers in the figure. Eq. 5.14 is was then



adjusted by the factor in Eq. 5.15, arriving at the final instantaneous strain rate amplification factor as applied within the BRBMP model:

$$P_{dyn} = P(1 + \omega_{dyn})R_{\eta}$$

$$P_{dyn} = P(1 + \omega_{dyn})(\eta^{SR5} - SR6 \eta) \quad (5.16)$$

### 5.8 BRBMP Correlation with Dynamic Test Results

The same comparison of Specimen 3 to BRBMP model in Figure 5.13, is revisited in Figure 5.20 with the strain rate functionality of the previous section. Part (a) of the figure shows the peak forces improved by the strain rate amplification, early in the loading (events A and B in the figure), and proper mix of amplification and reduction, later in the loading (events C and D, among others). Note that all peak forces are displayed in the comparisons of the normalized peak forces, in part (f) of the figure, and most of the error shown is from smaller excursions. The deviation in dissipated energy is attributed to this and the fact that there are some portions of the later cycles which contain hysteretic attributes which are not representative of the actual BRB behavior. This is due to measurement noise and instrumentation vibration under the violent loading of these full-scale braces. Some of this behavior is seen in part (d) of Figure 5.20.

The effectiveness of the strain rate formulation on BRBs with A36 steel cores is demonstrated in Figure 5.21, through the simulation of loading applied to Specimen 6. Both the peak forces and the dissipated energy are very well simulated.

A key test of this method for integrating strain rate to the BRBMP model is the application of a pseudo-static rate. A consistent method would produce similar results

between a simulation using no strain rate information, and those using the actual pseudo-static rate. This was investigated through the comparison of Figure 5.22 and Figure 5.23. In the former, no strain rate information is utilized in the model predictions. Very good results are obtained, with a tendency for the model to overpredict the forces. Figure 5.23 shows very similar results upon applying the actual pseudo-static loading rate to the strain-rate-enabled BRBMP model. A similar comparison was made with the SS BRB of Specimen 4. Again, excellent results showed that this strain rate method is indeed consistent despite applying straining rates over orders of magnitude in range.

Note the removal of the minor reversals from the recorded test strain time history caused by bolt slip, input to the model, as discussed in Section 5.6. The method used did not affect the strain rate, nor the peak strain values.

## **5.9 Conclusions and Future Improvements**

The comparisons provided in Figure 5.11, Figure 5.12, and Figure 5.20 through Figure 5.23 demonstrate that the new features added to the MP model provide excellent energy dissipation (i.e., hysteretic shape) and peak force replication of both A36 and SS BRBs. Note that all peak forces are displayed in the comparisons of the normalized peak forces (usually part (f) of the figures), and most of the error shown is from smaller excursions. The major excursions are visible in the hysteretic plots, and are easily identified as being very similar to those recorded from testing. Furthermore, the instantaneous strain rate has been incorporated, with good results shown in Figure 5.20 through Figure 5.23. Not only does the strain rate functionality perform well with

high strain rate, but its robustness has been demonstrated by applying pseudo-static rates with almost identical results of those with no rate considered. Therefore, the methodology employed is consistent with the actual strain rate dependence of BRBs with yielding cores of these two steel materials.

There is room for improvement upon this modified formulation of the MP model. Addition of a compression slope rule will certainly be valuable. Note the changing compression slope around 1% compressive core strain in the test response shown in Figure 5.11(b). This is a somewhat common phenomenon in some BRB designs. The current BRBMP model is unable to account for this increased slope. However, with the MP algorithm modified to treat compression and tension post-yield slopes separately, the framework is in place to implement a rule to capture this behavior. Good results are, however, still obtained from the current constant compression slope assumption. It will be desirable, as well, for this added rule to be based on the physical interaction between the core and the restrainer, since this is the mechanism behind the increasing participation of the core in compressive excursions.

The Dodd-Restrepo (Dodd and Restrepo 1995) model may be able to provide an insight into the friction behavior, as it operates under the observed condition of the tension and compression monotonic material curves are nearly identical in the true stress-strain coordinate system. Therefore, through examining and comparing the compression branches from tested specimens to the theoretical compression branch with the above assumption, a measure of the friction force may be attainable. Figure 5.24 provides a preliminary effort aimed at verifying that the basic assumption of the Dodd-Restrepo model for SS. The significant excursions of one SS specimen, from

Section 5.5, together with the monotonic tensile coupon test (tensile backbone curve shown in Figure 3.2), shows that the use of the ultimate stress coordinate,  $(\epsilon'_{su,shift}, \sigma'_{su,shift})$ , does in fact provide the correct tangent from the measured excursions. This indicates that the compression and tension backbone curves for SS do follow the same behavior as observed and demonstrated by the Dodd-Restrepo model. Future work may also adapt this model to characterize BRBs. However at minimum, the compression behavior examined in the context of the Dodd-Restrepo model, may provide the compression slope rule to be applied in the BRBMP model.

As mentioned in Section 5.4.1, and pointed out by several researchers the spurious loading path after a small reversal, shown in Figure 5.3(b), should be addressed. For the planned implementation of the BRBMP model in Opensees, this functionality will be addressed. It seems most reasonable to enforce a rule based on major and minor reversals defined by the change in stress of  $2F_y$ , as by Dodd and Restrepo (1995) and Balan and Filippou (1998)a.

Dynamic cyclic low-cycle fatigue coupon testing was not found in the literature, and will be valuable for improved characterization of the strain rate effect on SS and A36 BRBs. Further, additional monotonic dynamic tensile coupon tests can also provide better correlation of the current rate-dependent surface, or the Johnson-Cook surface. And, compressive coupon tests may also be valuable at both pseudo-static and high strain rates.

Table 5.1 Identified Menegotto-Pinto Parameters

## (a) Hysteretic Shape Parameters

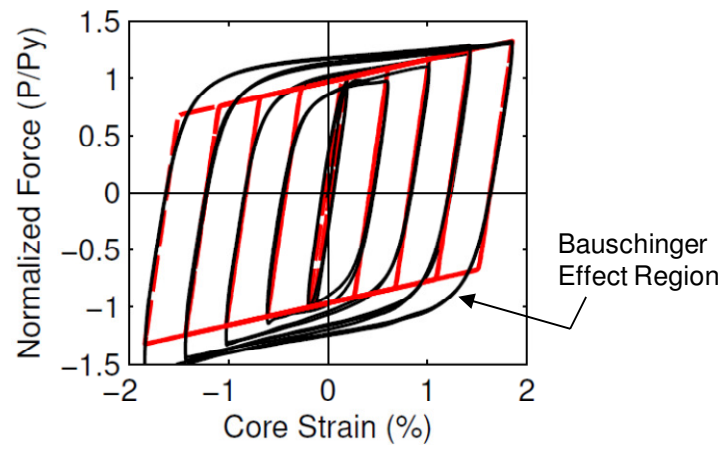
Parameter	A36 Steel BRBs	Stainless Steel BRBs	Equation No.
$R$	20	11.8	5.4
$cR1$	18.5	10.2	
$cR1$	0.15	0.5	
$b_{T0}$	0.02		5.10
$b_{T1}$	0.017		
$b_{T2}$	0.9		
$b_{C0}$	0.02		5.11

## (b) Strain Hardening Parameters

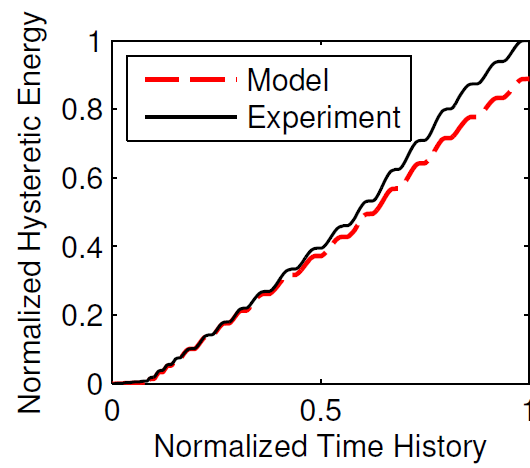
Parameter	A36 Steel BRBs	Stainless Steel BRBs	Equation No.
$a_1$	0.06	0.04	5.13
$a_2$	0.04	0.96	
$a_3$	0.008	0.0012	

## (c) Strain Rate Parameters

Parameter	A36 Steel BRBs	Stainless Steel BRBs	Equation No.
$SR1$	0.0004	0.0015	5.16
$SR2$	0.07	0.10	
$SR3$	0.09	0.15	
$SR4$	0.0014	0.0012	
$SR5$	0.02	0.03	
$SR6$	0	0.0001	



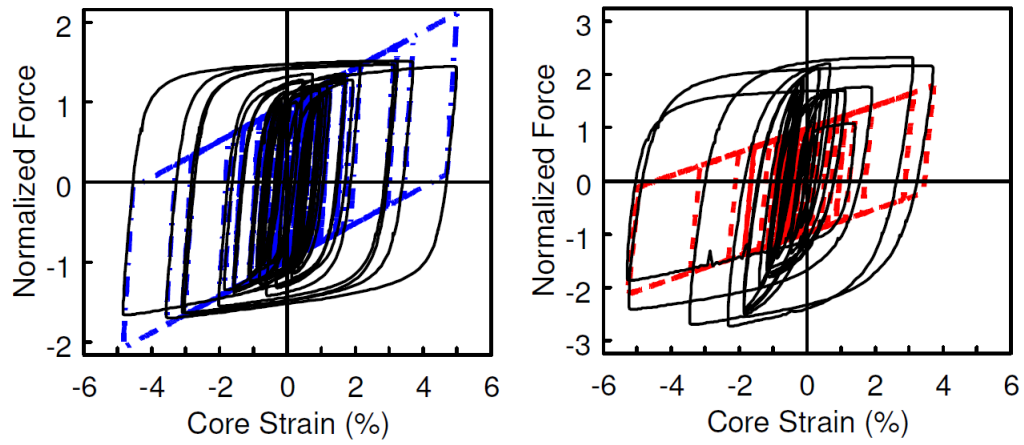
(a) Hysteretic Response



(b) Dissipated Energy

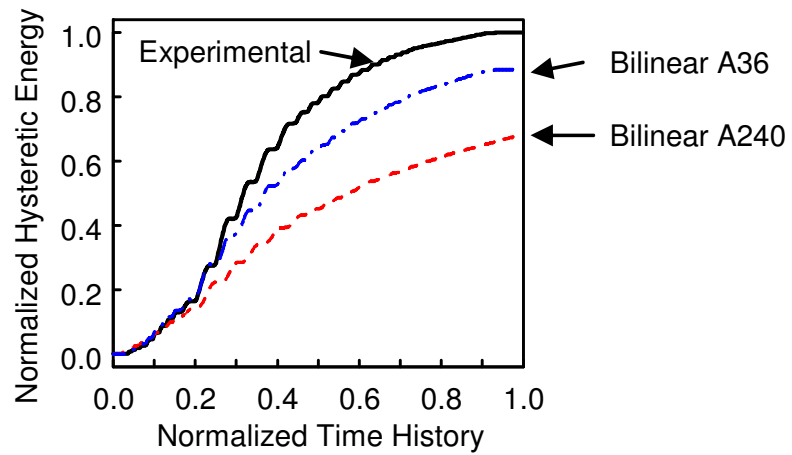
(c) Peak Normalized Forces

Figure 5.1 Correlation of Bilinear Element Prediction and Typical BRB Test



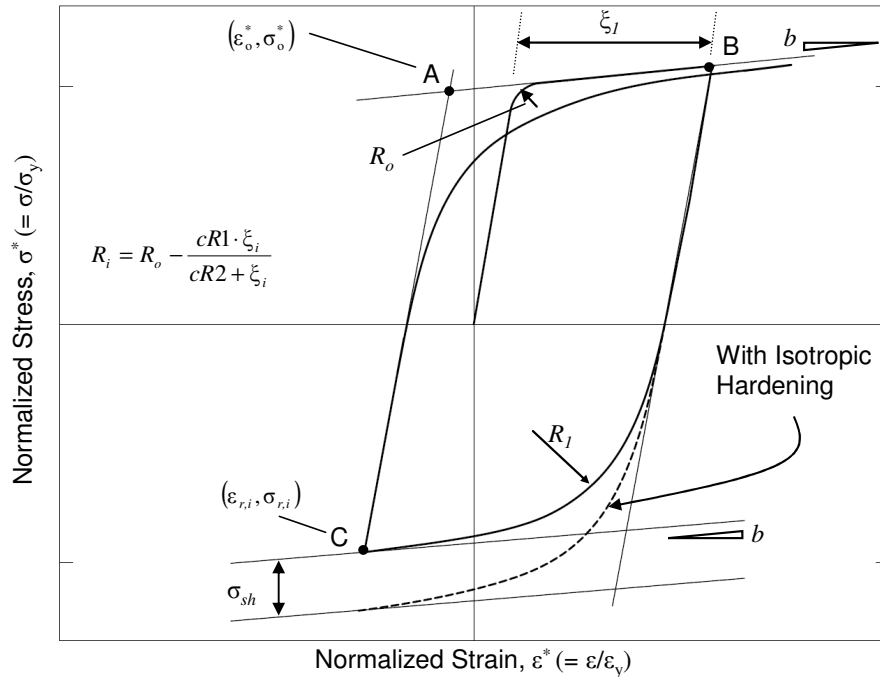
(a) A36 BRB (Specimen 5)

(b) Stainless Steel BRB (Specimen 4)

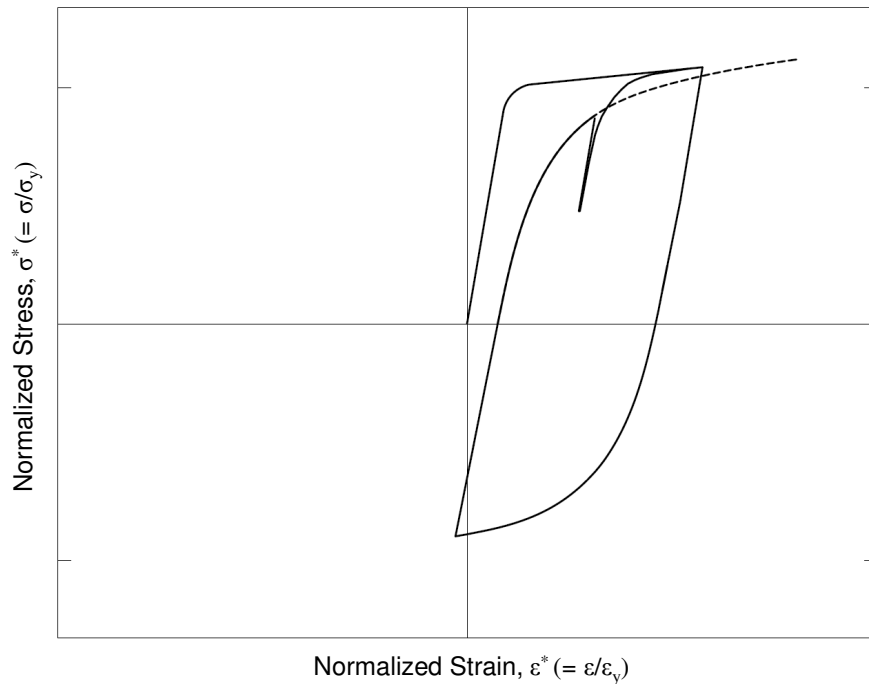


(c) Dissipated Energy

Figure 5.2 Bilinear BRB Element Simulation of Near Fault Test Results (Chapter 3)



(a) Model Components



(b) Partial Unloading and Reloading

Figure 5.3 Menegotto-Pinto Material Model  
(Adapted from Filippou et al. 1983)



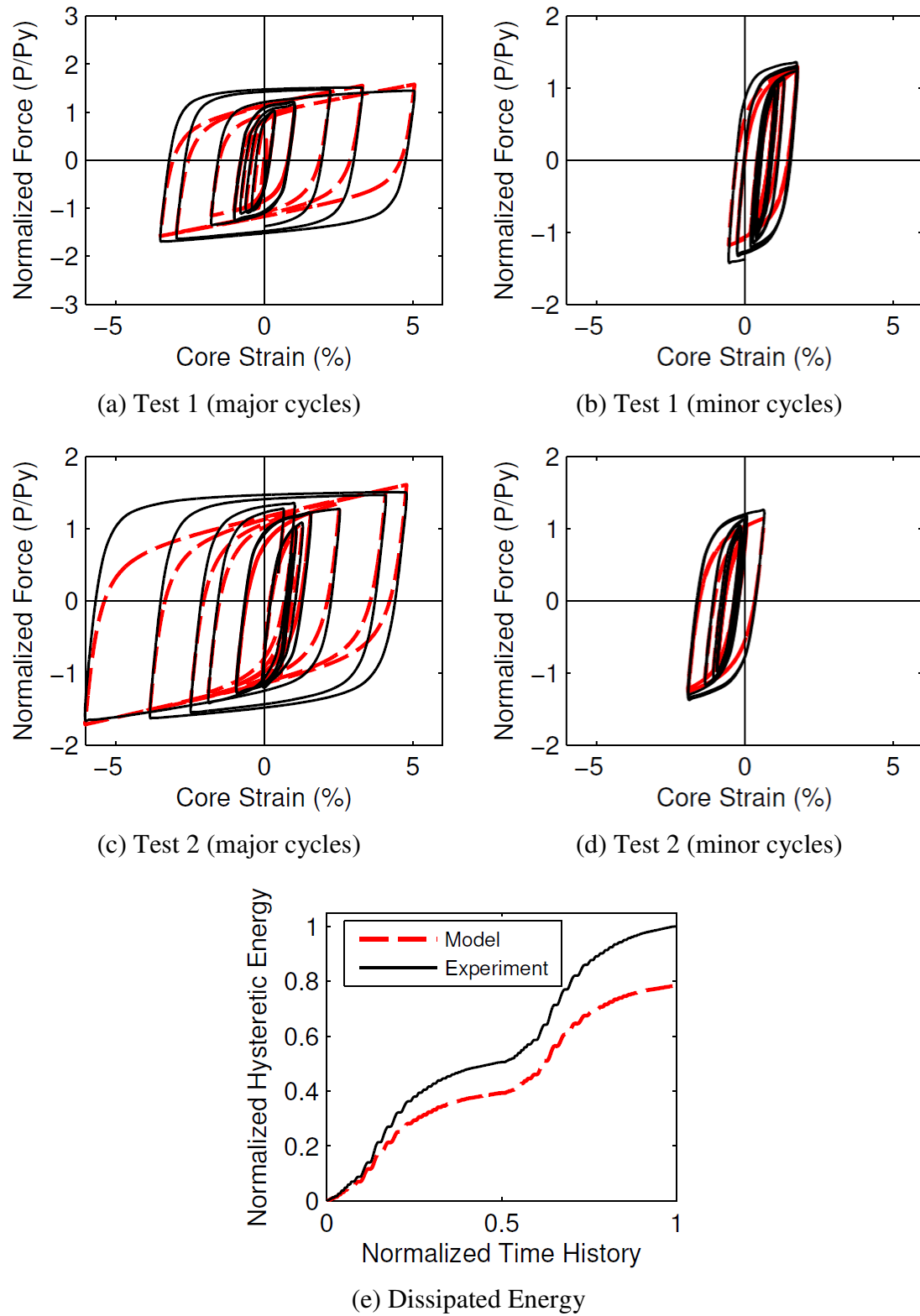


Figure 5.4 Basic Menegotto-Pinto (MP) Model versus Pseudo-Static A36 Specimen 5

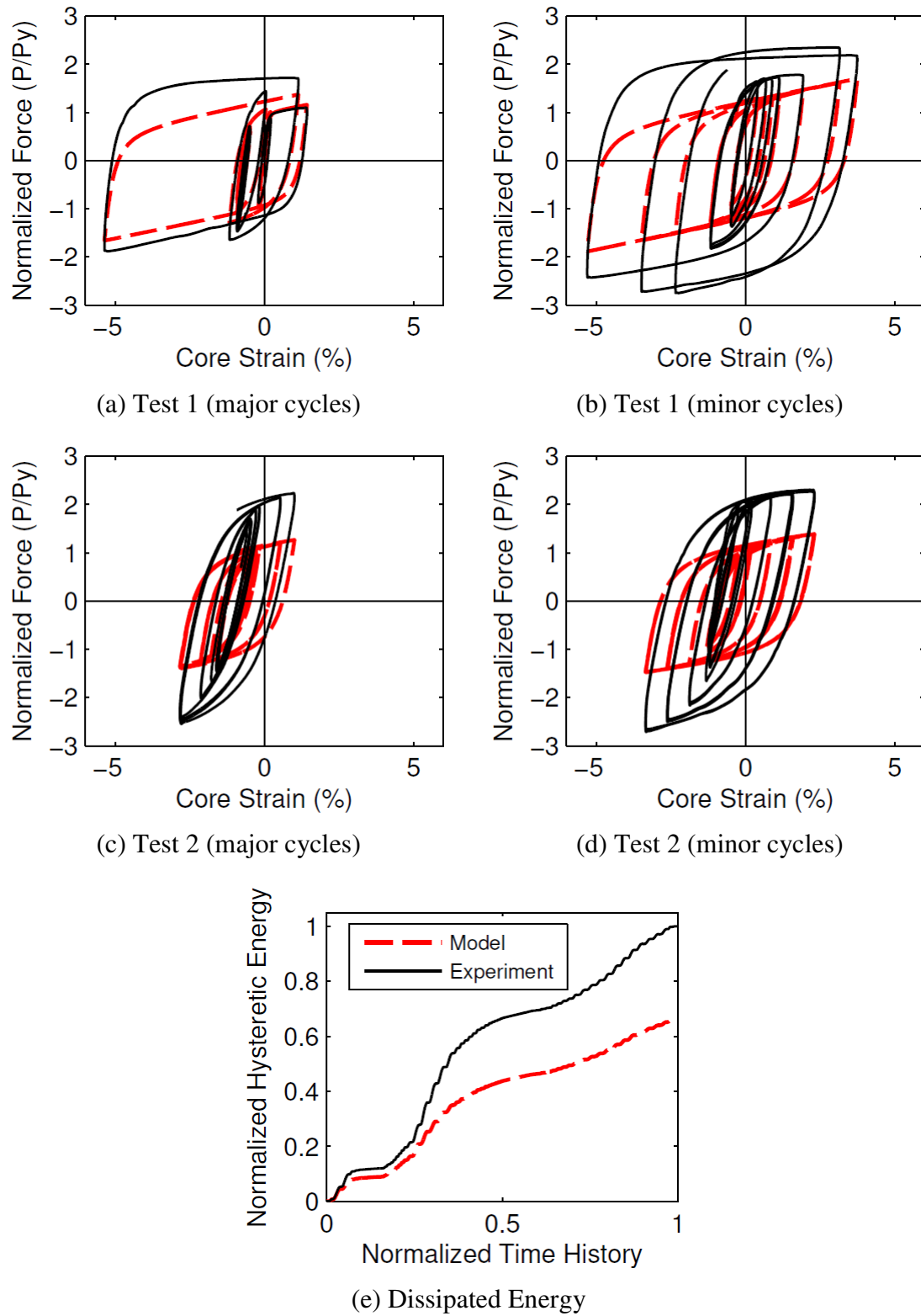


Figure 5.5 Basic MP Model versus Pseudo-Static SS Specimen 4

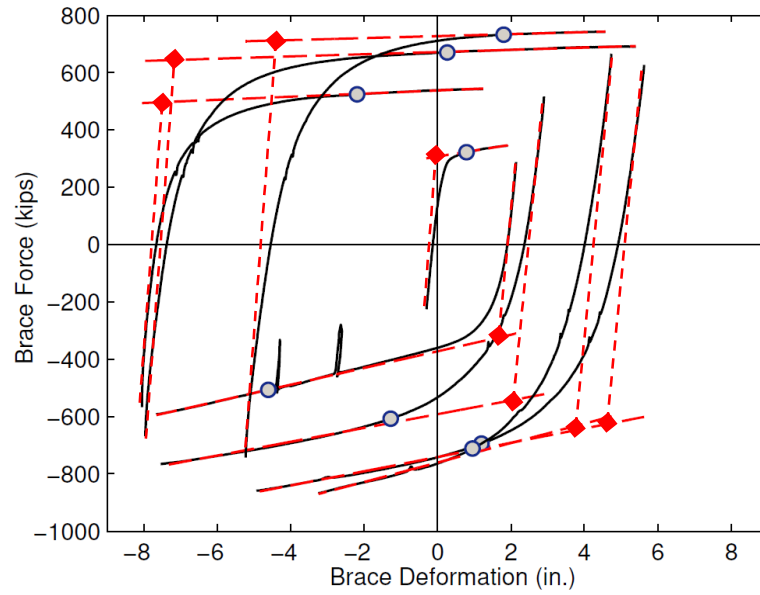


Figure 5.6 Example Significant Cycles for MP Parameter Measurement (Specimen 4)

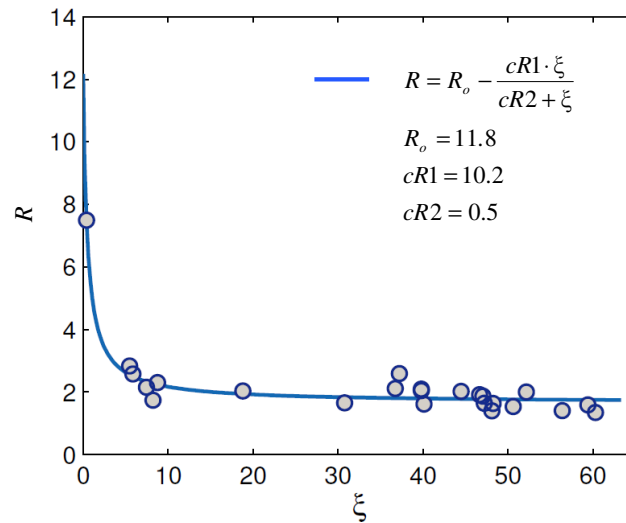


Figure 5.7 Variation of  $R$  for SS BRB

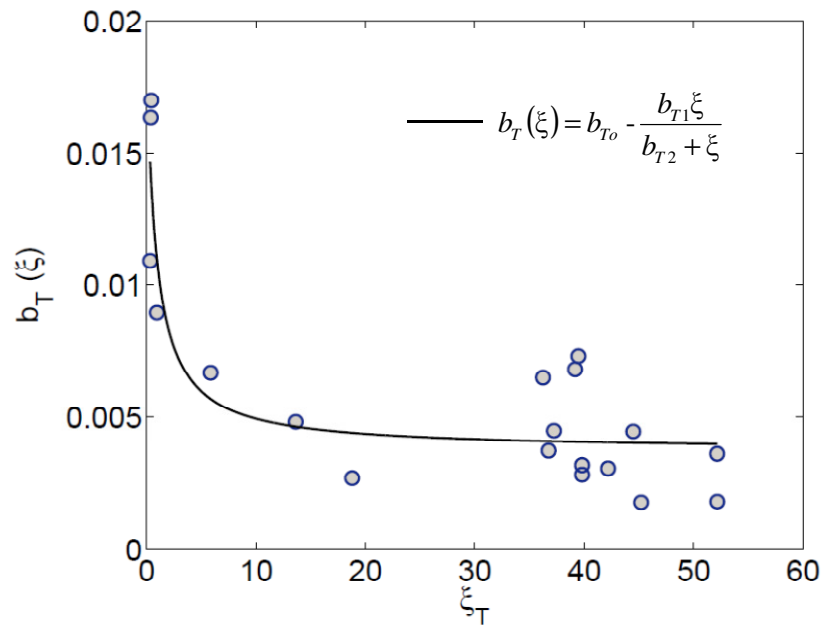


Figure 5.8 Variation of Tension Post-Yield Stiffness,  $b_T$ , (All Specimens)

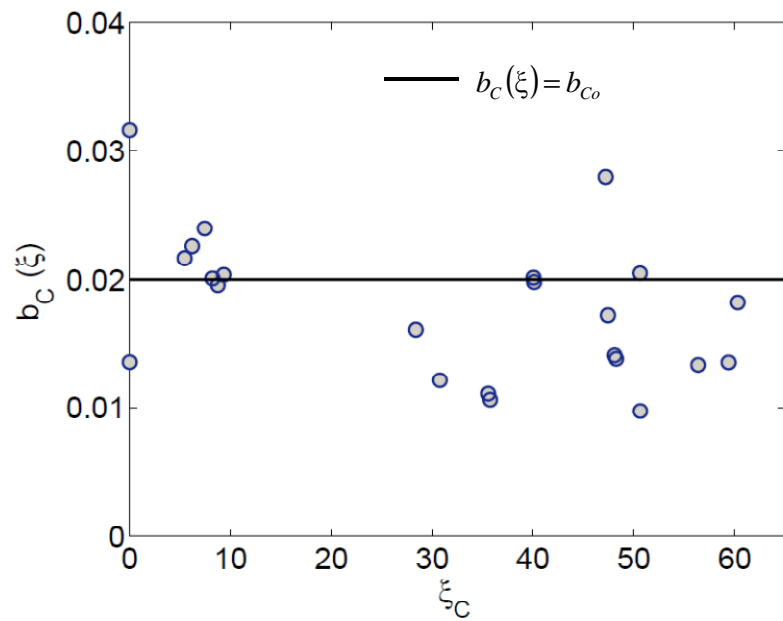
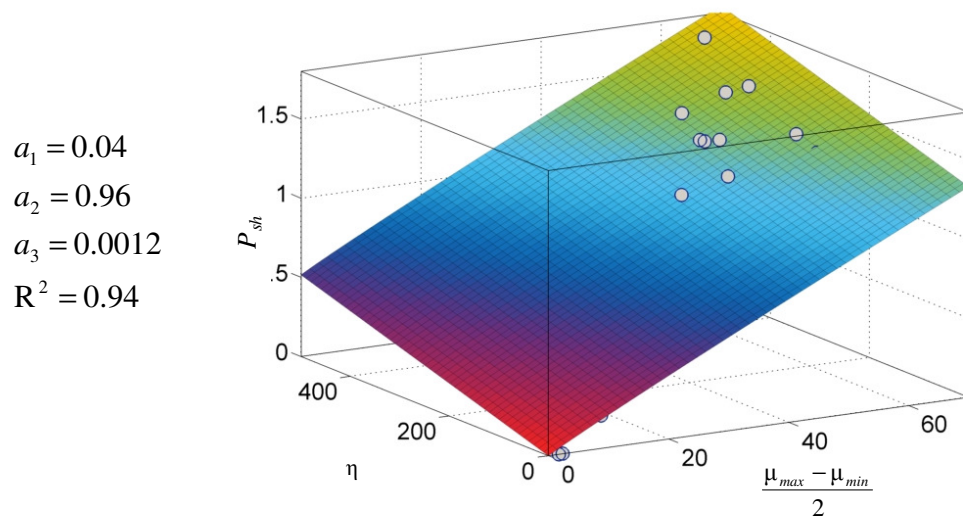
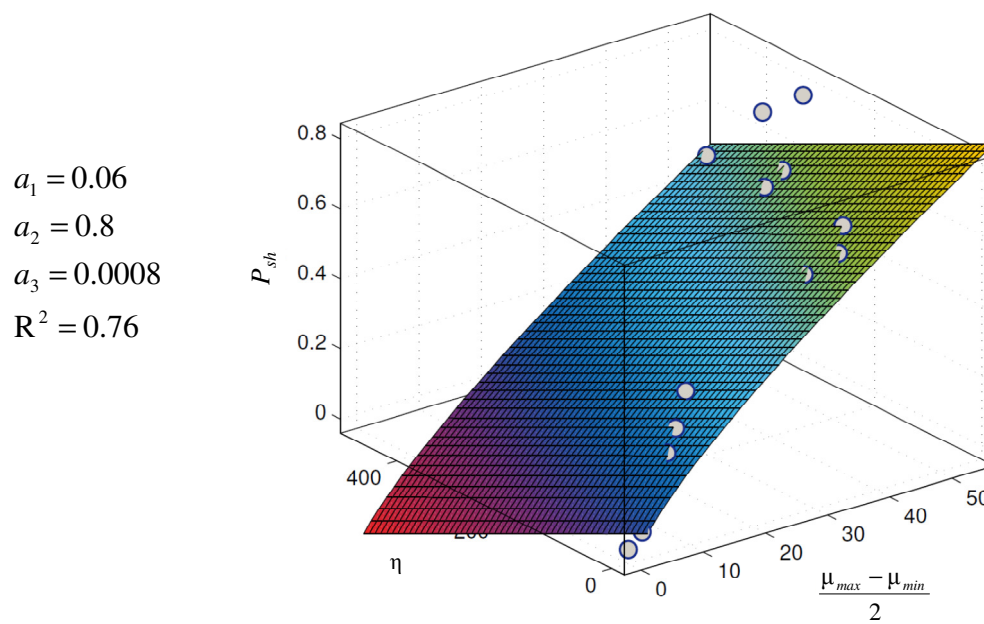


Figure 5.9 Variation of Compression Post-Yield Stiffness,  $b_C$ , (All Specimens)

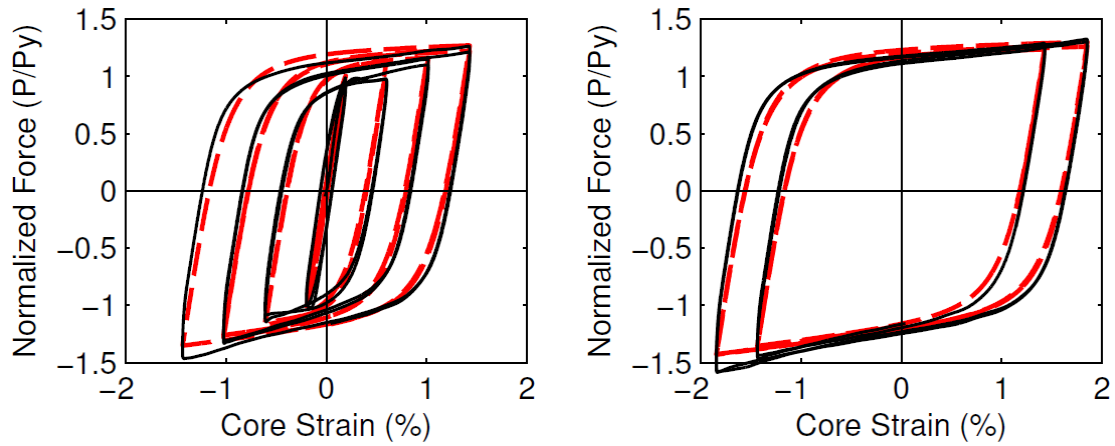


(a) Stainless Steel



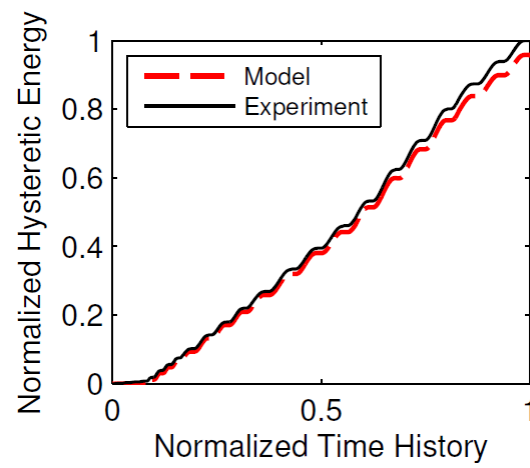
(b) A36 Steel

Figure 5.10 Isotropic Hardening,  $P_{sh}$ , Surfaces



(a) Test 1

(b) Test 1 continued



(c) Dissipated Energy

Figure 5.11 BRBMP Model versus Pseudo-Static Tested A36 Specimen 2P

(Lanning et al. 2012)

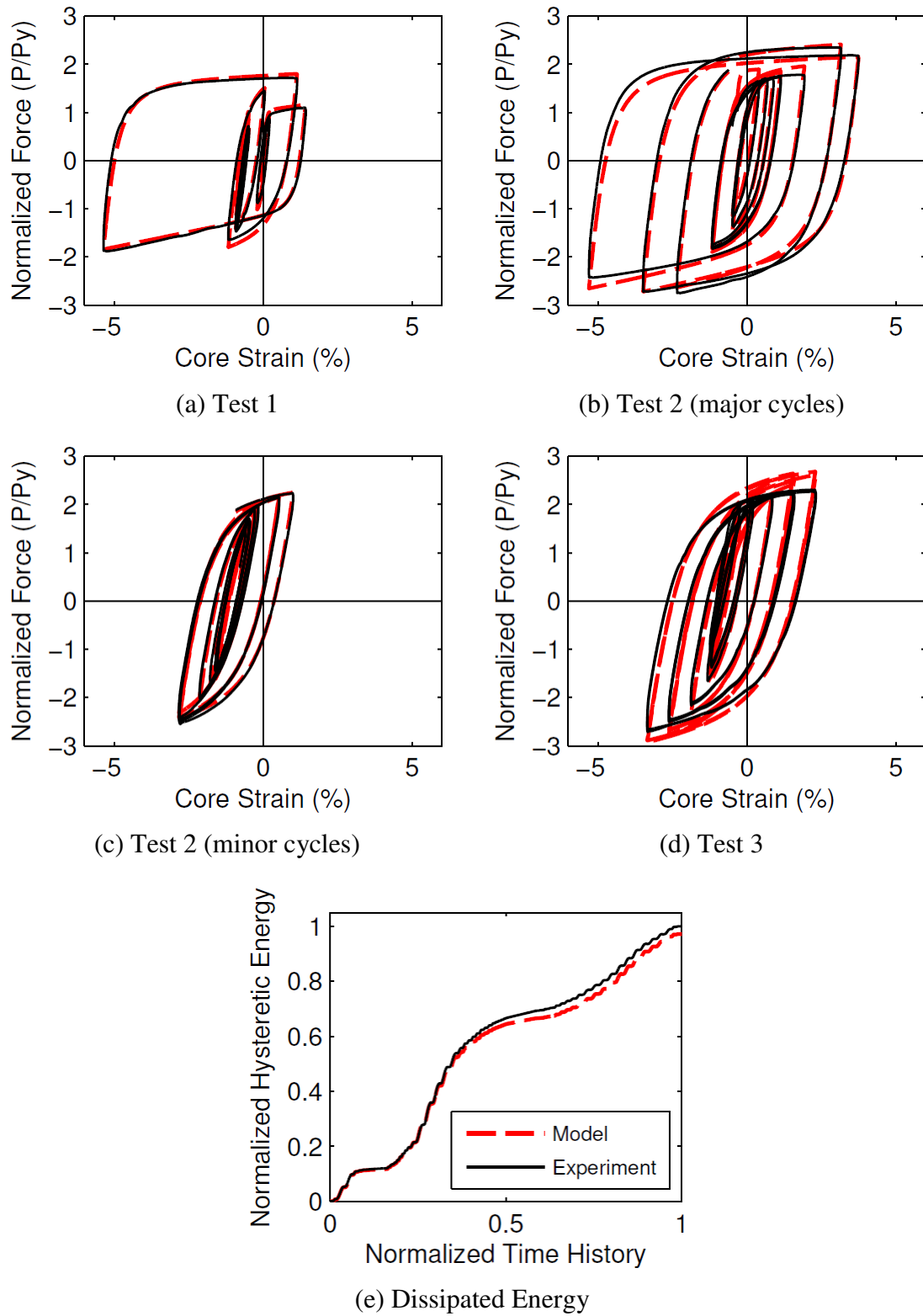


Figure 5.12 BRBMP Model versus Pseudo-Statically Tested SS Specimen 4

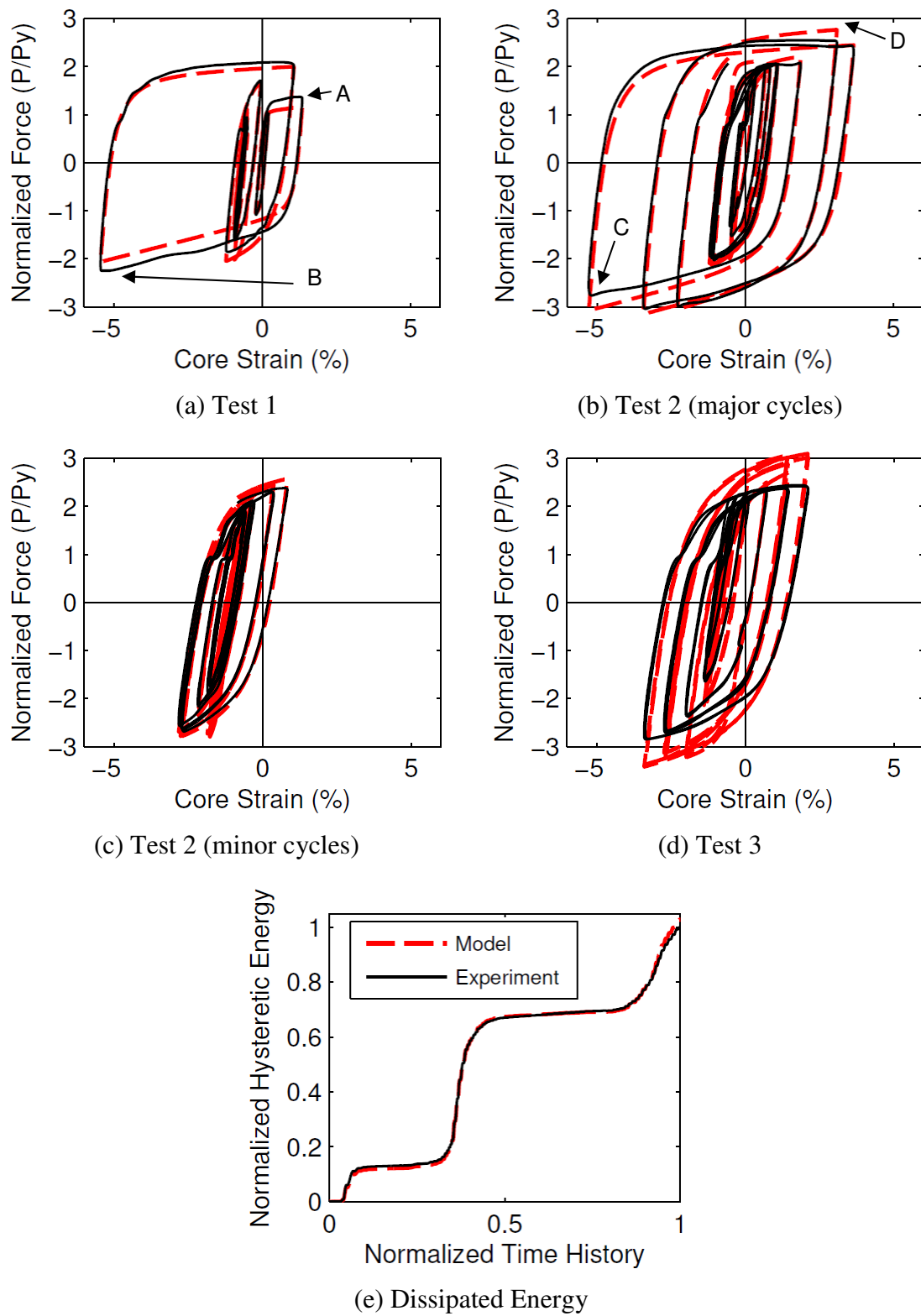


Figure 5.13 BRBMP Model versus Dynamically Tested SS Specimen 3



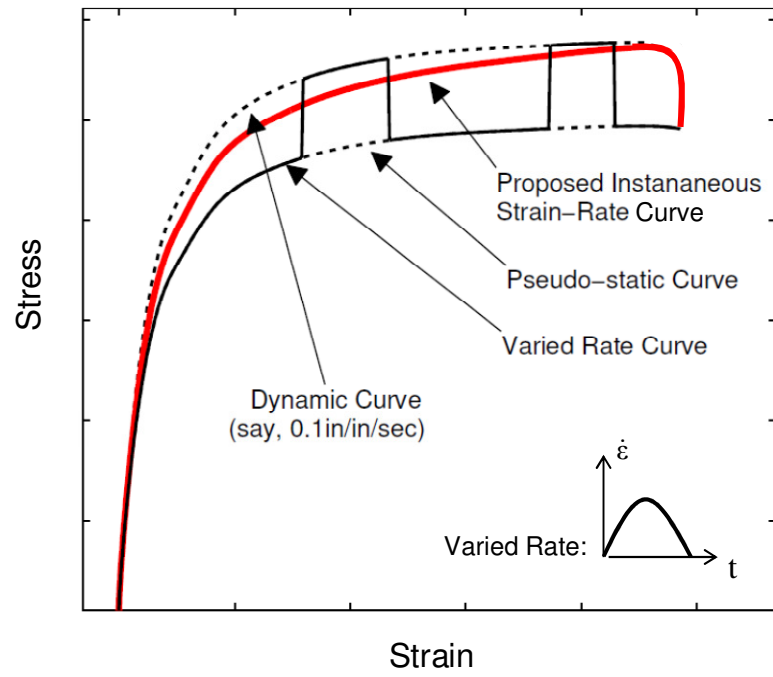


Figure 5.14 Concept for Proposed Instantaneous Strain Rate Response

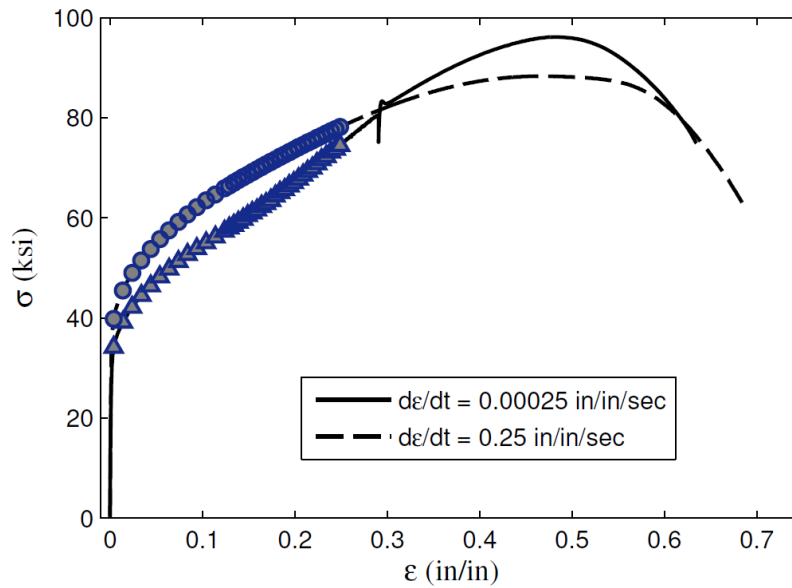


Figure 5.15 Pseudo-Static and High Strain Rate Tensile Test

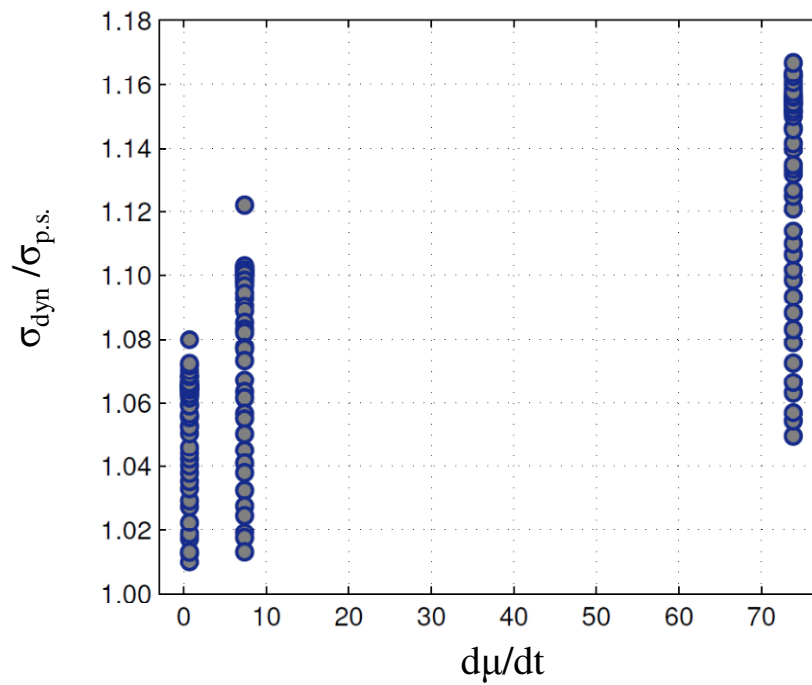
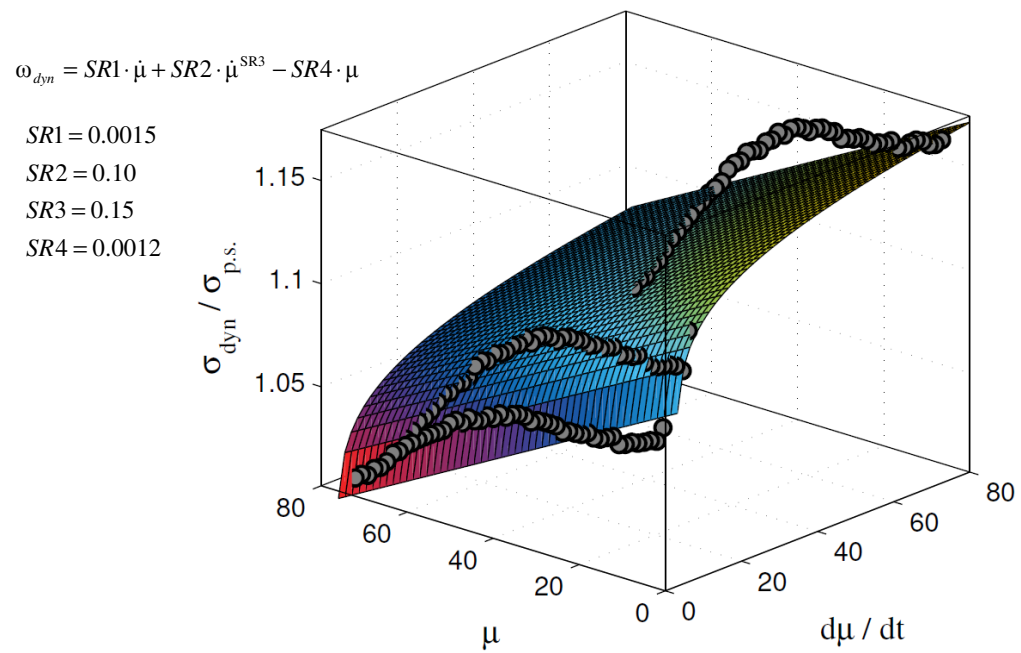
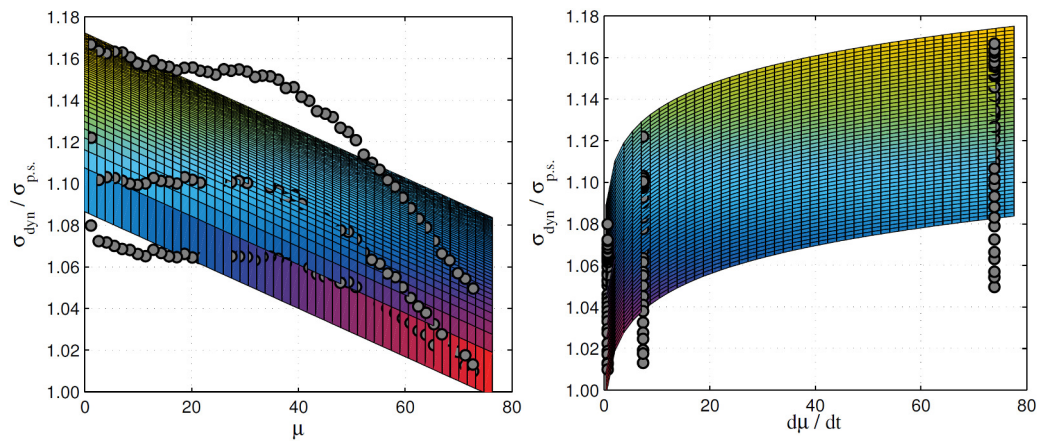


Figure 5.16 Dynamic Overstrength from SS Tensile Tests

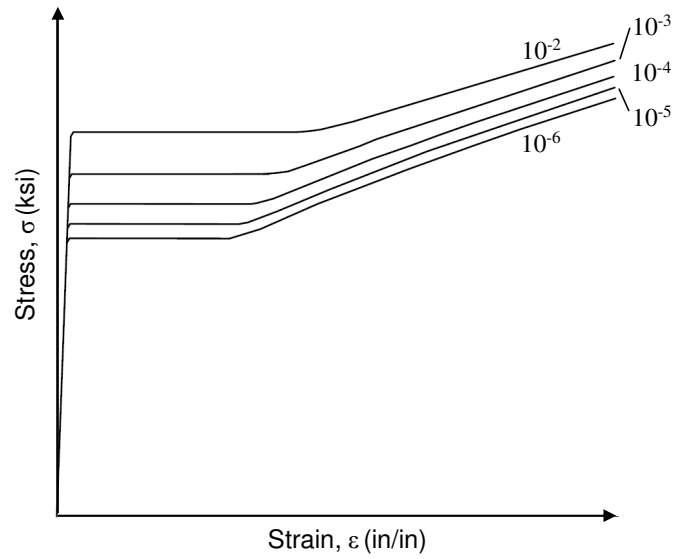


(a) Ductility and Ductility Rate Surface

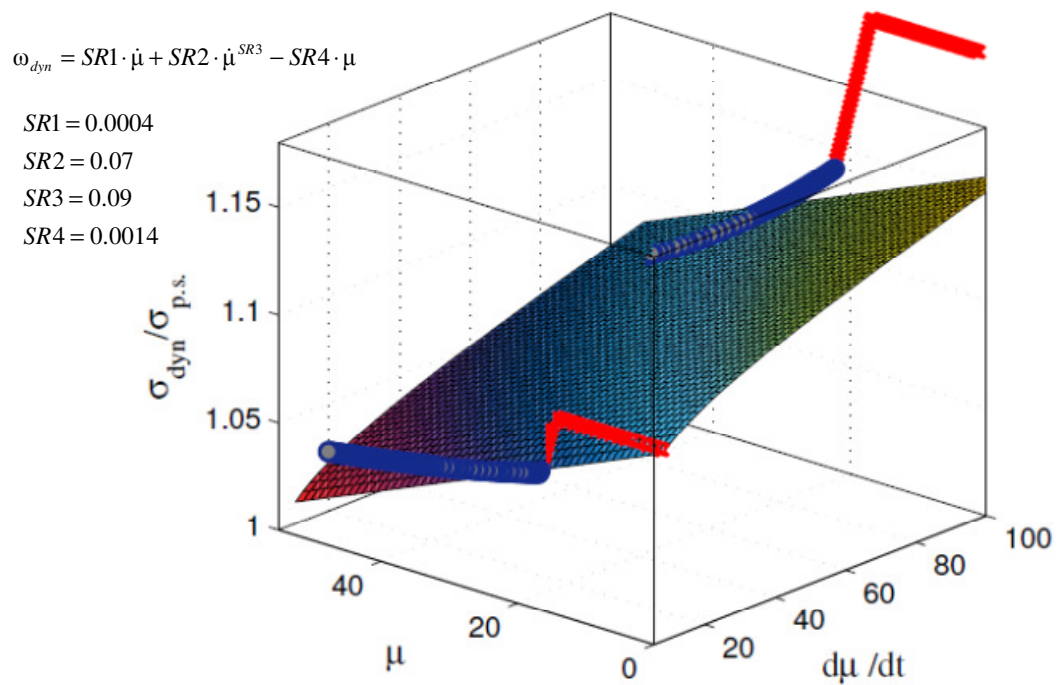


(b) Ductility-Overstrength and Ductility-Rate-Overstrength Planes

Figure 5.17 Dynamic Overstrength Surface for SS

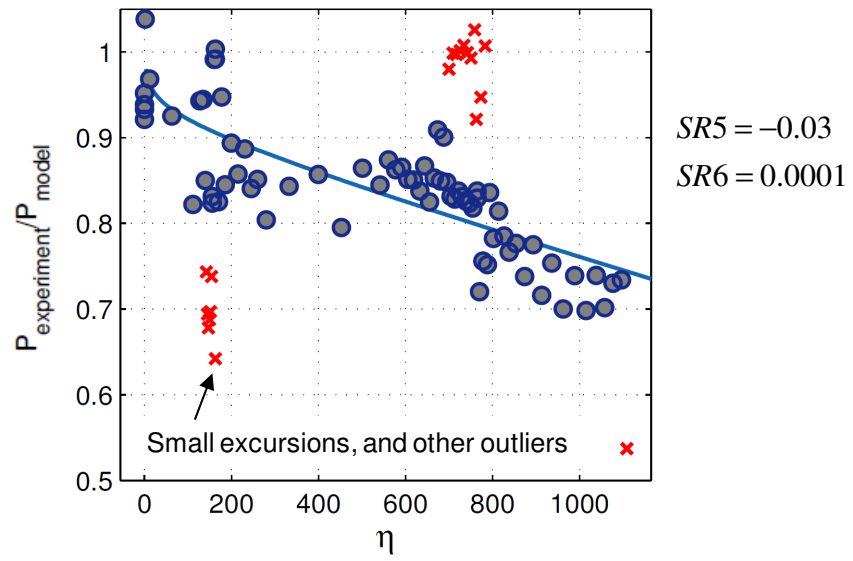


(a) Dynamic A36 Tensile Tests (Chang et al. 1989)

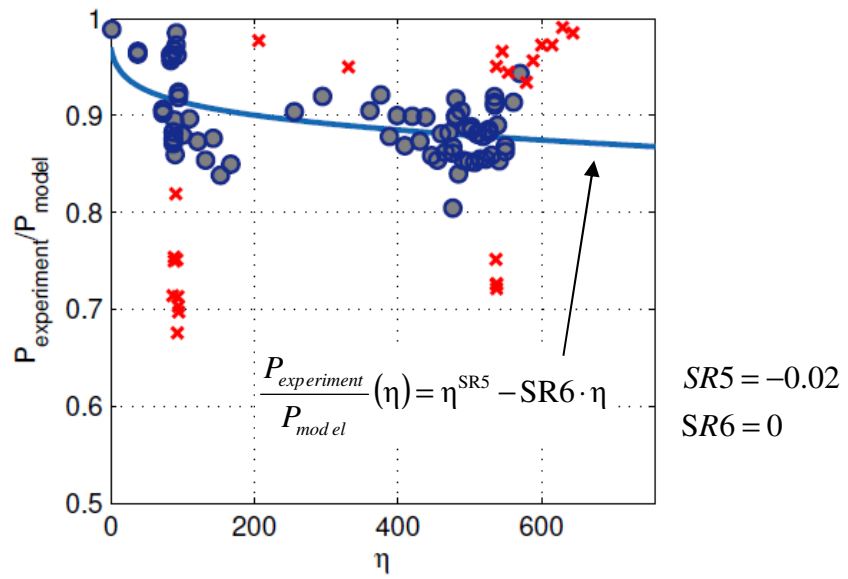


(b) Dynamic Overstrength Surface

Figure 5.18 Dynamic Overstrength from Tensile Tests for A36 Steel



(a) Stainless Steel



(b) A36 Steel

Figure 5.19 Dynamic Overstrength Cumulative Ductility Dependency

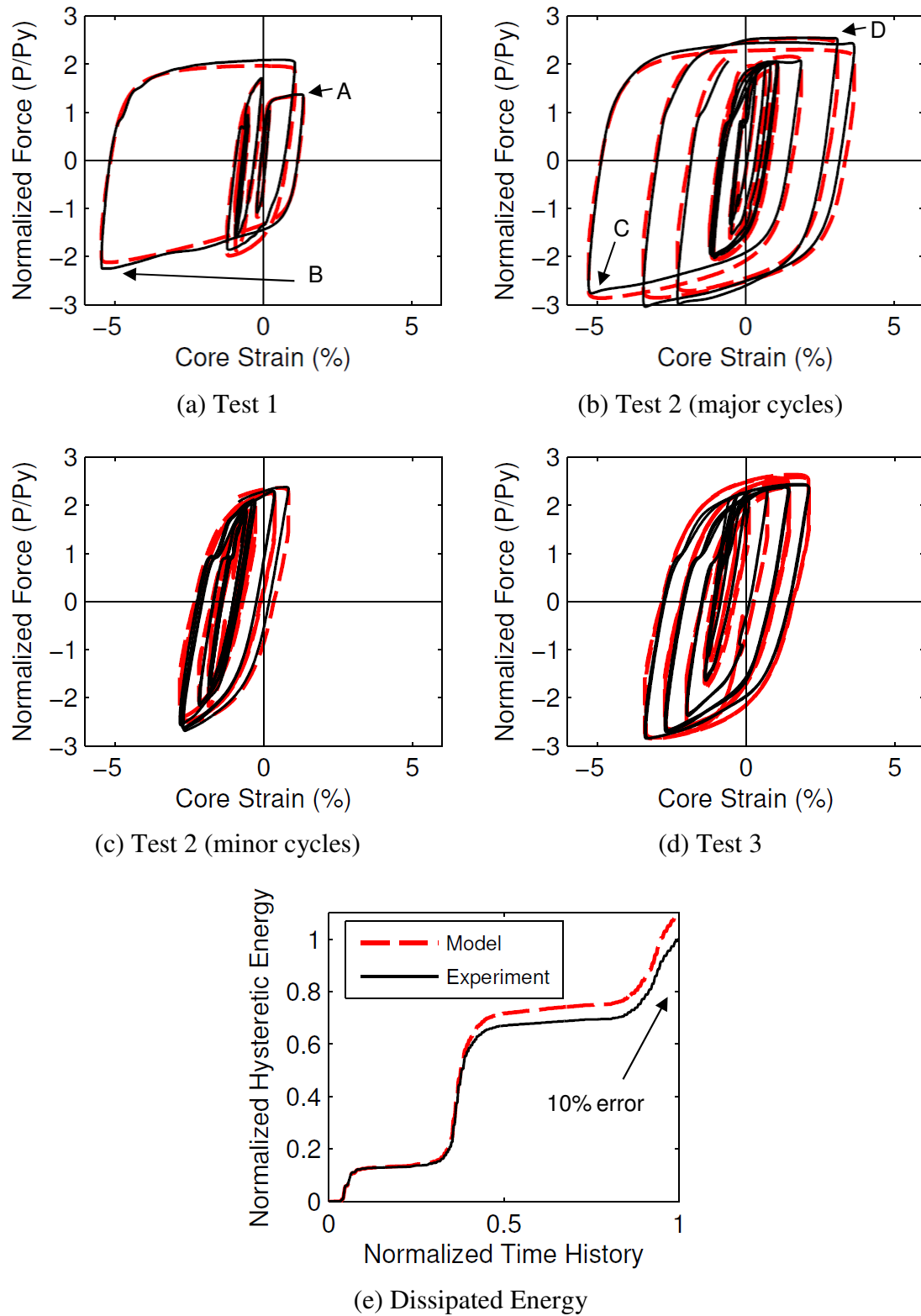
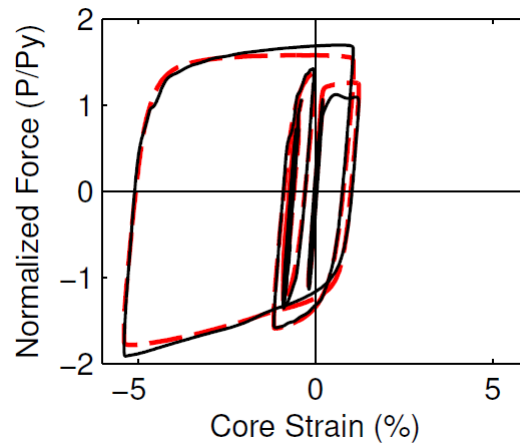
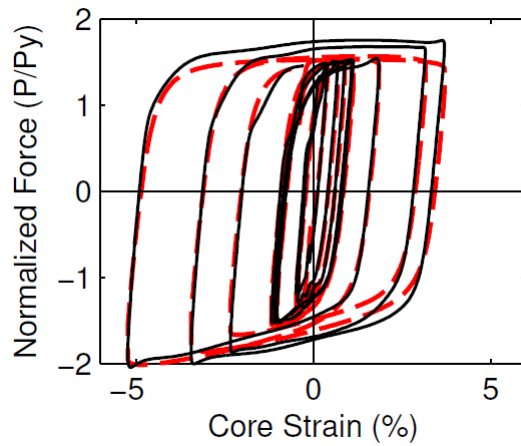


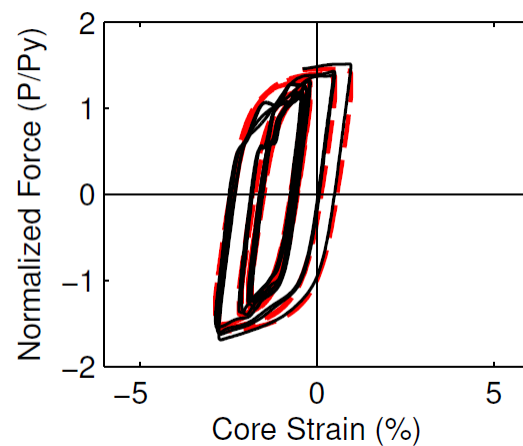
Figure 5.20 Dynamic BRBMP versus Dynamically Tested SS Specimen 3



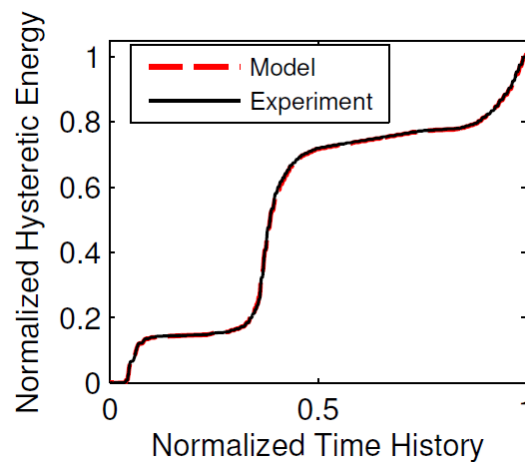
(a) Test 1



(b) Test 2 (major cycles)



(c) Test 2 (minor cycles)



(d) Dissipated Energy

Figure 5.21 Dynamic BRBMP versus Dynamically Tested A36 Specimen 6

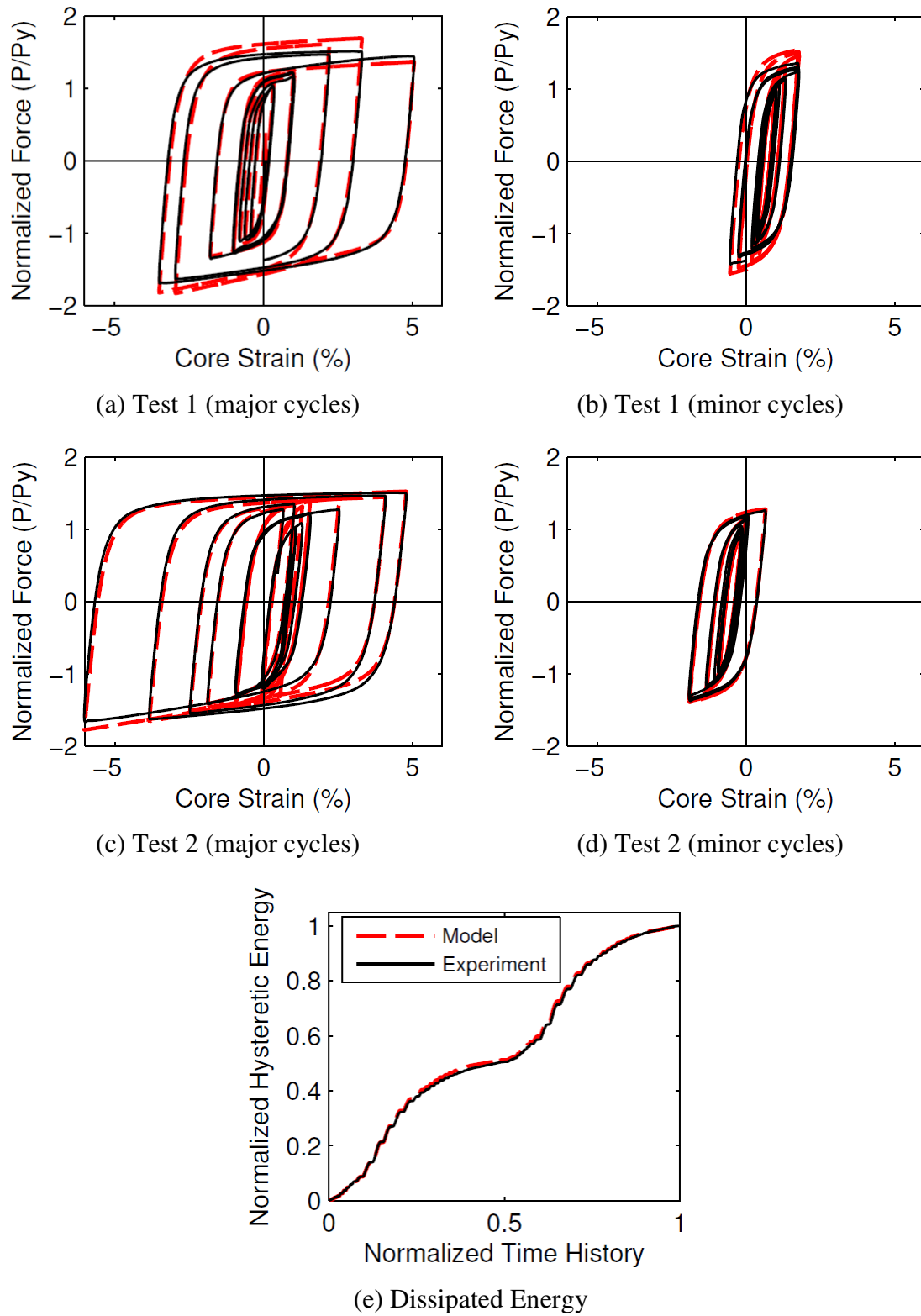


Figure 5.22 BRBMP versus Pseudo-Statically Tested A36 Specimen 5



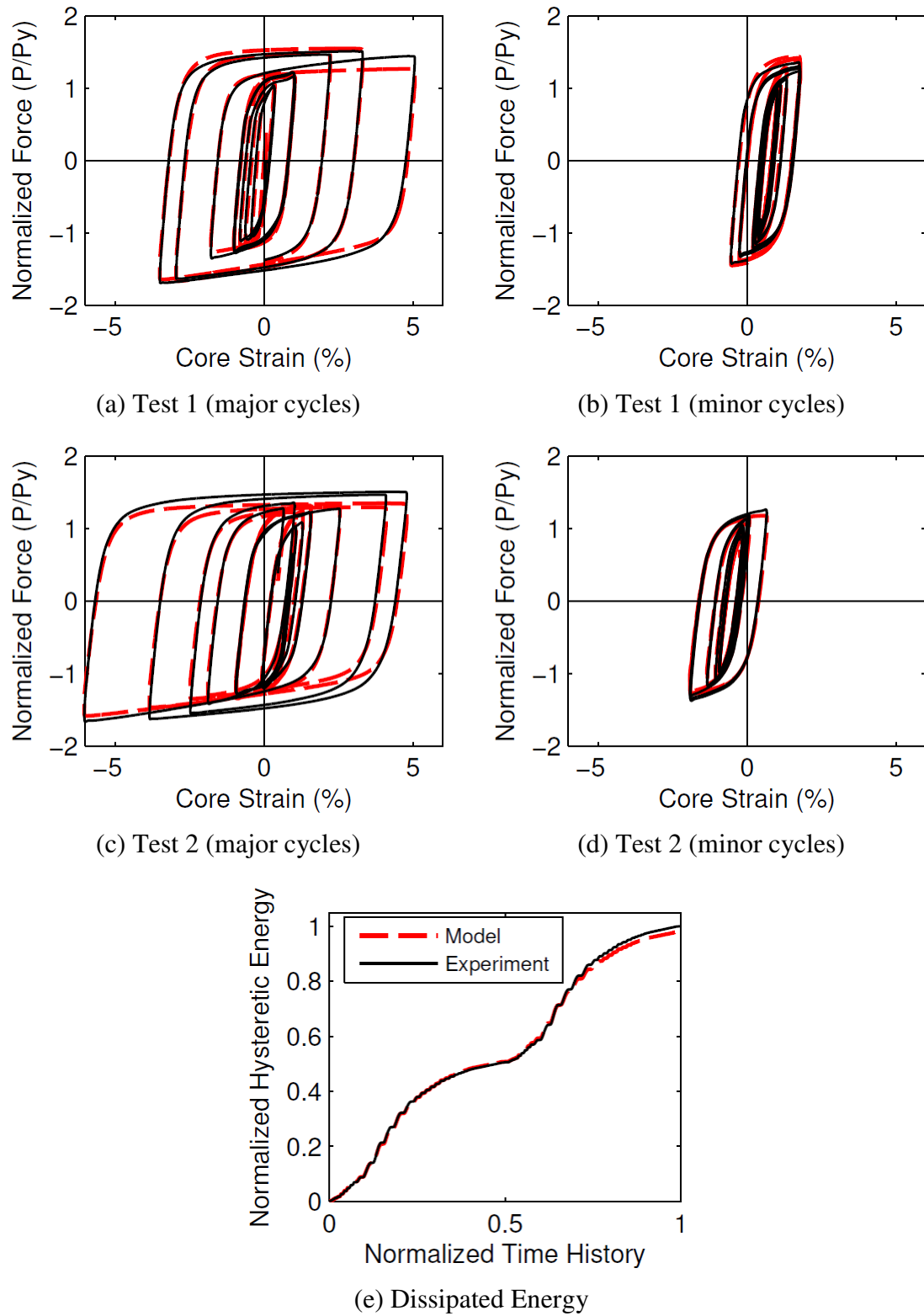
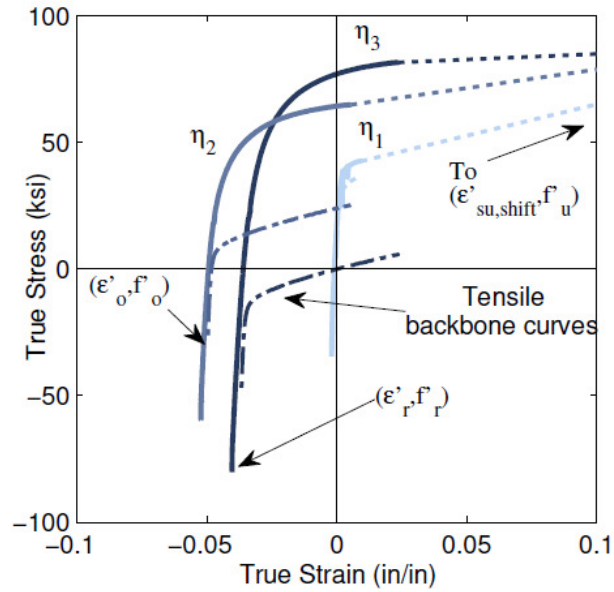
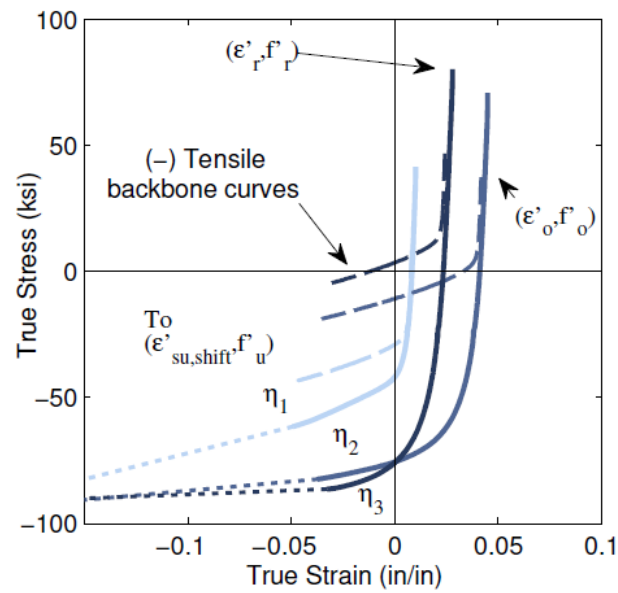


Figure 5.23 Dynamic BRBMP versus Pseudo-Statically Tested A36 Specimen 5



(a) Significant Tension Excursions



(b) Significant Tension Excursions

Figure 5.24 Dodd-Restrepo Model Backbone Curve Tangent for Stainless Steel

## 6 BRB GUSSET PLATE OUT-OF-PLANE STABILITY

### 6.1 Introduction

The observed gusset plate failure and incipient failure of Specimen 1 and Specimen 4, respectively, in Section 3.5 is further investigated. Figure 3.11 shows the failed Specimen 1 connection immediately after testing. Although these connections were designed by current conventions, BRB gusset plate connections have been observed to fail in a similar manner in several other testing programs. Here two practice-oriented methods are provided for calculating critical values needed for a simplified BRB connection stability design approach. Finite element (FE) models of several gusset plates were used to verify the accuracy of and assumptions used in these methods, resulting in excellent correlation. Finally, the frame work of the stability model is utilized to analyze the two test specimens mentioned above. The results are suggestive of possible design recommendation, however further work is needed to provide a more comprehensive solution.

### 6.2 Current Design Practice

Current gusset plate design for compression utilizes the concept of the well-known Whitmore section. This section is found by assuming the brace force is distributed through the gusset plate at a 30-degree angle from the beginning of the gusset-brace connection to the end of the brace, as shown in Figure 6.1(a), where  $b_e$  is the Whitmore width. From this area the tensile yield and rupture calculations can be

made. The flexural buckling design equations in Section E3 of AISC 360-10 *Specification for Structural Steel Buildings* are used for compressive strength:

$$P_n = F_{cr} A_g \quad (6.1)$$

and

$$F_{cr} = (0.658^{\lambda^2}) F_y \quad \text{for } \lambda \leq 1.5 \quad (6.2)$$

or

$$F_{cr} = \frac{0.877}{\lambda^2} F_y \quad \text{for } \lambda \geq 1.5 \quad (6.3)$$

where

$$\lambda = \frac{KL}{r\pi} \sqrt{\frac{F_y}{E}} \quad (6.4)$$

In the equations above, the gusset plate steel has properties of yield stress,  $F_y$ , and Young's modulus,  $E$ . The radius of gyration,  $r$ , and plate length,  $L$ , are determined as the worst case of three imaginary strip columns of plate extending from the Whitmore section. Effective length factor,  $K$ , equal to 2 has been suggested by several researchers for BRB connections, including Tsai et al. (2008), to more closely resemble the fixed-free buckled shape observed.

Also for BRBs in particular, Bruneau et al. (2011) describes the gusset equation suggested by Nakamura (2000):

$$P_e = \frac{\pi^2 EI_{trans}}{(KL_{eff})^2} \quad (6.5)$$

where  $I_{trans}$  is the out-of-plane moment of inertia of the portion of the yielding core outside of the restraining member, and  $L_{eff}$  is the unbraced connection length, taken as

the distance from the end of the restrainer to the working point of the brace, column, and beam, as shown in Figure 6.1(b). However, the values used in this method are highly subjective as it is unclear exactly where  $I_{trans}$  is measured and whether or not the length  $L_{eff}$  is an appropriate length to consider for this instability.

Despite being designed per these current conventions, this type of failure has occurred several times in testing. As discussed below, the failure mode points to system-level stability rather than gusset plate buckling alone.

### **6.3 BRBF System-Level Stability**

In studying the behavior of buckling-restrained brace frames (BRBFs) in buildings, a similar failure mode observed in Section 3.5.1 has been observed by a number of researchers. Tsai et al. (2002) reported BRB gusset failure during testing of a half-scale 1-story BRBF. Mahin et al. (2004) conducted large-scale BRBF testing with a similar failure, partially caused by cracked connecting welds, but noted that the conventional empirical-based gusset plate design methods may not be appropriate for large frame drifts and further development of design methods was needed. Tsai et al. (2008) experienced a set of gusset plate failures during pseudo-dynamic testing of a full-scale 3-story BRBF. The first and third story gusset plates failed in this manner, and exhibited clear bending lines, as shown in Figure 6.2. Testing was continued only after substantial edge stiffeners were added to the free-edges, and new BRBs were installed. The specimens tested by the author in Chapter 3, after the instability of Specimen 1, were also equipped with large edge stiffeners for the successful testing of subsequent braces (see Section 3.5.2).

Koetaka et al. (2008), Hikino et al. (2013), and Takeuchi et al. (2013) all conducted testing with the intent of verifying buckling load and out-of-plane BRB strength equations for BRBFs. Figure 6.3 shows the stability model based on the components of BRBFs, such as the torsional stiffness and weak-axis bending stiffness of the frame beam, denoted by  $K_R$  and  $K_H$ , respectively, and the segmentation of the system into connection and restrainer portions denoted in the figure by  $L_1$  and  $L_2$ , respectively. The induced failures are similar, but are a result of the frame beam flexibility, which is clear from the buckled shapes. Takeuchi focused testing efforts on the moment transfer capacity of the core and restrainer end, with respect to out-of-plane frame drifts.

These researchers have developed a sophisticated set of buckling equations which explicitly consider many details of the BRB anatomy such as the bending stiffness of both the  $L_1$  and  $L_2$  regions, as well as detailed mechanisms of the moment transfer capacity of the core at the end of the restraining member (Takeuchi et al. 2013). Including the very large elastic flexural stiffness of the connection and restrainer regions may be superfluous, and complicates the buckling equations that are perhaps too complicated for basic brace stability design purposes. Further, the fundamental goal of using BRBs in a capacity design is controlled yielding for energy dissipation and ductile behavior. Therefore, accounting for plastic moment transfer of the core is perhaps not necessary for a method aimed at ensuring brace stability. However, it certainly is an important topic in terms of maximum strength available in the presence of large out-of-plane relative deformation of the brace connections.

Hikino et al. (2013) took a more simplified approach to the problem, formulating the out-of-plane buckling equations through equilibrium conditions resulting in a more directly useable solution to the system critical load. The configuration shown at the far right of Figure 6.3, with out-of-plane deformed shape follows the assumptions that yielding only occurs in the BRB core and that deformation of the gusset plate is negligible. The latter is based on the use of the connection details in Figure 6.4(a) and (b), as specified by the Architectural Institute of Japan *Recommendations for stability design of steel structures*. The more flexible connection, in part (c) of the figure, is common of BRB gusset plates in the U.S. (Hikino et al. 2013).

#### **6.4 Simplified System Stability**

In recognition of the more applicable approach based on simple equilibrium conditions of the gusset-plate-BRB system, and the more flexible gusset plate detail commonly used in the U.S., the method presented here focuses on the behavior of the system when boundary conditions are very stiff, thereby isolating the gusset plate influence on system stability. These boundary conditions are consistent with the test data generated in this research as well as with the hypothetical implementation of BRBs on the VTB, as discussed in Chapter 2.

The configuration is presented in Figure 6.5(a) with two levels of complexity in parts (b) and (c). Similar assumptions are made here as the researchers above. A pin is assumed at the transition of extended core and restrained core. Note the figure is

only schematic, and does not appear to support this assumption. However for many BRBs this is deemed a reasonable assumption.

The rigid connection length, between the pin and the rotational spring, is represented by the ratio:

$$\alpha = \frac{L_{con}}{L_b} \quad (6.6)$$

and so,

$$L_{con} = \alpha L_b \quad (6.7)$$

where  $L_{con}$  is the length of the stiffened extended portion of the yielding core and  $L_b$  is the overall length of the brace. Using this convention the restraining member length,  $L_R$  has a length of

$$L_R = L(1 - 2\alpha) \quad (6.8)$$

The remaining components in Figure 6.5(b) are the rotational springs, denoted by  $K_\theta$ , which represent the gusset plate connection elastic rotational stiffness, or gusset rotational stiffness (GRS, or  $K_\theta$ ). Figure 6.5(c) shows an extension to this model with the pin between the restrainer and connection rigid portions replaced by a rotational stiffness representing the elastic stiffness of the portion of the yielding core extended from the restraining member. Although not used here, this model is presented for reference as it may be useful for future expansion of the method covered in the following sections.

The buckling load of the system in Figure 6.5(b) is found from equilibrium of the forces in the deformed configuration, shown in Figure 6.6. Here, and an initial imperfection angle,  $\theta_o$ , is included. From equilibrium:



$$\theta K_{\theta} = P_V(\alpha L) + P_{cr}(\alpha L)(\theta_0 + \theta)$$

where the vertical force is found from the left side of the system as

$$P_V = \frac{P_{cr} \alpha(\theta_0 + \theta)}{1 - \alpha}$$

Substituting the vertical force in the equilibrium equation and factoring  $\alpha L(P_{cr})$

$$\frac{\theta K_{\theta}}{\alpha L} = P_{cr} \left[ \frac{\alpha}{1 - \alpha} + 1 \right] (\theta_0 + \theta)$$

and simplifying to

$$P_{cr} = \frac{K_{\theta}(1 - \alpha)}{\alpha L} \left( \frac{\theta}{\theta_0 + \theta} \right)$$

where the total buckled brace angle is  $\theta_T = \theta_0 + \theta$ , giving

$$P_{cr} = \frac{K_{\theta}(1 - \alpha)}{\alpha L} \left( 1 - \frac{\theta_0}{\theta_T} \right) \quad (6.9)$$

The second term indicates the linear dependence of the initial imperfection on the buckling load. Note that without the rotation term, the ideal elastic buckling load is provided, and is found quite easily from the Figure 6.6.

With knowledge of the BRB geometry and  $K_{\theta}$ , the elastic stability can be determined from Eq. 6.9. However, the convenience of this simple relation faces several challenges. First, the value of  $K_{\theta}$  is not evident and no calculation method was found in the literature. Second, the assumed pin within the brace shifts the responsibility of system stability solely on the stiffness of the gusset, and therefore the plastic rotational capacity, of the gusset must to be included in the design procedure. No method was found in the literature for the calculation of the plastic rotational

capacity, either. These issues are addressed here, first, to provide a starting point in analyzing this system.

### **6.5 Gusset and Brace Finite Element Models**

In order to provide verification of the design-oriented hand calculation methods in the coming sections, the full geometry of several gusset plates was modeled in Abaqus software package (Simula 2011). An example of one specimen model is provided in Figure 6.7. The material property used was an elastic-perfectly plastic model to more closely correspond with the hand calculations proposed in the coming sections. The default solid element, 8-node linear brick (C3D8R), was used in the construction of the models. Typically, shell elements might be used for this application, and a few cases were considered, however the stress distributions obtained from the solid element models were more consistent with those expected.

A mesh refinement study was conducted on five of the seven connections, and the final mesh size was similar for all specimens. The brace-to-gusset fillet was provided for this sharp transition between gusset and brace geometry, due to possible numerical stress concentrations affecting this area of interest. The fillet radius was subjected to a refinement study, where the dimension was very small and provided results negligibly different than the theoretically converged value provided by Richardson extrapolation.

The similarity between the observed deformation of the failed plate and that of the model is shown in Figure 6.8.

## 6.6 Gusset Elastic Rotational Stiffness

From the previous sections, it is obvious that knowledge of the gusset plate out-of-plane elastic rotational stiffness, or gusset elastic rotational stiffness (GRS),  $K_{\theta}$ , is critical for analysis of the BRB system stability. It is not obvious, though, how to find the GRS, as the boundary conditions of this plate, the deformation experienced, and the geometry can be complicated, especially for corner gusset plates. However, no method was found in the literature for explicitly finding this property. Here, a design-oriented method is presented for calculating the GRS with good correlation to that found from FE models described above.

Takeuchi et al. (2013) make use of GRS in the testing of the BRB connection stability for out-of-plane frame drifts, however no details were provided of how the values were obtained.

### 6.6.1 GRS Calculation

An approach to calculating the GRS is presented here, assuming several gusset plate zones idealized as a summation of strip beams. The gusset plate is divided into zones designated by areas observed to undergo relatively uniform deformation during gusset plate rotation. The deformations are then used to arrive at a representative resistance to the gusset plate rotating about the end of a relatively rigid connected brace using well-known Euler beam theory stiffness coefficients. Treating the plate in this way represents a greatly simplified method over solving as a plate bending problem. A set of assumptions has been established for identifying the proper dimensions used in this calculation.

The gusset to brace configuration, the ideal zones, and details of their dimensions (used below) are provided in Figure 6.9. An example of dimensions from one test specimen are given in Figure 6.10. Zone 1 represents the portion of plate immediately at the end of the brace, as in Figure 6.11. Zone 2 represents the angled portions of the gusset along the brace connection, shown in Figure 6.12. Finally, Zone S corresponds to a transition zone between Zones 1 and 2 when the brace end is very near the boundary as shown in the figures.

Rotational stiffness is found by assuming a unit out-of-plane rotation about the end of the brace, shown in Figure 6.12 in section cut B-B. The primary deformation modes corresponding to Zones 1 and 2, observed from rotational failures of Specimen 1 and FE model simulations, are shown in Figure 6.13. Additionally, the beam strips undergo a torsional deformation, depicted in Figure 6.14. The deformation of Zone S is discussed later.

### Zone 1

The representative strips of beam in Zone 1 sum together for a rotational stiffness:

$$K_{\theta 1} = \frac{4EI_u}{L_L} W_L \quad (6.10)$$

where  $I_u$  is the moment of inertia of a unit width of plate ( $= t^3/12$ ),  $L_L$  is assumed as the average dimension between the brace end and the boundary measured perpendicular to the brace end as shown in Figure 6.11, and  $W_L$  is the width of Zone 1 (see Figure 6.11). Therefore, rotational stiffness of this zone is simply found as the moment

required to obtain a unit rotation at the end of a beam element with length  $L_L$  and width  $W_L$ .

### Zone 2

Zone 2 is analyzed by assuming the idealized strips of beam have width  $dx$  with variable length and deformation quantities. As shown in Figure 6.13, these strips of beam are assumed to deform in a shape formed by superposition of a beam with unit displacement and unit rotation, each scaled by an amount consistent with the deformed geometry of the plate with  $\theta = 1$ . The rotational stiffness is thereby given as the product of the translational force, applied at the end of each strip beam, to cause a unit rotation and the perpendicular distance from the axis of rotation (the end of the brace). The transverse force required at the end of each strip causes a translation of  $(x - x_{min})$ , and acts about a moment arm of the same distance and considering the moments at the ends of each strip beam. These deformations and forces are summarized in Figure 6.12 through Figure 6.16, and all dimensions are shown in Figure 6.9 with an example plate in Figure 6.10.

The moment required (i.e. the rotational stiffness) is found as the integral over this zone:

$$K_{\theta 2} = \int_{x_{min}}^{x_{max}} \left( \begin{array}{l} \frac{12EI_u}{l^3(x)} \delta(x)^2 + \frac{6EI_u}{l^2(x)} \delta(x) \sin(\beta) + \frac{GJ_u}{l(x)} \cos(\beta) \psi_t \\ - \frac{6EI_u}{l^2(x)} \psi_b \delta(x) - \frac{4EI_u}{l(x)} \psi_b \sin(\beta) \end{array} \right) \cos \beta dx \quad (6.11)$$

where  $x_{min}$  is the value of  $x$  where out-of-plane translation of the plate begins,  $I_u$  is the bending moment of inertia for a unit width of plate:

$$I_u = \frac{1}{3}(1)t^3 \quad (6.12)$$

where  $t$  is the thickness of the plate,

$$l(x) = x \frac{\sin \beta}{\sin \eta} \quad (6.13)$$

where  $\beta$  is the angle between the brace and the boundary,  $\eta$  is the angle between  $l(x)$  and the boundary. The out of plane deformation is defined as:

$$\delta(x) = (x - x_{min})\theta = (x - x_{min}) \quad (6.14)$$

due to the unit brace rotation and the definition of the x-axis. The strip beam end rotations are governed by:

$$\psi_b = 1 - \frac{\varphi}{90^\circ} \quad (6.15)$$

and

$$\psi_t = \frac{\varphi}{90^\circ} \quad (6.16)$$

where  $\varphi$  is the angle between  $l(x)$  and the brace as described in Figure 6.14.

## 6.6.2 Comparisons to Finite Element Model Results

The accuracy of the proposed GRS calculation method is demonstrated here. Table 6.1 contains the dimensions utilized in calculating the GRS from the equations in Section 6.6.1, and drawings of the example gussets are provided in Appendix C. Table 6.2 provides the values and errors observed between those values found from finite element analysis of each connection. Although some errors are as high as almost 100%, many are very reasonably well matched to FE model results with error around

10-30% for most cases. This method appears very promising for a use as a design-oriented stiffness calculation for use in the stability model discussed here, and for application to more sophisticated models.

The gussets demonstrating higher error typically are those in which the brace is not centered on the gusset. This may cause a shift in the angle of the axis of rotation, which is currently assumed to be perpendicular to the brace edge. Furthermore, the assumption of the domain of Zone 1 can likely be improved as the deformation around the corners of the brace is complex.

## 6.7 Gusset Plastic Moment Capacity

Since this simplified model accounts only for the GRS, there is a need to identify a limit state based on the bending moment capacity of the gusset. Similar to inelastic buckling concept used in steel design of beam-columns, certain gusset configurations will not reach the elastic buckling load ( $P_{cr}$ ) before yielding. Knowledge of the plastic moment capacity should provide an axial force limit that is likely much lower than the elastic  $P_{cr}$ .

Much of the literature on the topic of gusset plate bending or buckling is focused on plates of concentrically braced frames (CBF) and special CBF (SCBF) gusset plate design. Conventionally, a  $2t$  ( $t$  = thickness of gusset plate) straight-line clearance perpendicular to the end of the brace and the fixed boundary of the plate are required. This is provided in order to ensure the gusset plate does not interfere with the intended out-of-plane buckling of the brace. Lehman et al. (2008) proposed an elliptical clearance which resulted in more compact gusset plates aiding the low-cycle

fatigue life of the plates, while still permitting this desired deformation. Here the actual plastic moment capacity of the BRB gusset plate is investigated, since this bending line is not desired for BRB connections and cannot assumed by these simple design conventions.

Two common gusset plate bending deformation modes are considered herein as the interrupted bend line (IBL) gusset, observed from testing in Figure 6.2(a) and Figure 6.8, and the uninterrupted bend line (UBL) gusset, observed in Figure 6.2(b). These are illustrated in Figure 6.18(a) and Figure 6.17(a), respectively, with the geometry defining the plastic rotation angles shown parts (b) and part (c).

### 6.7.1 Yield Line Analysis

The plastic analysis method of yield line analysis (YLA) is used to predict the ultimate moment capacity of the gusset plate. This method is commonly used to analyze the plastic capacity of reinforced concrete slabs, but is also used for steel connections involving the bending of plates (Bruneau et al. 2011). The ultimate load capacity of a structure or a component can be found through the principle of virtual work by considering only the plastic deformations of an rigid-plastic structural idealization and the externally applied loading condition. This means the structure deforms through rotations at idealized plastic hinges and undergoes rigid rotations about these hinges. The externally applied loads work through the resulting global deformations. This is expressed as the equilibrium between internal work,  $W_I$ , and external work,  $W_E$ :

$$W_I = W_E$$



$$\sum_{i=1}^N L_i m_{pu} \theta_i = \sum_{j=1}^N P_j \Delta_j \quad (6.17)$$

where  $L_i$  is the length of the  $i$ -th yield line,  $m_{pu}$  is the plastic moment of a unit width of plate assuming a fully plastic section,  $\theta_i$  is the plastic rotation of the  $i$ -th yield line,  $P_j$  is the  $j$ -th externally applied force, and  $\Delta_j$  is the corresponding global deformation. The plastic moment of a unit width of rectangular section, or plate, is equal to:

$$m_{pu} = \frac{t^2}{4} F_y \quad (6.18)$$

where  $F_y$  is the yield stress of the material. Here, the expected yield stress ( $F_{ye} = R_y F_y$ , where  $R_y$  is set by AISC 341-10) was used to better correlate with the testing data. Each plate analyzed here (except one) had  $F_{ye} = 55$  ksi, with  $R_y = 1.1$ .

Calculating the ultimate plastic moment of the gusset plate by YLA results in an upper-bound solution, so various possible yield mechanisms need to be considered to find the true (i.e., lowest) collapse load. Here, the bending line is observed in testing and FE analysis and is, therefore, used directly to compare to that found from the FE models.

### 6.7.2 Calculation and Verification of Gusset Plate Plastic Moment Capacity

The FE models of Section 6.5 were used to verify that the assumed YLA mechanism correlated well with the actual and simulated behavior. To simplify the comparison to the FE models, a vertical force,  $P_v$ , is applied to the gusset at the end of the length  $\alpha L$ . The balance of external and internal work is calculated using the external force on the system in Figure 6.19:

$$W_E = P_v \Delta_v \quad (6.19a)$$

where  $\Delta_v = \alpha L \sin \theta$  and  $\sin \theta \approx \theta$  by assuming small angles, so that

$$W_E = P_v \alpha L \sin(\theta) \quad (6.19b)$$

and by assuming small angles,  $\sin(\theta) = \theta$ , making

$$W_E = P_v \alpha L \theta \quad (6.19c)$$

The internal work, of the IBL for example, is found as the product of the plastic rotation about the yield lines shown in Figure 6.18 and the plastic moment of the plate section, calculated as:

$$W_I = \theta M_p \quad (6.20a)$$

$$W_I = [2(\theta \csc(\beta)L + \theta \cot(\beta) \cdot L_c) + \theta L_0] m_{pu} \quad (6.20b)$$

$$W_I = [2(L_{eff} + L_{c,eff}) + L_0] \theta m_{pu} \quad (6.20c)$$

where  $L_{eff}$  and  $L_{c,eff}$  are effective lengths due to the ratio of the plastic rotation experience by yield lines  $L$  and  $L_c$ , found in Figure 6.18(b) and (c). Eq. 6.20 assumes a symmetric gusset plate, but the calculation can be extended to incorporate different geometry as well as the UBL configuration. The vertical force,  $P_{v,mp}$ , required to cause the plastic mechanism is then found by equating Eqs. (6.19) and (6.20c):

$$P_{v,mp} = \frac{[2(L_{eff} + L_{c,eff}) + L_0] m_{pu}}{\alpha L}$$

Here, the IBL gusset is assumed to be symmetric about the brace axis, but the relation is easily adapted for a nonsymmetrical case. This force was then evaluated as the plastic moment,  $M_{mp}$ , equal to the product of  $P_{v,mp}$  and  $\alpha L$ .

The calculated values are listed in Table 6.4, along with the idealized plastic moment values from the full analyses of the Abaqus FE models, shown in Figure 6.21. The good agreement between the simulation and the hand calculation suggests that the plastic mechanism is appropriate. Note the very large value of Specimen 5 due to the large stiffener plates (Figure 3.24). The calculation of  $m_{pu}$  for these portions was found by using the depth and thickness of the stiffener as  $t$  with the above formulation.

### 6.7.3 Gusset Plate Moment Capacity under Brace Axial Load

As discussed in the previous sections, the gusset plate and BRB initial imperfection have a large influence on the system buckling load. Similarly, the axial force applied with an initial imperfection will have an appreciable impact on the force required to form the full plastic yield line. From the same system as used above, with axial and vertical forces, shown in Figure 6.20, the ultimate capacity can again be found from YLA. The external work is given as:

$$W_E = P\Delta_H + P_V\Delta_V \quad (6.21)$$

where  $\Delta_H = \alpha L(1 - \cos \theta)$ ,  $\Delta_V = \alpha L \sin \theta$ , and

$$P_V = \frac{P \cdot \alpha \cdot \sin(\theta + \theta_o)}{(1 - \alpha)} \quad (6.22)$$

where  $\theta_o$  is the initial imperfection angle. Substituting into Eq. 6.22:

$$W_E = P \alpha L \left[ (1 - \cos \theta) + \frac{\alpha \sin(\theta + \theta_o)}{(1 - \alpha)} \sin \theta \right] \quad (6.23)$$

assuming small angles:

$$\cos(\theta) \approx 1 - \frac{\theta^2}{2}, \quad \sin(\theta) \approx \theta, \quad \text{and} \quad \sin(\theta + \theta_o) \approx \theta + \theta_o$$

then, Eq. 6.23 to simplifies to

$$W_E = P_{mp} \alpha L \theta \left[ \frac{\theta}{2} + \frac{\alpha}{1-\alpha} (\theta_o + \theta) \right] \quad (6.24)$$

The initial imperfection does not affect the internal plastic rotations, and therefore the internal work remains equal to Eq. 6.20. Equating the internal and external work:

$$P_{mp}(\theta_T) = \frac{[2(L_{eff} + L_{c,eff}) + L_0] m_{pu}}{\alpha L \left( \frac{\theta}{2} + \frac{\alpha}{1-\alpha} \theta_T \right)} \quad (6.25)$$

where  $\theta_T$ , is the total rotation including the initial imperfection angle.

To include the interaction between axial force and bending moment on the plastic capacity of the plate section, the forces found in Eq. 6.25 were used to reduce  $m_{pu}$  for a subsequent calculation of the ultimate force. The reduction of plastic moment capacity for a rectangular section found by considering the superposition of the axial and bending plastic stress diagram across the section is (Bruneau et al 2011):

$$\frac{m_{pu,c}}{m_{pu}} = 1 - \left( \frac{P}{P_y} \right)^2 \quad (6.26)$$

where  $P_y$  is axial yield force of the cross section, and  $P$  is the applied axial force. Here  $P_{mp}$  is used for each  $\theta_T$  value, and the revised capacity is found as:

$$P_{mp,Mpc}(\theta_T) = \frac{[2(L_{eff} + L_{c,eff}) + L_0] m_{pu,c}}{\alpha L \left( \frac{\theta}{2} + \frac{\alpha}{1-\alpha} \theta_T \right)} \quad (6.27)$$

This is the approximate ultimate load for a given gusset plate geometry providing the numerator (internal work) and the applied brace force with initial imperfection from the angle  $\theta_o$  (external work). The value found here is due to only a single iteration,

however a converged solution may provide more accurate results. In keeping with the simple formulation, only one iteration is carried out.

## 6.8 Framework Simplified Stability Model

The BRB gusset plate system stability is compared here to the testing results of failed Specimen 1 and Specimen 4 with incipient failure. Coupling the stability and strength equations derived in the previous sections could predict the system ultimate strength in terms of the simplified BRB gusset system (i.e., no core transverse or bending strength is considered, so actual ultimate load is actually higher.) This is a similar approach as that presented by Takeuchi et al. (2013), but has potential to be developed into a greatly simplified version aimed at easy implementation for the design of BRB gussets to prevent this observed failure mode for those used in both buildings and bridges.

One complicating issue for the test data correlation is the unknown amount of initial imperfection. However, after each specimen was tested to one protocol in this research program, an estimation of the initial imperfection angle for the start of the second test was attainable. Figure 6.22 shows this estimation for each brace, where the beginning of the second test is indicated at  $\theta_o = 0.004$  rad. For reference, the out-of-straight limitation for columns is 0.002 (=1/500) per Section 7.13 of the AISC Code of Standard Practice Section (AISC-COSP 2005). Therefore, this amount of rotation represents a fairly significant imperfection, which may not be realistic as the test specimens had been subjected to one near fault testing protocol.

With knowledge of the initial out-of-plane rotation, the rotational stiffness of the gusset plate, and the plastic moment capacity, a correlation is made with the test data in Figure 6.23. The test data shown is the compression force versus measured deformation angle from the displacement transducers described in Section 3.2. Together with the force-versus-rotation are the stability and strength equations, Eq 6.9 and Eq. 6.27, respectively. The intersection these two equations suggests brace-connection failure. Intersection A in Figure 6.23(a), coincides very close to the axial force at which Specimen 1 appears to become unstable. However, there are two points of intersection which corresponds with the descending branch of the YLA curve (Eq. 6.27). It is likely that the point B is the correct predicting point since the axial-moment interaction curve will converge, after several iterations, to a shape similar to the right of the peak force supplied by the single iteration curve. Furthermore, both Eq. 6.9 and Eq. 6.27 will shift to the right and down, in the figure, when the large deformations of the core and gusset plate are considered. Also affecting the correlation the realistic boundary conditions of the gusset plate are assumed, since here the gusset stiffness was found by assuming ideally fixed ends.

Somewhat similarly, Specimen 4 appears to possess much great rotational ductility, as it reached a total out-of-plane rotation of nearly 0.04 radians [see Figure 6.23(b)]. The stability-strength intersection points are much further from the peak load. Again, the point B is likely more meaningful, however the relatively large axial force reserve capacity seems to be present in this case. With the shift described above, point B is likely to show that Specimen 4 was close to failure.

Table 6.1 GRS Gusset Plate Dimensions

Gusset Name	t (in.)	$L_L$ (in.)	$W_L$ (in.)	$\beta$ (deg.)	$\phi$ (deg.)	$x_{min}$	$x_{max}$
Specimen 1 <sup>a</sup>	1.25	5.6	12.4	45	45	5.6	24.9
Specimen 4 <sup>a</sup>	1.25	3.6	8.9	45	63.4	4.4	17.8
Specimen 3P <sup>b</sup>	1.25	3.6	8.9	45	45	4.3	18.2
Specimen 5 <sup>a</sup> (stiffeners)	1.25	5.7	11.5	44	33	4.4	23.9
	14.5		0.38				
Tsai 1 <sup>c</sup>	0.75	11.1	6.5	36.8	53.2	4.3	10.8
Tsai 3-1 <sup>d</sup> (Zone 2.1) (Zone 2.2)	0.63	7.2	6.9	47.5	42.5	3.9	18.1
				42	48	10.4	24.6
Tsai 3-3 <sup>d</sup> (Zone 2.1) (Zone 2.2)	0.63	4.4	7	47.5	26.5	11	20.1
				41.9	31.1	8.75	17.9
Takeuchi <sup>e</sup>	0.47	4	7.1	N/A			

<sup>a</sup> Chapter 3<sup>b</sup> Lanning et al. (2012)<sup>c</sup> Tsai et al. (2002)<sup>d</sup> Tsai et al. (2008)<sup>e</sup> Takeuchi et al. (2013)

Table 6.2 Accuracy of GRS Calculation

Gusset Name	$K_{\theta}$ (kip-in/rad)				Error (%)
	Zone 1	Zone 2**	Total Predicted	FE Model	
Specimen 1 <sup>a</sup> (stiffeners)	41,806	36,803	123,336	141,870	13.1
		3,962			
Specimen 4 <sup>a†</sup>	46,676	44,112	134,900	130,080	3.7
Specimen 3P <sup>b</sup>	46,886	44,207	135,299	119,890	12.9
Specimen 5 <sup>a</sup> (stiffeners)	38,226	58,669	538,223	462,290	16.4
		191,330			
Tsai 1 <sup>c</sup>	6,045	6,746	12,791	11,550	10.7
Tsai 3-1 <sup>d</sup> (Zone 2.1) (Zone 2.2)	2,333	5,063	9,588	4,880	96.6
		89			
Tsai 3-3 <sup>d</sup> (Zone 2.1) (Zone 2.2)	1,527	N/A	2,014	1461	37.8
		523			
Takeuchi <sup>c</sup> (Zone 2.1) (Zone 2.2)	1,743	N/A	1,743	1420	22.9
		N/A			

\*See Table 6.1 footnote

\*\*When symmetric about the brace axis, Zone 2 is counted twice.

†Edge stiffeners were neglected



Table 6.3 Gusset Plate Dimensions for YLA

Gusset Name	Type	$L_o$ (in.)	$L$ (in.)	$L_c$ (in.)	$\beta$ (deg.)	$t$ (in.)	$F_{ye}$ (ksi)	$m_{pu}$ (kip-in.)
Specimen 1 <sup>a</sup>	IBL	26.8**	12.4	27.8	45	1.25	55	21.5
Specimen 4 <sup>a</sup>	IBL	8.9	17.8	17.7	45	1.25	55	21.5
Specimen 3P <sup>b</sup>	IBL	8.9	13.7	19.3	45	1.25	55	21.5
Specimen 5 <sup>a</sup>	IBL	8.9	14.4	19.5	45	1.25	55	21.5
Specimen 5 <sup>a</sup> Stiffeners	IBL	0.375	N/A			20	55	5500
Tsai 1 <sup>c</sup>	IBL	6.5	11.4	10.8	36.8	0.75	55	7.7
Tsai 3-1 <sup>d</sup> ( $L_1$ )	IBL	7	14.8	13.2	87	0.63	55	5.5
Tsai 3-1 <sup>d</sup> ( $L_2$ )			10.2		64.6			
Tsai 3-3 <sup>d</sup>	UBL	17	N/A	N/A	N/A	0.63	55	5.5
Takeuchi <sup>e</sup>	UBL	9.9	N/A	N/A	N/A	0.47	46	2.6

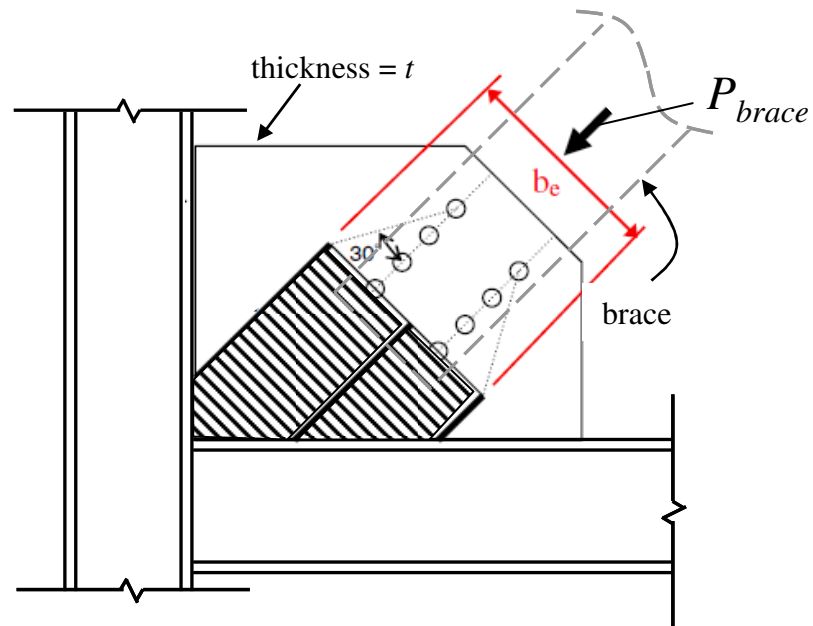
\*See Table 6.1 footnote

\*\*Special case, see bend line in Figure 6.21

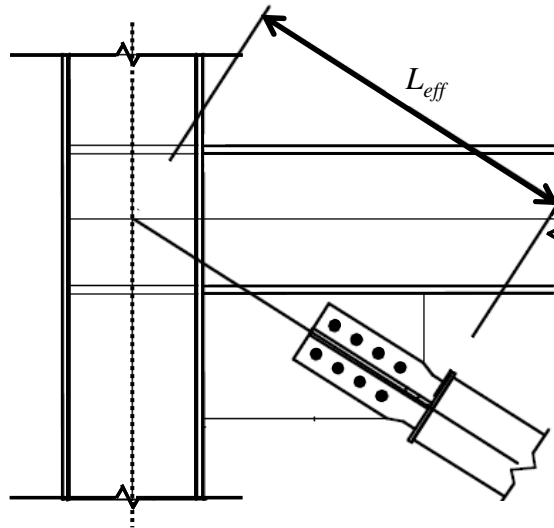
Table 6.4 Accuracy of Gusset YLA

Gusset Name	$M_{mp}$ (kip-in)		Error (%)
	Section 6.7	FE Model	
Specimen 1 <sup>a</sup>	2,196	2,143	2.5
Specimen 4 <sup>a</sup>	2,033	2,434	16.5
Specimen 3P <sup>a</sup>	1,854	2,263	18.1
Specimen 5 <sup>a</sup>	6,384	6,156	3.7
Tsai 1 <sup>c</sup>	307	308	0.3
Tsai 3-1 <sup>d</sup>	215	240	10.7
Tsai 3-3 <sup>d</sup>	93	100	7
Takeuchi <sup>e</sup>	25	28	10.7

\*See Table 6.1 footnote



(a) Strip Column Concept for Thornton Method



(b) Nakamura Unbraced Connection Length  
(Adapted from Bruneau et al. 2011)

Figure 6.1 Aspects of Current BRB Gusset Plate Design Procedures



(a) First Story



(b) Third Story

Figure 6.2 Observed BRB Gusset Failures in BRBF Testing  
Tsai et al. (2008)

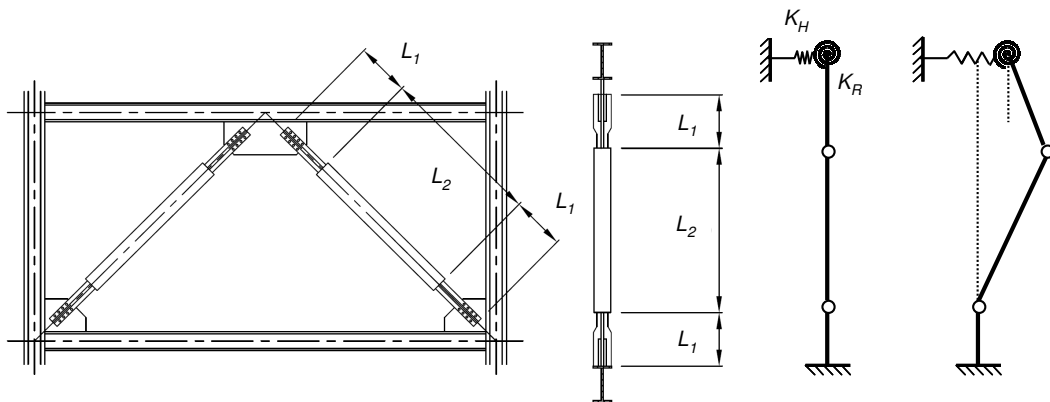
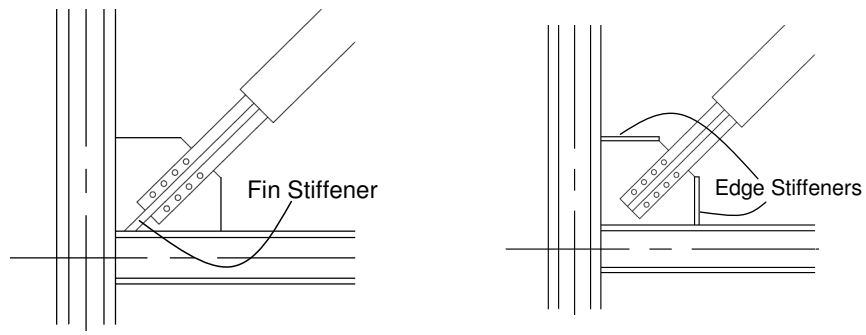
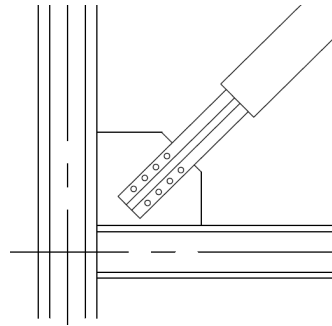


Figure 6.3 BRBF System Stability Model  
(Adapted from Hikino et al. 2013)



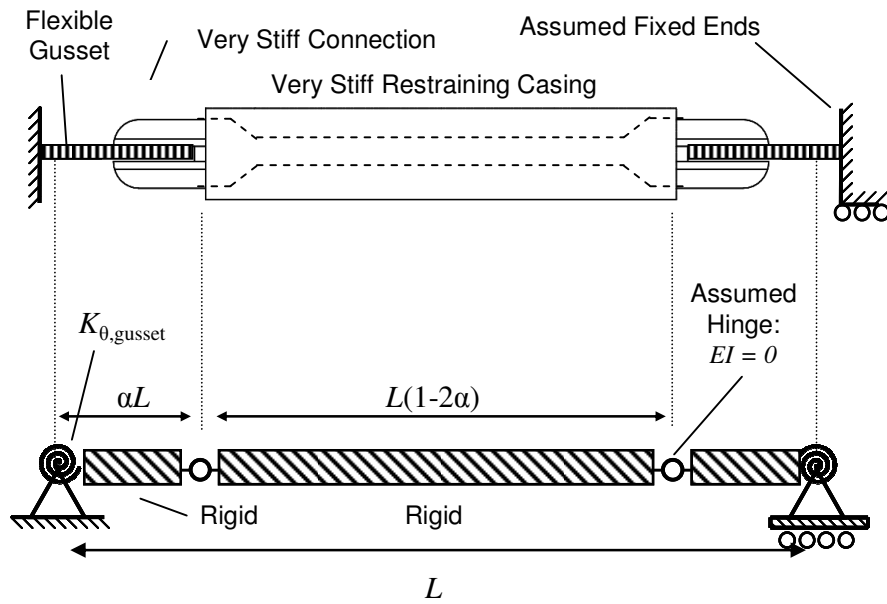
(a) AIJ Standard 1

(a) AIJ Standard 2

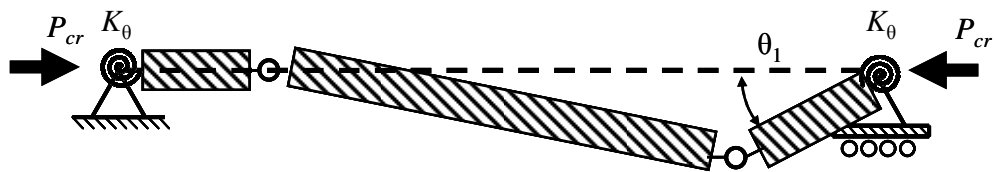


(c) Detail Common in the U.S.

Figure 6.4 BRB Connections  
(Adapted from Hikino et al. 2013)



(a) Idealization of BRB and Gusset Plate



(b) 2-Spring Model



(c) Specimen 1 Overall, after Compression Proof Protocol

Figure 6.5 Simplified BRB-Gusset System Stability Model

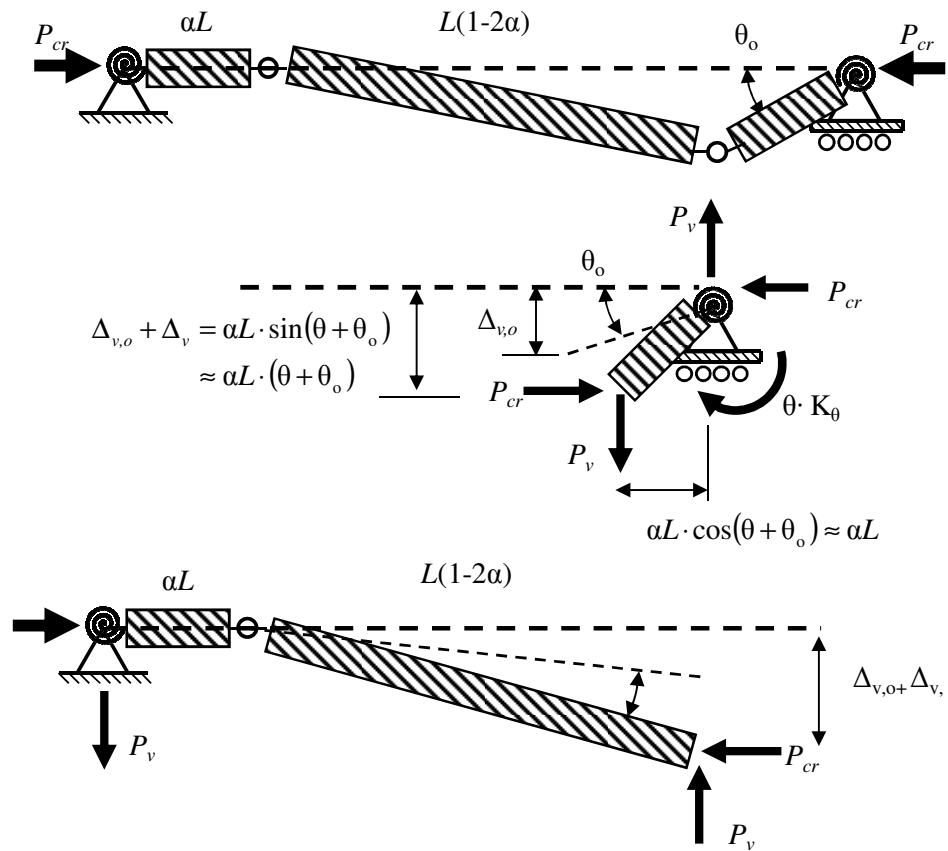


Figure 6.6 Buckling Load of 2-Spring System with Initial Imperfection

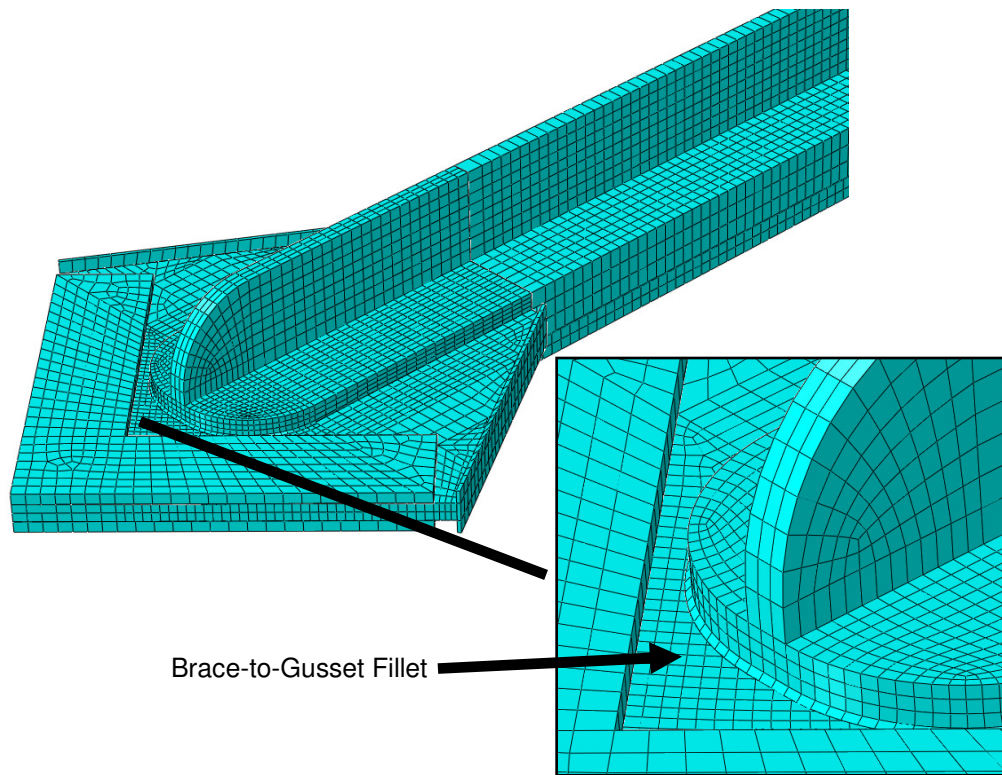
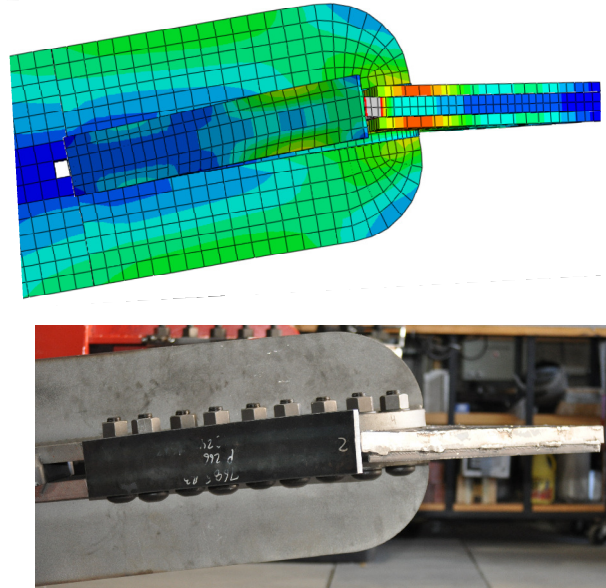
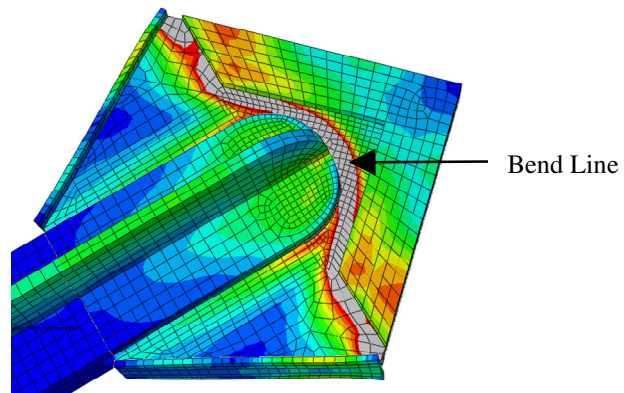


Figure 6.7 Abaqus Finite Element Model of Gusset and Brace Connection





(a) Comparison of Gusset Deformation and FE model Simulation



(b) Simulation of the Observed Bend Line

Figure 6.8 Specimen 1 Gusset Plate Instability and Bend Line Simulation

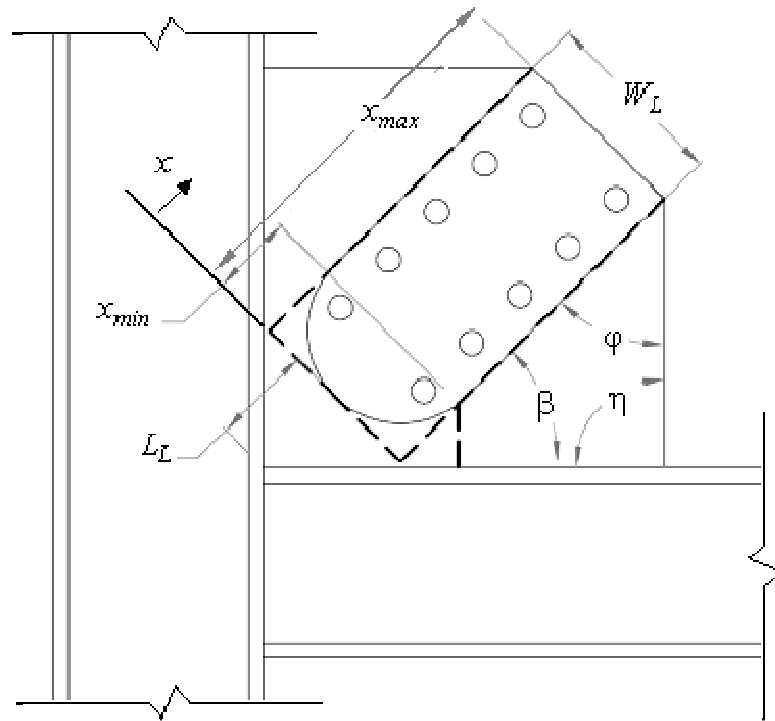


Figure 6.9 Dimensions for Calculating Gusset Plate Rotational Stiffness (GRS)

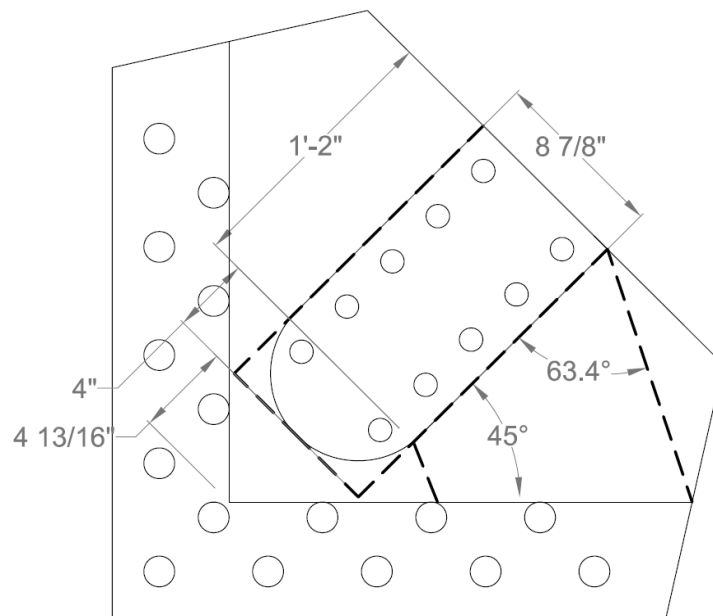


Figure 6.10 Gusset Plate Dimensions for GRS Calculation, Specimen 4

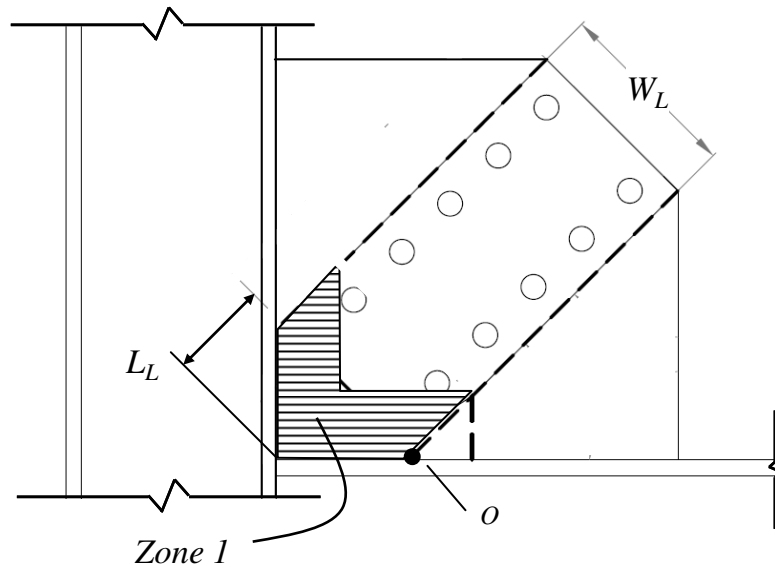


Figure 6.11 Definitions of GRS Zone 1

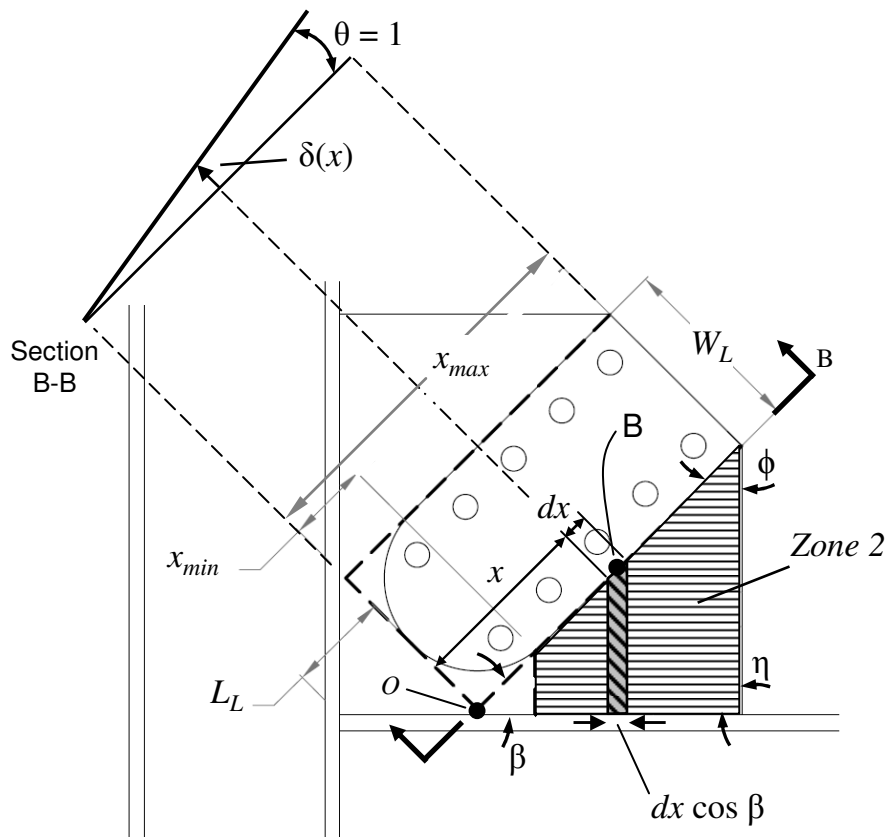


Figure 6.12 Definition of GRS Zone 2

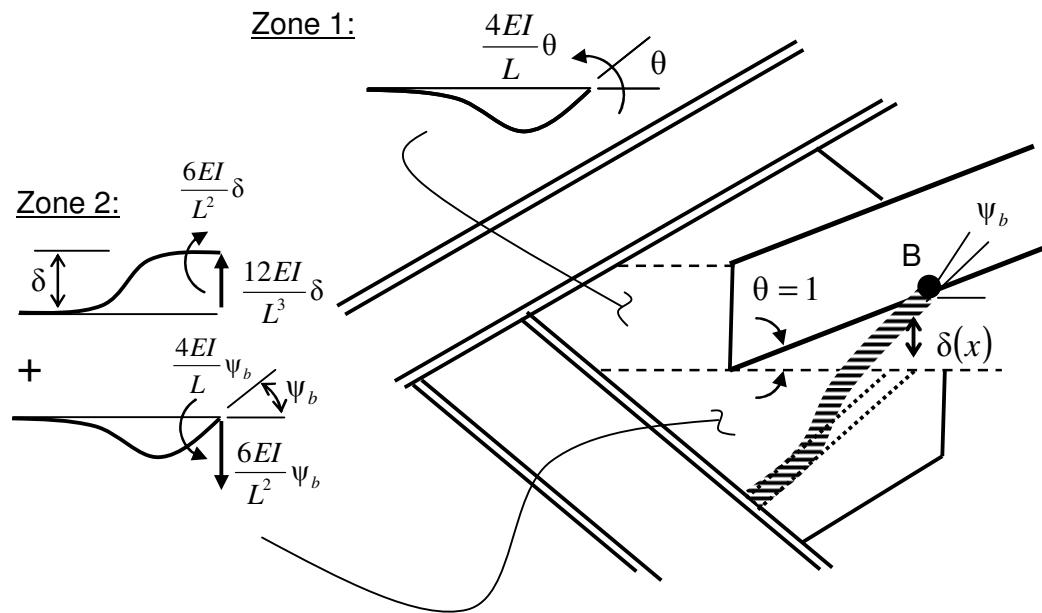
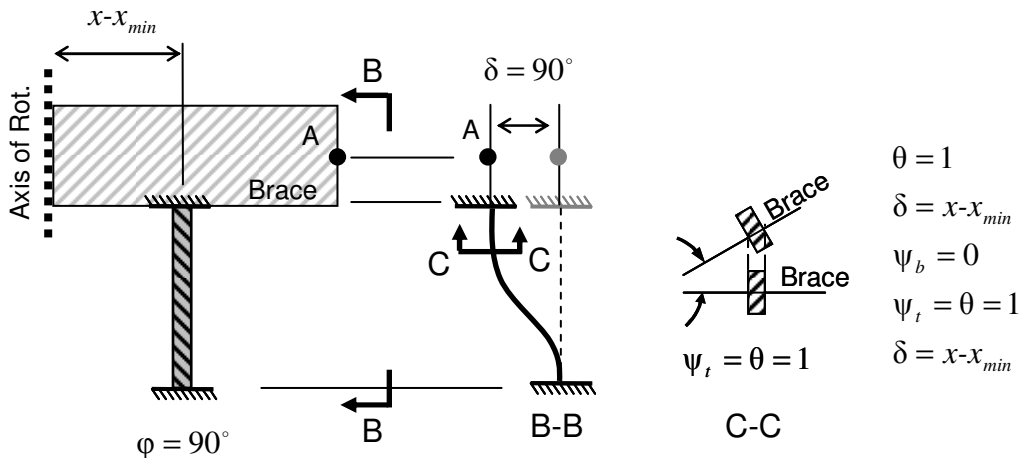
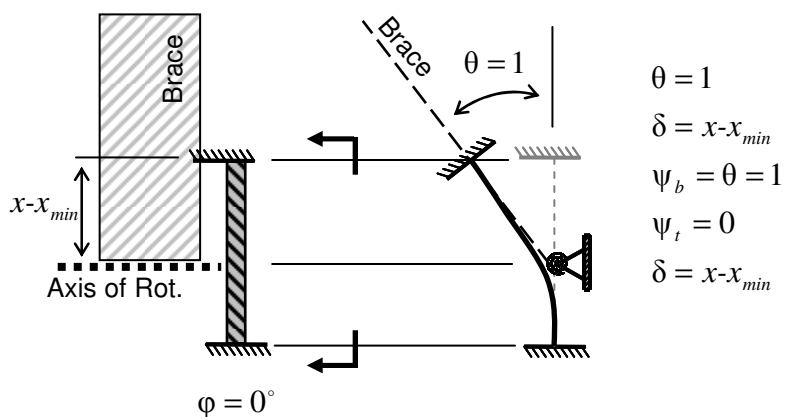


Figure 6.13 Idealization of Plate for GRS Zone 1 and 2



(a) Perpendicular Strip Beam



(b) Parallel Strip Beam

Figure 6.14 Strip Beam End Rotations

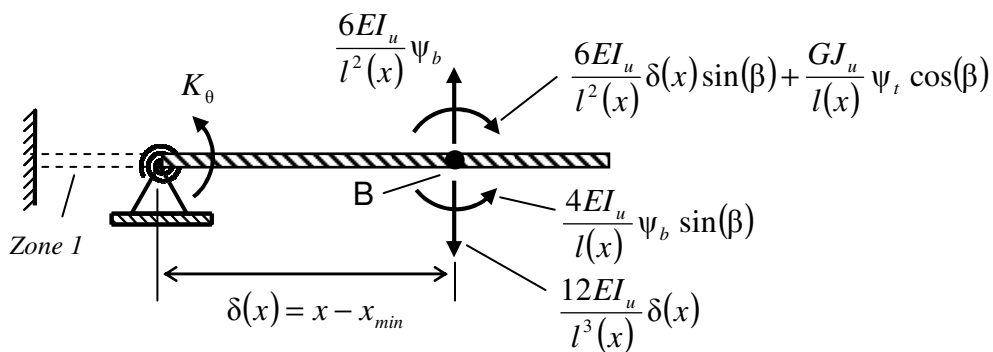


Figure 6.15 Internal Forces from Strip Beam Due to Brace Unit Rotation

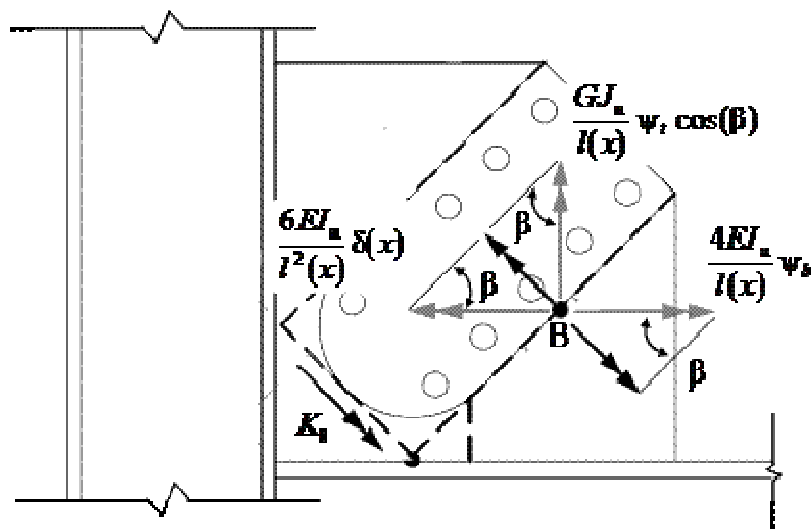
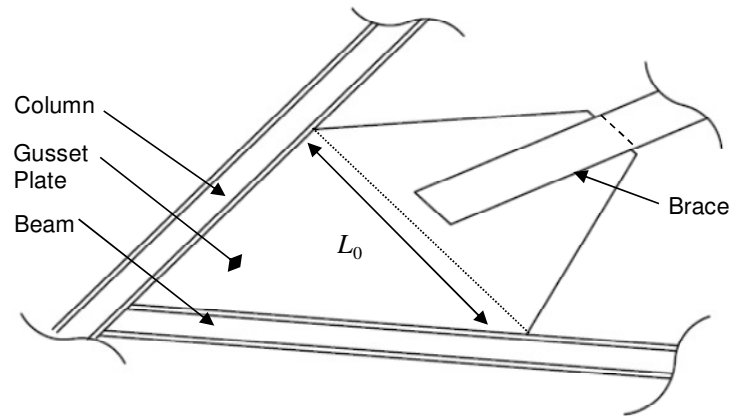
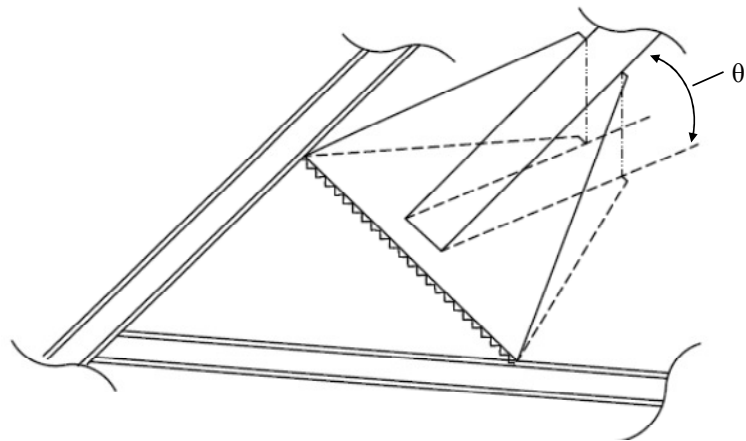


Figure 6.16 Internal Moments from Strip Beam Due to Brace Unit Rotation

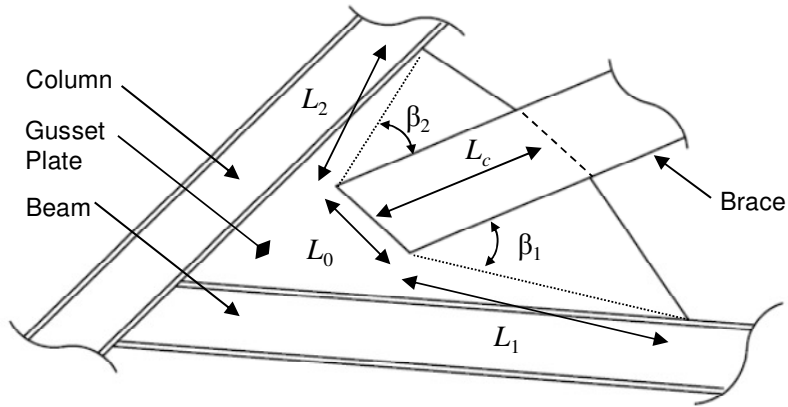


(a) Undeformed Gusset Plate

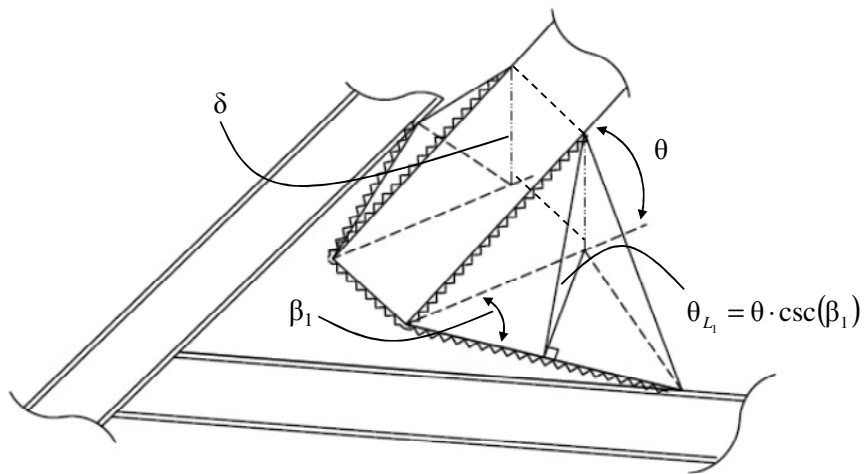


(b) Full Yield Line Rotation

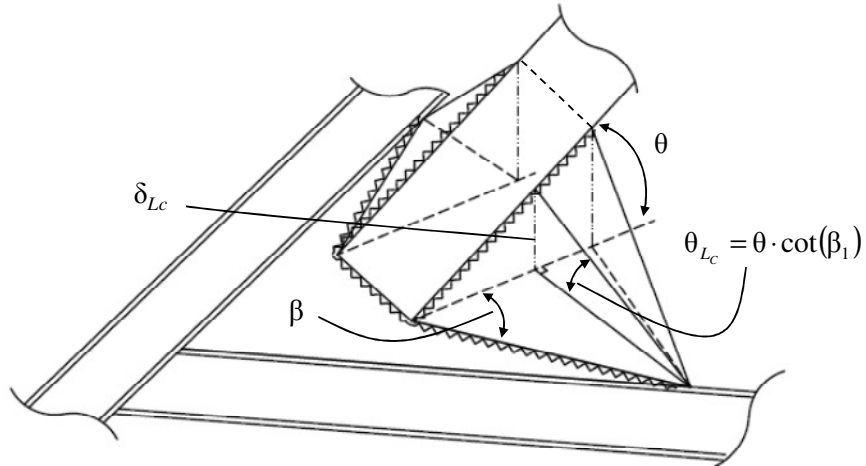
Figure 6.17 Geometry for YLA of Uninterrupted Bend Line Gusset



(a) Undeformed Gusset Plate



(b) Yield Line Rotation Angle along  $L_1$  ( $L_2$ )



(c) Yield Line Rotation Angle along  $L_c$

Figure 6.18 Geometry of YLA for Interrupted Bend Line Gusset



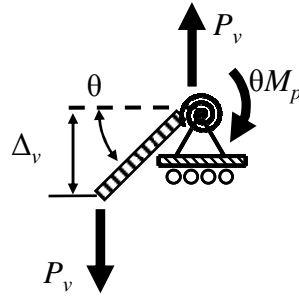


Figure 6.19 External Work by Transverse Force on Gusset

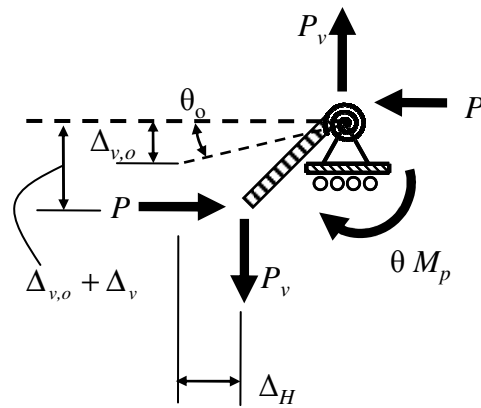


Figure 6.20 External Work by Axial Force on Gusset with Initial Imperfection

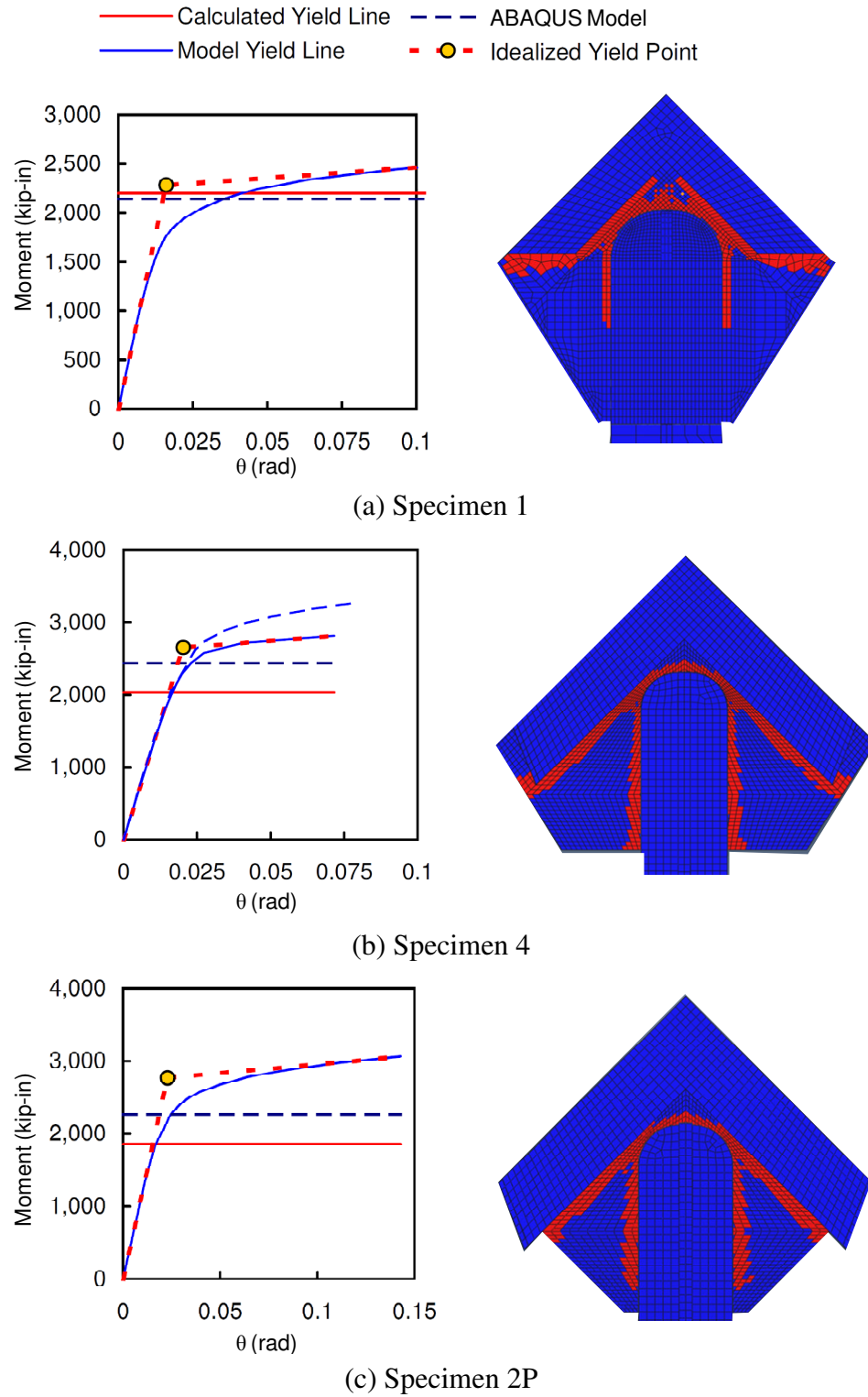
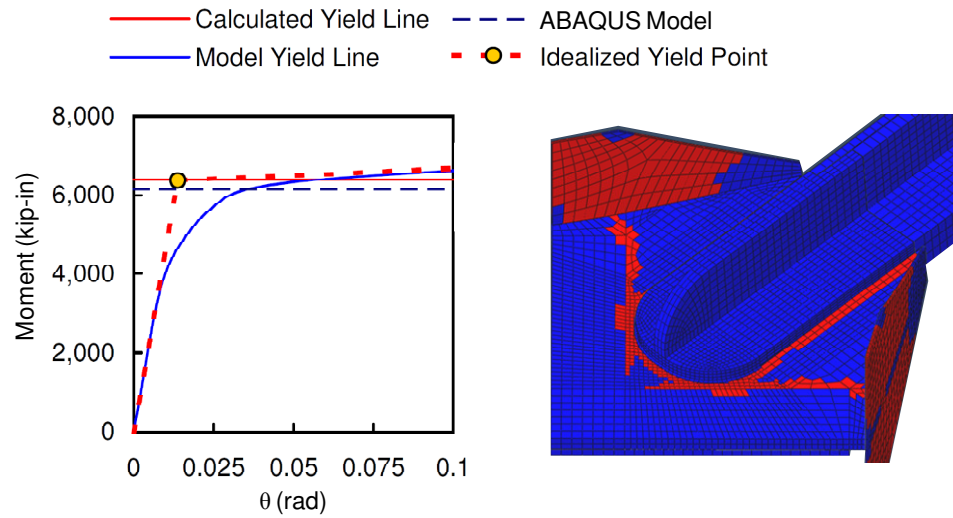
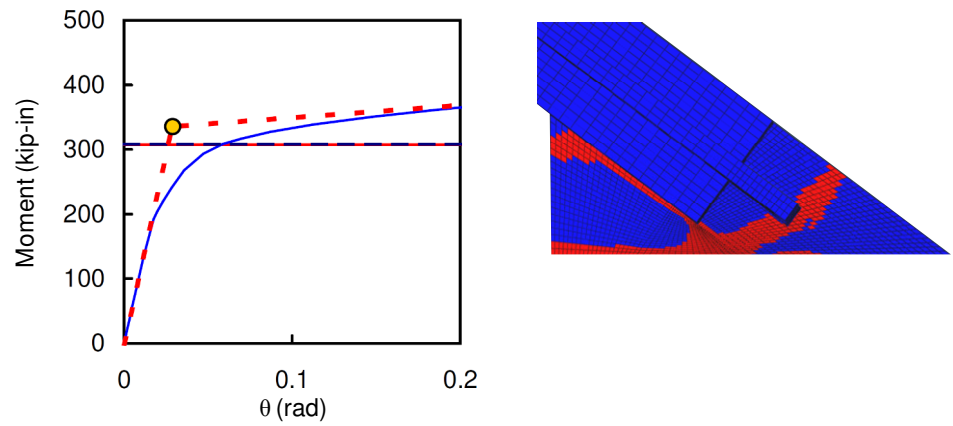


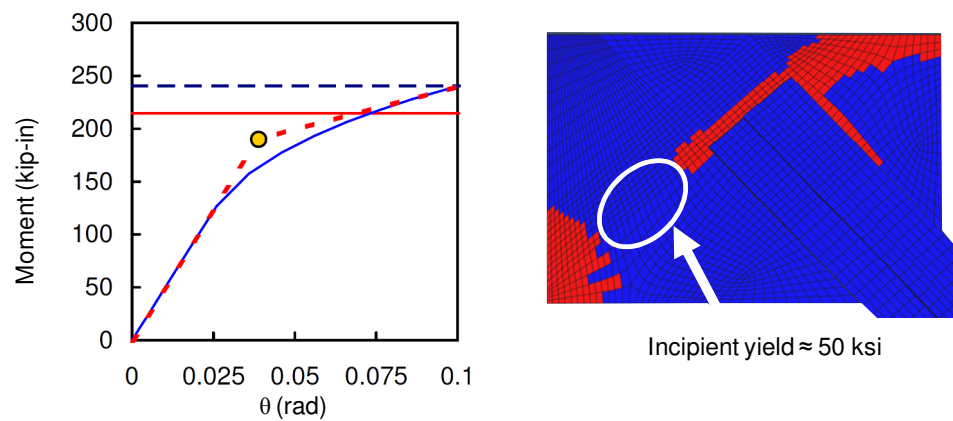
Figure 6.21 Abaqus Verification of Yield Line Analysis



(d) Specimen 5

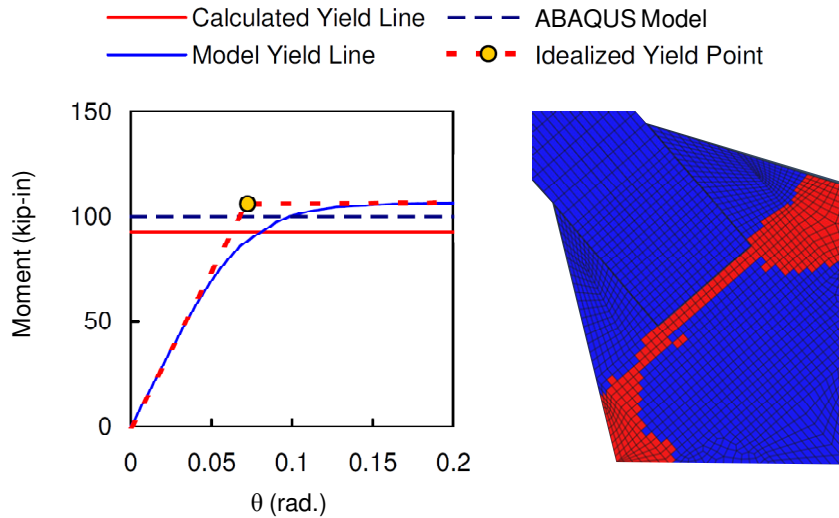


(e) Tsai 1 Story

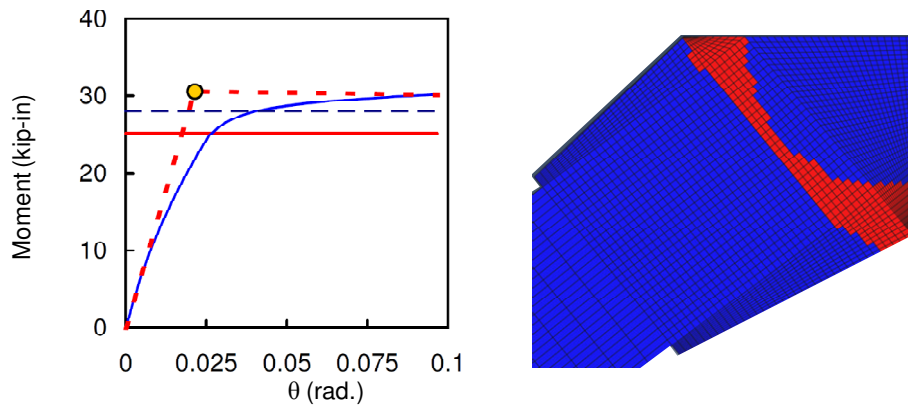


(f) Tsai 3-1

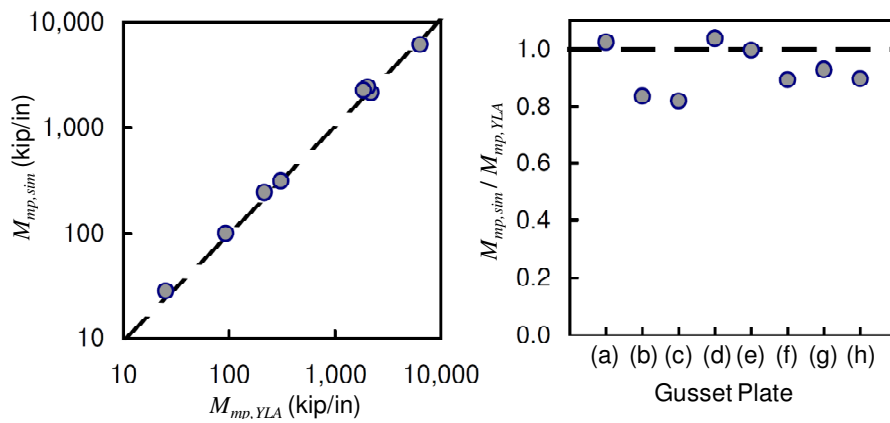
Figure 6.21 Abaqus Verification of Yield Line (continued)



(g) Tsai 3-3 Story

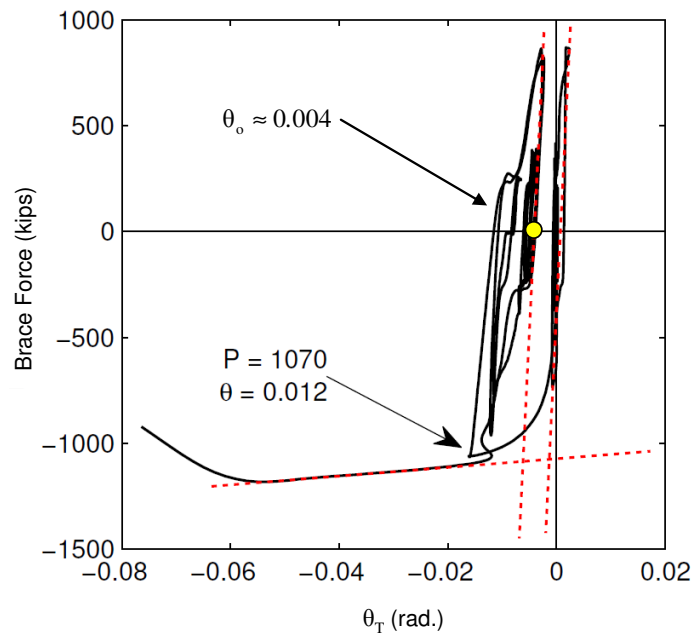


(h) Takeuchi

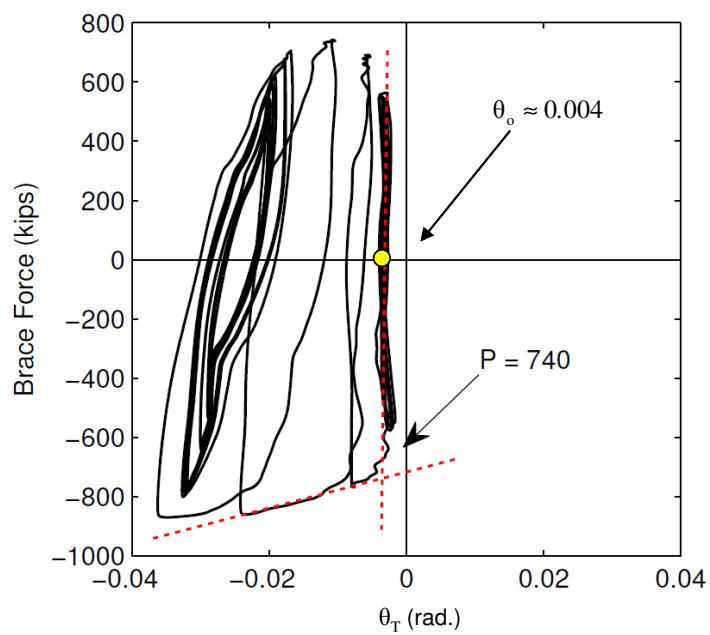


(c) Summary of Model and Transverse YLA Calculation

Figure 6.21 Abaqus Verification of Yield Line (continued)

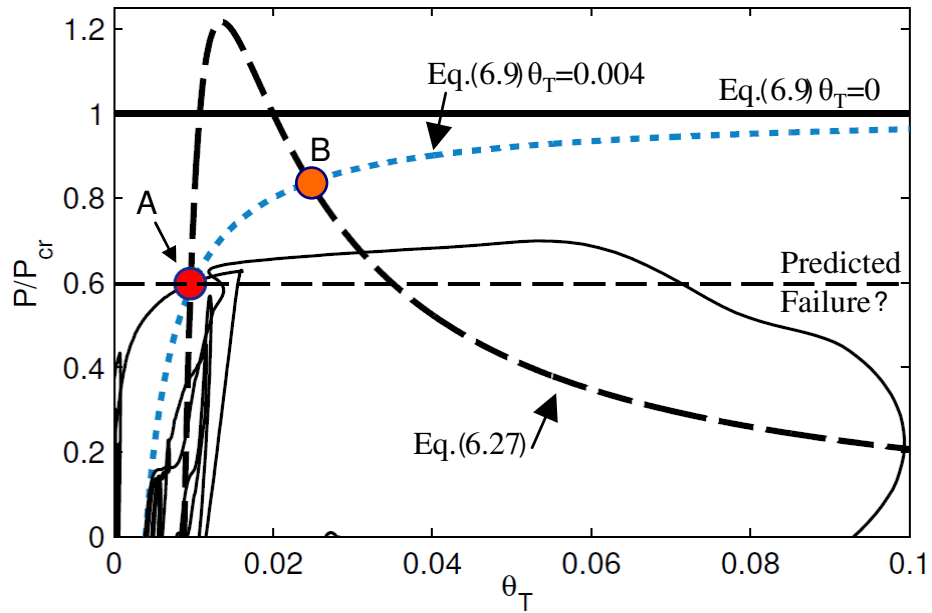


(a) Specimen 1

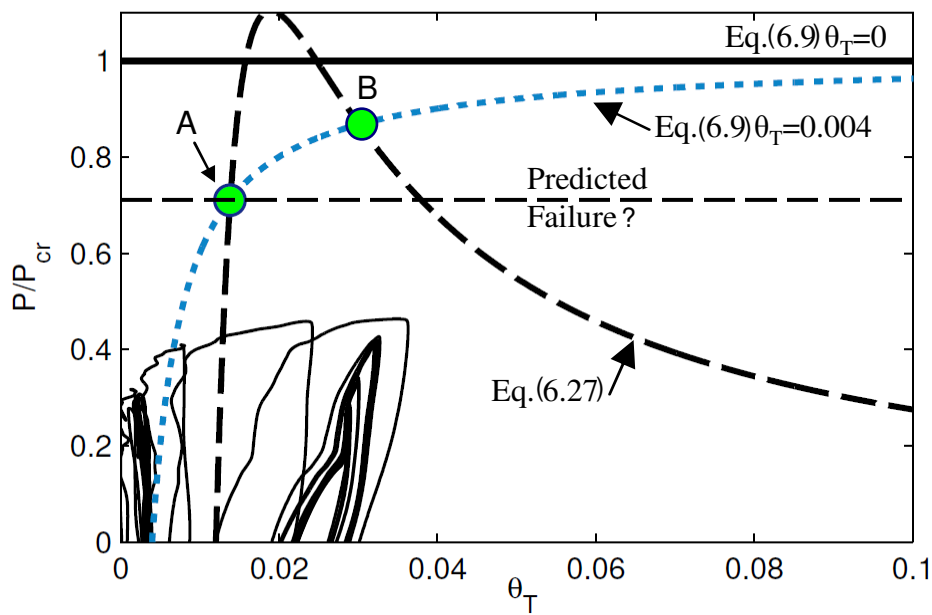


(b) Specimen 4

Figure 6.22 Measured Initial Imperfection



(a) Specimen 1



(b) Specimen 4

Figure 6.23 Preliminary BRB Gusset Plate Stability Prediction

## 7 SUMMARY AND CONCLUSIONS

### 7.1 Summary

Current design and testing practices, governed by AISC, address the capacity design of building frames equipped with buckling-restrained braces (BRBs) considering far-field ground motions. The highly ductile properties and low-maintenance requirements of BRBs make them attractive for bridge applications, especially for long-span bridges like the Vincent Thomas Bridge (VTB), which has viscous fluid dampers for seismic protection that are leaking due to traffic and ambient oscillations and in need of replacement. This research demonstrated BRBs as both feasible and beneficial for use this type of bridge (Section 2.1), which helps to pave the way towards bridge BRB design provisions.

Since the VTB spans the Palos Verdes Fault, the BRB deformation demands were dominated by near-field ground motion characteristics that were incongruent with current far-field building frame provisions. So, a new Near Fault Protocol (Section 2.2) for long-span bridges, which has more than twice the deformation and cumulative inelastic demands required by AISC for BRB frames, was developed. This statistically relevant protocol is appropriate for the prequalification testing of BRBs for near-field bridge applications.

Testing carried out with the Near Fault Protocol then demonstrated the excellent performance of six full-scale braces which included typical mild steel (A36) BRBs, the inaugural use of stainless steel (SS) BRBs, and the application of high strain rate which accompanied the near-field ground excitations. The large cyclic over-

strength of SS BRBs, over the usual A36 steel, accompanies its superior ductility properties. Current BRB testing requires only pseudo-static loading rates, but applying the high strain rate which caused an increased force response was observed for both steel materials. Therefore, both BRB yielding core material and strain rate were shown to have significant implications for capacity design of the surrounding members and connections.

Deficiencies in the AISC BRB testing and design provisions were exposed, including the inconsistency of the  $\beta$ -method (Figure 1.4) in predicting unbalanced forces of opposing BRBs for capacity design, and the incorrect assumption of only one unbalanced force loading scenario (see Figure 4.1 and Figure 4.2). A new testing procedure was suggested which uses two tested braces, not one, to provide the correct measurement of the unbalance between compression and tension BRB forces through the new  $\gamma$ -method (Section 4.2 and Figure 4.2).

The characterization of BRB response under near-fault loading provided by the commonly used bilinear truss element was shown to be poor, especially for SS BRB (Figure 5.2). Although the popular Menegotto-Pinto (MP) model (Figure 5.3), available in the OpenSees modeling environment, offers better representation, improvements were needed to reflect the unique characteristics of BRBs and of those observed in testing. These included (i) the separate treatment of the tension and compression post-yield stiffness, which is distinctive of BRBs (ii) expansion of the isotropic hardening relation with a new parameter to account for the cumulative ductility effect and a new hardening exponent for SS or other materials (iii) and the



incorporation of the instantaneous strain rate effect on the material properties through the addition of a new relation and set of model parameters.

Finally, the inability of current BRB gusset plate design procedures to protect against out-of-plane instability was made obvious by this and other testing (Figure 6.2 and Figure 6.8). Even with the fixed boundary conditions of the gusset plates, here, gusset failure and incipient failure were experienced by Specimen 1 and Specimen 4, respectively (Figure 3.11 and Figure 3.63). So, rather than treating the gusset plate like a buckling column, a model that focuses on the out-of-plane rotational stiffness and strength of the gusset is highlighted (Figure 6.5). The initial out-of-straightness linearly reduces the elastic buckling load of the system and the rotational strength of the gusset. Since both rotational stiffness and strength are required, practical methods are presented for designing this system (Sections 6.6 and 6.7). These tools should aid the future development of this simplified stability model.

## **7.2 Conclusions**

BRBs in the U.S. have barely been considered outside of the context of building frames. The case study performed as part of this research represents a leap in knowledge about how BRBs can be used. The identified realistic properties required for use on the long-span bridge provided improved seismic response, even under near-fault loading conditions. Currently, neither bridge application nor near-fault loading are addressed by current design provisions. Furthermore, the excellent performance of the full-scale specimens confirms that BRBs have great potential for use on bridges. Together, these should provide technical basis to extend building code development

for bridge BRB application, especially for application in near-fault environments, and promote their use as effective bridge seismic response mitigation structural elements.

This study pioneered the BRB testing, performance, and design issues associated with near-fault loading. The Near Fault Protocol developed in this study can be considered for adoption as a prequalifying protocol, and provides a clear performance goal for future BRB development. This further closes the gap between building and bridge BRB implementation.

Relevant to both building and bridge structure types, capacity design of the structure surrounding BRBs is critical for ensuring the expected response. The following conclusions are drawn from the findings in this research:

- (1) Testing of BRBs should include two nominally identical specimens subjected to equal but opposite loading protocols such that the  $\gamma$ -method (Figure 4.2) of measuring unbalanced forces can be assessed. Braces within a frame do not follow the loading history assumed by the current  $\beta$ -method (Figure 4.1), which is also invalid for nonsymmetrical loading. The impact of the  $\gamma$ -method is perhaps greater for near-fault loading, but should also be used for far-field loading like that considered by AISC to make the testing procedure consistent with reality.
- (2) The significant isotropic hardening of SS necessitates special testing procedures. As a preliminary suggestion, the AISC Protocol representing a functional-evaluation earthquake should be applied to SS BRB prequalification specimens prior to applying the Near Fault Protocol (or other appropriate protocol). This will provide reasonably conservative evaluation of the maximum overstrength values,

since a minor earthquake is likely to occur before the fault-rupture (or design) level event.

- (3) Near-field ground motion demands on BRBs are likely to be of relatively large strain rates, demonstrated in this study to be on the order of 0.35in/in/sec. The tests carried out showed both A36 and SS BRBs to exhibit a maximum of about 20% higher force response under high strain rate loading. Therefore, it is suggested that this effect be accounted for by increasing pseudo-statically obtained overstrength factors by 1.2 for near-fault application of BRBs.

SS BRB was very poorly represented by the bilinear element (Figure 5.2), and near-fault loading of A36 was of acceptable accuracy. However, the improved Menegotto-Pinto (MP) material model for BRBs was shown to provide excellent correlation to the near-fault demands of the tested specimens. Many accumulated less than 5% error in the predicted dissipated energy, and displayed very good peak force correlation for most all significant excursions (Figure 5.11, Figure 5.12, and Figure 5.20 through Figure 5.23). Model parameters were suggested for both A36 and SS BRB, including those for simulating of the strain rate effect. Thus, modeling of near-fault structures with either A36 or SS BRB can now be carried out with this new tool.

It is clear from testing results that the current BRB gusset plate design procedures are inadequate. With the simplified stability model, a prediction method for the critical load was presented with moderate accuracy (Figure 6.23). Further analysis may provide a better correlation. However, the proposed methods for calculating the out-of-plane stiffness and strength were found to correlate well with

finite element models (Table 6.2 and Table 6.4, respectively). These tools promote the further analysis of gusset plate connections in general.

### 7.3 Future Work

Currently BRBs for steel buildings are required by AISC 341-10 to be tested to transverse motion consistent with the relative displacement of the end connections, or subassembly rotations, in addition to axial deformations. Since the near-fault long-span bridge axial deformation demands found from analysis were approximately 2.5 times larger than the maximum required by AISC, the developed protocol and testing focused first on demonstrating the ability of BRBs to accommodate this severe demand, alone. Upon the very favorable test results, the Near Fault Protocol should be expanded to incorporate these end rotations, and further testing should be carried out.

Before implementation of the BRB MP model into OpenSees, the model should be given the ability to properly reflect hysteretic behavior under minor strain reversals, as discussed in Section 5.9. This is critical for the model to more accurately simulate the response due to a smaller range of strain reversal amplitudes experienced during nonlinear time history analysis using ground acceleration input.

Further development of the BRB gusset stability problem is needed. However, the practical solution to the issue is obvious. By providing transverse stiffeners to the BRB gusset plates, the rotational stiffness and strength are drastically increased. The more pertinent question may be the identification of existing BRB frames at risk of this failure mode. Since this unstiffened gusset detail is common in the U.S., a retrofit solution should be developed to avoid any surprises in the next large seismic event.

## APPENDIX A. PARAMETRIC STUDY PLOTS

Table A.1 Parametric Matrices for Global Adjustment of BRB Mechanical Properties

### (a) Variation of Post-Yield Stiffness and Member Length

$\alpha$ (%)	$\gamma$	Scheme 1*			Scheme 2			Scheme 3		
		S-C	S-T	M-T	S-C	S-T	M-T	S-C	S-T	M-T
1	0.70	Response Parameter Investigated: Maximum Impact-direction Relative Displacement Absolute Maximum BRB Axial Strain Absolute Maximum BRB Axial Force Cumulative Ductility Demand  Goal: Determine response sensitivity								
2										
3										
4										
5										

\* See Figure 2.8 for scheme designation

### (b) Variation of Yield Force and Member Length

$\alpha$ (%)	$\gamma$	Scheme 1			Scheme 2			Scheme 3		
		S-C	S-T	M-T	S-C	S-T	M-T	S-C	S-T	M-T
3.25	0.35	Response Parameter Investigated: Maximum Impact-direction Relative Displacement Absolute Maximum BRB Axial Strain Absolute Maximum BRB Axial Force Cumulative Ductility Demand  Goal: Determine sensitivities and preliminary feasibility								
	0.525									
	0.70									
	1.05									
	1.40									

### (c) Correlation between Perform-3D and ADINA

$\alpha$ (%)	$\gamma$	Scheme 2		
		S-C	S-T	M-T
3.25	0.525	Response Parameter Investigated: Same as Table A.1(a) and (b)  Goal: Produce crucial data points verifying Perform-3D and ADINA models providing similar trends and values		
	1.05			

Table A.2 Parametric Matrices for Local Adjustment of BRB Mechanical Properties

## (a) Effect of Yield Force Variation

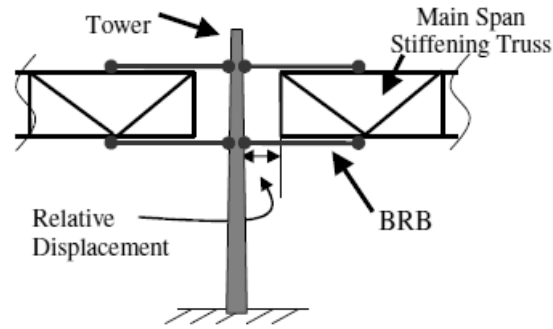
$\gamma_{S-C}$	$\gamma_{S-T}$	$\gamma_{M-T}$		$\gamma_{S-C}$	$\gamma_{S-T}$	$\gamma_{M-T}$		$\gamma_{S-C}$	$\gamma_{S-T}$	$\gamma_{M-T}$
0	1.05	1.05		1.05	0	1.05		1.05	1.05	0
0.525					0.35					0.525
0.70					0.525					0.70
1.05					0.70					1.05
1.25					1.05					1.25

Note: All BRB lengths correspond to Scheme 2

## (b) Effect of Yield Force and Length Variation

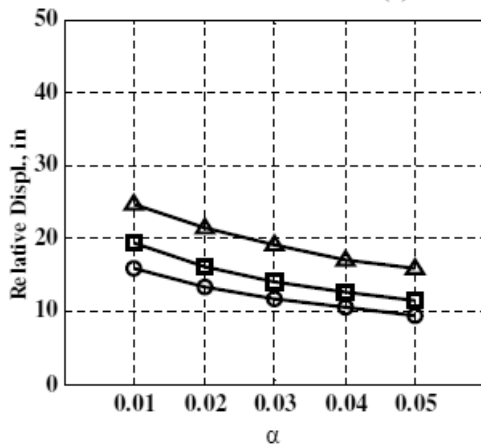
Location	S-C			S-T	M-T		
$\gamma$	0.70	1.05	1.25	1.05	0.70	1.05	1.25
$L$	Scheme 2, Scheme2.1, Scheme 2.2 (each location together with $\gamma$ )						

Note: All  $\gamma = 1.05$  and  $L = \text{Scheme 2}$  unless noted otherwise

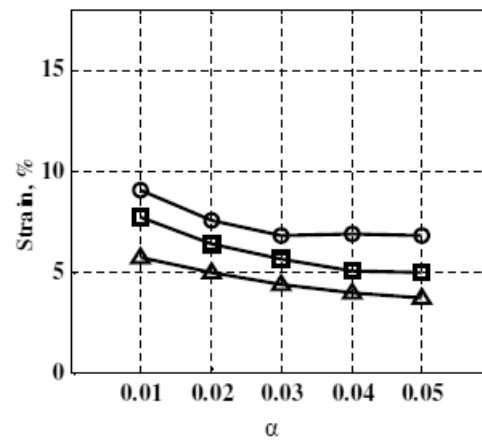


Scheme	BRB Length	Marker
1	15 ft	
2	21 ft	
3	37 ft	

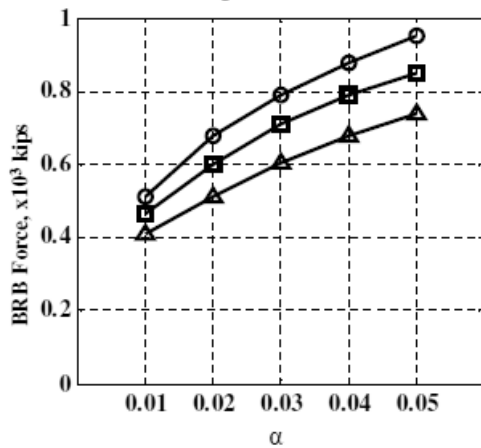
(a) Main / Tower Location



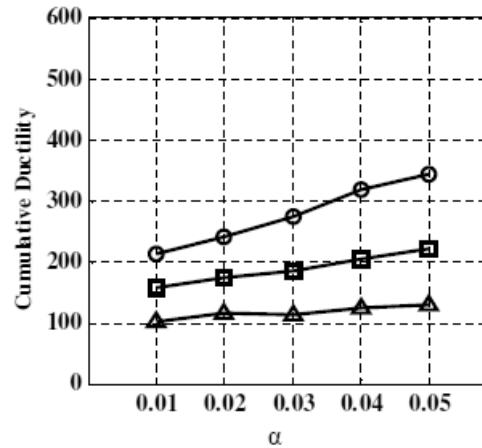
(b) Impact-direction Relative Displacement



(c) Absolute Maximum Strain

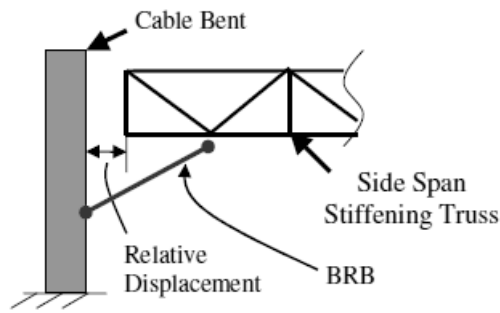


(d) BRB Axial Force



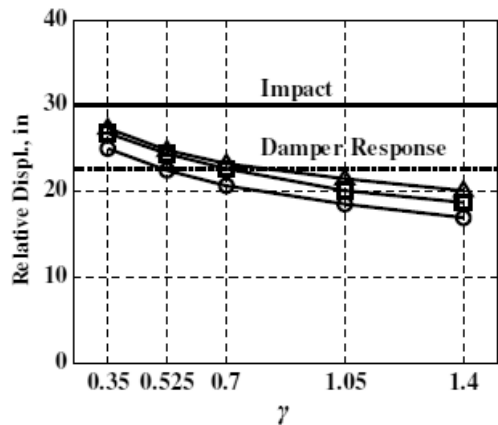
(e) Cumulative Ductility

Figure A.1 Effect of BRB Post-Yield Stiffness,  $\alpha$ , on VTB Response: Main/Tower

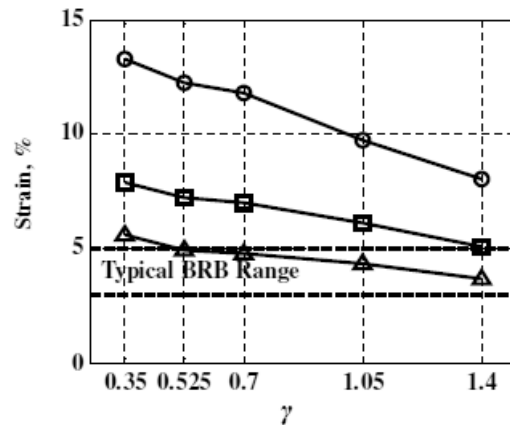


Scheme	BRB Length	Marker
1	14 ft	○
2	29 ft	□
3	44 ft	△

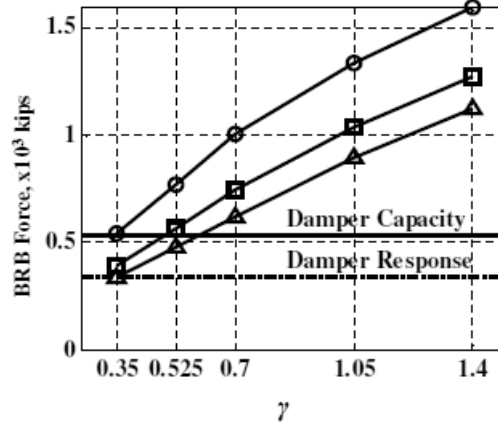
(a) Side / Cable Bent Location



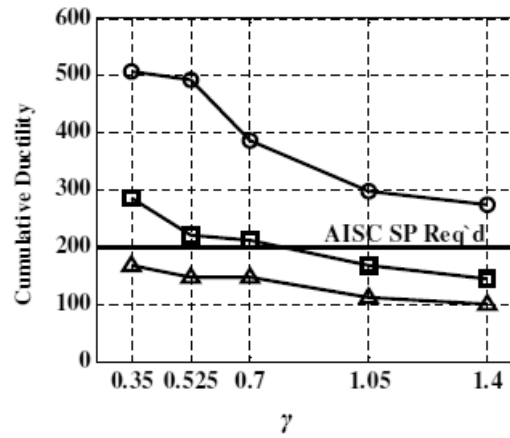
(b) Impact-direction Relative Displacement



(c) Absolute Maximum Strain



(d) Maximum Axial Force

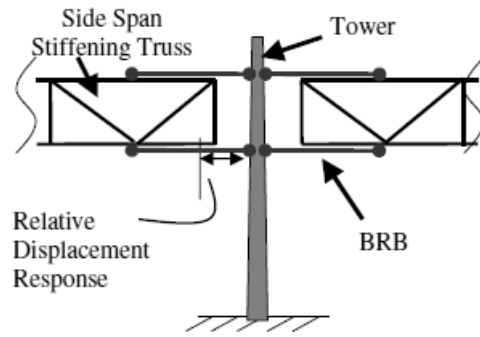


(e) Cumulative Ductility

d

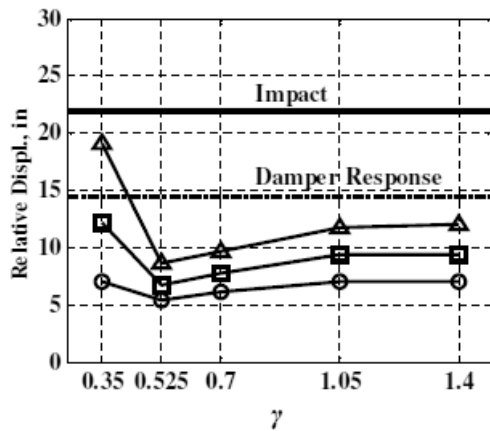
Figure A.2 Effect of BRB Yield Strength,  $\gamma$ , on VTB Response: Side/Cable Bent



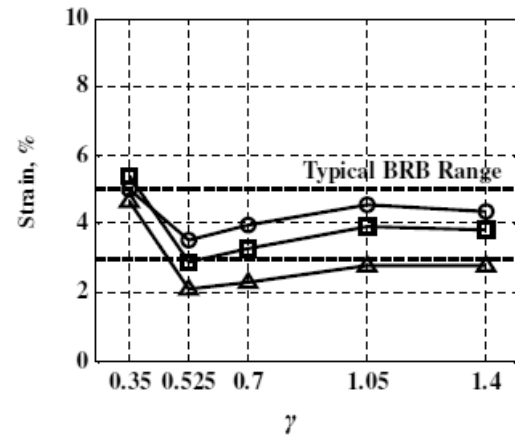


Scheme	BRB Length	Marker
1	13 ft	○
2	20 ft	■
3	35 ft	▲

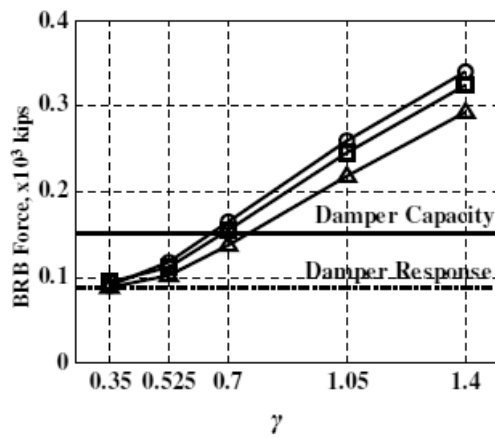
(a) Side / Tower Location



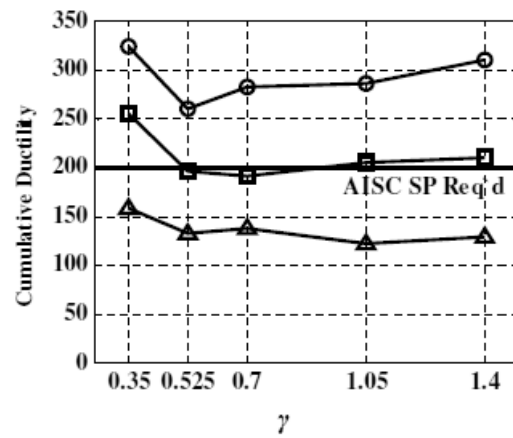
(b) Impact-direction Relative Displacement



(c) Absolute Maximum Strain

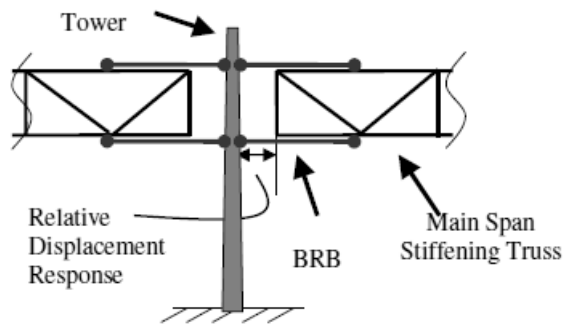


(d) Maximum Axial Force



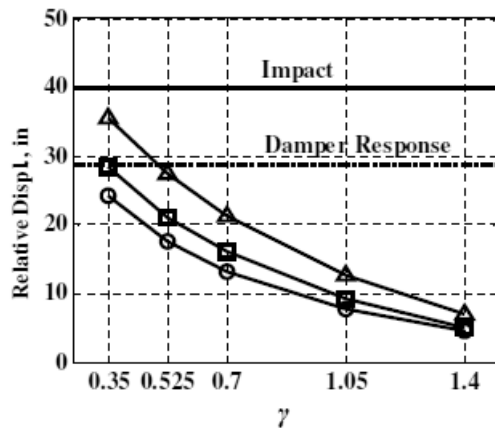
(e) Cumulative Ductility

Figure A.3 Effect of BRB Yield Strength,  $\gamma$ , on VTB Response: Side/Tower

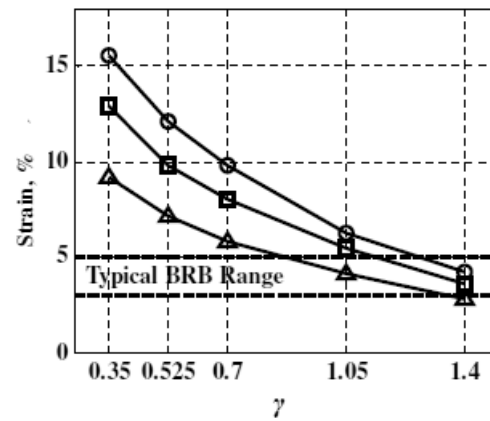


Scheme	BRB Length	Marker
1	15 ft	○
2	21 ft	□
3	37 ft	△

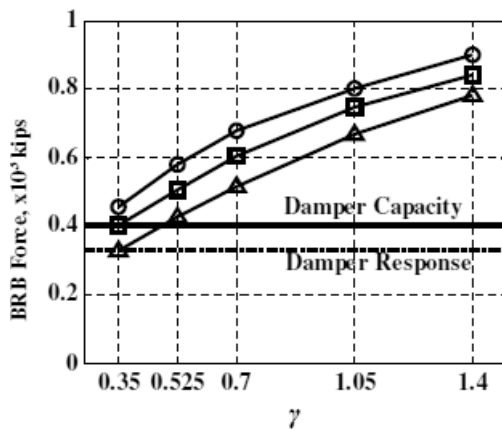
(a) Main / Tower Location



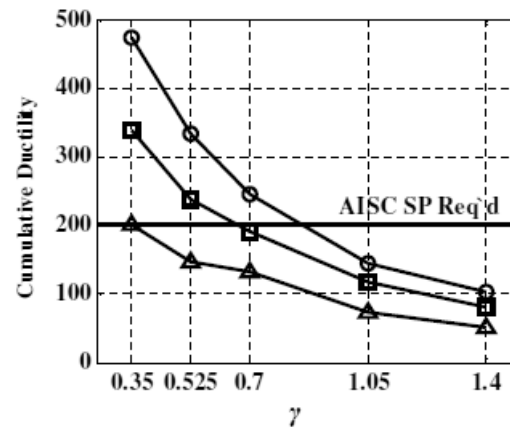
(b) Impact-direction Relative Displacement



(c) Absolute Maximum Strain

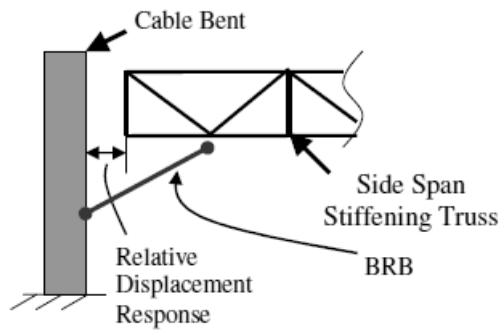


(d) Maximum Axial Force



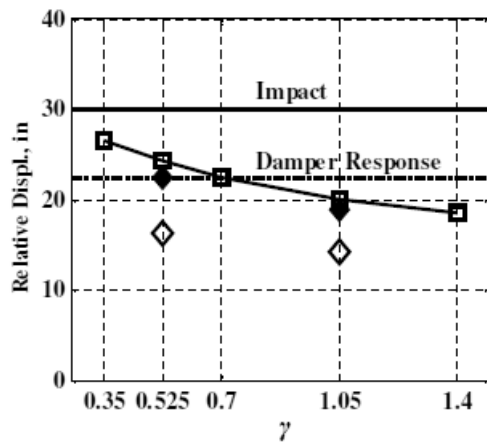
(e) Cumulative Ductility

Figure A.4 Effect of BRB Yield Strength,  $\gamma$ , on VTB Response: Main/Tower

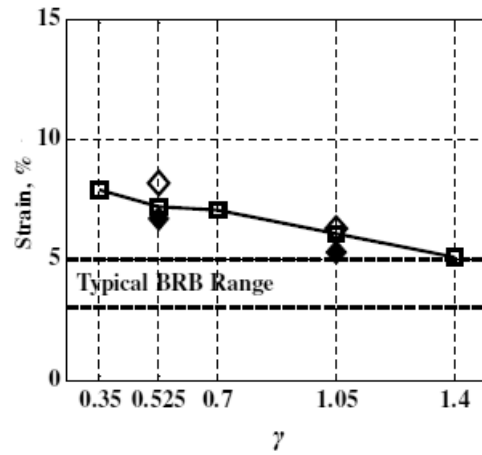


Model	Input Excitation	Marker
Perform-3D	Longitudinal	—■—
ADINA	Longitudinal	◆
ADINA	All Directions	◇

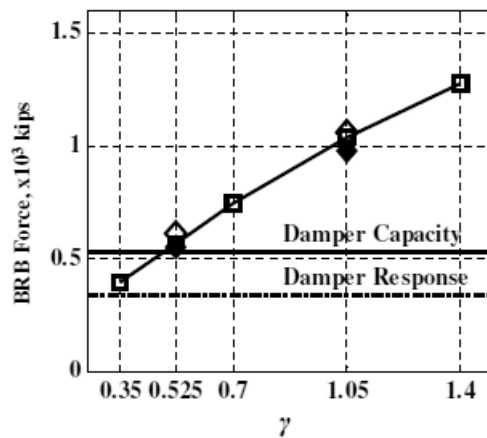
(a) Side / Cable Bent Location



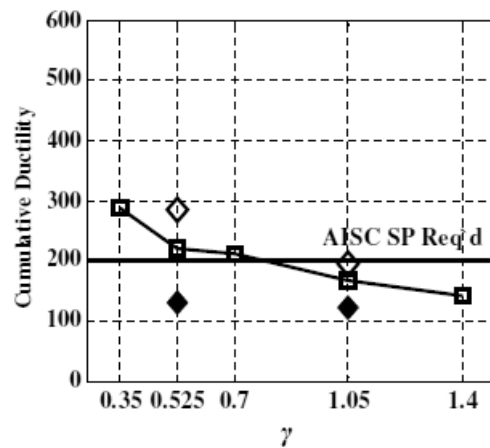
(b) Impact-direction Relative Displacement



(c) Absolute Maximum Strain

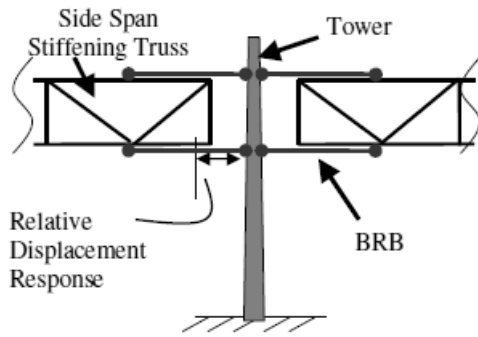


(d) Maximum Axial Force



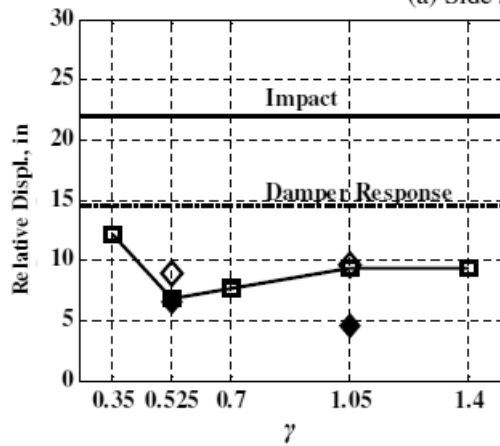
(e) Cumulative Ductility

Figure A.5 Comparison of Perform-3D and ADINA Responses: Side/Cable Bent

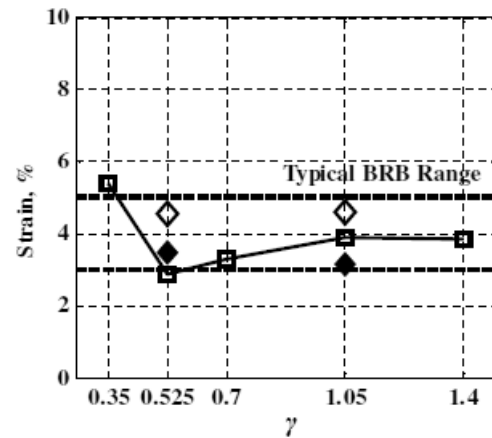


Model	Input Excitation	Marker
Perform-3D	Longitudinal	■
ADINA	Longitudinal	◆
ADINA	All Directions	◇

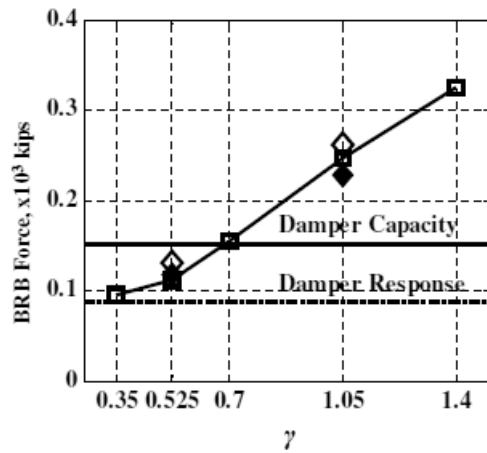
(a) Side / Tower Location



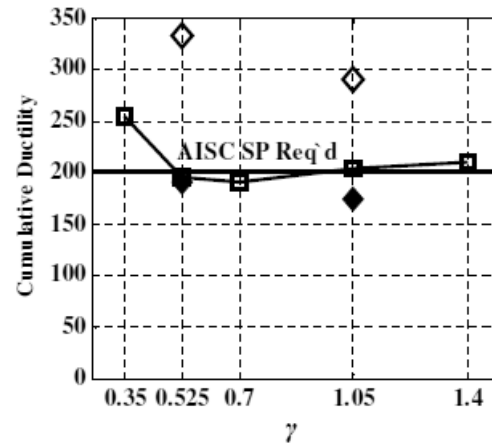
(b) Impact-direction Relative Displacement



(c) Absolute Maximum Strain

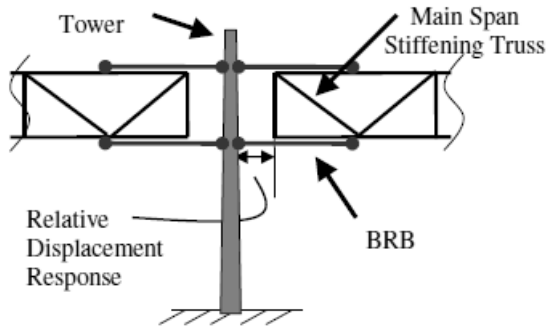


(d) Maximum Axial Force



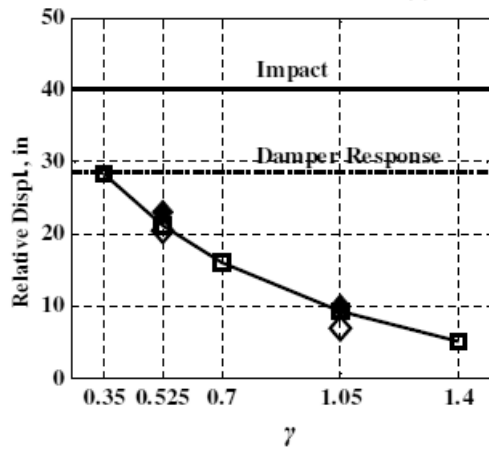
(e) Cumulative Ductility

Figure A.6 Comparison of Perform-3D and ADINA Responses: Side/Tower

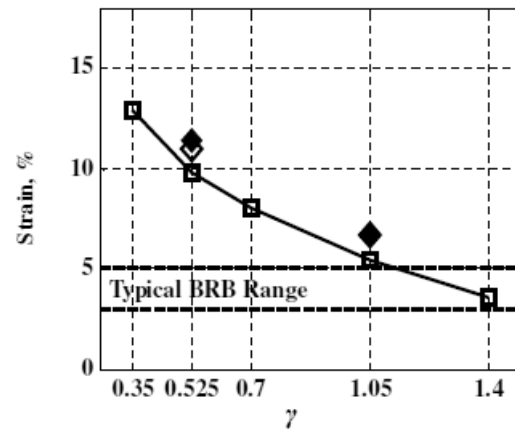


Model	Input Excitation	Marker
Perform-3D	Longitudinal	■
ADINA	Longitudinal	◆
ADINA	All Directions	◇

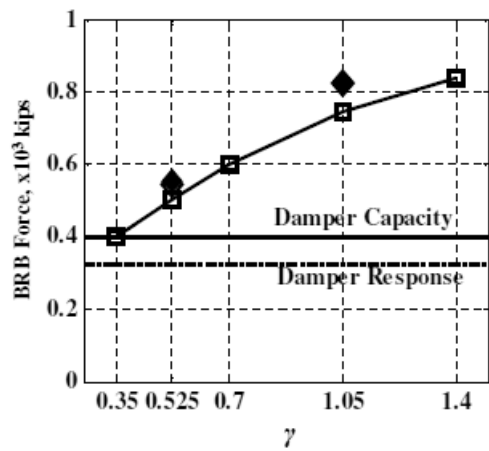
(a) Main / Tower Location



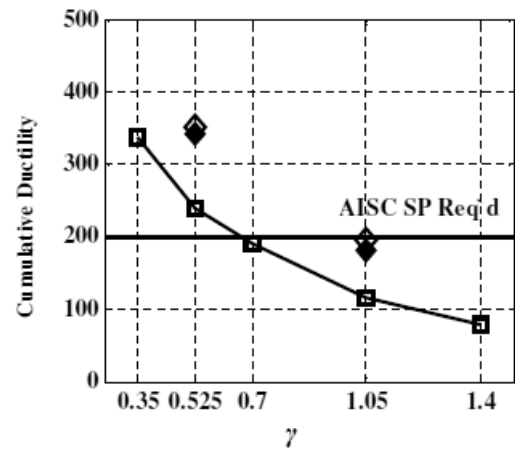
(b) Impact-direction Relative Displacement



(c) Absolute Maximum Strain



(d) Maximum Axial Force



(e) Cumulative Ductility

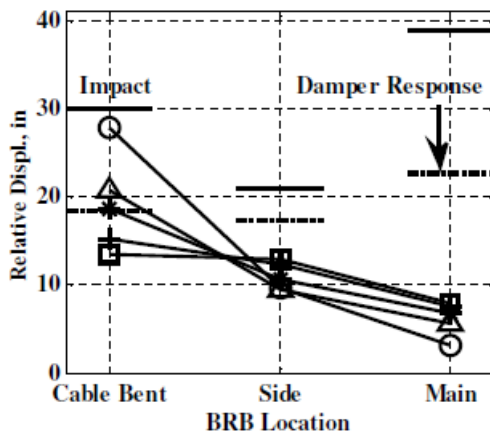
Figure A.7 Comparison of Perform-3D and ADINA Responses: Main/Tower

Location	$\gamma$				
	0	0.525	0.70	1.05	1.25
S-C	0	0.525	0.70	1.05	1.25
S-T	1.05				
M-T	1.05				

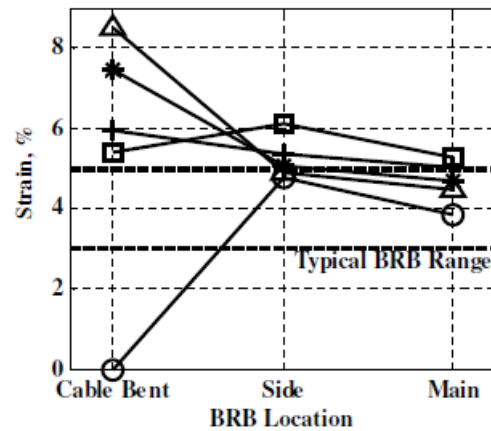
  

$\gamma_{s-c}$	Marker
0	
0.525	
0.7	
1.05	
1.25	

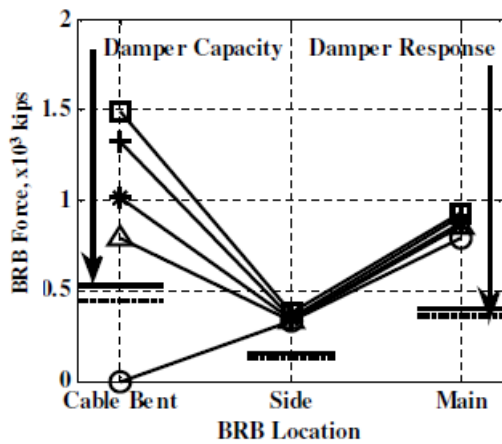
(a) Parameter Information



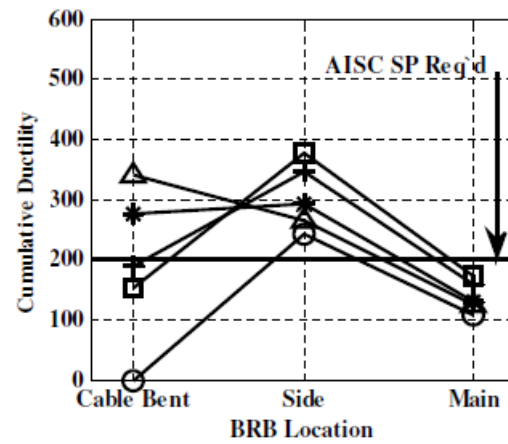
(b) Impact-direction Relative Displacement



(c) Absolute Maximum Strain



(d) Maximum Axial Force



(e) Cumulative Ductility

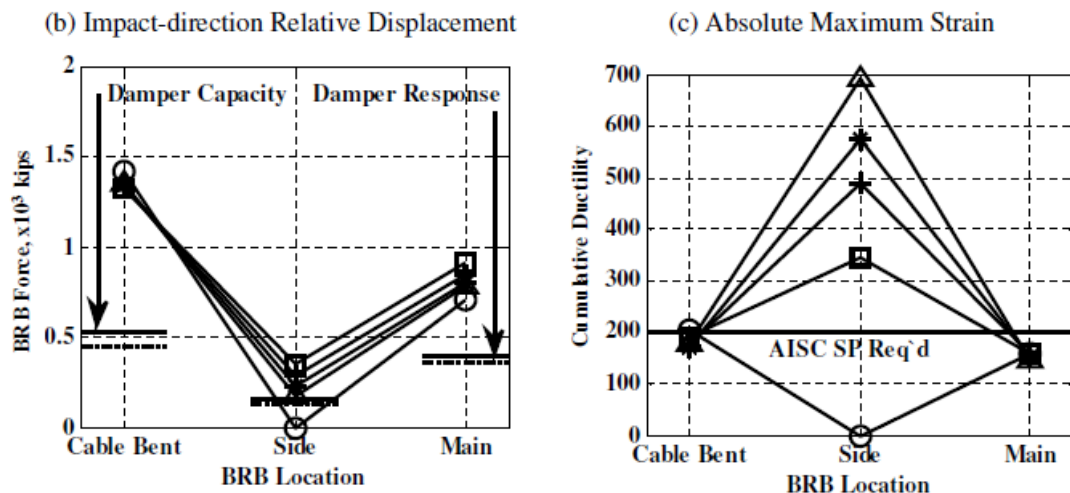
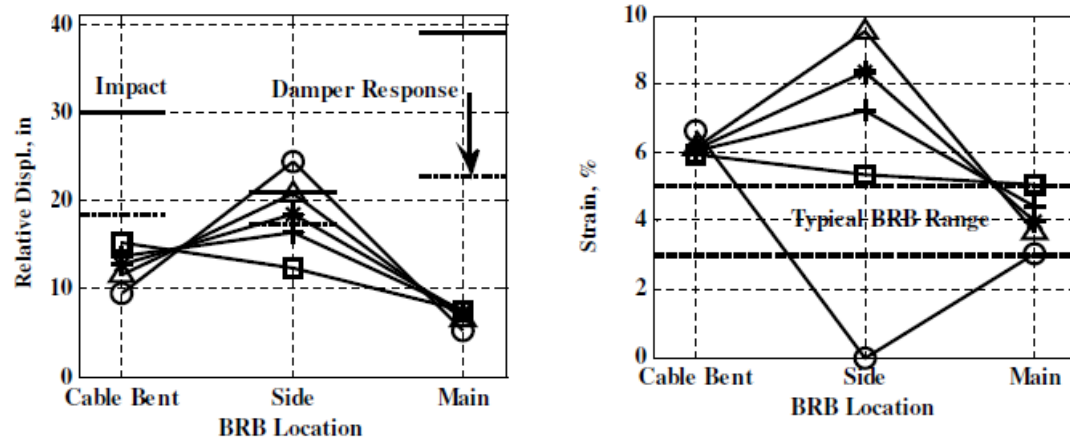
Figure A.8 Effect of Local BRB Yield Strength,  $\gamma$ , on VTB Response: Side/CableBent

Location	$\gamma$				
S-C	1.05				
S-T	0	0.35	0.525	0.70	1.05
S-C	1.05				

$\gamma_{S-T}$	Marker
0	○
0.35	△
0.525	*
0.7	+
1.05	□

(a) Parameter Information



(d) Maximum Axial Force

(e) Cumulative Ductility

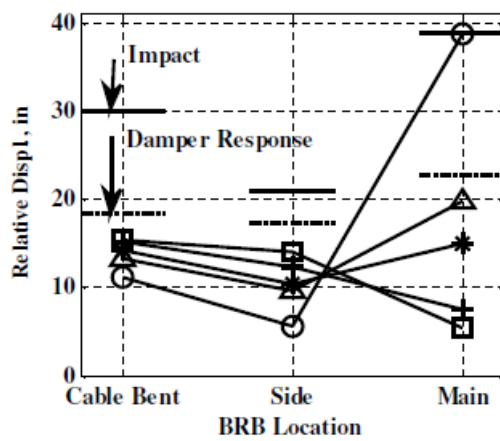
Figure A.9 Effect of Local BRB Yield Strength,  $\gamma$ , on VTB Response: Side/Tower

Location	$\gamma$				
S-C	1.05				
S-T	1.05				
M-T	0	0.525	0.70	1.05	1.25

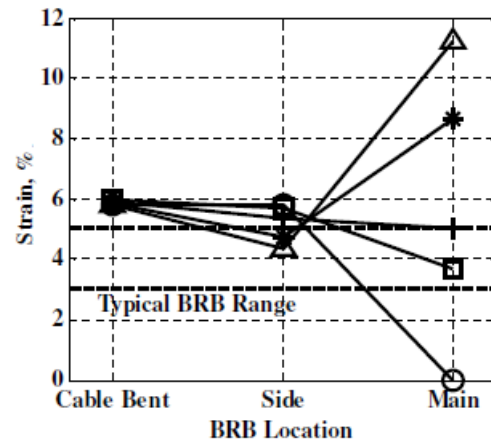
  

$\gamma_{M-T}$	Marker
0	○
0.525	△
0.7	*
1.05	+
1.25	□

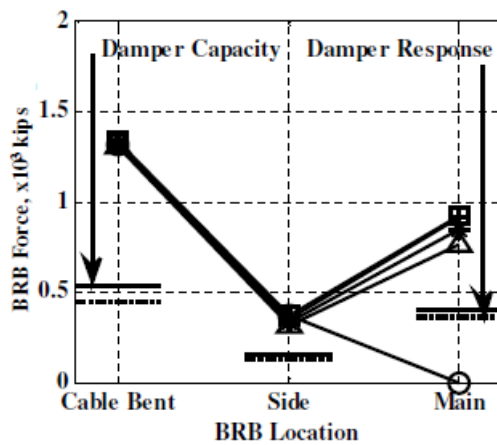
(a) Parameter Information



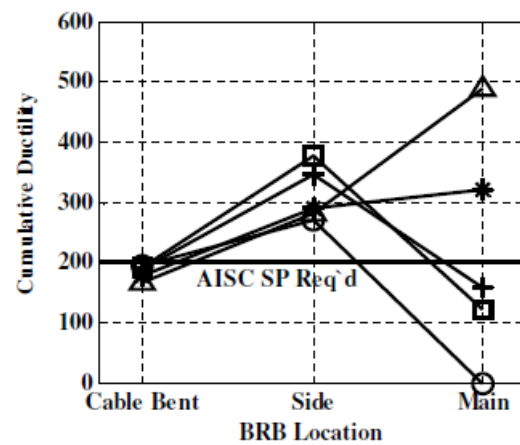
(b) Impact-direction Relative Displacement



(c) Absolute Maximum Strain



(d) Maximum Axial Force



(e) Cumulative Ductility

Figure A.10 Effect of Local BRB Yield Strength,  $\gamma$ , on VTB Response: Main/Tower



Location	Parameters			
S-C	$\gamma$	0.70	1.05	1.25
	$L$	Sch2 = 29 ft	Sch2.1 = 34 ft	Sch2.2 = 39 ft
S-T	$\gamma = 1.05$ $L = \text{Scheme 2}$			
M-T	$\gamma = 1.05$ $L = \text{Scheme 2}$			

$\gamma$ s-c	Marker
0.70	—*—
1.05	—+—
1.25	—□—

(a) Parameter Information

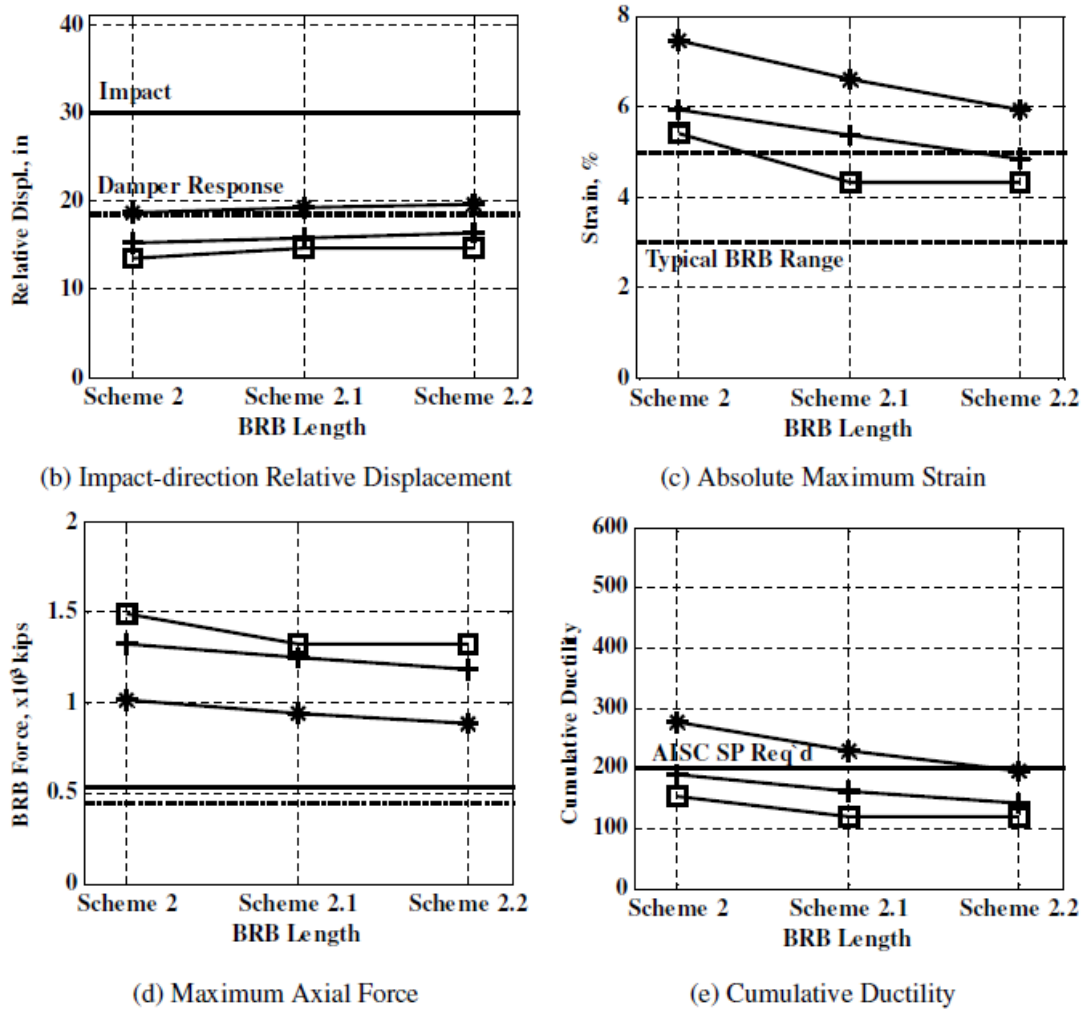
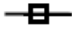


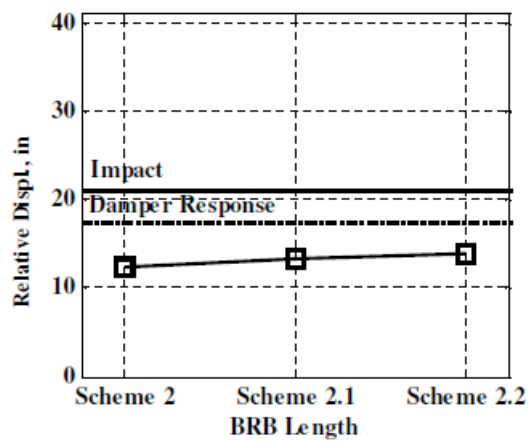
Figure A.11 Local Parameter Refinement: Side/Cable Bent

Location	Parameters			
S-C	$\gamma = 1.05$ $L = \text{Scheme 2}$			
S-T	$\gamma$	1.05		
	$L$	Sch2 = 21 ft	Sch2.1 = 25 ft	Sch2.2 = 30 ft
S-C	$\gamma = 1.05$ $L = \text{Scheme 2}$			

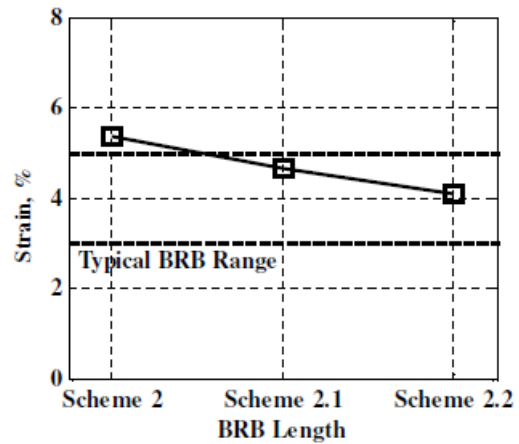
  

$\gamma_{S-T}$	Marker
1.05	

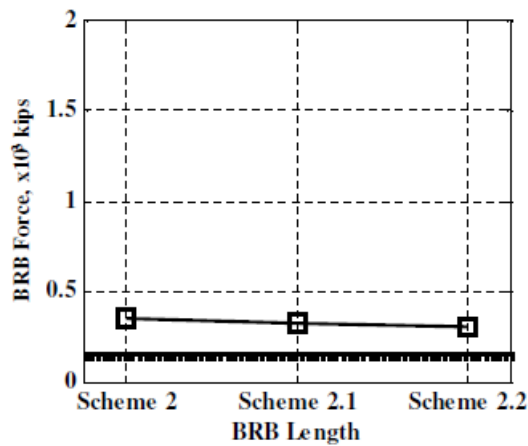
(a) Parameter Information



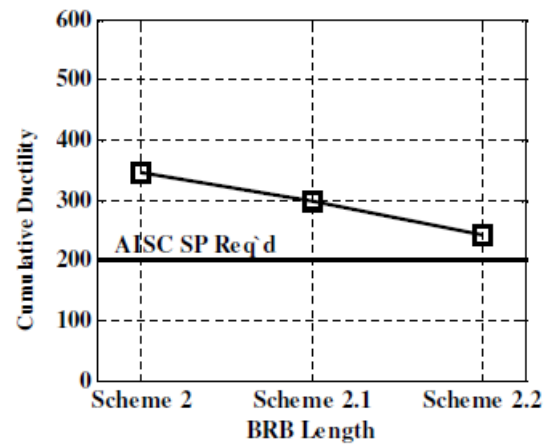
(b) Impact-direction Relative Displacement



(c) Absolute Maximum Strain



(d) Maximum Axial Force



(e) Cumulative Ductility

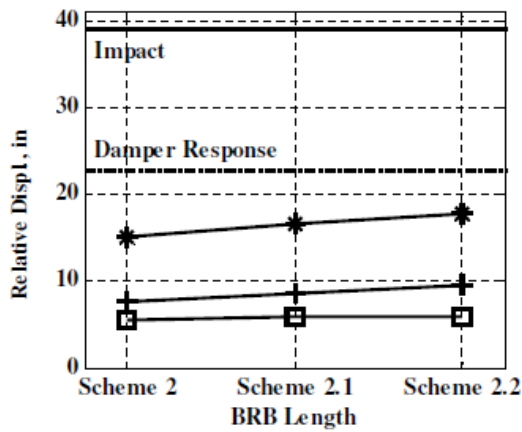
Figure A.12 Localized Parameter Refinement: Side/Tower

Location	Parameters			
S-C	$\gamma = 1.05$ $L = \text{Scheme 2}$			
S-T	$\gamma = 1.05$ $L = \text{Scheme 2}$			
M-T	$\gamma$	0.70	1.05	1.25
	$L$	Sch2 = 21 ft	Sch2.1 = 25 ft	Sch2.2 = 30 ft

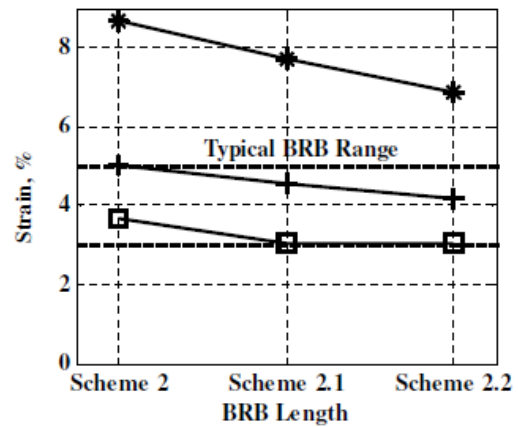
  

$\gamma_{M-T}$	Marker
0.7	—*—
1.05	—+—
1.25	—□—

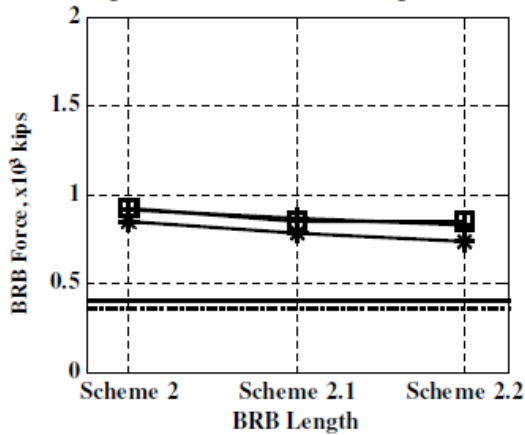
(a) Parameter Information



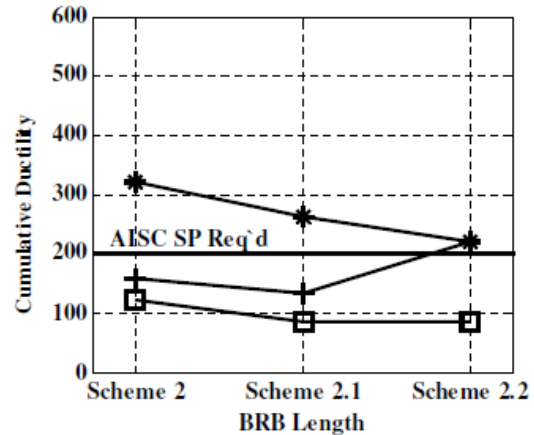
(b) Impact-direction Relative Displacement



(c) Absolute Maximum Strain

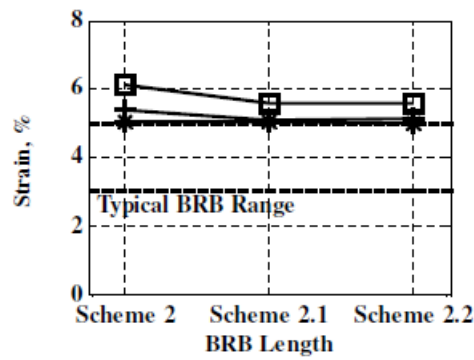


(d) Maximum Axial Force

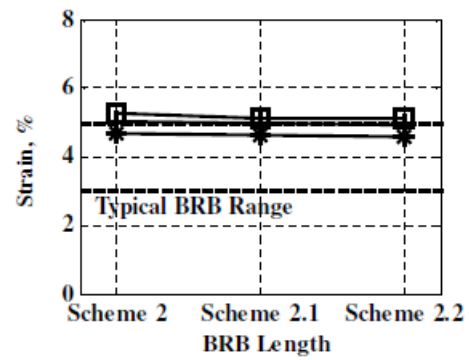


(e) Cumulative Ductility

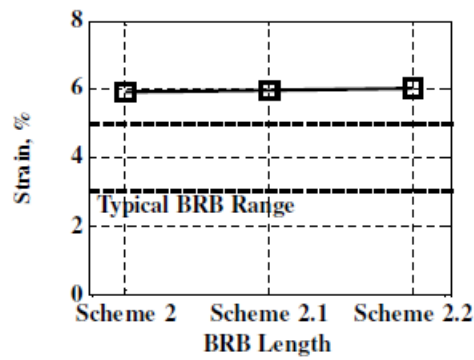
Figure A.13 Localized Parameter Refinement: Main/Tower



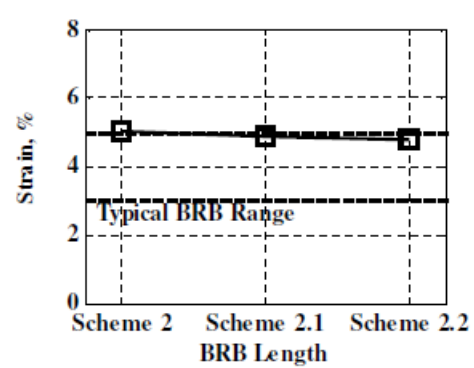
(a) Step 3.1 Side/Tower Max Strain



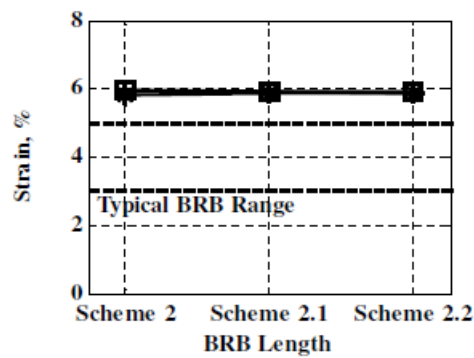
(b) Step 3.1, Main/Tower Max Strain



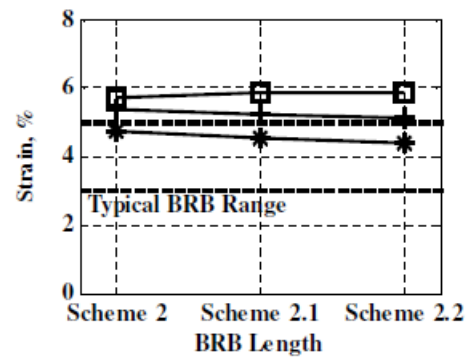
(c) Step 3.2, Cable Bent Max Strain.



(d) Step 3.2, Main/Tower Max Strain



(e) Step 3.3, Cable Bent Max Strain

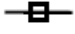


(f) Step 3.3, Side/Tower Max Strain

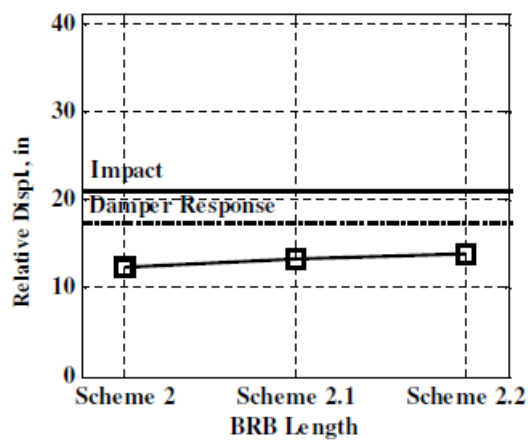
Figure A.14 Local Parameter Refinement: Adjacent Location Insensitivities  
 (For legend see Figure A.12, A.13, and A.14, respectively)

Location	Parameters			
S-C	$\gamma = 1.05$ $L = \text{Scheme 2}$			
S-T	$\gamma$	1.05		
	$L$	Sch2 = 21 ft	Sch2.1 = 25 ft	Sch2.2 = 30 ft
S-C	$\gamma = 1.05$ $L = \text{Scheme 2}$			

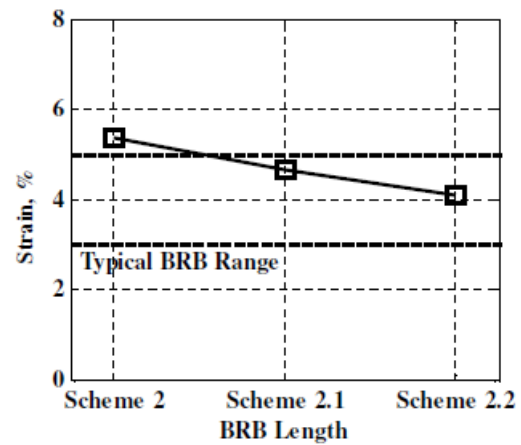
  

$\gamma_{S-T}$	Marker
1.05	

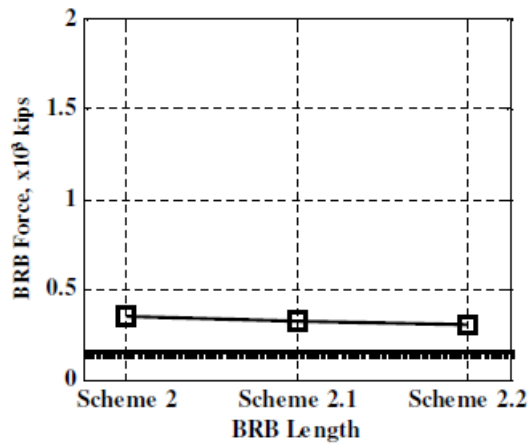
(a) Parameter Information



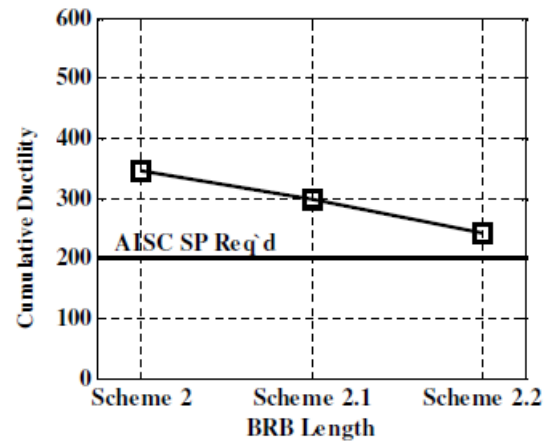
(b) Impact-direction Relative Displacement



(c) Absolute Maximum Strain



(d) Maximum Axial Force



(e) Cumulative Ductility

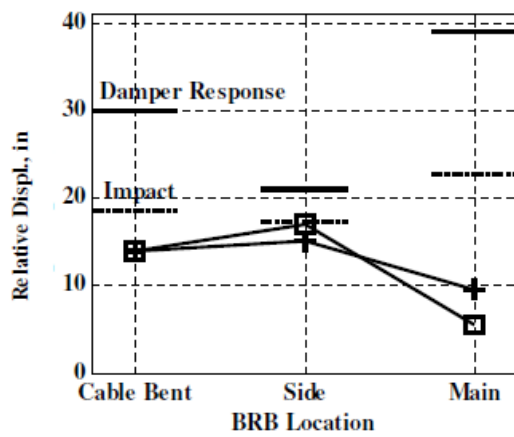
Figure A.15 Final Feasible BRB Solutions

Location	Parameters		
S-C	$\gamma = 1.25$ $L = \text{Scheme 2.1}$		
S-T	$\gamma = 1.05$ $L = \text{Scheme 2.2}$		
M-T	$\gamma$	1.05	1.25
	$L$	Scheme 2.1	Scheme 2.2

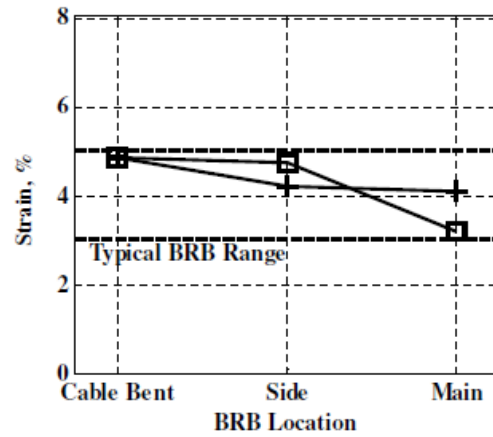
  

$\gamma_{M-T}$	Marker
1.05	+
1.25	□

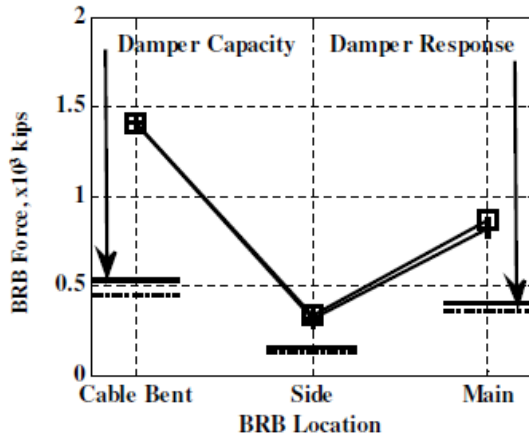
(a) Parameter Information



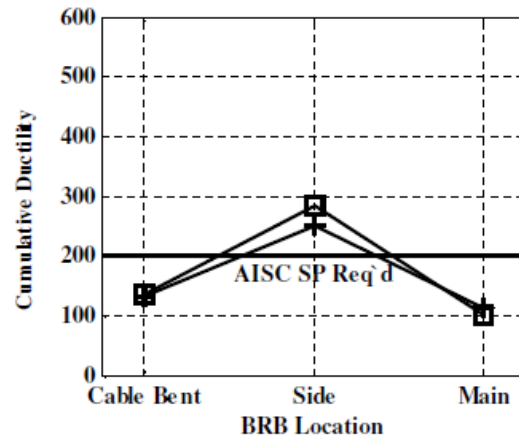
(b) Impact-direction Relative Displacement



(c) Absolute Maximum Strain



(d) Maximum Axial Force



(e) Cumulative Ductility

Figure A.16 Final Feasible BRB Solutions

## APPENDIX B. PROTOCOL DEVELOPMENT GROUND MOTIONS

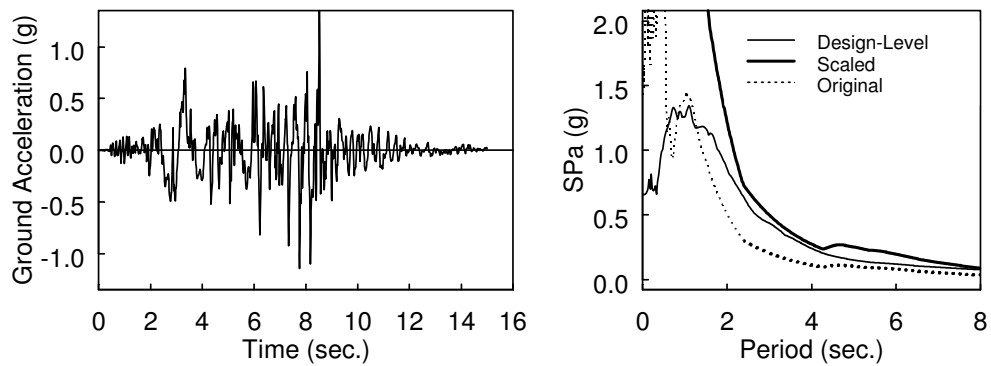
Table B.1 Near-Fault Pulse-Type Ground Motions Used for Near Fault Protocol Development

Rec. No.	Event	NGA No.	PGA * (g)	Epicenter Distance (km)	Mag.	Scale **
1	VTB design-level	N/A	0.66	N/A	N/A	N/A
2	San Fernando (1971)	77	1.43	1.81	6.6	2.41
3	Cape Mendocino (1992)	825	1.27	6.96	7.0	2.51
4	Loma Prieta (1989)	779	0.94	3.88	6.9	1.34
5	Kobe (1995)	1106	0.85	1.00	6.9	1.90
6	San Salvador (1986)	568	0.85	6.30	5.8	2.69
7	Northridge (1994)	1085	0.84	5.19	6.7	1.61
8	Chi-Chi (1999)	1503	0.82	0.60	7.6	1.20
9	Landers (1992)	879	0.72	2.19	7.3	2.84
10	Kobe (1995)	1119	0.65	0.30	6.9	1.74
11	Chi-Chi (1999)	1505	0.56	0.30	7.6	1.28
12	Erzikan, Turkey (1992)	821	0.49	4.40	6.7	1.92
13	Imperial Valley (1979)	182	0.46	0.56	6.5	1.87
14	Superstition Hills (1987)	723	0.42	0.95	6.5	1.66
15	Imperial Valley (1979)	171	0.38	0.07	6.5	2.30
16	Kocaeli, Turkey (1999)	1605	0.36	6.60	7.5	1.76
17	Denali (2002)	2114	0.33	2.70	7.9	1.62
18	Kocaeli, Turkey (1999)	1176	0.28	4.80	7.5	2.09

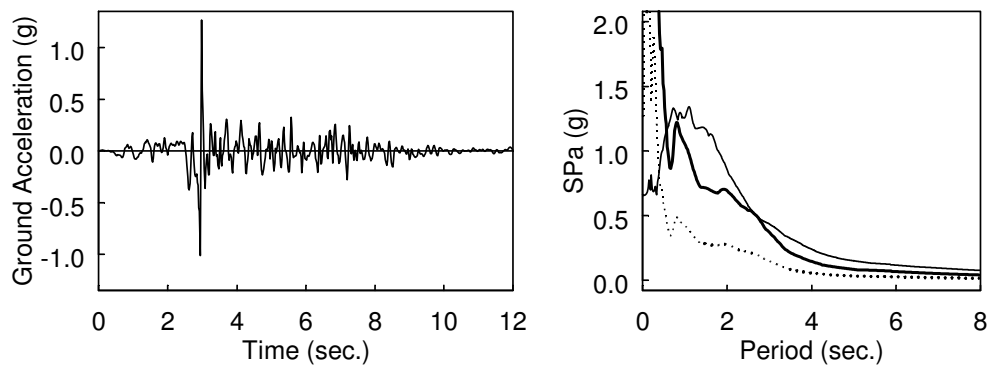
\* Before scaling

\*\* Scaled based on response spectrum within period range of interest

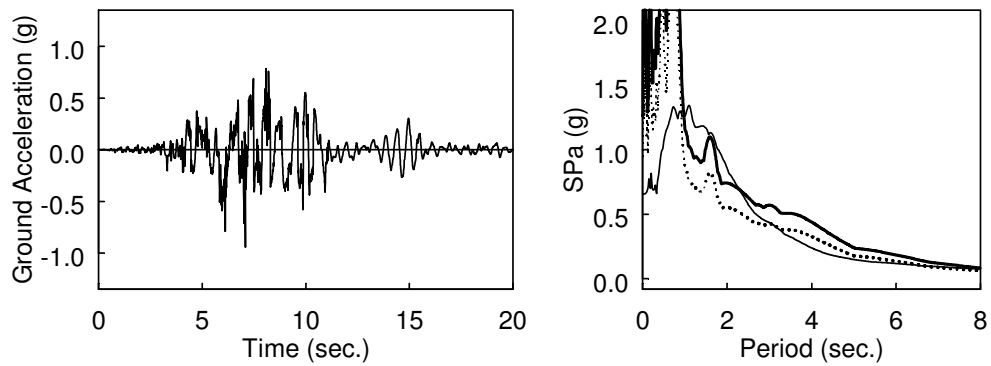
+ Determined from ground velocity



(a) San Fernando (1971)



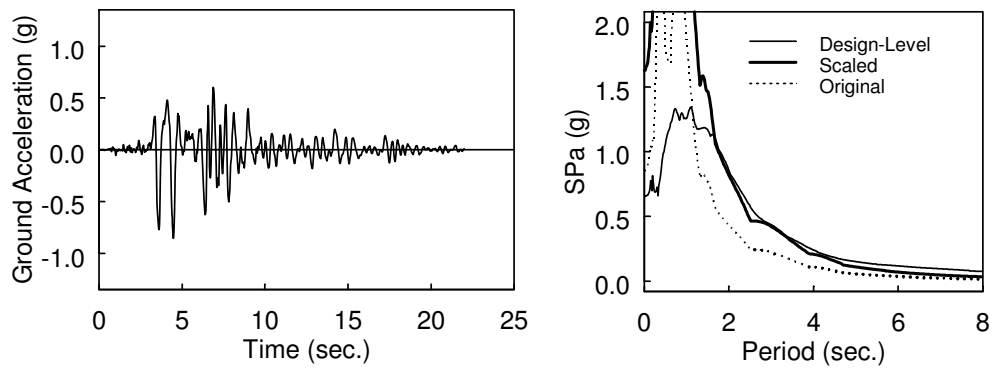
(b) Cape Mendocino (1992)



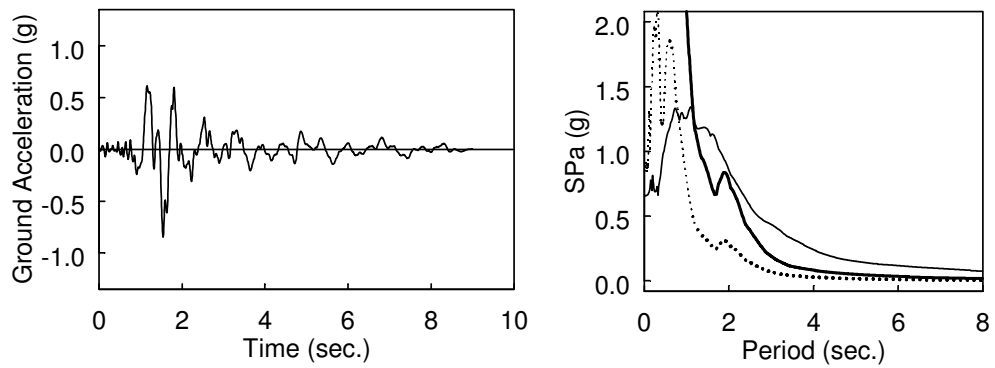
(c) Loma Preita (1989)

Figure B.1 Ground Motions for Near-Fault Protocol Development

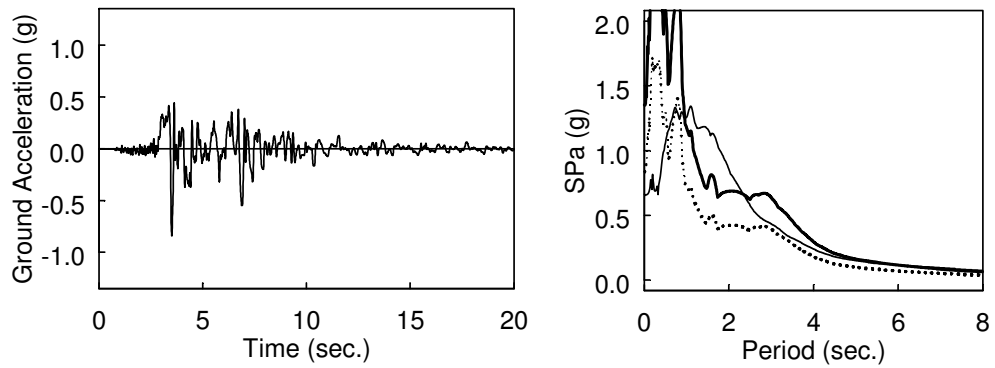




(d) Kobe, NGA 1106 (1995)

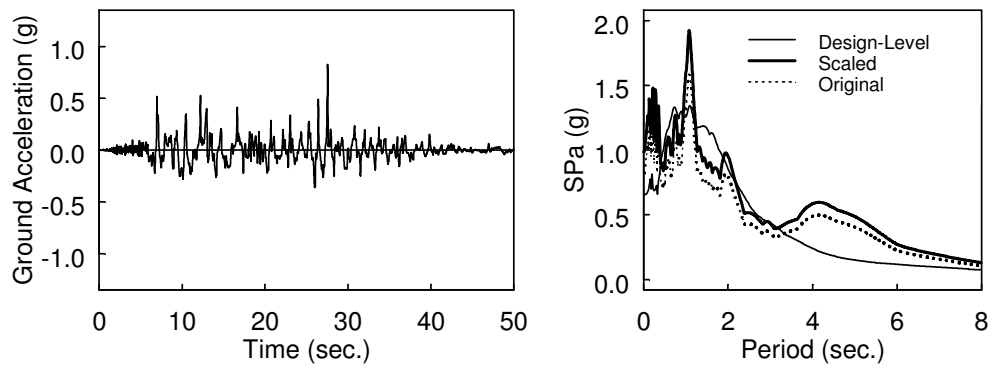


(e) San Salvador (1986)

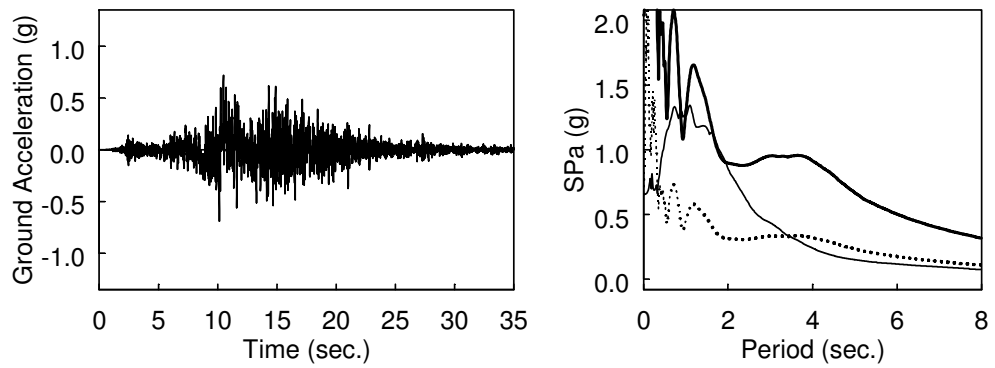


(f) Northridge (1994)

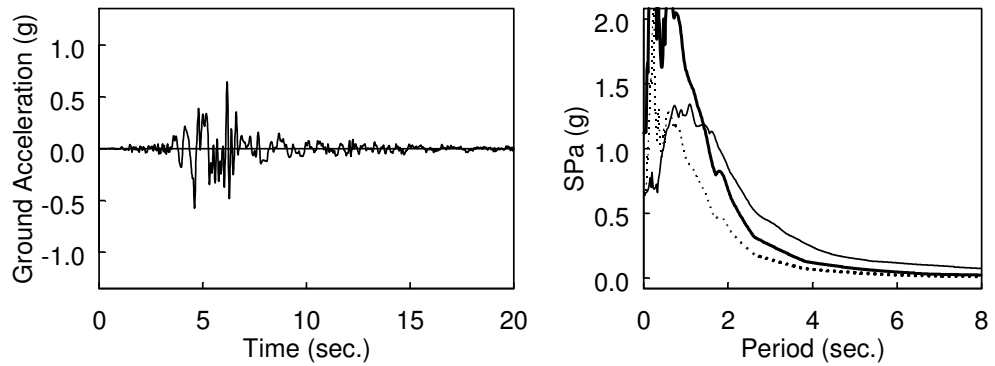
Figure B.1 Ground Motions for Near-Fault Protocol Development (continued)



(g) ChiChi, NGA 1503 (1999)

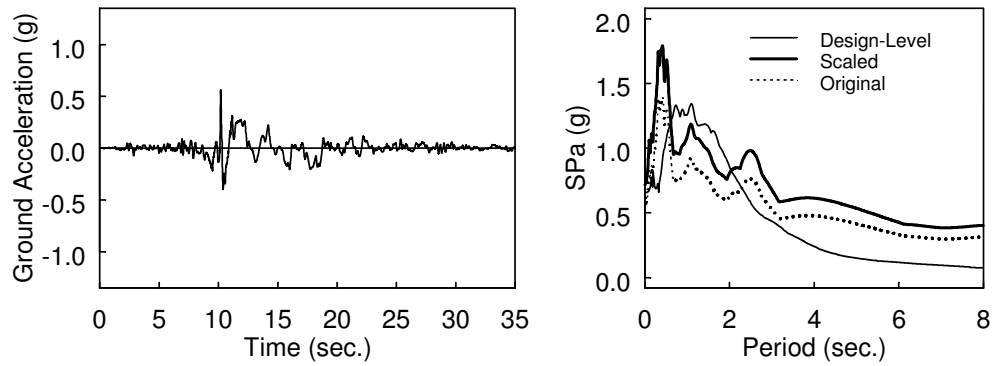


(h) Landers (1992)

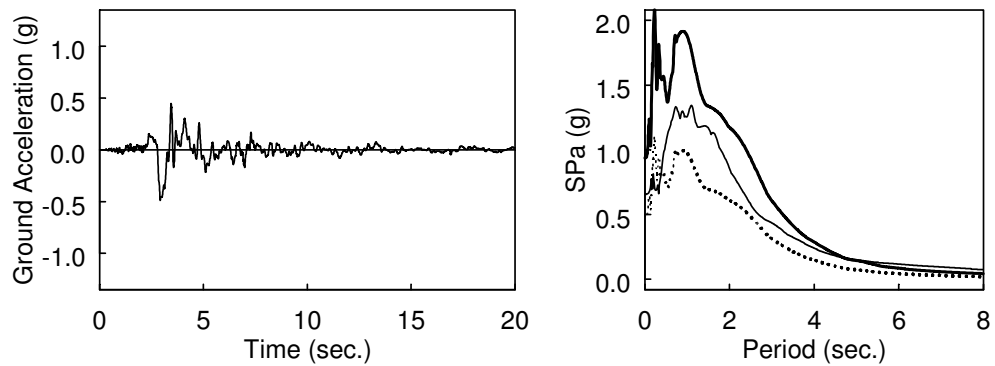


(i) Kobe, NGA 1505 (1995)

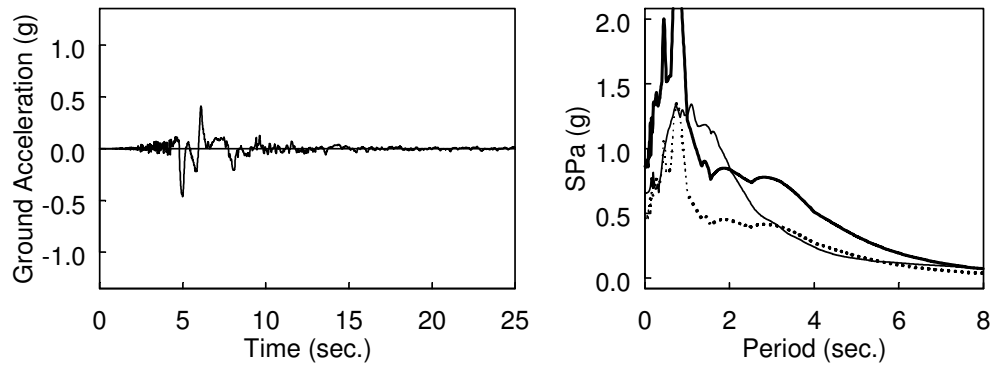
Figure B.1 Ground Motions for Near-Fault Protocol Development (continued)



(j) ChiChi, NGA 1505 (1999)

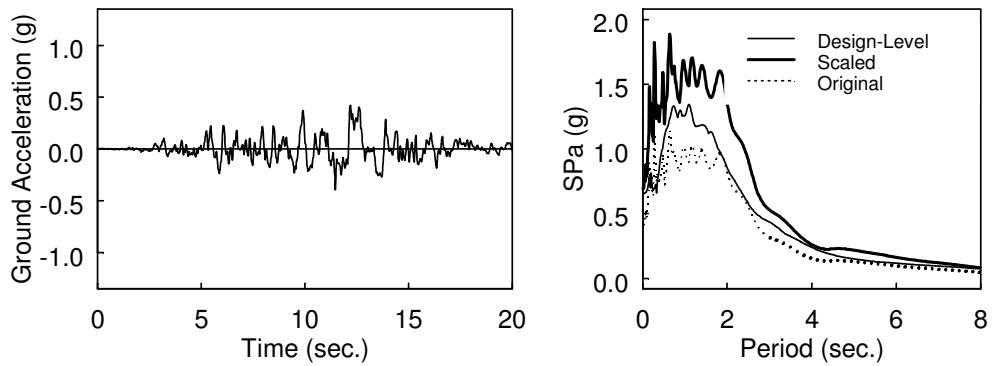


(k) Erzikan, Turkey (1992)

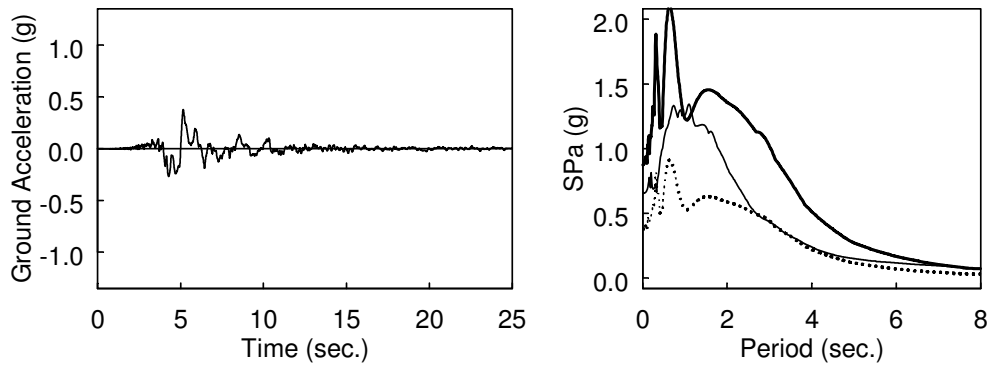


(l) Imperial Valley, NGA 182 (1979)

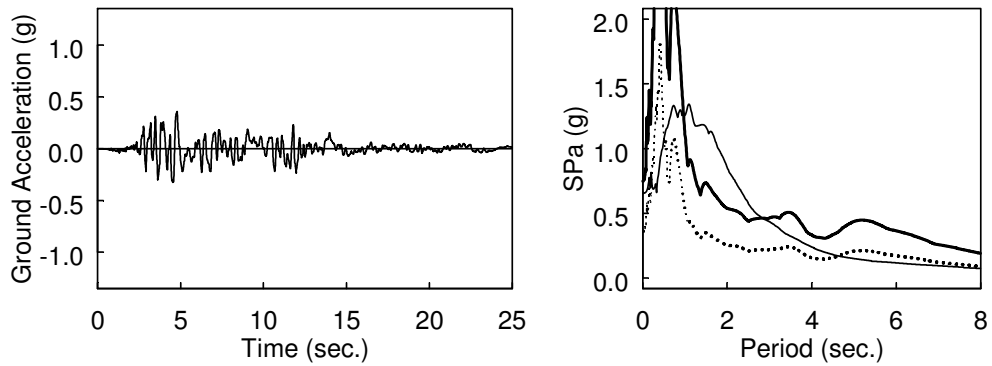
Figure B.1 Ground Motions for Near-Fault Protocol Development (continued)



(m) Superstition Hills (1987)



(n) Imperial Valley, NGA 171 (1979)



(o) Kocaeli, Turkey, NGA 1605 (1999)

Figure B.1 Ground Motions for Near-Fault Protocol Development (continued)

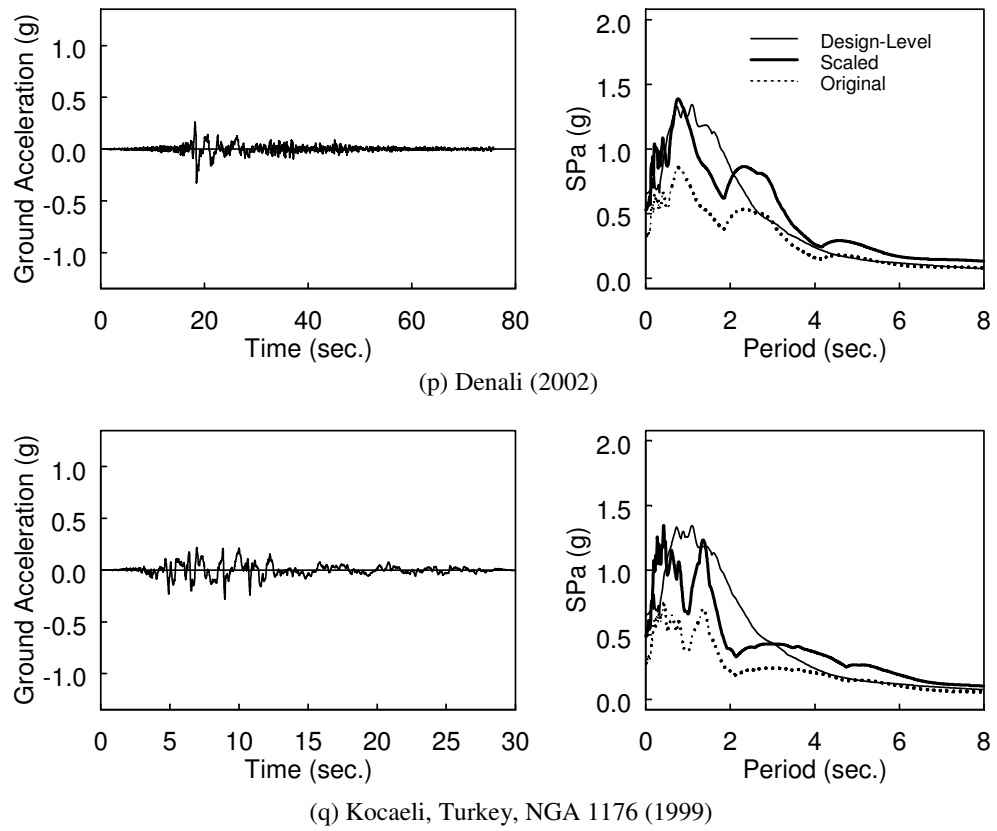


Figure B.1 Ground Motions for Near-Fault Protocol Development (continued)

## APPENDIX C. BRB GUSSET PLATE DIMENSIONS

See Figure 6.1 for gusset plate source.

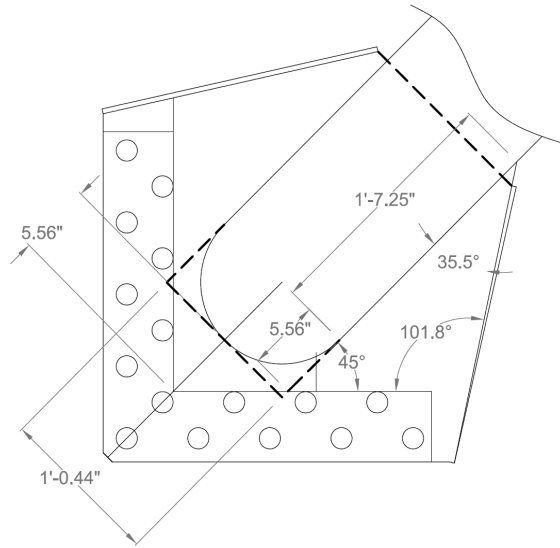


Figure C.1 Specimen 1

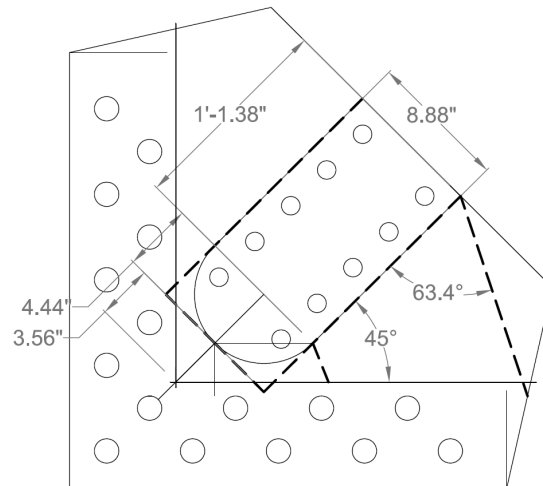


Figure C.2 Specimen 4

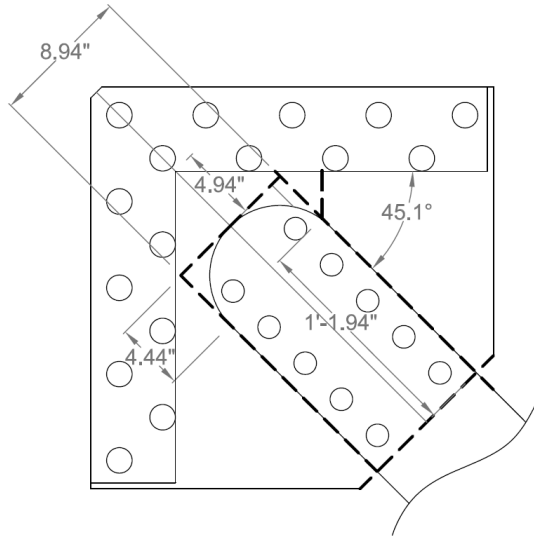


Figure C.3 3P

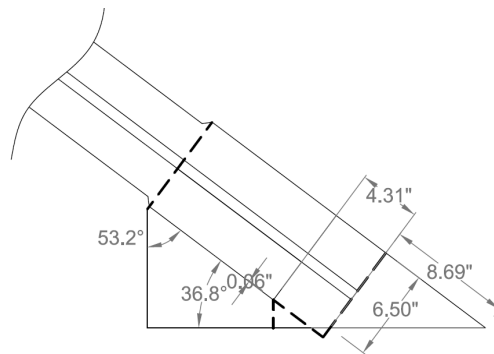
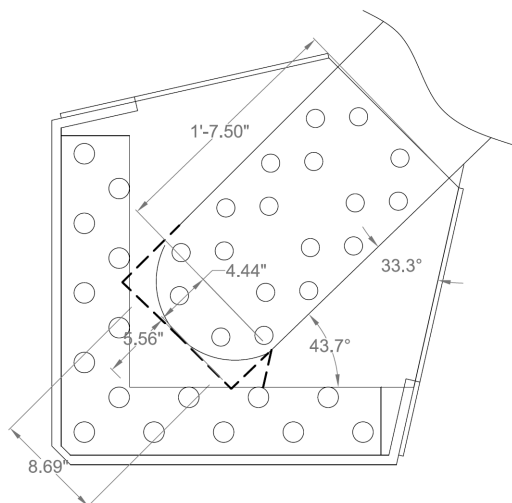
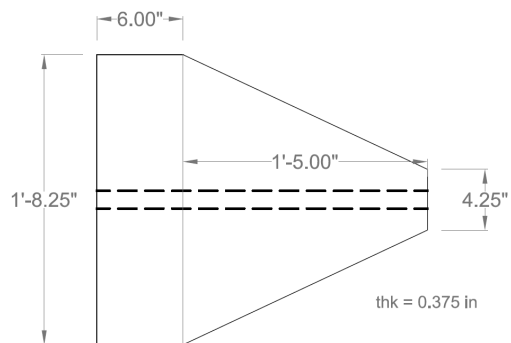


Figure C.5 Tsai 1



(a) Gusset



(b) Stiffeners

Figure C.6 Specimen 5



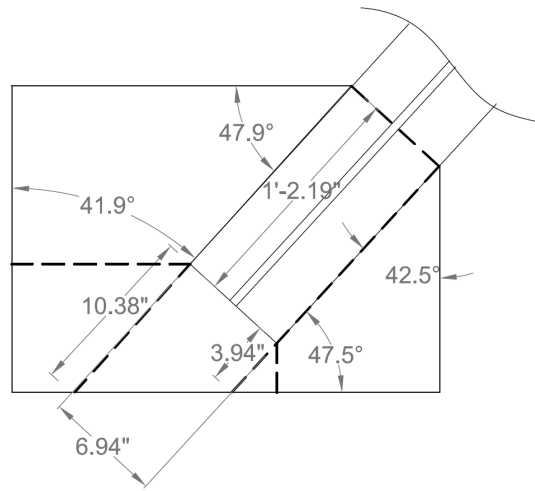


Figure C.7 Tsai 3-1

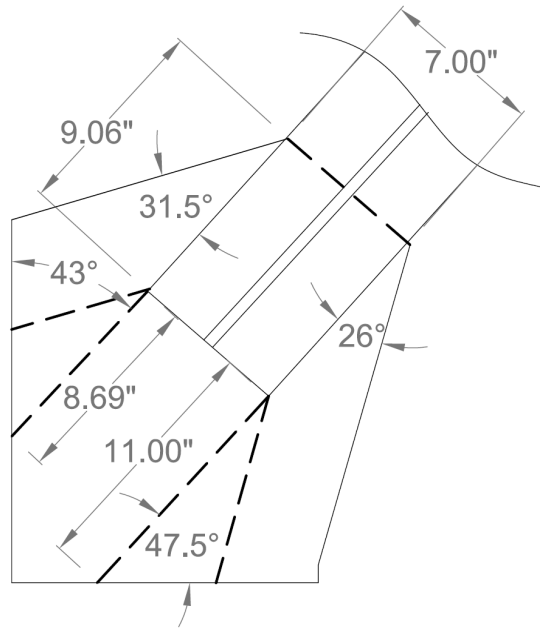


Figure C.8 Tsai 3-3

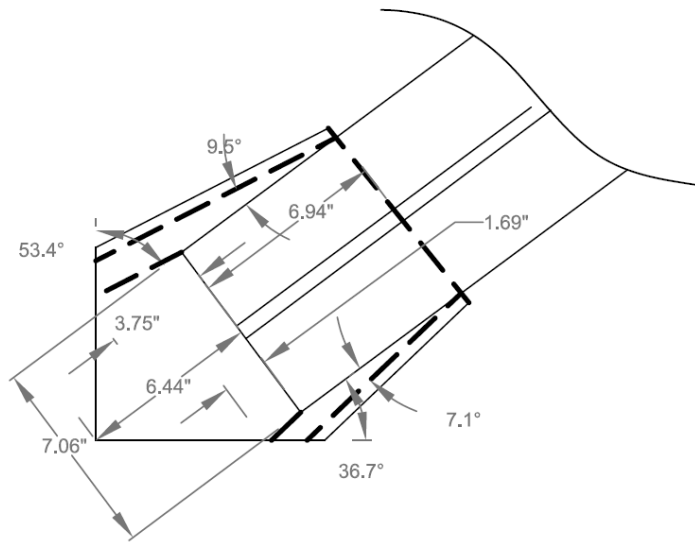


Figure C.9 Takeuchi

## REFERENCES

- (1) AASHTO. (2011). "Guide Specifications for LRFD Seismic Bridge Design." LRFDSEIS-2, Washington D.C.
- (2) ADINA R & D, Inc. (2003). *Automatic Dynamic Incremental Nonlinear Analysis*. ADINA R&D, Inc., Watertown, Massachusetts.
- (3) AISC. (2005). *Code of Standard Practice for Structural Steel Buildings and Bridges*. AISC 303-05, Chicago, IL
- (4) AISC. (2005, 2010). *Seismic provisions for structural steel buildings*. AISC 341, Chicago, IL
- (5) ASCE. (2010). *Minimum design loads for buildings and other structures*. ASCE 7-10, Reston, VA.
- (6) Balan, T., Filippou, F., Popov, E. (1998). "Hysteretic model of ordinary and high-strength reinforcing steel." *J of Struc. Eng.*, 124, 288-297.
- (7) Benzoni, G., Amaddeo, C., DiCesare, A., Palermo, G. (2008). "A damage identification procedure for bridge structures with energy dissipation devices" *Report No. SRMD-2007/09*. Dept. of Structural Engineering, Univ. of California, San Diego, La Jolla, Calif.
- (8) Black, C., Makris, N., Aiken, D. (2004). "Component testing, seismic evaluation and characterization of buckling-restrained braces." *J. Struct. Eng.*, 130(6), 880-894.
- (9) Bruneau, M., Uang, C.M., Sabelli, R. (2011). *Ductile design of steel structures*, McGraw-Hill, Inc.
- (10) Carden, L., Itani, A., Buckle, I., Aiken, I. (2004). "Buckling restrained braces for ductile end cross frames in steel plate girder bridges." *Proc.*, 13th World Conf. on Earthquake Eng., Vancouver, Paper No. 503.
- (11) Chang, K.C., Lee, G. (1987). "Strain rate effect on structural steel under cyclic loading." *J. Eng. Mech.*, 113, 1292-1301.
- (12) Chang, K.H., Jang, G.C., Stiemer, S., Loewen, N. (2013). "Dynamic hysteretic characteristics of high-strength steels (POSTEN60, POSTEN80) and application of dynamic hysteresis model to FE analysis ." *J. Mater. Civ. Eng.*, 25, 1549-1557.

- (13) Chou, C.C., Chen, S.Y. (2010). "Subassemblage tests and finite element analysis of sandwiched buckling-restrained braces." *Eng. Struct.*, 32(8), 2108-2121.
- (14) CESMD (2011) *Information for Strong-Motion Station*, Los Angeles–Vincent Thomas Bridge, CGS–CSMIP Station 14406, [www.strongmotioncenter.org](http://www.strongmotioncenter.org)
- (15) Computers and Structures (2006) *Perform-3D*. CSI Inc., Berkeley, Calif
- (16) Dehghani, M., Tremblay, R. (2012). "Standard dynamic loading protocols for seismic qualification of BRBFs in eastern and western Canada." *Proc.*, 15th World Conf. on Earthquake Eng., Lisbon, Portugal.
- (17) Di Sarno, L., Elnashai, A.S., Nethercot, D.A. (2002). "Comparison between seismic response characteristics of carbon steel and stainless steel." *Proc.*, 12th European Conf. Earthquake Eng., London, Paper No. 765.
- (18) Dodd, L., Restrepo, J. (1995). "Model for predicting cyclic behaviour of reinforcing steel" *J. of Struct. Eng.*, 121(3), 433-445.
- (19) Fell, B., Kanvinde, A., Deierlein, G., Myers, A. (2009). "Experimental investigation of inelastic cyclic buckling and fracture of steel braces." *J. Struct. Eng.*, 135, 19-32.
- (20) Filippou, F., Popov, E., Bertero, V. (1983) "Effects of bond deterioration on hysteretic behavior of reinforced concrete joints." *Report No. UCB/EERC-83/19*, Earthquake Engineering Research Center, Univ. of Calif, Berkeley, 1983-08, 184
- (21) Fragiadakis, M., Pinho, R., Antoniou, S. (2007) "Modelling inelastic buckling of reinforcing bars under earthquake loading" *Proc.*, ECCOMAS Thematic Conf. on Comp. Methods in Struct. Dyn. and Earthquake Eng., Rethymno, Crete, Greece
- (22) Graziotti, F. (2010). "Seismic bridge response modification due to degradation of viscous dampers." *Thesis*. Dept. of Structural Engineering, Univ. of California San Diego, La Jolla, Calif.
- (23) Hasegawa, H., Takeuchi, T., Iwata, M., Yamada, S., and Akiyama, H. (1999). "Dynamic performances of unbonded braces." *AIJ Technical Rep. No. 9*. 103-106 (in Japanese)
- (24) He, X., Moaveni, B., Conte, J., Elgamal, A., Masri, S. (2008). "Modal identification study of Vincent Thomas Bridge using simulated wind-induced ambient vibration data." *Computer-Aided Civil and Infrastrct. Eng.* 2008, 5(23), 373-388

- (25) Hikino T., Okazaki, T., Kajiwara, K., Nakashima, M. (2013) "Out-of-plane stability of buckling-restrained braces placed in chevron arrangement" *J. Struc. Eng.*, 139, 1812-1822.
- (26) Infanti, S., Papanikolas, P., Benzoni, G., Castellano, M.G., (2004). "Rion-Antirion bridge: Design and full-scale testing of the seismic protection devices." *Proc.*, 13th World Conf. Earthquake Eng., Vancouver, Canada, Paper No. 2174.
- (27) Ingham, T J., Rodriguez, S., Nader, M. (1997). "Nonlinear analysis of the Vincent Thomas Bridge for seismic retrofit.." *Computers and Structures*, 64(5), 1221-1238.
- (28) Iwata, M., (2004). "Applications-design of buckling restrained braces in Japan." *Proc.*, 13th World Conf. Earthquake Eng., Vancouver, Canada, Paper No. 3208.
- (29) Kanaji, H., Kitazawa, M., Suzuki, N., (2005). "Seismic retrofit strategy using damage control design concept and the response reduction effect for a long-span truss bridge." *Proc.*, US-Japan Bridge Workshop, Tsukuba, Japan.
- (30) Kaufmann, E.J., Metrovich, B.R., Pense, A.W. (2001). "Characterization of cyclic inelastic strain behavior on properties of A572 Gr. 50 and A913 Gr. 50 rolled sections." *ATLSS Report No. 01-13*, Lehigh University, Bethlehem, PA.
- (31) Kim, J., Choi, H. (2004). "Behavior and design of structure with buckling-restrained braces." *Eng. Struct.*, 26(6), 693-706.
- (32) Koetaka, Y., Kinoshita, T., Inoue, K., Iitani, K. (2008) "Criteria of buckling-restrained braces to prevent out-of-plane buckling"
- (33) Krawinkler, H. (1983). "Recommendations for experimental studies on the seismic behavior of steel components and materials." *John A. Blume Center Report No. 61*. Dept. of Civil Engineering, Stanford Univ., Stanford, Calif.
- (34) Krawinkler, H. (1992). "Guidelines for cyclic seismic testing of components of steel structures." *ATC-24*, Applied Technology Council, Redwood City, Calif.
- (35) Lanning, J., Benzoni, G., Uang, C.M. (2011). "The feasibility of using buckling-restrained braces for long-span bridges: A case study." *Report No. SSRP 11/09*. Dept. of Structural Engineering, Univ. of California, San Diego, La Jolla, Calif.
- (36) Lanning, J., Uang, C.M., Benzoni, G. (2012) "Subassemblage testing of CoreBrace buckling-restrained braces (P-Series)" *Report No. TR-12/03*. Dept. of Structural Engineering, Univ. of California, San Diego, La Jolla, Calif.

- (37) Lanning, J., Benzoni, G., Uang, C.M., (2013). "The feasibility of using buckling-restrained braces for long-span bridges: Near-fault loading protocols and full-scale testing." *Report No. SSRP 13/17*. Dept. of Structural Engineering, Univ. of California, San Diego, La Jolla, Calif.
- (38) Lanning, J., Benzoni, G., Uang, C.M. (2014). "Using buckling-restrained braces on long-span bridges: Full-scale testing and design implications." *Submitted to J. Bridge Eng.*, ASCE.
- (39) Lanning, J., Benzoni, G., Uang, C.M. (2014). "Using buckling-restrained braces on long-span bridges: Case study and near-fault loading protocol development." *Submitted to J. Bridge Eng.*, ASCE.
- (40) Lanning, J., Uang, C.M. (2014). "Full-scale BRB testing: Dynamic near-fault protocols." Online video clip. *YouTube*, Dec. 13, 2012, Web. Feb. 11, 2014.
- (41) Lehman, D., Roeder, C., Herman, D., Johnson, S., Kotulka, B. (2008) "Improved seismic performance of gusset plate connections." *J. Struct. Eng.*, 134, 890-901.
- (42) Mahin S., Uriz, P., Aiken, I., Field, C., Ko, E. (2004) "Seismic performance of buckling restrained braced frame systems." *Proc. 13th World Conf. on Earthquake Eng.*, Paper No, 1681, Tokyo, Japan.
- (43) McKenna, F., Fenves, G. L., Scott, M. H., and Jeremic, B., (2000). Open System for Earthquake Engineering Simulation (OpenSees). Pacific Earthquake Engineering Research Center, University of California, Berkeley, CA.
- (44) Merritt, S., Uang, C.M., Benzoni, G. (2003) "Subassembly testing of Corebrace buckling-restrained braces" *Report No. TR 03/01*. Dept. of Structural Engineering, Univ. of California, San Diego, La Jolla, Calif.
- (45) Moaveni, B., Asgari, E. (2012) "Deterministic-stochastic subspace identification method for identification of nonlinear structures as time-varying linear systems." *Mech. Systems and Signal Processing*, 31, 40-55.
- (46) Moffatt and Nichol Engineers (1996). "Toll road seismic retrofit project Vincent Thomas Bridge, strategy report." *Report to Caltrans*.
- (47) Newell, J., Uang, C.M., Benzoni, G. (2006). "Subassembly testing of CoreBrace buckling-restrained braces (G Series)." *Testing Report No. TR-06/01*. Dept. of Structural Engineering, Univ. of California, San Diego, La Jolla, Calif.
- (48) Nordberg, H. (2004) "Note on the sensitivity of SSs to strain rate." *Research Report No. 04-0-1*, AvestaPolarit Research Foundation.

- (49) Nip, K.H., Gardner, L., Davies, C.M., Elghazouli, A.Y. (2010). "Extremely low cycle fatigue tests on structural carbon steel and stainless steel." *J. Constr. Steel Research*, 66, 96-110.
- (50) Celik, O., Bruneau, M. (2009). "Seismic behavior of bidirectional-resistant ductile end diaphragms with buckling restrained braces in straight steel bridges." *Eng. Struct.*, 31(2), 380-393.
- (51) Paul, S.K., Sivaprasad, S., Dhar, S., Tarafder, S. (2010). "Cyclic plastic deformation and cyclic hardening/softening behavior in 304LN stainless steel." *Theor. App. Fract. Mech.*, 54, 63-70.
- (52) Pollino, M., Bruneau, M. (2007). "Seismic retrofit of bridge steel truss piers using a controlled rocking approach." *J. Bridge Eng.*, ASCE, 12(5), 600-610.
- (53) Ravi K.G., Satish, S.R., Kalyanaraman, V. (2007). "Behaviour of frames with non-buckling bracings under earthquake loading." *J. Constr. Steel Research*. 63(2), 254-262.
- (54) Reno, M., Pohll, M., (2010). "Seismic retrofit of California's Auburn-Foresthill bridge." *Transp. Research Rec.: J. Transp. Research Board*, 2201, 83-94.
- (55) Richards, P., Uang, C.M. (2006). "Testing protocols for short links in eccentrically braced frames." *J. of Struct. Eng.* 132(8), 1183-1191
- (56) Sabelli, R., Mahin, S., Chang, C., (2003). "Seismic demands on steel braced frame buildings with buckling-restrained braces." *Eng. Struct.*, 25(5), 655-666.
- (57) Seible, F. (2000) "Long span bridges in California – Seismic design and retrofit issues" *Proc.*, 12th World Conf. on Earthquake Eng., Paper No. 2614
- (58) Simula (2011), *Abaqus*, Standard Version 6.11.2. Dassault Systemes Simulia Corp. Providence, RI
- (59) Soroushian, P., Choi, K.B. (1987). "Steel mechanical properties at different strain rates." *J. Struct. Eng.* 113, 663-672.
- (60) Takeuchi, T., Ozaki, H., Matsui, R., Sutcu, F. (2013) "Out-of-plane stability of buckling-restrained braces including moment transfer capacity" *Earthquake Eng. Struc. Dyn.*, 43, 851-869.
- (61) Tremblay, R., and Bouatay, N. (2002). "Loading protocols for the seismic testing of ductile bracing members in concentrically braced steel frames." *Proc.*, 12th European Conf. on Earthquake Eng., London, Paper No. 480.

- (62) Tremblay, R., Bolduc, P., Neville, R., DeVall., R., (2004). "Testing and design of buckling restrained braces for Canadian application." *Proc.*, 13th World Conf. on Earthquake Eng., Vancouver B.C., Paper No. 2893
- (63) Tremblay, R., Bolduc, P., Neville, R., DeVall., R., (2006). "Seismic testing and performance of buckling-restrained bracing systems." *Canadian J. Civil Eng.*, 33(2), 183-198.
- (64) Tsai, K.C., Lai, J.W., Hwang., Y.C., Lin, S.L., Weng, Y.T., (2004). "Research and application of double-core buckling restrained braces in Taiwan." *Proc.*, 13th World Conf. Earthquake Eng., Vancouver, Canada.
- (65) Uang, C.M., Nakashima, M., Tsai, K.C., (2004). "Research and application of buckling-restrained braced frames." *Intrn. J. Steel Struct.*, 4, 301-313.
- (66) Usami, T., Lu, Z., Ge, H.B., (2005). "A seismic upgrading method for steel arch bridges using buckling-restrained braces." *Earthquake Eng. Struct. Dyn.*, 34(4-5), 471-496.
- (67) Usami, T., Hanbin, G., Luo, X.Q. (2009). "Experimental and analytical study on high-performance buckling restrained brace dampers for bridge engineering" *Proc. 3rd Intern. Conf. on Adv. in Exper. Struct. Eng.*, San Francisco, Calif.
- (68) Yamaguchi, M., Yamada, S., Takeuchi, T., Wada, A. (2004). "Seismic performance of buckling resistant brace within a steel frame in the case of ultimate earthquake.." *J. Constr. Steel*, 12 207-210. (in Japanese)
- (69) Zhang, R. (2000) Ch. 41: "Seismic isolation and supplemental energy dissipation" *Bridge Engineering Handbook*, CRC Press, Boca Raton, FL.